Springer-Verlag Berlin Heidelberg GmbH

Physics of Earth and Space Environments

www.springeronline.com

The series *Physics of Earth and Space Environments* is devoted to monograph texts dealing with all aspects of atmospheric, hydrospheric and space science research and advanced teaching. The presentations will be both qualitative as well as quantitative, with strong emphasis on the underlying (geo)physical sciences. Of particular interest are

- contributions which relate fundamental research in the aforementioned fields to present and developing environmental issues viewed broadly
- concise accounts of newly emerging important topics that are embedded in a broader framework in order to provide quick but readable access of new material to a larger audience

The books forming this collection will be of importance for graduate students and active researchers alike.

Series Editors:

Professor Dr. Rodolfo Guzzi
Responsabile di Scienze della Terra
Head of Earth Sciences
Via di Villa Grazioli, 23
00198 Roma, Italy

Professor Dr. Dieter Imboden
ETH Zürich
ETH Zentrum
8092 Zürich, Switzerland

Dr. Louis J. Lanzerotti
Bell Laboratories, Lucent Technologies
700 Mountain Avenue
Murray Hill, NJ 07974, USA

Professor Dr. Ulrich Platt
Ruprecht-Karls-Universität Heidelberg
Institut für Umweltphysik
Im Neuenheimer Feld 366
69120 Heidelberg, Germany

S. J. Bauer H. Lammer

Planetary Aeronomy

Atmosphere Environments in Planetary Systems

With 62 Figures

Springer

Professor Dr. Siegfried J. Bauer
Karl-Franzens-Universität Graz
Institut für Geophysik, Astrophysik und Meteorologie
Universitätsplatz 5
8010 Graz
Austria

Dr. Helmut Lammer
Österreichische Akademie der Wissenschaften
Institut für Weltraumforschung
Schmiedlstr. 6
8042 Graz
Austria

Library of Congress Control Number: 2004103352

ISSN 1610-1677

ISBN 978-3-642-05990-2 ISBN 978-3-662-09362-7 (eBook)
DOI 10.1007/978-3-662-09362-7

This work is subject to copyright. All rights are reserved, whether the whole or part of the material is concerned, specifically the rights of translation, reprinting, reuse of illustrations, recitation, broadcasting, reproduction on microfilm or in any other way, and storage in data banks. Duplication of this publication or parts thereof is permitted only under the provisions of the German Copyright Law of September 9, 1965, in its current version, and permission for use must always be obtained from Springer-Verlag Berlin Heidelberg GmbH. Violations are liable to prosecution under the German Copyright Law.

springeronline.com

© Springer-Verlag Berlin Heidelberg 2004
Originally published by Springer Berlin Heidelberg New York in 2004
Softcover reprint of the hardcover 1st edition 2004

The use of general descriptive names, registered names, trademarks, etc. in this publication does not imply, even in the absence of a specific statement, that such names are exempt from the relevant protective laws and regulations and therefore free for general use.

Typesetting by the authors
Print data prepared by PTP-Berlin Protago-TeX-Production, Germany
Cover design: Erich Kirchner, Heidelberg

Printed on acid-free paper 54/3141/ts - 5 4 3 2 1 0

Preface

Aeronomy, a part of atmospheric science, is defined as the study of the physics and chemistry of the upper atmosphere of a planet. The name was coined about 50 years ago by a pioneer of this discipline, the British geophysicist Sydney Chapman, to differentiate it from *meteorology*, which is concerned with the lower atmosphere where the prevailing weather phenomena can be described by bulk properties of a gas. In contrast to this, aeronomy, dealing with the tenuous upper part of the atmosphere, must apply a gas kinetic approach, describing processes such as molecular diffusion and heat conduction as well as photochemical processes such as dissociation and ionization of gases.

Sydney Chapman himself is credited with such fundamental contributions to aeronomy as the formation of stratospheric ozone and the theory of ionospheric layer formation, which carries his name, as well as with the highly useful concept of atmospheric scale height. Beyond photochemistry, aeronomy is also concerned with atmospheric escape by thermal and non-thermal processes that are playing an important role in the evolution of planetary atmospheres.

The present book is not intended as a traditional textbook but rather as a compendium of the most important physical and chemical processes occurring in planetary atmospheres. Most of the material is taken in slightly modified or corrected form from the monograph by one of us (SJB), *Physics of Planetary Ionospheres*, published by Springer Verlag thirty years ago (1973) as Vol. 6 of the series "Physics and Chemistry of Space", which had a similar purpose: to address the physical and chemical processes that lead to the formation of ionized layers, as well as to the heating of the thermosphere as the result of the interaction of ionizing radiation with a neutral atmosphere. The references cited in the text therefore are a selective mix of "old" and new contributions with a separate bibliography containing comprehensive reviews of topics covered by this monograph.

Just as the "old" book was intended to concentrate on the underlying physical processes for explaining observations then expected as the result of the early exploration by space probes of the planets and moons in our Solar System, the new version, called *Planetary Aeronomy*, aims at providing in succinct form also the physical background to be applied to information about

the atmospheric environments and evolution of planets outside our Solar System, the so-called exoplanets, whose atmospheres will become observable at an increasing rate during the next few decades by space missions like ESA's Darwin and NASA's Terrestrial Planet Finder (TPF) (launch foreseen in the second decade of this century) and their precursors like CoRoT (Convection Rotation and planetary Transits; CNES, launch 2006), Kepler (NASA, launch 2007), Eddington (NASA), etc. that are currently under development.

Our book does not contain sophisticated *models*, some already in the literature, but rather limits itself to their *physical background*. It is in consonance with an adage attributed to Aristotle: *It is the mark of an instructed mind to rest satisfied with the degree of precision which the nature of the subject permits and not to seek an exactness where only an approximation of the truth is possible!*

Graz, February 2004 S.J. Bauer and H. Lammer

Contents

Introduction

For almost 50 years investigations of the Earth's upper atmosphere have provided comprehensive knowledge about the subdiscipline of atmospheric science, now generally known as aeronomy. Since the advent of the space age observations made by spacecraft have made some of the traditional sciences into a "space science". This is particularly true of the possibilities created for astronomical observations outside our Earth's atmosphere with complex astronomical observatories, which have led to an unprecedented increase of information about stellar radiation sources beyond our own Sun.

While "visible" radiation from a stellar source usually penetrates the atmosphere of a planet down to its surface (unless blocked by clouds and dust particles), the "short wave" radiation of high photon energy in the extreme ultraviolet and X-ray (XUV) part of the spectrum is generally absorbed in the more tenuous part of the upper atmosphere by its constituents, leading to dissociation of molecular species, ionization and heating. Thus, properties of this radiation (including its long term evolution) and the neutral atmosphere with which it interacts, as well as the results of this interaction, i.e., heating leading to its characteristic temperature, the formation of ionized layers and the attendant photochemistry as well as transport processes of the neutral and ionized species, have to be considered in the treatment of aeronomical processes.

As the result of the low particle concentrations reached at the high altitudes on account of the exponential decay of pressure and density, collisions among gas particles become increasingly less important, so that a gas kinetic theory approach has to be used. In the limit the upper part of a gravitationally bound atmosphere, the "exosphere" becomes essentially collisionless, so that particles arising from below with sufficient velocities can even escape and this leads to a loss of atmospheric constituents to space due to their thermal motion. Beyond this, escape can also occur via photochemical processes and plasma processes (i.e., interaction of stellar winds with ionospheric plasma, when there is no protective planetary magnetic field).

In the following chapters we discuss in a succinct fashion the relevant properties and processes, keeping in mind the more general case of planets (and their satellites) even beyond our own Solar System, the so-called exoplanets, and their stellar energy sources. Although most of our knowledge

about aeronomical processes has been gained from the study of our own Solar System, they obviously can be applied to extrasolar planetary systems.

In spite of the broad general adherence to the "International System" of units (SI), some scientific disciplines (including our own) are still using units based on the old cgs system (particularly the length scale centimeters instead of meters) even in the recent published international literature. In this book we therefore adhere to the same custom, although providing the appropriate conversions in the text and the appendix. In addition commonly used units in astronomy and aeronomy as well as numerical values for planetary bodies are also given in the appendix.

I Radiation and Particle Environments from Stellar and Cosmic Sources

The principal ionizing radiation responsible for the heating of the upper planetary atmospheres and the formation of planetary ionospheres from stellar or solar sources are extreme ultraviolet and X-rays (XUV) and corpuscular radiation, i.e., galactic cosmic rays and energetic particles having their origin in stellar systems (cosmic ray protons, auroral particles, stellar wind).

The atmosphere of a planet can be divided into a number of regions. It is quite natural that the terminology which has evolved for the terrestrial atmosphere should also be applied to other planetary atmospheres. The terminology which is generally accepted is based on the vertical distribution of temperature and composition, i.e., the parameters necessary for describing an atmosphere for which the hydrostatic condition can be used.

In terms of the temperature variation, a planetary atmosphere can be divided as follows (see Fig. 1.1). The lowermost part of the atmosphere is the *troposphere*, where the primary heat source is the planetary surface and heat is convected by turbulent motion. This leads to a convective or adiabatic temperature distribution. The vertical temperature gradient $\partial T/\partial z$, or adiabatic lapse rate is given by $\partial T/\partial z = -g/c_\mathrm{p}$, where g is the acceleration of gravity and c_p is the specific heat at constant pressure. It is therefore dependent on the planet's acceleration of gravity and the atmospheric composition. For Earth, the observed adiabatic lapse rate is about -6.5 K/km due to the presence of water vapor and large-scale planetary motions.

The troposphere terminates at the *tropopause*, the level at which the temperature decrease with an adiabatic lapse rate ceases. Above the tropopause the temperature distribution is governed by radiative rather than convective processes and the temperature decreases much more slowly ($|\partial T/\partial z| < g/c_\mathrm{p}$) or becomes essentially constant ($\partial T/\partial z \simeq 0$). For Earth the tropopause occurs at an altitude of about 13 km. Above the actual tropopause is the *stratosphere*. This region was originally thought to be isothermal throughout. In the terrestrial stratosphere the temperature, after being initially constant, increases with altitude due to the ultraviolet (UV) absorption by ozone (O_3), reaching a temperature maximum at the *stratopause* (about 50 km). Above this level the *mesosphere* begins, where $\partial T/\partial z < 0$, reaching a temperature minimum at the *mesopause* (Earth: about 85 km), due to the presence of CO_2 and H_2O which provide a heat sink by radiating in the infrared. Above the

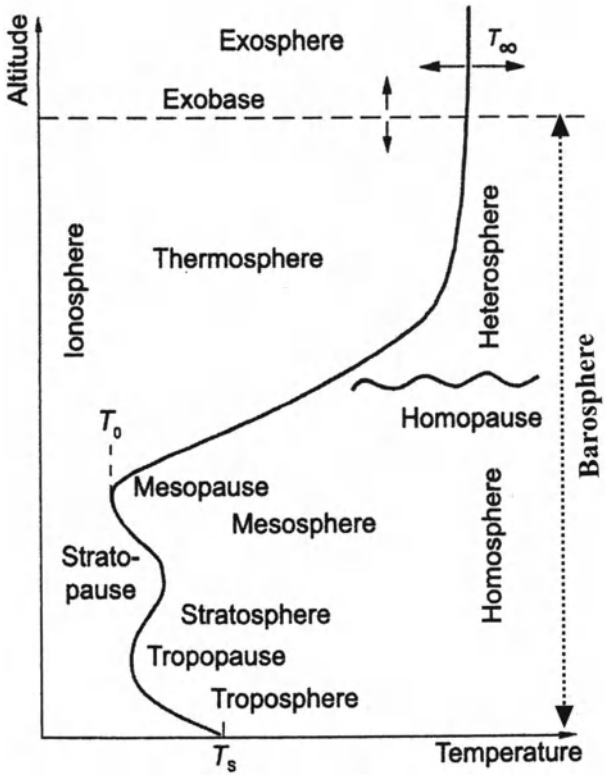

Fig. 1.1. Nomenclature of atmospheric regions based on terrestrial analogies.

mesopause, XUV radiation is absorbed and in part is used for heating, leading to a positive temperature gradient, $\partial T/\partial z > 0$. This region is called the *thermosphere*. In the lower thermosphere convection is the principal process of heat transport, while in the upper thermosphere heat is transported by conduction, leading to an isothermal region (T = const.). The start of the isothermal region is termed the *thermopause*. In this region, the mean free path of the gas becomes large and collisions become negligible, so that light atmospheric constituents, whose velocity exceeds the gravitational escape velocity, v_∞, can thermally escape from the planet.

This region is called the *exosphere*; the isothermal temperature above the thermopause is therefore also referred to as the *exospheric temperature*. The exosphere begins at an altitude which was originally called the *critical level*, but which is now generally referred to as the *exobase*. This level is defined by the condition that the mean free path is equal to the local scale height, i.e., the logarithmic decrement of pressure with altitude. The exobase may also be called the *baropause*, since the entire atmosphere below that level is also referred to as the *barosphere*, i.e., the region where the barometric law

holds perfectly. In the exosphere the velocity distribution is non-Maxwellian due to the escape of the high velocity particles and the density does not strictly follow the barometric formula, but has to be derived by considering the individual ballistic components of the atmospheric gas.

The troposphere and stratosphere together are also referred to in a less precise way as the *lower atmosphere*, while the regions above the stratosphere are called the *upper atmosphere*. It should be noted that without a stratospheric heat source, such as the absorbtion of O_3 in the case of Earth, a planetary atmosphere may not possess a stratopause and the region above the tropopause may be called either the stratosphere or the mesosphere. The lower atmosphere is the principal domain of meteorology whereas the upper atmosphere is that of aeronomy. However, it would be a mistake to rigidly compartmentalize the atmosphere, since interactions between the various regions do occur. For the discussion of planetary aeronomic processes, the emphasis must be, however, on the upper atmosphere.

The atmosphere can also be divided in terms of its composition into the *homosphere* and the *heterosphere*. These terms are somewhat less frequently used than the nomenclature based on the temperature distribution. In the homosphere the composition is uniform (Earth: 78% N_2, 21% O_2, 1% Ar plus minor constituents). This region is characterized by turbulent mixing. In the heterosphere, the composition varies due to dissociation of molecular constituents and as the result of diffusive separation. The level where diffusion rather than turbulent mixing becomes the controlling process is generally called the *homopause* (formerly also called the *turbopause*). More precisely, the homopause can be defined as the level where the *eddy diffusion* (mixing) coefficient is equal to the molecular diffusion coefficient. Since these coefficients are different for different constituents, they will have different homopause levels. In the terrestrial atmosphere, homopause levels occur at altitudes of about 100 km. The homopause concentrations of atmospheric constituents represents important boundary conditions for their distribution in the upper atmosphere and the ionosphere.

The *ionosphere* is that region of the upper atmosphere where charged particles (electrons and ions) of thermal energy are present, which are the result of ionization of the neutral atmospheric constituents by electromagnetic and corpuscular radiation. The lower boundary of the ionosphere, which is by no means sharp, coincides with the region where the most penetrating radiation (generally, cosmic rays) produce free electron and ion pairs in numbers sufficient to affect the propagation of radio waves (the D-layer). The upper boundary of the ionosphere is directly or indirectly the result of the interaction of the solar wind flow outward from the Sun at supersonic speeds with the planet. For weakly or essentially non-magnetic planetary bodies (Venus, Mars, Saturn's satellite Titan), the interaction region between the solar wind and the ionospheric plasma represents the termination of the ionosphere on the sunward side; it is called the *ionopause*.

On the nightside the ionosphere can extend to greater distances in a tail-like formation, representing the solar wind shadow. In the tail the extent of the ionosphere is limited by the condition for ion escape. For magnetic planets with atmospheres (Earth, Jupiter, Saturn, Uranus, Neptune), the ionosphere terminates within the *magnetosphere* which comprises all charged particles of low (thermal) and high energies (radiation belts). In this case the solar wind interacts with the intrinsic planetary magnetic field terminating at the *magnetopause*. The termination of the ionosphere is then the indirect result of the solar wind interaction; e.g., in the case of Earth, represented by the boundary between solar-wind induced convective motions inside the magnetosphere and the corotating ionospheric plasma called the *plasmapause*. (The region inside the plasmapause is also called the *plasmasphere*; however, according to our definition this is simply part of the ionosphere.)

I.1 Extreme Ultraviolet Radiation (EUV) and X-Rays

The extreme ultraviolet (EUV) radiation nominally spans the wavelength range from 1000 to 100 Å, although the edges are often somewhat indistinctly defined and extend shortward into the soft X-ray or longward into the far ultraviolet (FUV). Like X-ray emission, the production of EUV photons is primarily associated with the existence of hot gas in the Universe.

Sources of EUV radiation can be divided into two main categories [1]. The first is where the emission arises from recombination of ions and electrons in a hot, optically thin plasma, which gives rise to emission line spectra; and the second is where objects are seen by thermal emission from an optically thick medium, resulting in a strong continuum spectra which contain features arising from transitions between different energy levels or ionization stages of several elements.

Single stars and binary systems containing active coronae, hot O and B stars with strong stellar winds, supernova remnants and galaxy clusters belong to the former category. Hot white dwarf stars, central stars or planetary nebulae and neutron stars are possible continuum sources. Binary stars, where material is being transferred from a normal main sequence star, which is usually an M dwarf star onto a white dwarf, may well contain regions of both optically thin and optically thick plasma [1].

The emission of EUV radiation from astrophysical objects can also be used as probes of the interstellar medium (ISM). The absorbing effect of the ISM can modify the flux received at the Earth allowing, if the radiating source is well understood, its structure and density to be studied. Further, X-ray and EUV observations of various solar-like low mass stars (F, G, K, M) shown in Fig. 1.2 can be used for studying stellar–planetary relations, the ionization and heating of upper atmospheres of short periodic giant exoplanets and more interestingly "hypothetical" terrestrial exoplanets, which are expected to be discovered in the near future. The main characteristics of stars are

Table 1.1. Characteristics of stellar spectral types.

Star type	Main characteristic	Color
O	Lines of highly ionized atoms are present, and lines of He^+ are visible in the spectrum.	"Blue"
B	Neutral He lines are strong. Lines of Mg^+ and Si^+ are present. Hydrogen lines are conspicuous.	"Blue"
A	Hydrogen lines are very strong. Lines of once-ionized and neutral metals (e.g., Fe) are also present	"White"
F	Hydrogen lines are weaker than in class A, but still clearly visible. The ion Ca^+ has conspicuous lines.	"White"
G	The spectrum looks like the Sun's spectrum. The lines due to Ca^+ are very strong.	"Yellow"
K	Many strong lines due to neutral atoms. Some molecular bands are present.	"Orange"
M	Many strong lines due to neutral atoms are present in the spectra of stars of class M. Molecules such as TiO have strong bands in the spectra.	"Red"

listed in Table 1.1. Until the early 1970s the conventional view was that EUV astrophysics was not a practical proposition, because most elements have outer electron binding energies in the range of 10 to 100 eV; photons in the corresponding energy range will be strongly absorbed in any photon–atom interaction when the ionization potential IP $< \hbar c/\lambda$, where λ is the photon wavelength, $\hbar$ the Planck's constant and c the speed of light. When $10 <$ IP < 100 eV, λ lies in the range 1000 to 100 Å, i.e., within the EUV band [1]. As a result, a planetary atmosphere is opaque to EUV radiation as in the case of Earth due to photoabsorption by N_2, O_2 and O, so that the 1/e absorption depth (*unit optical depth*) at 100 Å is at an altitude of about 120 km.

The source of the EUV (1750–70 Å) and X-ray radiation (170–1 Å) of a solar-like G star such as the Sun is produced in the various layers of the stars' atmosphere. Table 1.2 lists the appropriate wavelengths at their point of origin [2, 3].

The absorption of the XUV radiation in a planetary atmosphere leads to *photoionization* and *photodissociation* of atmospheric constituents. Table 1.3 lists the penetration depth of the solar radiation and particles as well as their energy fluxes.

The relevant wavelengths for the heating of upper atmospheres are the ionizing wavelengths less than 1000 Å, which contain only a small fraction

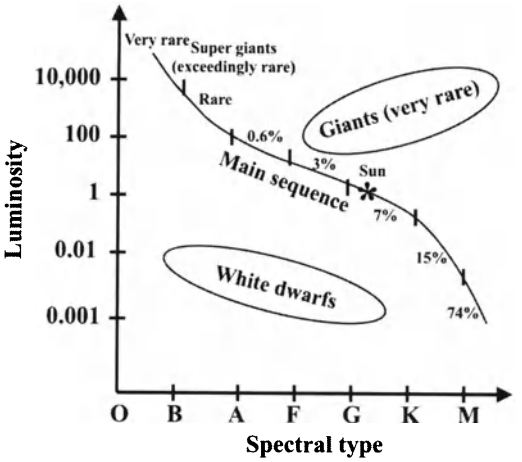

Fig. 1.2. Hertzsprung–Russell diagram: stellar bolometric luminosity in solar units as a function of spectral type of various stars. One can see that low mass K and M stars are more numerous than solar-like G-type stars.

Table 1.2. XUV wavelengths and their origin in the solar atmosphere.

λ [Å]	Source of radiation	
>1800	Photosphere,	
1200–2000	Transition photosphere–chromosphere,	
900–1800	Chromosphere,	
100–1000, Lyα (1216)	Transition to corona	
10–200	Quiet corona,	
5–100	Coronal active region	
1–50	Thermal radiation	} solar flares
0.01–10	Non-thermal burst	

10 Å= 1 nm

[4] of the present solar spectral power as shown in Fig. 1.3 and Table 1.3. Figure 1.3 shows the altitude of penetrating solar radiation on Earth as a function of wavelength.

The molecular constituents H_2O, CO_2 and O_2 can be dissociated by relatively long wavelength radiation in the Schumann–Runge continuum range of 1750–1300 Å, according to

$$O_2 + \hbar\nu(\lambda < 1750\,\text{Å}) \rightarrow O(^3P) + O(^2D)$$

$$CO_2 + \hbar\nu(\lambda < 1670\,\text{Å}) \rightarrow CO + O(^1D)\,.$$

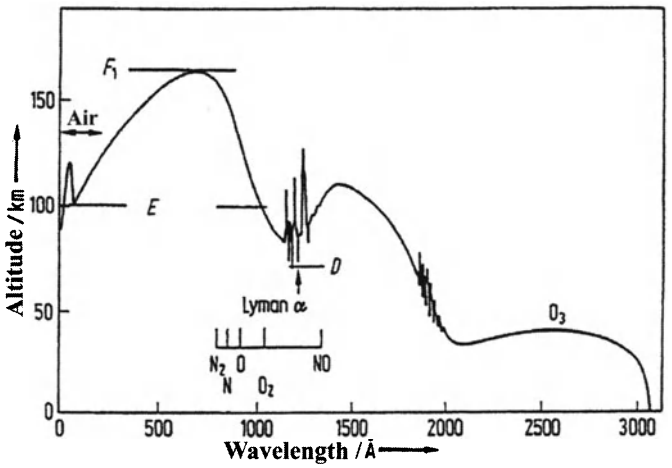

Fig. 1.3. Penetration depth of solar radiation as a function of wavelengths in the Earth's atmosphere. D, E and F_1 refer to peaks of ionospheric Chapman layers. Ionization thresholds are also indicated.

Table 1.3. Solar radiation and its penetration in the Earth's atmosphere.

λ [Å]	Penetration depth	Energy flux [W m^{-2}] or [10^3 erg $cm^{-2}sec^{-1}$]
> 3000 visible + IR	Troposphere	1360 (outside the atmosphere)
2000–3000	Stratosphere	14
UV	Mesosphere	
1500–2000	Mesosphere	
EUV	Thermosphere	0.25
	Ionosphere	
1000–1500	Thermosphere	8×10^{-3}
EUV	Ionosphere	
100–1000	Thermosphere	2×10^{-3}
XUV	Ionosphere	
10–100	Thermosphere	5×10^{-5}
X-rays	Ionosphere	
1	Mesosphere	10^{-4}
X-rays	Ionosphere	
Particles		
Solar protons	Stratosphere	10^{-3}
(MeV)	Mesosphere	
Solar wind	Magnetosphere	10^{-4}
(keV)		

The wavelength range with an energy flux of $\geq 2\,\mathrm{erg\,cm^{-2}\,sec^{-1}}$ represents the predominant XUV heat source for the terrestrial thermosphere. Dissociation can also take place below the true dissociation limit due to excitation of molecules into a state which dissociates. This *predissociation* occurs for O_2, CO_2 and H_2, but not significantly for N_2, accounting for its apparent stability against photodissociation.

The dissociation of O_2 is the first step in the old Chapman process of ozone (O_3) formation by a three-body collision

$$O + O_2 + M \rightarrow O_3 + M$$

where M is a molecule ensuring momentum balance. The photochemical loss of O_3 occurs via dissociation and combination with O

$$O + O_3 \rightarrow O_2 + O_2.$$

More recently catalytic loss processes for O_3 have been identified according to the following scheme

$$\begin{aligned} O_3 + X &\rightarrow XO + O_2 \\ XO + O &\rightarrow X + O_2 \\ O_3 + O &\rightarrow O_2 + O_2 \end{aligned}$$

where the catalyst X are trace gases like NO, Cl, Br but also H and OH. O_3 absorbs in UV in the range 3000–2000 Å and is therefore important for damage of DNA, absorbing most strongly at 2600 Å.

For H_2, radiation $\lambda < 850$ Å leads to either dissociation or ionization. Atomic hydrogen possesses a strong continuum absorption cross-section below 912 Å and strong Lyman-series lines, principally the intense Lyman-α line at 1216 Å.

The ionization thresholds (ionization potentials, IP) for common constituents of planetary atmospheres are listed in Table 1.4 (Note: λ [Å] = 12,395/IP [eV]). Accordingly, XUV radiation of wavelengths below the Lyman-α line (1216 Å) is primarily responsible for the formation of planetary ionospheres and thermospheric heating. However, trace constituents, of meteoric origin, can be ionized by even longer wavelengths. Typical examples are: Na (2410 Å/5.14 eV); Ca (2028 Å/6.11 eV); Mg (1622 Å/7.64 eV); Fe (1575 Å/7.87 eV); and Si (1520 Å/8.15 eV).

Rocket and satellite observations have led to a detailed identification of the solar emission line spectrum; relatively accurate values for the intensities of these radiations have become available [5, 6, 7]. Solar photon fluxes at Earth for moderate activity are summarized in Table 1.5 [6]. The solar photon flux Φ_∞ is used for the ionization process, while the XUV energy flux $I_\infty = (\hbar\nu)\Phi_\infty$ is applicable to thermospheric heating.

The solar photon fluxes vary both over a long period (11 year solar cycle) as well as over short periods (27 days) during disturbances. Although the

Table 1.4. Ionization thresholds/ionization potentials of atmospheric constituents.

Constituent	λ [Å]	IP [eV]
NO	1340	9.25
NH_3	1221	10.15
C	1100	11.3
O_2	1026	12.1
H_2O	985	12.60
CH_4	954	13.00
H	912	13.59
O	911	13.61
CO_2	899	13.79
CO	885	14.0
H_2	804	15.41
N_2	796	15.58
A	787	15.75
Ne	575	21.56
He	504	24.58

Table 1.5. Solar XUV photon and energy fluxes.

λ [Å]	Φ_∞ [10^9 ph cm^{-2} sec^{-1}]	I_∞ [erg cm^{-2} sec^{-1}]
1215.7 (Ly α)	300	5
1027–911	11.61	0.23
(1025.7, Ly β)	(3.5)	(0.067)
(977, C III)	(4.4)	(0.090)
911–800	8.3	0.20
800–630	2.4	0.064
630–460	4.7	0.17
(584.3, He I)	(0.9)	(0.03)
460–370	0.63	0.03
370–270	10.3	0.65
(303.8, He II)	(5.4)	(0.35)
270–205	4.5	0.36
205–153	4.6	0.49
153–100	0.4	0.06
120–80	0.3	0.066
80–40	0.33	0.108

Table 1.6. Variations in the X-ray energy flux I_X with solar activity.

Condition of the Sun	I_X [erg cm^{-2} sec^{-1}]	2 Å	4 Å	6 Å
	Completely quiet	10^{-8}	10^{-7}	10^{-6}
Solar minimum				
	Quiet	10^{-7}	10^{-6}	10^{-5}
	Lightly disturbed	10^{-6}	10^{-5}	10^{-4}
Solar maximum				
	Disturbed	10^{-5}	10^{-4}	10^{-3}
	Special events	10^{-4}	10^{-3}	10^{-2}
Flares				
	Class 3 flares	10^{-3}	10^{-2}	10^{-1}

exact amplitude of these variations is not yet fully established, it appears to be for the EUV range of the order of 2. The 10.7 cm solar radio flux $F_{10.7}$ is usually considered to be an excellent indicator of solar activity; according to limited data the integrated flux in the range 1310–270 Å changes by a factor of about 1.5 for a change in $F_{10.7}$, by a factor of 2 [5].

The solar cycle variation for the range 100–10 Å amounts to a factor of 7; the energy flux in this range is $\sim$0.9 erg cm^{-2} sec^{-1} at solar maximum. The X-ray energy flux I_X at 8 Å in the absence of flares varies over the solar cycle by a factor of 300; the variation in the range 8–2 Å from a completely quiet Sun to a class 3 flare can amount to five orders of magnitude (10^5), as shown in Table 1.6 [3].

Production of Ionization by Photons

In the photoionization process the production of an ion pair (ion + electron) occurs as the result of the action of a photon whose energy $\hbar\nu$ is equal to or greater than the ionization potential of the constituent X, according to

$$X + \hbar\nu(\geq IP) \rightarrow X^+ + e\,.$$

For the general discussion of the production of electrons and ions by photoionization of neutral atmospheric constituents we will make some simplifying assumptions. The more general case can easily be obtained from this starting point by summation over all wavelengths.

The following derivations are based on the assumptions of 1) monochromatic radiation, i.e., a small wavelength interval over which the absorption and ionization cross-sections can be taken as constant; 2) an isothermal atmosphere where the atmospheric scale height is H=const. ($H = k_B T/mg$: cf. Sect. II.1) and a horizontally stratified atmosphere (i.e., neglecting the curvature of the planetary surface). The ionizing radiation is assumed to be

incident at an angle χ with the vertical (the solar zenith angle), having a photon flux outside the atmosphere Φ_∞. The ion production rate depends on the number density of the ionizable constituent n_j, its ionization cross-section σ_i for the particular wavelength interval and the local photon flux Φ, according to

$$q = \sigma_\mathrm{i} n_j \Phi \,. \tag{1.1}$$

Along a path length $\mathrm{d}s$, $n_j \sigma_\mathrm{a} \mathrm{d}s$ photons are absorbed, where σ_a is the absorption cross-section which is usually larger than σ_i. Hence we can write

$$\frac{\mathrm{d}\Phi}{\mathrm{d}z} = n_j \sigma_\mathrm{a} \Phi_\infty \sec\chi$$

where $\mathrm{d}s = \mathrm{d}z \sec\chi$, and obtain by integration

$$\Phi = \Phi_\infty \exp\left[-\sigma_\mathrm{a} \sec\chi \int_z^\infty n_j(z)\,\mathrm{d}z\right] \tag{1.2}$$

i.e., the ionizing photon flux decreases from its value outside the atmosphere as the result of absorption. The ion production rate can now be expressed for

$$n_j(z) = n_{j0} \exp\left(-\frac{z}{H}\right)$$

as

$$q = \sigma_\mathrm{i} n_{j0} \Phi_\infty \exp\left[-\frac{z}{H} - \sigma_\mathrm{a} \sec\chi \int_z^\infty n\,\mathrm{d}z\right] \tag{1.3}$$

or in terms of the optical depth $\tau = \sigma_\mathrm{a} \sec\chi \int_z^\infty n_j\,\mathrm{d}z = \sigma_\mathrm{a} n(z) H \sec\chi$

$$q = \sigma_\mathrm{i} n_j(z) \Phi_\infty \mathrm{e}^{-\tau} \,. \tag{1.4}$$

The ion production rate has a maximum where $\mathrm{d}q/\mathrm{d}z = 0$, which also corresponds to the condition $\tau = 1$, for overhead Sun. Accordingly, the altitude where the maximum of ion production occurs can be found from this condition. Since

$$\tau = \sigma_\mathrm{a} n_{j0} H \sec\chi \cdot \exp\left(-\frac{z^*}{H}\right) = 1$$

we have $\exp(z^*/H) = \sigma_\mathrm{a} n_0 H \cdot \sec\chi$ where it should be noted that z^* is the *relative* height above the reference level $z = 0$, represented by an absolute altitude h_0, usually close to or above the homopause.

Hence the absolute altitude of the ion production maximum, h^*, is given by

$$h^* = H \ln(\sigma_a n_0 H \sec\chi) + h_0 = h_0^* + H \ln\sec\chi \,. \tag{1.5}$$

The maximum value of the ion production rate is given by

$$q_m = \frac{\sigma_\mathrm{i}}{\sigma_\mathrm{a}} \frac{\Phi_\infty}{\mathrm{e}H} \cos\chi = q_0 \cos\chi \tag{1.6}$$

where the ratio $\sigma_i/\sigma_a = \eta_i$ is called the ionization efficiency. The condition of $\tau = 1$ for overhead Sun ($\chi = 0$) is often used to indicate the penetration depth of ionizing radiation, i.e., where it decreases by 1/e or where for H =const., the ionization rate would reach an absolute maximum

$$q_0 = \frac{\eta_\mathrm{i}\Phi_\infty}{\mathrm{e}H} .$$

The altitude h_0^* is also called the *altitude of unit optical depth*, i.e., where $\sigma_\mathrm{a} n(h_0^*)H = 1$. It should be noted that the height of maximum ion production depends on the optical depth and solar zenith angle ($\sec\chi$), but not on the photon flux, whereas the maximum value of the ion production rate depends on the photon flux outside the atmosphere, the scale height and $\cos\chi$.

The ion production rate as a function of altitude can be written using the above definitions

$$q = q_\mathrm{m} \exp\left\{1 - \frac{h - h^*}{H} - \sec\chi \exp\left[-\frac{(h - h^*)}{H}\right]\right\} . \tag{1.7}$$

This is the well-known Chapman ion pair production function [8] which is illustrated in Fig. 1.4 in normalized form

$$q = q_0 \cos\chi \exp\{1 - z - \sec\chi \exp(-z)\} \tag{1.8}$$

where $z = (h - h_0^*)/H$. The optical depth and thus the penetration of ionizing radiation depends on the absorption cross-section. In the XUV range, most major constituents of planetary atmospheres have absorption cross-sections of order $\sigma_\mathrm{a} \approx 10^{-17}$–$10^{-18}$ cm^2, whereas at X-ray wavelengths (see Table 1.7) the cross-sections are much smaller [9, 10]. Between 50 and 20 Å the K absorption limits occur, which correspond to an abrupt change in σ_a by about one order of magnitude. The (total) absorption cross-sections are the upper

Table 1.7.

λ [Å]	σ_a [cm^2]
1	$\sim 10^{-22}$
3	$\sim 10^{-21}$
5	$\sim 10^{-20}$
15	$\sim 10^{-19}$
50	$\sim 10^{-19}$
100	$\sim 10^{-18}$

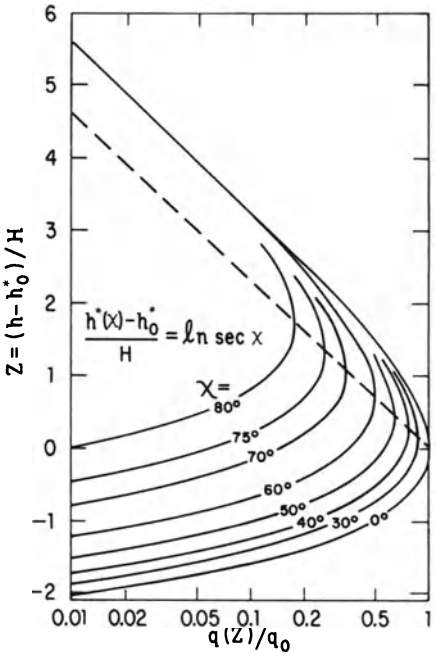

Fig. 1.4. Ion–pair production function, as a function of solar zenith angle χ, normalized to the absolute ionization maximum q for overhead Sun [$\chi = 0$] occurring at an altitude h_0^*. The height parameter corresponds to $z = (h - h_0^*)/H$.

limit for the ionization cross-sections; for atomic species $\sigma_a = \sigma_i$, i.e., the ionization efficiency is $\eta_i = 1$, whereas for molecular species $\sigma_i \lesssim \sigma_a$, i.e., $\eta_i \lesssim 1$.

Figs. 1.5–1.8 show the absorption cross-sections for various important constituents of planetary atmospheres [9].

The ion production rate derived above under a number of simplifying assumptions can be extended to be more generally applicable. For an atmosphere with a constant scale height gradient $\mathrm{d}H/\mathrm{d}z = \beta$, the ionization maximum occurs where $\tau = 1 + \beta$ and the ion production rate is given by

$$q = q_m(1 + \beta)\{1 - \zeta - \mathrm{e}^{-\zeta \sec \chi}\}$$

where ζ is a height variable defined by $H = H_0 \mathrm{e}^{\beta\zeta}$.

Near sunrise and sunset, i.e., $\chi > 75°$, the $\sec \chi$ term in the ion production function, which is a consequence of the flat planet approximation, has to be replaced by the so-called Chapman function $\mathrm{Ch}(\chi)$ [11].

$$\mathrm{Ch}(\chi) = \frac{\int_s^\infty n(s)\,\mathrm{d}s}{\int_h^\infty n(h)\,\mathrm{d}h}.$$

This function is defined as the ratio of the total content n of the atmosphere in the line of sight (s) to the Sun to the vertical content (h).

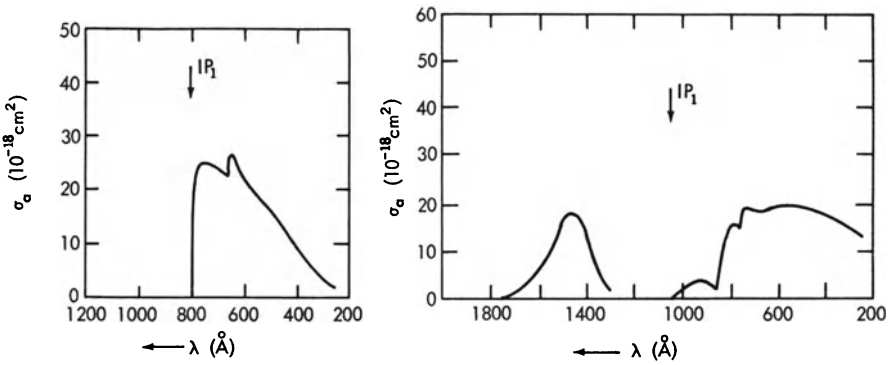

Fig. 1.5. Absorption cross-section of N_2 from experimental data (left); O_2, (right) (after E. W. McDaniel [9]).

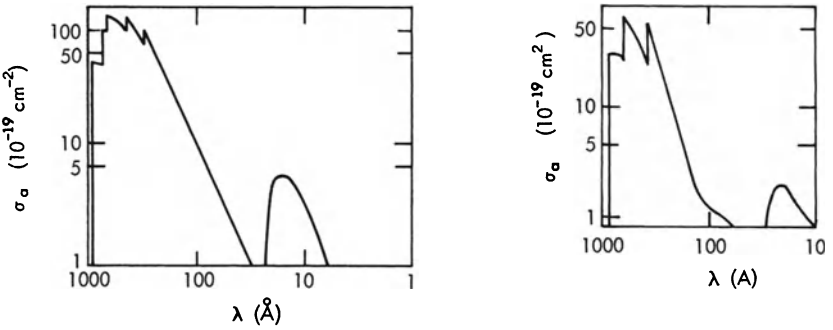

Fig. 1.6. Absorption cross-section of O (left) and N (right) from theoretical calculations (after E. W. McDaniel [9]).

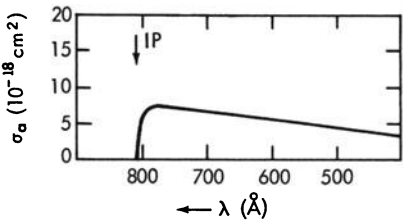

Fig. 1.7. Absorption cross-section of H_2 based on experimental data (after E. W. McDaniel [9]).

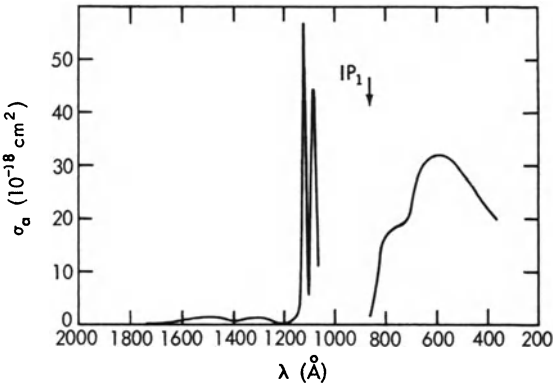

Fig. 1.8. Absorption cross-section of CO_2 from experimental data (after E. W. McDaniel [9]).

A number of analytical approximations to the Chapman function have been developed, including the extension to a constant scale height gradient β (cf. Sect. II.1). For an isothermal atmosphere a useful approximation of the Chapman function is given in terms of the tabulated error function

$$\mathrm{Ch}\left(x, \frac{\pi}{3} \leq \chi \leq \frac{\pi}{2}\right) \cong \left(\frac{\pi x}{2}\right)^{\frac{1}{2}} \left\{1 - \mathrm{erf}\left(\frac{x^{\frac{1}{2}} \cos\chi}{\sqrt{2}}\right)\right\} \exp\left(\frac{x\cos^2\chi}{2}\right)$$

$$\mathrm{Ch}\left(x, \chi \geq \frac{\pi}{2}\right) \cong \left(\frac{\pi x}{2}\sin\chi\right)^{\frac{1}{2}} \left\{1 + \mathrm{erf}\left(\frac{x^{\frac{1}{2}} \cos\chi}{\sqrt{2}}\right)\right\} \exp\left(\frac{x\cos^2\chi}{2}\right) \quad (1.9)$$

where $x = R/H = (R_0 + h)/H$ with H the scale height and R_0 the planetary radius. The *Chapman function* for different values of x and its comparison with $\sec\chi$ is shown in Fig. 1.9.

For $\chi = 90°$, $\mathrm{Ch}(x, \pi/2) = (x\pi/2)^{\frac{1}{2}}$, representing the ratio of the total content in the line of sight to the vertical content of an atmospheric constituent, a quantity of interest in occultation experiments. At high enough altitudes where the optical depth is small the exponential factor in (1.9) can be neglected and the ion production function in this "low attenuation region" assumes the simple form

$$q = J(\sigma_i, \lambda) n_j(z) \quad (1.10)$$

where $J = \langle \sigma_i \Phi_\infty \rangle$ is the photoionization rate coefficient (or frequency of ionization ν_{ion}, $[\sec^{-1}]$). The ionization coefficient is based on the averaged ionization cross-sections and photon fluxes over all pertinent wavelengths. For the light atmospheric constituents H and He, which will make up the main constituents of planetary exospheres, the ionization coefficients are listed for Venus, Earth and Mars in Table 1.8. Since many wavelengths will contribute

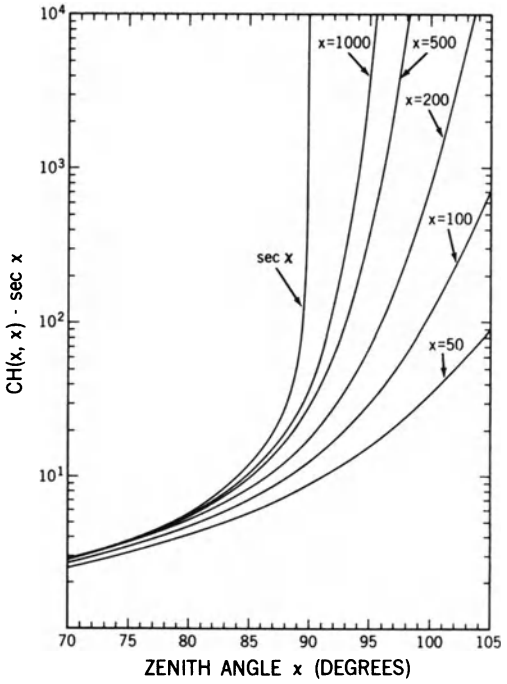

Fig. 1.9. Chapman function $\mathrm{Ch}(x, \chi)$ for parametric values of $x = R/H$, compared with $\sec \chi$.

Table 1.8. Photoionization rate coefficients.

J [sec^{-1}]	Venus	Earth	Mars
Atomic hydrogen (H)	2×10^{-7}	1.5×10^{-7}	4×10^{-8}
Helium (He)	10^{-7}	6×10^{-8}	2.5×10^{-8}

to the ionization of a particular constituent n_j and will also be absorbed by other atmospheric constituents, the ion production rate in this generalized form can be expressed by

$$q = \sum_{j,\lambda} n_j \sigma_{ij} \Phi_{\mathrm{XUV}}(\lambda) \exp\left(- \sum_l \sigma_a \int_z^\infty n_j \sec \chi \, \mathrm{d}z \right) . \tag{1.11}$$

In the photoionization process, photoelectrons are produced whose energy, $E_{pe} = \hbar\nu - \mathrm{IP}$, may be large enough, especially in the X-ray range, to lead to additional ("secondary") ionizations. In the X-ray range, the ion production is also computed by using the X-ray energy flux I_X divided by 35 eV, the average energy expended in the formation of an ion pair for air or CO_2. It should be noted that the calculation of secondary ionization depends on

the initial photoelectron distribution and their collision processes with atmospheric particles.

I.2 Corpuscular Radiation

Galactic cosmic rays, energetic solar particles, solar wind protons and lower energy electrons and protons populating a planetary magnetosphere are responsible for the formation of electron–ion pairs at the lower level of planetary ionospheres [12]. Because of their high energy, cosmic rays penetrate deepest into the planetary ionosphere.

Galactic cosmic rays with energies $E > 10^9\,\mathrm{eV}$ are responsible for the formation of the lowermost ionospheric layer (sometimes called the cosmic ray or C-layer) actually representing the lower part of the D-layer.

Relativistic solar cosmic rays (protons) produced during highly disturbed solar conditions, which are a rather rare occurrence (once in several years) having energies $E > 10\,\mathrm{BeV}$, cause a substantial enhancement in the ionization of the D-layer [13].

Subrelativistic solar cosmic ray protons with energies $10\ \mathrm{MeV} \lesssim E \lesssim 100\ \mathrm{MeV}$ produce strong ionization effects at polar caps which are accessible on a magnetic planet, leading to polar cap absorption (PCA) events in the terrestrial ionosphere. These events are generally observed at periods of maximum solar activity, but are almost non-existent during solar minimum [14]. The general formula for ion-pair production by charged particles (corpuscular radiation) can be written [15]

$$q(h) = \frac{1}{W} \int_E \int_\Omega \frac{\mathrm{d}E}{\mathrm{d}x} \cdot j(E)\,\mathrm{d}E\,\mathrm{d}\Omega \tag{1.12}$$

where $W \cong 35\,\mathrm{eV}$ is the average energy required for the formation of an ion pair in air or CO_2, $\mathrm{d}E/\mathrm{d}x = \sec\chi\,\mathrm{d}E/\mathrm{d}h$ is the energy loss in an inelastic collision process (ionization loss), $j(E) = KE^{-\gamma}$ represents the differential energy spectrum of the ionizing particles and Ω is the solid angle. $j(E) = \mathrm{d}J/\mathrm{d}E$, where $J(> E_0) = \int_{E_0}^{\infty} j(E)\,\mathrm{d}E$ is the integral (spectrum) flux for energies grater than E_0.

In the presence of a planetary magnetic field, the penetration of charged particles is inhibited; for a dipolar field only the most energetic particles can penetrate to low latitudes, so that the particle ionization effects are normally restricted to high magnetic (polar) latitudes. The ability of a charged particle with momentum (mv) to penetrate a magnetic field of strength B can be expressed by the rigidity P which is defined by

$$P = \frac{mvc}{Ze} \qquad [\mathrm{Volt}] = Br_\mathrm{B} \qquad [\mathrm{Gauss/cm}]$$

where Z is the charge number, e is the electronic charge, and r_B is the Larmor or gyro radius (cf. Chap VI) of a charged particle of momentum mv moving in a plane perpendicular to the magnetic field vector $\boldsymbol{B}$.

The ion production rate resulting from galactic cosmic rays can be written in simplified form [13]

$$q(\varphi) = \frac{q_0(\varphi)n}{n_0} \qquad [\mathrm{cm^{-3}\,sec^{-1}}] \tag{1.13}$$

where $q_0(\varphi)$ is the ionization rate at magnetic latitude φ for an atmospheric level with the corresponding number density $n_0 = 2.6 \times 10^{19}\,\mathrm{mol\,cm^{-3}}$. The ionization rate at geomagnetic latitudes $\varphi \geq 70°$ corresponds to that which would prevail if the galactic cosmic rays were unimpeded by a planetary magnetic field; the ionization rate at the geomagnetic equator is reduced by an order of magnitude relative to that at the pole. The polar ionization rate at solar maximum has been found to be $q_0 \cong 200\,\mathrm{cm^{-3}\,sec^{-1}\,atm^{-1}}$, whereas that at solar minimum is larger by about a factor of 4, while that at middle and low latitudes varies by about a factor of 2, ranging from 150 to $300\,\mathrm{cm^{-3}\,sec^{-1}}$ at $\varphi = 50°$ [13]. This inverse relationship of cosmic ray intensity with solar activity, also called the *solar modulation of cosmic rays*, is due to the interplanetary magnetic field carried by the solar wind [14]. The penetration depth $\tilde{h}$ of charged particles in a planetary atmosphere is expressed by the range $\mathfrak{R}$ in units of $\mathrm{g\,cm^{-2}}$, according to

$$\mathfrak{R} = \sec\chi \int_{\tilde{h}}^{\infty} \rho(h)\,\mathrm{d}h \tag{1.14}$$

where χ is the zenith angle of the incident particles, and ρ is the mass density ($\rho = nm$).

The range $\mathfrak{R}$ is related to the ionization loss or *stopping power* according to

$$\mathfrak{R} = \int_{E(\tilde{h})}^{E} \left[\frac{1}{\rho} \cdot \frac{\mathrm{d}E}{\mathrm{d}h}\right]^{-1} \mathrm{d}E\,. \tag{1.15}$$

Range–energy relations are usually based on experimental data or theoretical expressions based on the Bethe formula [16]. Empirical formulas exist for air, and since the pertinent physical parameters for CO_2 are very close to those for air, they may be applied to the atmospheres of the terrestrial planets. The range of protons with energies $E < 500\,\mathrm{MeV}$ is approximately given by [17]

$$\mathfrak{R}_\mathrm{p}[\mathrm{g\,cm^{-2}}] \cong \frac{E^{1.78}}{420}$$

and for electrons of energy $E < 200\,\mathrm{keV}$ by

$$\mathfrak{R}_\mathrm{e}[\mathrm{g\,cm^{-2}}] \cong \frac{E^{1.96}}{0.75}$$

where E is the particle energy in MeV.

Since charged particle trajectories are not rectilinear due to changes in direction in the collision process, as well as due to a planetary magnetic field, accurate analysis of energy deposition has to take these effects into account. Such calculations have been performed for low energy electrons using a statistical Monte Carlo method [18].

The approximate penetration depths at vertical incidence of energetic electrons and protons in the atmospheres of Earth, Venus and Mars, based on range–energy relations, are shown in Fig. 1.10. The most penetrating charged particles are galactic cosmic rays and energetic solar protons, which produce ionization at altitudes below 100 km while lower energy particles, such as auroral electrons (1–10 keV), deposit their energy at altitudes 100 km in the terrestrial atmosphere. Charged particles penetrate to lower altitudes on Mars, than on Earth, but not as deep into the atmosphere of Venus as on Earth. This is a consequence of the fact that in the lower thermospheres of these planets the scale heights are not greatly different, whereas the densities are highest for Venus and lowest for Mars, with Earth lying in between. On Saturn's satellite Titan an ionospheric layer produced due to cosmic rays is expected at an altitude of about 90 km.

For energetic solar protons and galactic cosmic ray protons, the use of an exponential rigidity spectrum of the form $J(>P) = J_0 \exp(-P/P_0)$ with $P_0 < 100\,\mathrm{MeV}$ for polar or non-magnetic conditions and $P_0 > 150\,\mathrm{MeV}$ for geomagnetic latitudes $\varphi < 65°$, has been found to give a good representation of their ionization rate [13]. Fig. 1.11 shows the ion-pair production functions over the polar cap for galactic cosmic rays during solar maximum and minimum and a solar proton event with a rigidity spectrum $J > 100\,MV = 0.05\,\mathrm{cm^{-2}sec^{-1}\,ster^{-1}}$ and $P_0 = 50\,\mathrm{MeV}$ [13]. (Some solar proton events result in a peak ionization rate 100 times larger than this.)

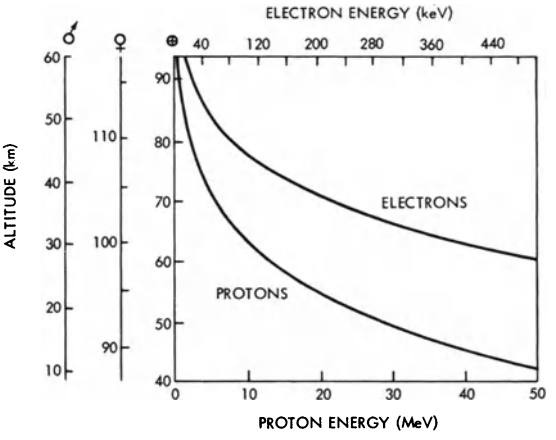

I.10 Approximate altitudes of penetration of energetic particles in the atmospheres of Earth (⊕), Mars (♂) and Venus (♀).

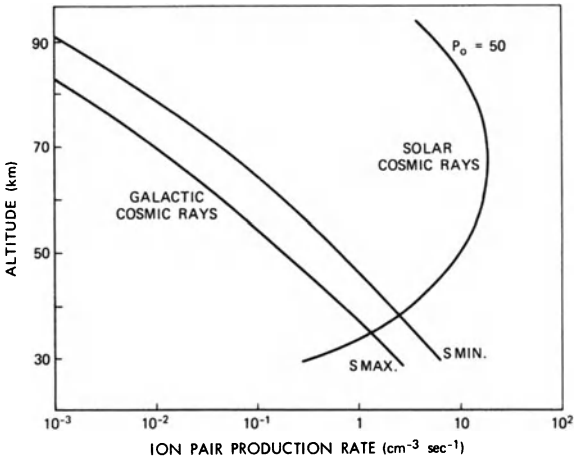

Fig. 1.11. Ionization rate due to galactic cosmic rays and high energetic solar protons in the terrestrial atmosphere over the polar cap (after W. Webber [13]).

The solar proton and galactic cosmic ray ionization rate for Mars and Venus [13, 18, 19] can be scaled from the terrestrial case according to

$$q(\tilde{h}_{\mathrm{M,V}}) = \frac{\rho(\tilde{h}_{\mathrm{M,V}})}{\rho(\tilde{h}_{\mathrm{E}})} q(\tilde{h}_{\mathrm{E}}) \tag{1.16}$$

where $q(\tilde{h}_{\mathrm{E}})$ is the ionization rate at the terrestrial poles, $\tilde{h}_{\mathrm{E}}$ and $\tilde{h}_{\mathrm{M,V}}$ are the atmospheric penetration altitudes resulting from the appropriate range $\mathfrak{R}(\mathrm{g\,cm^{-2}})$ for the same cutoff energy for solar protons, and $\rho(\tilde{h}_E)$ and $\rho(\tilde{h}_{V,M})$ are the respective mass densities. For low energy electrons and protons, such as auroral particles, the ion production rate due to particles in the energy range $E_{\min}$ to $E_{\max}$ can be expressed for Earth by

$$q = \frac{\rho(h)}{0.032} \int_{E_{\min}}^{E_{\max}} L(E) j(E,h)\, \mathrm{d}E \tag{1.17}$$

where $\rho(h)$ is the atmospheric density in units of $\mathrm{g\,cm^{-3}}$ at altitude h. The ionization loss for electrons can be approximated by [17]

$$L_{\mathrm{e}}(E) = -\frac{\mathrm{d}E}{\mathrm{d}\mathfrak{R}} = 0.38E^{-0.96}$$

and for protons by

$$L_{\mathrm{p}}(E) = -\frac{\mathrm{d}E}{\mathrm{d}\mathfrak{R}} = 236E^{-0.78}$$

where $\mathfrak{R}$ is the range in $\mathrm{g\,cm^{-2}}$ and E is in MeV.

The number of particles of energy E arriving at altitude h, i.e., the differential energy spectrum $j(E,h)$ in $\mathrm{cm}^{-2}\,\mathrm{sec}^{-1}\,\mathrm{ster}^{-1}\,\mathrm{keV}^{-1}$, has to be obtained by integrating over both pitch (α) and solid (Ω) angle if a magnetic field is present, according to

$$j(E,h) = \int_0^{\Omega} \int_0^{\frac{\pi}{2}} j(E) \exp\left[-\frac{x}{\lambda(E)\cos\alpha}\right] \sin\alpha \,\mathrm{d}\alpha \,\mathrm{d}\Omega \tag{1.18}$$

where x is the range at height h and $\lambda(E) = 3.15\times10^{-7}E^{2.2}$ is the attenuation mean free path.

Another possible ionization source for planetary ionospheres is the solar wind. Although most of the solar wind flows around the planetary obstacle (cf. Chap. VI), a small fraction of the solar wind protons may leak through the magnetopause or ionopause, especially in the tail region.

Ionization by the stellar wind is due to two processes: 1) direct impact ionization of atmospheric constituents by stellar wind protons having an energy $E \sim 1\,\mathrm{keV}$, and 2) ionization by hot hydrogen generated by charge exchange (cf. Chap. IV) between stellar wind protons and atmospheric constituents. The ionization rate due to the stellar wind can be expressed by

$$q = \sigma'_{\mathrm{i}} n_j \Phi'_{\mathrm{sw}} + \sigma''_{\mathrm{i}} n_j \Phi'_{\mathrm{H}^*}$$

where the σ_{i} are the ionization cross-sections ($\sim 10^{-11}\,\mathrm{cm}^2$), Φ'_{sw} is the stellar wind proton leakage flux, i.e., a small fraction ($\lesssim 10\%$) of the stellar wind flux outside the planetary magnetopause or ionopause Φ_{sw}, and Φ'_{H^*} is the effective ionizing flux of hot hydrogen. The latter is governed by a continuity equation of the form

$$\frac{\mathrm{d}\Phi'_{\mathrm{H}^*}}{\mathrm{d}s} = -\frac{1}{2}\frac{\mathrm{d}\Phi'_{\mathrm{sw}}}{\mathrm{d}s} - \frac{\mathrm{d}\Phi_{\mathrm{H}^*}}{\mathrm{d}E}\frac{\mathrm{d}E}{\mathrm{d}s}$$

where the factor $\frac{1}{2}$ denotes the downward part of an isotropic flux of hot hydrogen generated by charge exchange between stellar wind protons and the neutral constituent n_j, according to $\mathrm{d}\Phi'_{\mathrm{sw}}/\mathrm{d}s = -\sigma_{\mathrm{c}} n_j \Phi_{\mathrm{sw}}$, with $\sigma_{\mathrm{c}} \approx 10^{-15}\,\mathrm{cm}^2$; the second term on the right-hand side represents the thermalization of the initially formed hot hydrogen beam along its path by scattering and ionization processes (cf. Chap. III).

I.3 Evolution of the Solar/Stellar XUV Flux with Time

Because the type of the star plays a major role in all atmospheric processes, the evolution of planetary atmospheres must be understood within the context of the evolving stellar energy and particle fluxes [4]. Because thermal escape of atmospheric constituents in planetary atmospheres depends on the stellar XUV radiation, which affects the temperature of the upper atmosphere

(cf. Chap. II) and photoionization processes, it is important to study the time evolution of stellar radiation and particle fluxes.

Observations of enriched heavy isotopes in planetary atmospheres [20, 21] and radiative stellar fluxes, stellar magnetic fields, stellar winds of solar-type stars with different ages [22, 23, 24, 25] and lunar and meteorite fossil records [26] indicate that our early Sun underwent a highly active phase after its arrival on the zero-age main-sequence (ZAMS).

Solar-Like G Stars

The observational evidence of an active XUV phase of the young Sun is also a representative for other solar-like G stars and lasted about 0.5 to 1.0 Gyr. It included continuous flare events, where the radiation environment was several hundred times more intense than today. The high radiation levels of young solar-like stars is triggered by strong magnetic activity. The magnetic activity is expected to have greatly decreased with time [24, 27, 28] as the solar rotation slowed down through angular momentum loss. Observational evidence and theoretical models suggest that young solar-like stars rotate about 10 times faster than the Sun today and have significantly enhanced magnetically generated coronal and chromospheric activity [24, 29].

Solar proxies are studied inside the so-called *Sun in Time* program [24], which was established to investigate the magnetic evolution of the Sun by using a homogeneous sample of single nearby G0-V main sequence stars, which have known rotation periods and well-determined physical properties, including temperatures, luminosities, metal abundances and ages. As can be seen in Table 1.9, the sample of studied solar proxies contains stars that cover most of the Sun's main sequence lifetime from 130 Myr to 8.5 Gyr.

A large amount of multiwavelength (X-ray, EUV, FUV, UV, optical) data have already been collected. The observations of solar proxies, obtained with the ASCA, ROSAT, EUVE, FUSE and IUE satellites, cover a range between 3300 and 1 Å, except for a gap between 920 and 360 Å, which is a region of very strong interstellar medium absorption. Details of the data sets and the flux calibration procedure employed are provided in [24]. Full spectral irradiance tables have already been completed for five of the stars in the *Sun in Time* sample (EK Dra (130 Myr), π^1 UMa (300 Myr), κ^1 Cet (750 Myr), β Com (1.6 Gyr), β Hyi (6.7 Gyr)) and show an excellent correlation between the emitted energy flux and stellar age.

The coronal XUV emissions of the young main-sequence Sun were about 100 to 1000 times stronger than those of the present Sun. Similarly, the transition region and chromospheric FUV–UV emissions of the young Sun are expected to be 10 to 100 and 5 to 10 times stronger, respectively, than present and the flux variation over age is therefore a steep wavelength function. Figure 1.12 shows the time evolution of the spectral range with 1 Å $< \lambda <$ 1000 Å, which includes X-rays and EUV and the Lyman-α line at 1215.6 Å [30] at a distance of 1 AU. The resulting relative XUV fluxes shown

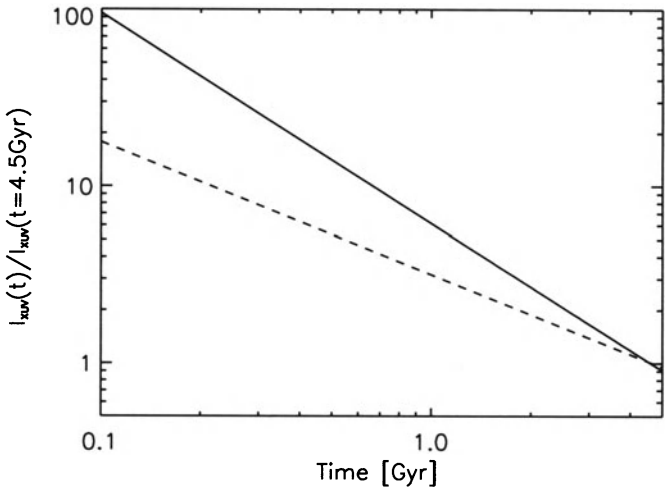

Fig. 1.12. Time evolution of the I_{XUV} energy flux for solar-like G stars (solid line: λ = 1000–1 Å; dashed line: Lyman-α = 1215.6 Å).

in Table 1.9 yield an excellent correlation between the emitted flux and stellar age. In the 1000–1 Å interval, the fluxes follow a power-law relationship [30]

$$\frac{I_{XUV}(t)}{I_{XUV}} = 6.16 \times (t[\mathrm{Gyr}])^{-1.19} . \tag{1.19}$$

Table 1.9. Solar-like G-type stars studied within the *Sun in Time* program. The parameters of the solar proxies shown below are: luminosity, distance, age, the XUV energy flux relative to the present value at 1 AU in the 1000–1 Å interval and Lyman-α [24].

Star	Lum [$L_\odot$]	Dist. [pc]	Age [Gyr]	P_{rot} [d]	$\frac{I_{XUV}(t)}{I_{XUV}}$	$\frac{I_{L_\alpha}(t)}{I_{L_\alpha}}$
EK Dra	0.94	34	0.13	2.75	69.8	14.6
π1 UMa	0.98	14.3	0.3	4.68	25.8	7.8
χ1 Ori	1.07	8.7	0.3	5.08	25.8	7.8
9 Cet	0.98	20.4	0.65	7.6	10.3	4.4
κ1 Cet	0.84	9.2	0.75	9.2	8.7	3.9
β Com	1.36	9.2	1.6	12.4	3.5	2.2
15 Sge	1.25	17.7	1.9	13.5	2.9	1.9
Sun	1.00	–	4.6	25.4	1	1
18 Sco	1.05	14.0	4.9	23.0	0.9	0.96
β Hyi	3.58	7.47	6.7	28.0	0.6	0.76
16 Cyg A	1.62	21.6	8.5	35.0	0.5	0.63

At longer wavelengths, the Lyman-α emission feature can contribute to a significant fraction of the XUV flux. High-resolution Hubble Space Telescope (HST) spectroscopic observations were used to estimate the net stellar flux. These measurements, together with the observed solar Lyman-α, define the following power-law relationship with high correlation

$$\frac{I_{\mathrm{L}_\alpha}(t)}{I_{\mathrm{L}_\alpha}} = 3.17 \times (t[\mathrm{Gyr}])^{-0.75} . \tag{1.20}$$

In both power laws, the XUV and Lyman-α expressions are valid for ages between 0.1 and 7 Gyr, I_{XUV} and I_{L_α} are the present integrated fluxes at 1 AU and $I_{\mathrm{XUV}}(\mathrm{t})$ and $I_{\mathrm{L}_\alpha}(\mathrm{t})$ are the integrated fluxes as a function of time. One finds fluxes of $\approx 6 \times I_{\mathrm{XUV}}$ and $\approx 3 \times I_{\mathrm{L}_\alpha}$ about 3.5 Gyr ago, and $\approx 100 \times I_{\mathrm{XUV}}$ and $\approx 20 \times I_{\mathrm{L}_\alpha}$ about 100 Myr after a solar-like G-type star arrived on the ZAMS.

Low Mass K and M Stars

Similar studies of the properties of X-ray and extreme ultraviolet fluxes and their typical evolution for low mass K and M stars are important, since "hypothetical" terrestrial exoplanets may also orbit in low mass star systems.

For an initial estimate of the evolution of XUV irradiances one can use a proxy indicator, which is the ratio of the X-ray luminosity to the bolometric luminosity ($\log [L_{\mathrm{X}}/L_{\mathrm{bol}}]$). This ratio is highest for the more active stars (i.e., fastest rotation period) and decrease monotonically with decreasing level of chromospheric activity [31, 32].

From the analysis of open cluster stars it is well established that all single late-type G, K and M stars spin down as they age, their activity decreases with time (see also P_{rot} in Table 1.9), and so does the ratio $\log(L_{\mathrm{X}}/L_{\mathrm{bol}})$. Another effect is that $\log(L_{\mathrm{X}}/L_{\mathrm{bol}})$ does not increase up to values arbitrarily close to unity for very active stars. Instead, a saturation phenomenon occurs and no active star seems to reach higher levels than $\log(L_{\mathrm{X}}/L_{\mathrm{bol}}) \approx -3$ [33, 34, 35].

Although some authors have interpreted this phenomenon as 100% surface coverage with stellar active regions like flares, the saturation phenomenon is not yet completely understood [1]. Qualitatively, the evolution of $\log(L_{\mathrm{X}}/L_{\mathrm{bol}})$ for a late-type star has a flat plateau from its arrival on the main sequence up to a certain age (the end of the saturation phase) and then decreases monotonically with age.

To study the activity level of K and M stars one can compare their values of $\log(L_{\mathrm{X}}/L_{\mathrm{bol}})$ and age with those of solar-like G-type stars. With the same underlying physical mechanism responsible for XUV emissions (magnetic dynamo) and a supposedly similar spectral energy distribution, it is reasonable to assume that stars with similar values of $\log(L_{\mathrm{X}}/L_{\mathrm{bol}})$ will also have similar $\log(L_{\mathrm{XUV}}/L_{\mathrm{bol}})$ (i.e., 1 Å$< \lambda <$1000 Å). One can use the XUV flux evolution

relationships for solar-like G stars and infer the XUV fluxes of K and M stars provided their X-ray fluxes are known. Astrophysical observations show that solar-like G0-V stars stay at saturated emission levels until ages of ~100 Myr and then their X-ray luminosity rapidly decreases following the power-law relationship discussed before as a function of age.

Recent studies of K type stars show that they stay at saturated emission levels for a little longer time and then also decrease following a power-law relationship of a very similar slope. Interestingly, M0–M5 stars seem to have saturated emission levels up to 1 Gyr (and possibly longer) and then decrease in an analogous way to G and K stars [36].

These preliminary results indicate that early K stars and early M-type stars may have XUV irradiances that are about 3 to 4 times and about 10 to 100 times higher, respectively, than solar-type stars of the same age. More accurate investigations are currently being carried out with an extended sample and a large variety of observational data [36].

EUV observations by the Einstein satellite on late G, K and M stars indicate that their main and median EUV luminosities of G, K stars broadly match the X-ray luminosity functions, while the M star EUV luminosities may be about a factor of 10 lower [1]. This probably arises from a high luminosity M dwarf tail in the X-ray function, but more research and observational data are needed.

However, high radiation on saturation levels up to several 100 Myr and even Gyr of M stars may result in large temperatures in the upper atmospheres on terrestrial exoplanets, which may result in problems of their atmospheric stability, evolution of their water inventories and planetary habitability (cf. Chap. II, Chap. VI, Chap. VII).

I.4 Solar/Stellar Winds

After the XUV radiation environment of stars, the evolution of the stellar wind mass flux as a function of age also has important implications for the evolution of planetary atmospheres. The average momentum flux of the present solar wind ions at 1 AU is about 1.5×10^{-8} g cm^{-2} s^{-1}, while the energy flux is about 2×10^{11} eV cm^{-2} s^{-1}. To obtain the evolution of the stellar wind velocity $v_{\rm sw}$ and stellar wind density $n_{\rm sw}$ of solar-like stars, one can use the scaling for stellar mass loss provided by [25] and the scaling for the velocity developed by [26].

The stellar mass loss can be estimated by using recent indirect stellar wind observations [25]. Recent HST high-resolution spectroscopic observations of the H Lyman-α feature of several nearby solar-like G and K main-sequence stars have revealed neutral hydrogen absorption associated with the interaction between the stars' fully ionized coronal winds with the partially ionized local interstellar medium (ISM). By modelling the absorption features formed

in the astrospheres of these stars one can provide empirically estimated coronal mass loss rates for G and K main-sequence stars [25].

It was found from a small sample of solar-like stars, where astrospheres can be observed, that stellar mass loss rates increase with stellar activity. The observations of younger solar-like stars indicate that these stars had much denser stellar winds than the Sun today. The correlation between mass loss and X-ray surface flux follows a power-law relationship, which indicates an average stellar wind density up to 1000 times higher than today during the first 100 Myr after the Sun reached the ZAMS. The mass loss as a function of the X-ray flux ϕ_X observed on G and K stars, when the coronal activity is at its maximum, can be written as [25]

$$\frac{\mathrm{d}M}{\mathrm{d}t} \propto \phi_{\mathrm{X}}^{1.15}. \tag{1.21}$$

Mass loss rates of cool main-sequence stars depend on their rotation periods P_{rot}, which are in turn correlated with the star's ages. According to [25] these relations can be expressed as

$$\phi_{\mathrm{X}} \propto P_{\mathrm{rot}}^{-2.9} \tag{1.22}$$

and

$$P_{\mathrm{rot}} \propto t^{-0.6} \tag{1.23}$$

respectively. From (1.21) and (1.22), one obtains a power-law relationship for the mass loss rate as a function of rotation period, $\mathrm{d}M/\mathrm{d}t(P_{\mathrm{rot}})$. Here, a complication occurs. Equation (1.21) does look like a scaling for the mass loss, but what is really measured by [25] is the total ram pressure, i.e., the product of mass loss and stellar wind velocity. The mass loss given was obtained by assuming a constant stellar wind velocity v_{sw}. For finding scalings for both n_{sw} and v_{sw}, one can write $\dot{M}v_{\mathrm{sw}}$ rather than M in (1.21) [37]. Thus,

$$\frac{\mathrm{d}M}{\mathrm{d}t} v_{\mathrm{sw}} \propto P_{\mathrm{rot}}^{-3.3}. \tag{1.24}$$

To obtain the time dependence, one has to insert a function for $P_{\mathrm{rot}}(t)$ into (1.24). In principle, (1.23) could be used, but for sake of consistency with the velocity scaling given below one can take the scaling derived by [26]

$$P_{\mathrm{rot}} \propto \left(1 + \frac{t}{\tau}\right)^{0.7} \tag{1.25}$$

with the time constant $\tau = 2.56 \times 10^7$yr. The time elapsed since the formation of the planetary system is denoted by t. For the present day solar system, $t = 4.6$ Gyr. Combining (1.24) and (1.25) it is possible to derive a power-law formula for the stellar mass loss as

$$\frac{\mathrm{d}M}{\mathrm{d}t} v_{\mathrm{sw}} \propto \left(1 + \frac{t}{\tau}\right)^{-2.3} . \tag{1.26}$$

The stellar mass loss linearly depends on v_{sw} and n_{sw}:

$$\frac{\mathrm{d}M}{\mathrm{d}t} = A n_{\mathrm{sw}} v_{\mathrm{sw}} m_{\mathrm{p}} \tag{1.27}$$

where A is the stellar surface area and m_{p} the mass of the stellar wind protons. Thus, the average time–behavior of the stellar wind velocity of solar-like stars can be achieved by [26, 38]

$$v_{\mathrm{sw}} = v_* \left(1 + \frac{t}{\tau}\right)^{-0.4} . \tag{1.28}$$

From the mass loss formula (1.26) and with (1.27) one can determine the evolution of the average particle density [37]

$$n_{sw} = n_* \left(1 + \frac{t}{\tau}\right)^{-1.5} . \tag{1.29}$$

The proportionality constants are determined by the present-day conditions. With $v_{\mathrm{sw}} = 400$ km s^{-1} and $n_{sw} = 10^7$ m^{-3} for $t = 4.6$ Gyr and at $r = 1$ AU

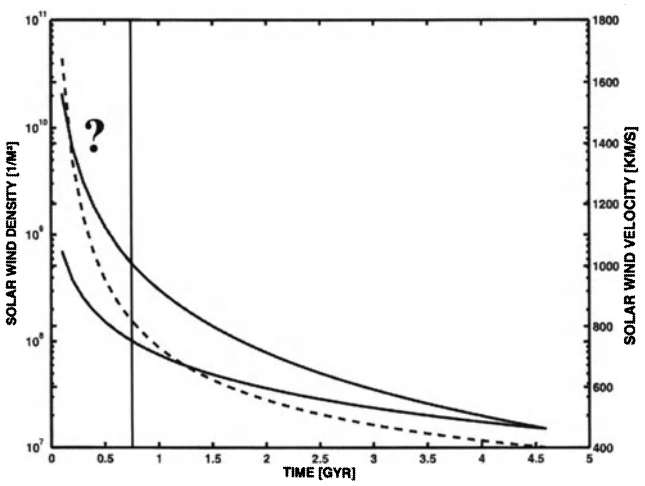

Fig. 1.13. Time evolution of the observational based minimal and maximal stellar wind densities scaled to 1 AU (left scale: solid lines) and obtained from several nearby solar-like G and K main-sequence stars due to observations from H absorption associated with the interaction between the stars' fully ionized coronal winds with the partially ionized local ISM. On the right scale one can see the temporal evolution of the stellar wind velocity (right scale: dashed curve). More observations of early active stars with ages less than 700 Myr are needed to obtain a better picture of the mass-loss/activity relation (courtesy of T. Penz).

[39] one obtains $v_* = 3200$ km s^{-1}, $n_* = 2.4 \times 10^{10}$ m^{-3} (density at 1 AU). The time constant is $\tau = 2.56 \times 10^7$yr [26]. For distances other than 1 AU, (1.29) is scaled with a $1/r^2$ dependency. The minimum and maximum time variation of $n_{\mathrm{sw}}(t)$ obtained from the observations of [25] and $v_{\mathrm{sw}}(t)$ [26] at 1 AU are shown in Fig. 1.13.

One can see from Fig. 1.13 that the observational data for solar-like G and K stars suggest that more active stars should have a higher mass loss rate and solar wind number density. However, recent observations of the M dwarf star Proxima Cen and the RS CVn system λ And (G8 IV + M V) are inconsistent with this relation and show lower mass loss rates. A recent observation of the ξ Boo binary system shows also a lower mass loss rate, which is consistent with the mass loss rates previously found for Proxima Cen and λ And (J. L. Linsky, private communication, 2004).

The common feature of these three stars is that they are all very active in X-ray surface fluxes at about 10^6 erg cm^{-2} s^{-1}, which is about a factor 30 larger than the todays Sun and corresponds to a time of about 700 Myr after solar-like young stars arrived at the ZAMS. These recent observations indicate the uncertainty of the early mass loss and solar wind estimations, because both stars in the ξ Boo system are usual but very active G and K stars, while Proxima Cen and λ And are different types than normal G and K stars.

It seems possible, that there could be a high-activity cutoff to the mass-loss/activity relation in (1.21) [25]; therefore, more active young solar-like G and K stars with X-ray surface fluxes larger than 10^6 erg cm^{-2} s^{-1} should be studied in the future.

II Neutral Atmospheres

II.1 Barosphere: Distribution Laws

Static Atmosphere

The upper atmosphere, in fact the entire barosphere, can be characterized by its pressure and density distribution. The starting point for the derivation of this distribution is the hydrostatic equation

$$\mathrm{d}p = -g\rho\mathrm{d}z \tag{2.1}$$

and the perfect gas law

$$p = nk_{\mathrm{B}}T \tag{2.2}$$

where p is the pressure, g is the acceleration of gravity, $\rho = nm$ is the mass density with n the number density, $m = \sum_j n_j m_j / n_j$ is the mean molecular mass, $k_B = 1.38 \times 10^{-16}$ erg/K is the *Boltzmann constant*, T is the absolute temperature and z is the height variable.

Combining (2.1) and (2.2) and assuming first the simplest case of T, g and m =const. we obtain after integration

$$\begin{aligned} p &= p_0 \exp\left(-\frac{mg}{k_{\mathrm{B}}T}z\right) = p_0 \exp\left(-\frac{z}{H}\right) \\ n &= n_0 \exp\left(-\frac{z}{H}\right) \\ \rho &= \rho_0 \exp\left(-\frac{z}{H}\right) \end{aligned} \tag{2.3}$$

where $H = k_{\mathrm{B}}T/mg$ ($H\,[\mathrm{km}] \doteq 825\; T\,[\mathrm{K}]/\hat{m}[\mathrm{amu}]\, g\,[\mathrm{cm\,sec}^{-2}]$) is the atmospheric scale height [40]. Equation (2.3) represent the barometric formula or hydrostatic distribution in its simplest form. The barometric formula is also a direct consequence of a Maxwellian velocity distribution, including the potential energy in a planetary gravitational field.

The total content in a column of unit cross-section of an atmosphere with constant scale height is given by

$$\mathfrak{N} = \int_0^\infty n\mathrm{d}z = n_0 H = \frac{p_0}{mg_0}\,. \tag{2.4a}$$

The total mass of a planetary atmosphere can be expressed by

$$M_{\text{atm}} = \left(\frac{p}{g}\right)_s 4\pi R_0^2 \tag{2.4b}$$

where the subscript "s" denotes the values of p and g at the planetary surface and R_0 is the planetary radius.

A more generally applicable form of the barometric law is given by the differential equation

$$\frac{\mathrm{d}p}{p} = \frac{\mathrm{d}n}{n} + \frac{\mathrm{d}T}{T} = -\frac{\mathrm{d}z}{H} \tag{2.5}$$

which can be used throughout the barosphere. It is often desirable to take into account the altitude variation of the acceleration of gravity in the barometric law, by defining a *potential* or *reduced* altitude z'. As long as the centrifugal force due to the planet's rotation is negligible, the acceleration of gravity is given by

$$g(z) = \frac{g_0 R_0^2}{(R_0 + z)^2} \tag{2.6}$$

where R_0 is the planetary radius and g_0 is the acceleration of gravity at the planet's surface ($g_0 = GM/R_0$, with M the planetary mass and $G = 6.6695 \times 10^{-8}\,\mathrm{cm^3\,g^{-1}\,sec^{-2}}$). Numerical values of g_0 for the planets and relevant satellites are listed in Table 2.1. The reduced or potential altitude can then be defined by

$$z' = \int_0^z \frac{g(z)}{g_0}\mathrm{d}z = R_0^2 \int_0^z \frac{\mathrm{d}z}{(R_0 + z)^2} = \frac{R_0 z}{R_0 + z}\,. \tag{2.7}$$

By using the reduced altitude, the variation of $g(z)$ is taken into account and g_0 can be used in the expression for the scale height, making H truly constant if $m, T = \text{const}$. Taking into account (2.5) the atmospheric scale height is defined by

$$H = -\left(\frac{\mathrm{d}\ln p}{\mathrm{d}z}\right)^{-1} \tag{2.8}$$

which is the inverse logarithmic decrement of pressure.

In the heterosphere and thermosphere the scale height varies with altitude as the result of the variation of m and T, leading to

$$\frac{1}{H}\frac{\mathrm{d}H}{\mathrm{d}z} = \frac{1}{T}\frac{\mathrm{d}T}{\mathrm{d}z} - \frac{1}{m}\frac{\mathrm{d}m}{\mathrm{d}z} - \frac{1}{g}\frac{\mathrm{d}g}{\mathrm{d}z}\,. \tag{2.9}$$

In this case a distinction must be made between atmospheric (pressure) scale height H and density scale height H_ρ, since $H \geq H_\rho$ [40]. (The two scale

Table 2.1. Surface gravitational acceleration of solar system bodies.

Planet	g_0 [cm/sec^2]
Mercury	370
Venus	887
Earth	980
Mars	371
Jupiter	2312
Saturn	896
Uranus	869
Neptune	1100
Pluto	81
Satellites	
Io	181
Europa	130
Ganymede	142
Callisto	125
Titan	135
Triton	78
Charon	33

heights are the same only for an isothermal atmosphere with m = const.) This fact is important since the deceleration of artificial satellites resulting from atmospheric drag depends on the product $\rho H_\rho^{1/2}$. The pressure and density scale heights are related by virtue of

$$H_\rho = -\left[\frac{1}{\rho}\frac{\mathrm{d}\rho}{\mathrm{d}z}\right]^{-1} = \frac{H}{1+\beta-2H/(R_0+z)} \tag{2.10}$$

where $\beta = \mathrm{d}H/\mathrm{d}z$; the term $2H/(R_0+z)$ arises from the variation of g with height. The scale heights in units of, "reduced" altitude are thus given by

$$H'_\rho = \frac{H'}{1+\beta'} \tag{2.11}$$

where $\beta' = \mathrm{d}H'/\mathrm{d}z'$.

Often the scale height gradient β can be assumed to be constant over certain height intervals. In this case the pressure and density distributions can be expressed by [41]

$$\begin{aligned} p &= p_0\left(\frac{H}{H_0}\right)^{-1/\beta} = p_0\exp(-\zeta) \\ n &= n_0\left(\frac{H}{H_0}\right)^{\beta-1)/\beta} = n_0\exp[-(1+\beta)\zeta] \end{aligned} \tag{2.12}$$

as the result of introducing a height variable ζ defined by $H = H_0 \exp(\beta\zeta)$ or equivalently $\mathrm{d}\zeta = \mathrm{d}z/H$, if we take $\beta = \mathrm{d}H/\mathrm{d}z = \text{const.}$, so that $H = H_0 + \beta z$.

Any of the distributions given by (2.3) and (2.12) are called hydrostatic distributions. They are representative of a mixing distribution when the scale height H corresponds to a mean molecular mass $m = \text{const}$. When each individual constituent is distributed according to its own scale height $H_j = k_B T/m_j g$, such a distribution is also called a diffusive equilibrium distribution. In this case the various constituents obey Dalton's law of partial pressures.

Dynamic (Transport) Effects

The principal transport process in the upper atmosphere is diffusion. It is due to a gradient in relative concentration arising from slight deviations from a Maxwellian distribution. The relevant properties can be described by gas-kinetic methods of transport theory.

In considering the behavior of a minor constituent under diffusion, it can be assumed that the total pressure remains practically constant, while the minor constituent diffuses upward or downward due to the presence of local sources or sinks. This requires that the divergence of the flux $F_j(z)$ of the j-th constituent obeys the continuity equation

$$\frac{\mathrm{d}F_j}{\mathrm{d}z} = q_j(z) - L_j(z) \tag{2.13}$$

where q_j and L_j are the sources and sinks, respectively, for the j-th constituent.

The flux F_j which can be supported by a given density distribution $n_j(z)$ is given by [40, 42]

$$\begin{aligned} F_j = n_j w_j &= -n_j D_j \left[\frac{1}{n_j} \frac{\mathrm{d}n_j}{\mathrm{d}z} + \frac{1}{H_j} + \frac{(1+\alpha_j)}{T} \frac{\mathrm{d}T}{\mathrm{d}z} \right] \\ &= -n_j K_D \left[\frac{1}{n_j} \frac{\mathrm{d}n_j}{\mathrm{d}z} + \frac{1}{H} + \frac{1}{T} \frac{\mathrm{d}T}{\mathrm{d}z} \right] \end{aligned} \tag{2.14}$$

where w_j is the flow velocity, D_j is the molecular diffusion coefficient, H_j is the scale height of the j-th constituent, H is the (average) atmospheric scale height, α_j is the thermal diffusion factor and K_D is the eddy diffusion or mixing coefficient. Equation (2.14) contains the effects of molecular diffusion (first term) as well as eddy diffusion (second term) which is of principal importance below the homopause, whereas molecular diffusion is predominant above the homopause. Figure 2.1 shows the effects of Eddy and molecular diffusion.

The molecular diffusion coefficient in a multiconstituent gas is given by [43]

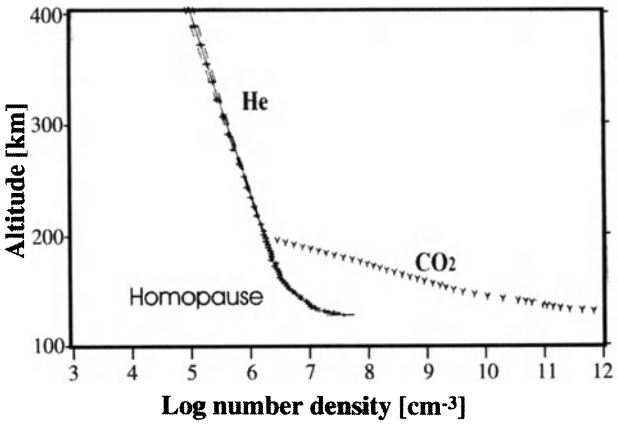

Fig. 2.1. Pioneer Venus measurements of He and CO_2 number densities obtained by a neutral mass spectrometer. The gradient of He densities above about 200 km altitude indicate exospheric temperatures of about 280 K. The curvature of the He profile below 200 km has been used after [44] to calculate the K_D profile in the lower atmosphere. One can identify the homopause from altitude variations of both species ($m_{CO_2} = 11 m_{He}$). According to (2.14) the homopause is defined where $D = K_D$ leading to a scale height of the minor constituent at the homopause of $H^* = 2k_B T/(m_{CO_2} + m_{He})g$; i.e. an effective mass $m^* = (m_{CO_2} + m_{He})/2$ [45].

$$\frac{1}{D_j} = \sum_{k \neq j} \frac{n_k}{b_{jk}} \tag{2.15}$$

where the b_{jk} are given by the binary encounters between particles of species j and k. Assuming rigid elastic spheres of diameters d

$$b_{jk} = \frac{3}{8 d_j^2} \left(\frac{k_B T (m_j + m_k)}{2\pi m_j m_k} \right)^{\frac{1}{2}} \tag{2.16}$$

where $d_{jk} = \frac{1}{2}(d_j + d_k)$.

Thus, the molecular diffusion coefficient is proportional to

$$D_j \propto T^{1/2} n^{-1} . \tag{2.17}$$

The thermal diffusion coefficient can also be estimated by assuming rigid elastic spheres. In the case of a minor constituent, $\alpha_j \to -5/13$. However, the rigid sphere model seems to overestimate α_j; a practical value for light minor constituents (H, D, He) is $\alpha_j = -0.25$ [44].

There is at present no completely satisfactory physical derivation of the eddy diffusion coefficient K_D. However, if it is assumed that K_D arises from turbulence produced by internal atmospheric gravity waves then

$$K_D = 1.4 \times 10^{-2} \tau_g^{-1} H^{-1} \lambda_x^4 \lambda_z^4 (\lambda_x^2 + \lambda_z^2)^{-\frac{5}{2}}$$

where λ_x and λ_z are the horizontal and vertical wavelength respectively. In contrast to the molecular diffusion coefficient $D_j \sim n^{-1}$, the eddy diffusion coefficient $K_D \sim n^{-1/2}$. For the case of a constant scale height gradient β, the diffusive flux above the homopause can be expressed by

$$F_j = -\frac{D_j}{H}\left[\frac{dn_j}{dz} + \left(\frac{m_j}{m} + \beta + \beta\alpha_j\right) n_j\right] . \tag{2.18}$$

Integration of (2.18) with $F_j = \text{const.}$ leads to the density distribution under flow conditions [42]

$$n_j = n_{j0} e^{-A\zeta}\left[1 + \frac{B}{C}(e^{-C\zeta} - 1)\right] \tag{2.19}$$

where

$$A = \frac{m_j}{m} + \beta\alpha_j + \beta \quad B = \frac{F_j H_0}{n_{j0} D_0} \quad C = 1 - \left(\frac{m_j}{m} + \alpha_j\beta + \frac{\beta}{2}\right) .$$

The parameters in B are taken at the lower reference level (subscript 0) of the diffusion-controlled region, i.e., above the homopause. The bracketed terms in (2.19) represent a correction factor to the non-flow (diffusive equilibrium) condition. The diffusive equilibrium distribution corresponds to the case $w_j = 0$ (cf. [41]–[52]). A more generally valid form of (2.19) for a variable flux $F_j(z)$ is given by [47]

$$n_j(z) = \overline{n_j(z)}\left[1 - \int_0^z \frac{F_j(z)}{D_j(z) n_j(z)} dz\right] \tag{2.20}$$

where $\overline{n_j(z)} = (T_0/T) n_{j0} \exp\left(-\int_0^z dz/H_j\right)$ is the zero flow or diffusive equilibrium distribution.

A good approximation for the density under flow conditions, n_j can be obtained in terms of the integrated column density (total content) $\mathfrak{N}$ of the main atmosphere (density n) through which the constituent j diffuses [48]. The flux F_j can be expressed in terms of the ratio of density under flow to the zero flow (static) density $\eta_j = n_j/\overline{n_j}$ according to

$$F_j = -D_j \overline{n_j} \frac{d\eta_j}{dz} = -\left(\frac{b_j \overline{n_j}}{n}\right) \frac{d\eta_j}{dz}$$

where $b_j = D_j n$ is the diffusion coefficient at unit concentration, with n the density of the main atmosphere. Using $n = -d\mathfrak{N}/dz$ we can write

$$\frac{d\eta_j}{dz} = \frac{F_j}{b_j \overline{n_j}} \frac{d\mathfrak{N}}{dz} \quad \eta_j = \frac{F_j \mathfrak{N}}{b_j \overline{n_j}} + \eta_\infty$$

where η_∞ is the ratio of actual to static density at great heights and the density under flow follows as

$$n_j = \eta_j \overline{n_j} = \frac{F_j \mathfrak{N}}{b_j} + \eta_\infty \overline{n_j} \,.$$

The flow which can be supported by diffusion in a given atmosphere without external sources or sinks ($\nabla \cdot \mathbf{F}_j = 0$) is limited by the condition $B = C$ in (2.19) and is given by

$$F_j^* = \frac{n_{j0} D_0}{H_0} \left[1 - \frac{m_j}{m} - \beta \left(\alpha_j + \frac{1}{2} \right) \right] . \tag{2.21}$$

This leads to a density distribution at the reference level ($z = 0$), $\mathrm{d}(\ln n_j)/\mathrm{d}z = -(1+\beta/2)/H$. This characteristic slope is approached at lower levels for near maximum flow, e.g., $0.95\, F_j^*$ and therefore the transition from a mixing distribution,

$$\frac{\mathrm{d}(\ln n_j)}{\mathrm{d}z} = -\frac{(1+\beta)}{H}$$

is almost indistinguishable. This is illustrated in Fig. 2.2 for hydrogen in N_2. For a constant scale height it can easily be shown that the maximum upward flux

$$F_j^* = \frac{n_0 D_0}{H} \left[1 - \frac{m_j}{m} \right]$$

leads to a density distribution $n_j = n_{j0} \exp(-z/H)$, i.e., a distribution corresponding to the main mixed atmosphere through which the minor constituent diffuses. The density distribution of a minor constituent under flow and diffusive equilibrium for $H_j = \text{const.}$ is illustrated in Fig. 2.3. The time constant for (molecular) diffusion can be derived from the continuity equation $\partial n_j/\partial t = -\partial F_j/\partial z$, noting that $\tau \equiv ((1/n)(\partial n/\partial t))^{-1}$, i.e., the characteristic time for attaining a diffusive equilibrium distribution is given by [42]

$$\tau_{\mathrm{D}j} \simeq \frac{H^2}{D_j} = \frac{H^2}{b_j} n(z) \,. \tag{2.22a}$$

For a constant scale height, τ_{D} decreases exponentially with altitude since it is proportional to $n(z)$.

Similarly, the time constant for turbulent mixing (eddy diffusion) is given by

$$\tau_{K_{\mathrm{D}}} \simeq \frac{H^2}{K_{\mathrm{D}}} \tag{2.22b}$$

where K_{D} is the eddy diffusion coefficient. (The altitude where $\tau_{\mathrm{D}} = \tau_{K_{\mathrm{D}}}$ is usually identified with the homopause.)

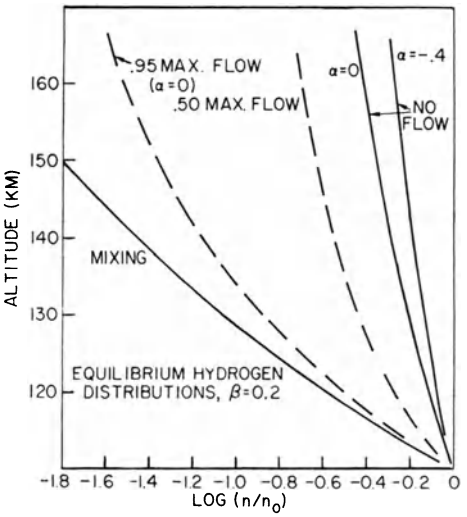

Fig. 2.2. Density distribution for mixing, diffusive equilibrium and flow conditions of the minor constituent hydrogen in a N_2 atmosphere, having a scale height gradient $\beta = 0.2$, including the effect of thermal diffusion (after P. Mange [42]).

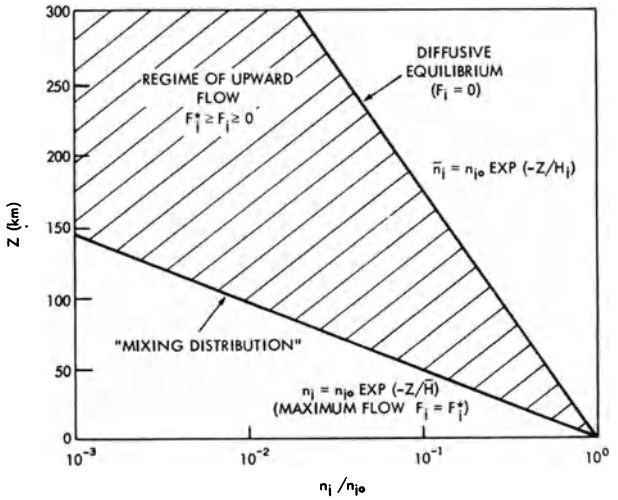

Fig. 2.3. Idealized density distribution of a minor constituent in an isothermal atmosphere under mixing, diffusive equilibrium and flow conditions.

The equation of motion of the neutral gas (such as a wind system set up by pressure gradients) can be expressed by [49]

$$\frac{\partial \boldsymbol{v}_\mathrm{n}}{\partial t} + \frac{\rho_\mathrm{i}}{\rho_\mathrm{n}}\nu_\mathrm{in}(\mathbf{v}_\mathrm{n} - \mathbf{v}_\mathrm{i}) = \mathbf{g} - \frac{1}{\rho_\mathrm{n}}\boldsymbol{\nabla} p_\mathrm{n} + 2(\boldsymbol{v}_\mathrm{n} \times \Omega) + \frac{\eta}{\rho_\mathrm{n}}\boldsymbol{\nabla}^2 \mathbf{v}_\mathrm{n} \qquad (2.23)$$

where $\boldsymbol{v}_\mathrm{n}$ is the (vector) velocity of the neutral gas, $\boldsymbol{v}_\mathrm{i}$ is the velocity of the ion gas (which may be constrained by a planetary magnetic field), ν_in is the ion-neutral collision frequency, $\rho_{n,(i)}$ is the neutral (ion) mass density, $\boldsymbol{v}_\mathrm{n} \times \Omega$ is the Coriolis acceleration, with Ω the angular velocity of the planet's rotation and η the coefficient of viscosity (η/ρ_n is the kinematic viscosity). The second term on the left-hand side is referred to as the *ion drag* term, which arises from the interaction between the neutral atmosphere and the ionosphere. Attempts have been made to deduce the wind-system in the terrestrial thermosphere arising from the diurnal pressure field [49].

Figure 2.4 shows the thermospheric wind field derived from (2.23). The atmospheric motion (winds) must also satisfy the conservation of mass through the equation of continuity

$$\frac{\partial \rho}{\partial t} = \boldsymbol{\nabla} \cdot (\rho \boldsymbol{v})$$

for the neutrals and simultaneously for the ions. Accordingly, vertical motions must occur which balance the divergence or convergence resulting from the horizontal wind field.

Atmospheric disturbances can propagate from the lower to the upper atmosphere where they may be responsible for oscillations in the neutral gas as well as in the ionospheric plasma in form of *travelling ionospheric disturbances* (TID) [50].

Oscillatory solutions can be obtained from the equations of motion and continuity for the neutral gas in (2.23), having the form

$$\frac{\Delta p}{p} \propto \frac{\Delta \rho}{\rho} \propto v_\mathrm{n} \propto \exp \mathrm{i}(\omega t - kr) \qquad (2.24\mathrm{a})$$

where $k = (k_x + k_z)^{\frac{1}{2}}$ is the complex wave number, with $k_{x,z} = 2\pi/\lambda_{x,z}$. For *upward* propagation in a lossless atmosphere one obtains the solution

$$\frac{\Delta \rho}{\rho} \propto \exp\left(\frac{\gamma g z}{2c_\mathrm{s}^2}\right) \equiv \exp\left(\frac{z}{2H}\right) \qquad (2.24\mathrm{b})$$

since the atmospheric scale height H and the sound speed $c_\mathrm{s} = (\gamma k_\mathrm{B} T/m)^{\frac{1}{2}}$ are related by $H = c_\mathrm{s}^2/\gamma g$, where γ is the ratio of the specific heats. This result is a direct consequence of the condition that the energy flux remain constant, i.e.,

$$\tfrac{1}{2}\rho v_n^2 = \text{const.}$$

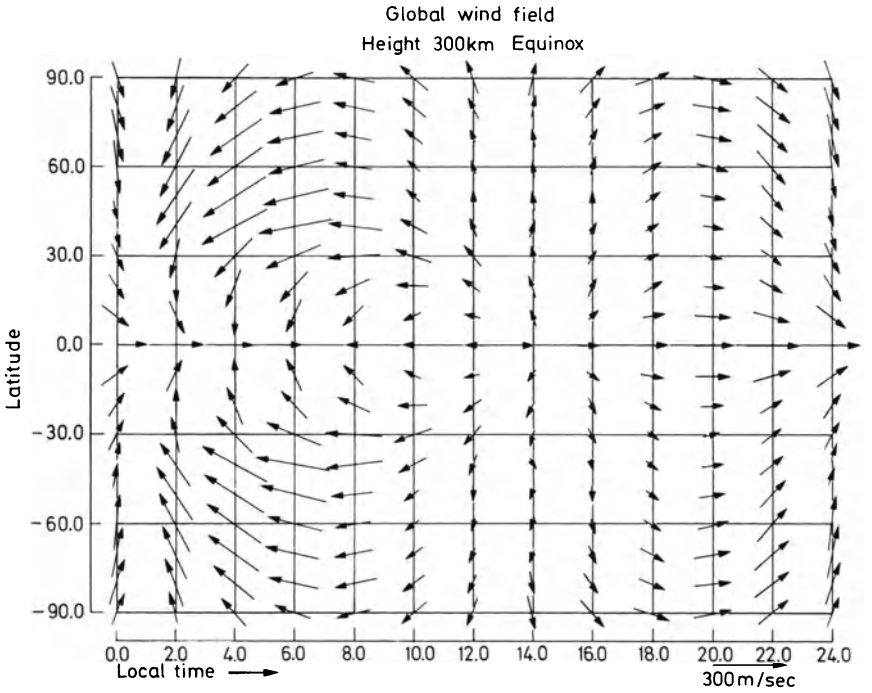

Fig. 2.4. Simplified global thermospheric wind system at equinox derived from (2.23) using model values of $\nabla p_n/\rho_n$ from satellite drag data and ion drag based on a semi-empirical model ionosphere (maximum wind speed $\sim$ 300 m/sec) (courtesy of P. Blum and I. Harris).

since in an isothermal atmosphere $\rho \propto \exp(-z/H)$. Waves for which such propagation can take place are determined by the following cutoff conditions. Waves whose angular frequency $\omega > \omega_g = \gamma g/2c_s$ are termed *acoustic waves*, whereas those for which $\omega < \omega_g = (\gamma - 1)^{\frac{1}{2}} g/c_s$ are termed *internal atmospheric gravity waves*. The cutoff frequency ω_a is called the *acoustic low frequency cutoff*; while the high frequency cutoff for internal atmospheric gravity waves ω_g is called the (isothermal) Brunt–Väisälä frequency. Internal atmospheric gravity waves can be considered a type of low frequency acoustic wave. (Tidal waves are essentially internal atmospheric gravity waves where the effect of the Coriolis force is included and which propagate primarily horizontally.) These waves can be produced from energy supplied by tidal forces, from large-scale (planetary) wind systems, or as the result of atmospheric heating by energetic particles as occurs in the auroral zone.

In reality, upward propagation of internal atmospheric gravity waves for a given ω is limited by the kinematic viscosity of the atmosphere as well as by reflections from a thermal barrier (i.e., where $dT/dz > 0$) so that only certain wavelengths are able to penetrate to higher altitudes [51].

II.2 Thermosphere: Thermal Structure

The energy budget of the upper atmosphere of planets is primarily governed by the heating of the gas due to the absorption of solar extreme ultraviolet and X-ray (XUV) radiation by atmospheric constituents, by heat transport due to conduction and convection and by heat loss due to emissions in the infrared (IR) [52, 53]. Radiative loss by IR occurs when atmospheric constituents are present which have transition levels in the infrared. This is the case for atomic oxygen in the terrestrial atmosphere and H_2, CO and CO_2 in other planetary atmospheres.

In addition to the XUV flux there are other possible sources of heating of the upper atmosphere of planets. Among them are collisions between charged particles and neutral constituents, Joule heating, conversion of dynamic energy into heat, such as from tidal motions and internal atmospheric gravity waves, absorption of hydromagnetic waves and either direct or indirect heating by the solar wind. Direct solar wind heating can occur in planetary atmospheres without a significant screening magnetic field (magnetosphere) as on Venus or Mars, while indirect effects can occur via magnetospheric processes which are again induced by the solar wind (e.g., heating associated with auroras).

The thermal balance in the thermosphere is governed by a heat conduction equation of the form [49]

$$\rho c_v \left[\frac{\partial T}{\partial t} + \boldsymbol{v}_n \cdot \boldsymbol{\nabla} T\right] + p \boldsymbol{\nabla} \cdot \boldsymbol{v}_n - \boldsymbol{\nabla} \cdot (K_n \boldsymbol{\nabla} T) = Q_{XUV} - L_{IR} \qquad (2.25)$$

where ρ is the atmospheric mass density, c_v is the corresponding specific heat at constant volume, $\boldsymbol{v}_n$ is the velocity and p the pressure of the neutral atmosphere, K_n is the thermal conductivity which is a function of temperature according to $K_n = K_0 T^s$, Q_{XUV} represents the total volume heat production rate, which may be the sum of a number of processes, including recombination heating and heating by collisions with charged particles of the form $Q_{in} = A(T_e - T_n) + B(T_i - T_n)$ where A and B depend on the appropriate collision frequencies between electrons and neutrals and ions and neutrals, respectively. L_{IR}, the radiative loss term, depends on the number density of the emitting state which is related to the total number of the emitting species n_x by a partition function $f(T)$ and is thus of the form [52]

$$L_{IR} = n_x f(T);$$

the details have to be derived from radiative transfer considerations [53].

A simplification of (2.25) has been considered by a number of workers in some detail, and has the form [54]

$$\rho c_p \left(\frac{\partial T}{\partial t} + v_{nz} \frac{\partial T}{\partial z}\right) - \frac{\partial}{\partial z}\left(K_n(T) \frac{\partial T}{\partial z}\right) = Q_{XUV} - L_{IR}$$

together with a diffusive equilibrium distribution for n. For the one-dimensional case (vertical variability z only) the condition $\mathrm{d}p/\mathrm{d}t = 0$ allows replacement of c_v by c_p and the expression of v_nz as the velocity of a parcel of air identical to the vertical velocity of the isobaric surface ("breathing velocity" of the atmosphere) given by

$$v_\mathrm{B} = T_\mathrm{n}(z) \cdot \int_0^z \frac{1}{T_\mathrm{n}^2} \frac{\partial T}{\partial t} \, \mathrm{d}z.$$

Actually, v_nz must be considered the sum of the breathing velocity and a divergence velocity arising from the horizontal wind system by virtue of continuity [55].

The principal heat source for the thermosphere is generally considered to be the conversion of absorbed solar XUV radiation into thermal energy by superelastic collisions. The heat production rate due to the absorption of solar XUV radiation for a given wavelength and constituent is given by

$$Q_\mathrm{XUV} = \varepsilon_j n_j \sigma_\mathrm{a} I_\mathrm{XUV} \mathrm{e}^{-\tau} \tag{2.26}$$

where ε_j is the fraction of absorbed XUV energy which is transformed into thermal energy, i.e., the photoionization *heating efficiency*, which is thought to lie in the range from 0.3 to 0.6 and may also differ for different spectral ranges; I_XUV is the energy flux [erg cm^{-2} sec^{-1}] at the XUV wavelength range outside the atmosphere and is related to the *photon flux* Φ_∞ by

$$I_\mathrm{XUV} = \left(\frac{\mathfrak{h}c}{\lambda}\right) \Phi_\mathrm{XUV}$$

where $\mathfrak{h}$ is Planck's constant, c the velocity of light; σ_a is the appropriate absorption cross-section (typically in the range 10^{-18}–10^{-16} cm^2) and τ is the optical depth defined by

$$\tau = \int_z^\infty \sec\chi \cdot \sigma_\mathrm{a} \cdot n_j \, \mathrm{d}z \tag{2.27}$$

with χ the solar zenith angle ($\cos\chi = \sin\varphi \sin\delta + \cos\varphi \cos\delta \cos(\Omega t)$, where φ is the latitude, δ is the solar declination, Ω is the atmospheric (planetary) rotation rate and t is time measured from the noon meridian); for $\chi > 75°$, $\sec\chi$ must be replaced by the Chapman function $\mathrm{Ch}(\chi)$ which allows for the curvature of the planet (cf. Sect. I.1). The solution of the time-dependent heat balance equation (2.25) leads to a time variation of the temperature in the thermosphere, having a maximum which occurs later than that of the XUV heat input, due to the thermal inertia of the atmosphere. Figure 2.5 illustrates the diurnal variation of the exospheric temperature T_∞ and that of the terms in the heat balance equation represented by their integrated values, i.e., the total XUV heat input, the total IR loss, the total conduction loss and the mechanical energy $\int p \nabla \cdot \boldsymbol{v}_\mathrm{n} \, \mathrm{d}z$, as obtained from a numerical

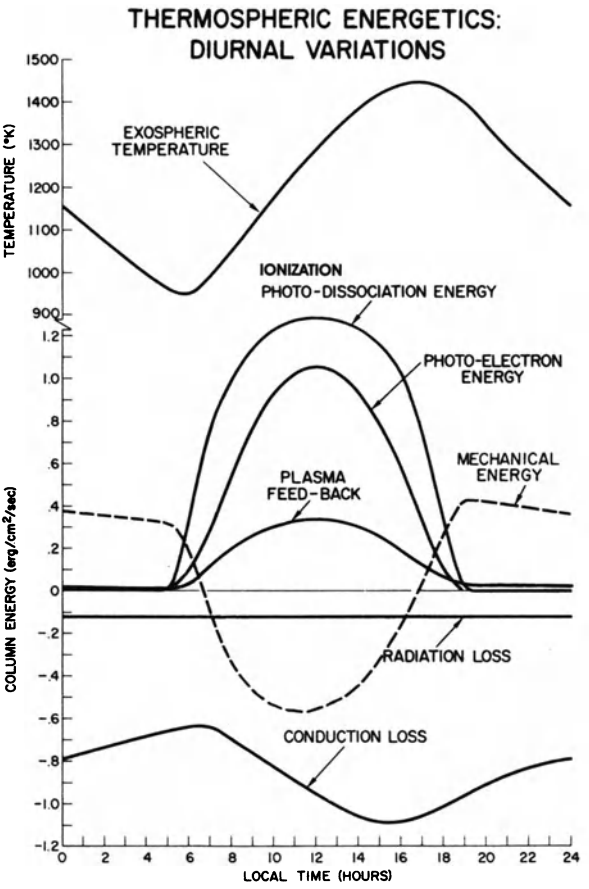

Fig. 2.5. Diurnal variation of Earth's exospheric temperature T_∞ and the integrated values (above 120 km) of the terms in the heat balance equation. "Ionization" due to XUV radiation contributes to thermospheric heating. "Photodissociation energy" represents the integrated heat input due to dissociation by the Schumann–Runge continuum; "Photoelectron energy" represents the heat input due to XUV photoelectrons; "Plasma feed-back" includes the heat source due to collisions between the neutral and electron–ion gas and due to exothermic chemical reactions (dissociative recombination); "Mechanical energy" represents the integrated heat input due to the expansion and contraction ($\int p\nabla \cdot v_n \, dz$) of the atmosphere; "Radiation loss" represents the IR radiation loss above 120 km and "Conduction loss" represents the integral of the heat conduction term (courtesy of S. Chandra).

solution of (2.25). In addition to the XUV heat input, collisions between the neutral and the electron–ion gas can provide an additional heat source for the thermosphere according to

$$Q_{\text{coll}} = 2N_{\text{i}}\frac{\mu_{\text{in}}^2}{m_{\text{i}}m_{\text{n}}}\nu_{\text{in}}\left[\frac{3}{2}k_{\text{B}}(T_{\text{i}} - T_{\text{n}}) + \frac{1}{2}m_{\text{n}}(v_{\text{i}} - v_{\text{n}})^2\right]$$

as can exothermic chemical reactions such as dissociative recombination (cf. Chap. IV)

$$XY^+ + \text{e} \rightarrow X + Y + \Delta E.$$

Figure 2.6 shows the vertical temperature profile at the diurnal maximum and minimum for the conditions shown in Fig. 2.5. A problem has arisen for the terrestrial thermosphere which has been termed the *diurnal phase anomaly* between atmospheric density and temperature. From satellite drag observation it was established [56] that the atmospheric density in the thermosphere reaches a maximum around 1400 LT (local time) and consequently a temperature maximum was inferred for the same time from atmospheric model considerations.

The magnitude of the diurnal phase anomaly is a function of atmospheric composition, since the individual atmospheric constituents attain their diurnal maxima at different times, e.g., He in the morning hours and O in the early afternoon. Thus, the lighter the constituent, the larger the phase anomaly. The solution of the heat conduction equation (2.25) on the other hand leads to a maximum in the temperature at about 1700 LT. A number of suggestions have been made to explain this phase discrepancy which range from the original assumption of a secondary ad hoc heat source [54] to the

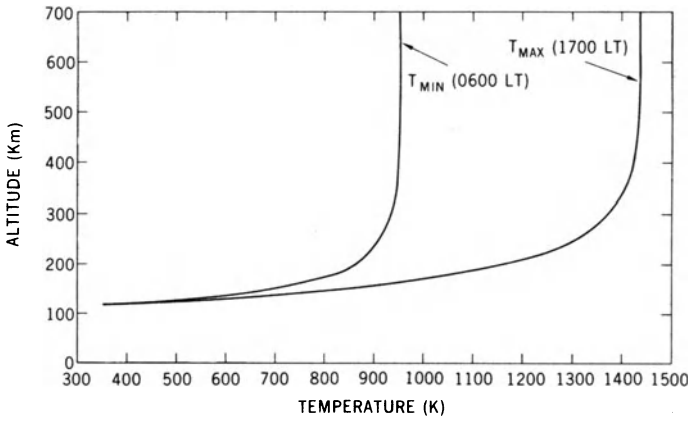

Fig. 2.6. Vertical temperature profiles in the terrestrial thermosphere at the time of diurnal minimum and maximum.

Table 2.2. Dependence of diurnal variation of exospheric temperature T_∞ on basic input parameters.

Cause	Effect		
Increase of:	T_{max}	$\frac{T_{min}}{T_0}$	$\frac{T_{max}}{T_{min}}$
Rotation rate of atmosphere, Ω' (superrotation)	$\rightarrow$	$\uparrow$	$\curvearrowright$
Specific heat c_p			
Thermal conductivity K_n	$\leftarrow$	$\downarrow$	$\curvearrowright$
Absorption cross section, σ_a	$\leftarrow$	$\uparrow$	$\uparrow$
Pressure at base level, p_0	$\rightarrow$	$\uparrow$	$\curvearrowright$
Solar activity, I_∞	$\updownarrow$	$\uparrow$	$\updownarrow$

$\uparrow$ increase, $\downarrow$ decrease, $\curvearrowright$ goes through max, $\updownarrow \sim$ const, $\leftarrow$ earlier, $\rightarrow$ later.

inclusion of dynamical effects and extension of the one-dimensional heat conduction to two and three dimensions [57, 58]. In addition, the ratio between the maximum and minimum temperature also differs between theory and that derived from satellite drag observations, the latter being 1.3, whereas the former is ~1.5–2. Thermospheric temperature data inferred from ground based incoherent scatter radar measurements suggest the peak temperature occurs near 1700 LT with a diurnal amplitude closer to the theoretical value. In the light of this result, a suggestion has been made [59] that the phase anomaly is due to the fact that the density and temperature at the homopause is not time independent but show a diurnal variation, whereas others [60] view the phase anomaly as the result of wind-induced diffusion. A parametric study of the thermospheric heat balance equation of the type

$$\rho c_p \left\{ \frac{\Omega'}{\Omega} \frac{\partial T}{\partial t} + v_B \frac{\partial T}{\partial z} \right\} = Q + \frac{\partial}{\partial z} \left(K_n \frac{\partial T}{\partial z} \right) \tag{2.28}$$

suggests that the diurnal variation of T_∞ responds to changes in the basic input parameters of (2.28) as shown in Table 2.2 [61]. One should also note that super-rotation of planetary atmospheres may occur; i.e., the atmosphere (or parts of it) may rotate faster than the planet [62].

When a two-dimensional atmospheric model including winds is considered [61], the "diurnal amplitude" of temperature is found to be

$$\frac{T_{max}}{T_{min}} \propto \frac{Q(\Omega)}{|L_{con} - \Omega C|}$$

where $Q(\Omega)$ is the diurnal XUV heat source and $\Omega = 2\pi/\mathrm{d}$ the angular frequency, with D the solar day, i.e., in general, Ω is the rotation rate of the planetary atmosphere; L_{con} is the heat loss due to conduction and convection,

i.e., mass transport by winds, both assumed to be proportional to temperature and $C = c_v \rho$ is the heat capacity of the atmosphere. The time of the diurnal temperature maximum is related to these quantities by

$$t_{max} \propto \frac{C}{L_{con}} .$$

Empirical relations have been derived for the variation of exospheric temperature with solar activity and geomagnetic activity. As an indicator of the solar XUV intensity, the 10.7 cm solar radio flux (2800 MHz) observed on Earth has generally been employed, since continuous observations over long time intervals of the solar XUV radiation are very difficult. However, the close correlation between solar XUV and the 10.7 cm radio flux, $F_{10.7}$, has been established over limited time intervals [63]. Typical values of $F_{10.7}$ in units of $10^{-22}\,\mathrm{W\,m^{-2}\,Hz^{-1}}$ averaged over several solar rotations are: 75 for low solar activity (solar minimum), 150 for medium activity and 230 for high solar activity (solar maximum).

Empirical relations between the terrestrial exospheric temperature derived from satellite drag and the 10.7 cm flux have been developed from observations extending over a full 11-year solar cycle [56]; a nearly linear correlation was found between T_∞ and $F_{10.7}$ (averaged over several solar rotations $\equiv$ 27 days), according to which

$$\frac{\Delta T_\infty}{\Delta F_{10.7}} \simeq \frac{4\,\mathrm{K}}{10^{-22}\,\mathrm{W\,m^{-2}\,Hz^{-1}}}$$

The temperature change due to magnetic activity is

$$\Delta T_\infty = 20\,K_p + 0.03\,\exp K_p$$

where K_p is the planetary magnetic index, which in turn is related to the solar wind velocity v_{sw} according to

$$v_{sw}\,[\mathrm{km/sec}] \doteq 330 + 67.5\,K_p .$$

It should be noted that for planets without an appreciable intrinsic magnetic field, more direct solar wind heating may occur.

More recently it has been recognized that $F_{10.7}$ is not a perfect proxy for the XUV radiation responsible for heating and ionization of the upper atmosphere. Particularly at high solar activity $F_{10.7}$ seems to overestimate the XUV flux. Studies of the solar control of the ionospheres of Venus [64] and Mars[65] suggest that $I_{XUV} \propto F_{10.7}^m$ with $m \approx 0.9$; i.e. a slightly non-linear dependence. A comparison between $F_{10.7}$ as proxy for the solar XUV input on the terrestrial thermosphere has led to a *corrected* $F_{10.7}$ flux, called $E_{10.7}$, as proxy for the integrated energy flux in the XUV range [71].

In the following we shall illustrate some of the general characteristics of planetary thermospheres which are the result of solar XUV heat input and

heat conduction. For this purpose we consider a simple form of the heat balance equation neglecting the IR heat loss. For steady state conditions ($\partial T/\partial t = 0$) we have

$$\frac{\mathrm{d}\mathfrak{F}}{\mathrm{d}z} \equiv -\frac{\mathrm{d}}{\mathrm{d}z}\left(K_\mathrm{n}\frac{\mathrm{d}T}{\mathrm{d}z}\right) = Q_\mathrm{XUV}$$

and by integration

$$\mathfrak{F} = \int_z^\infty Q_\mathrm{XUV}\,\mathrm{d}z = -\alpha\varepsilon_j I_\mathrm{XUV}(1-\mathrm{e}^{-\tau})$$

noting from the definition of optical depth that $\mathrm{d}z = \mathrm{d}\tau/n_j\sigma_\mathrm{a}$. Since the heat flux is $\mathfrak{F} = -K_{\mathrm{n}j}(T)\,\mathrm{d}T/\mathrm{d}z$, we can write

$$\frac{\mathrm{d}T}{\mathrm{d}z} = \frac{\varepsilon_j I_\mathrm{XUV}(1-\mathrm{e}^{-\tau})}{\alpha K_{\mathrm{n}j}(T)}\,. \tag{2.29}$$

This represents the thermospheric temperature gradient which can be supported by the XUV heat input and heat conduction.

The factor α takes on values appropriate for the rotation of the planet: about 4 for rapidly rotating planets like Jupiter and about 2 for slowly rotating or tidally locked planets, because of the ratio to the cross-sectional area of the surface of the planetary sphere. The value of α may be reduced close to 1/4 by the action of strong thermospheric winds expected on exoplanets at close orbital distances.

In the exosphere, where the density is low, $\tau \to 0$ which leads to $\mathrm{d}T/\mathrm{d}z = 0$, i.e., an isothermal atmosphere. This constant temperature is also called the exospheric temperature T_∞

$$T(z) = T_\infty\{1 - a\exp(-bz)\}$$

where

$$a = \frac{T_\infty - T_0}{T_\infty}$$

and

$$b = \frac{1}{T_\infty - T_0}\left(\frac{\mathrm{d}T}{\mathrm{d}z}\right)_{z_0}\,.$$

The temperature gradient will have its maximum value where the optical depth is large ($\tau \to \infty$), i.e., in the lower thermosphere. This maximum temperature gradient is given by

$$\left(\frac{\mathrm{d}T}{\mathrm{d}z}\right)_\mathrm{max} \simeq \frac{\varepsilon_j I_\mathrm{XUV}}{K_{\mathrm{n}j}(T)}\,.$$

Table 2.3. Solar energy flux of a 4.5 Gyr old G-type star (Sun) outside a planetary atmosphere normalized to that observed in the terrestrial exosphere as a function of orbital distance.

Planet	$\frac{I_{\mathrm{XUV}}(P)}{I_{\mathrm{XUV}}(\oplus)}$	d [AU]
OGLE-TR-56 b	1890.35	0.023
HD209458 b	493.82	0.045
Mercury	6.65	0.387
Venus	1.9	0.723
Earth	1.0	1.0
Mars	0.43	1.52
Jupiter	3.7×10^{-2}	5.2
Saturn	1.1×10^{-2}	9.54
Uranus	2.7×10^{-3}	19.18
Neptune	1.1×10^{-3}	30.06
Pluto	0.65×10^{-3}	29.4

The thermospheric temperature gradient is therefore directly dependent on the XUV heat input (and the heat conductivity). For medium solar activity, the total flux at Earth in the wavelength range 1310 – 270 Å (excluding the strong Lyman-α line, 1216 Å) is about $2\,\mathrm{erg\,cm^{-2}\,sec^{-1}}$ (for further details see Chap. I).

The energy flux for a given wavelength λ outside the planet's (P) atmosphere can be scaled from the terrestrial values according to $I_{\infty}^{\lambda}(P) = I_{\infty}^{\lambda}(\oplus)/d^2$, where d is the mean distance of the planet from the Sun in astronomical units (AU). Table 2.3 shows XUV energy fluxes at various objects and orbital distances. The time constant for equalization of a temperature difference by means of heat conduction is given by

$$\tau_{\mathrm{cond}\ j} \simeq \frac{n_j c_{\mathrm{v}} k_{\mathrm{B}} L^2}{K_{\mathrm{n}j}(T)} \tag{2.30}$$

where L is a scale length over which this temperature difference exists.

By performing a second integration of the simple heat balance equation we can also determine the variation of the "exospheric" temperature T_{∞} with the variation in solar XUV heat input over a solar cycle [67].

The integrated form of (2.29) is given by

$$\int_{T_0}^{T_{\infty}} K_0 T_j^{\mathrm{s}}\,\mathrm{d}T = \int_{z_0}^{z_{\infty}} \varepsilon_j I_{\mathrm{XUV}}(1 - \mathrm{e}^{-\tau})\,\mathrm{d}z$$

where T_{∞} is the exospheric temperature, T_0 is the temperature at the mesopause (which depends strongly on the IR loss) and z and z_0 are the corresponding altitudes. If we assume that $\tau \to 0$ at z_{∞}, i.e., in the exosphere, and $\tau \to \infty$ at z_0, i.e., at the base of the thermosphere, and allowing

Table 2.4. $K_{nj} = K_{0j} T^{s_j}$ [ergs cm^{-2}sec^{-1} °K^{-1}]

Constituent	K_{0j}	s_j
N_2	27.21	0.80
O_2	18.64	0.84
CO_2	1.5	1.23
CO	26.16	0.80
O	67.1	0.71
He	20.92	0.75
H	16.36	0.73
Ar	18.3	0.80

for $(n[z_\infty]\sigma_a)^{-1} \gg z - z_0$ (since the absorption cross-section $\sigma_a \simeq 10^{-17}$ cm^2 and exospheric densities are of the order of 10^8 cm^{-3}) we obtain

$$K_0(T_\infty^{s_j+1} - T_0^{s_j+1}) \simeq \frac{\varepsilon_j I_{XUV}}{n_j(z_\infty)\sigma_a}.$$

For $n_j(z_\infty)$ we can substitute the density at the base of the exosphere $n_c = (\sigma H)^{-1}$ (see next section), where $H = k_B T_\infty / mg$ is the exospheric scale height, and σ is the gas-kinetic collision cross-section.

The variation of T_∞ with solar XUV energy flux is therefore determined by the temperature dependence of the thermal conductivity. It has been generally assumed, based on a rigid sphere approximation, that $K_{nj} = A_j T^{\frac{1}{2}}$. (Note that the heat conductivity is related to viscosity η by $K_n = \frac{5}{2}\eta c_v$, cf. [43].) However, experimental data [68] and quantum mechanical calculations [69] show that for atmospheric gases

$$K_{nj} = K_{0j} T^{s_j}$$

where $s_j > \frac{1}{2}$. The heat conductivity and its temperature dependence for likely constituents of planetary atmospheres is given in Table 2.4.

From the effective heat production below the exosphere, which is balanced by the divergence of the conductive heat flux of the XUV radiation, one gets the following expression for T_∞^s [70]

$$T_\infty^{s_j} = \frac{s_j\, \varepsilon_j\, k_B}{K_{0_j}\, \alpha\, m_j\, g} \int_{\lambda_1}^{\lambda_2} I_{XUV}(\lambda) \times$$
$$\left\{ E[\tau(\lambda)] + \ln[\tau(\lambda)] + \gamma - \frac{m_j}{m_k}\left[1 - e^{-\tau(\lambda)}\right] \right\} d\lambda + T_0^{s_j}, \qquad (2.31)$$

where λ is the wavelength, τ is the optical thickness, E is the exponential integral, γ is Euler's constant, m_j and m_k are the masses of the atmospheric constituents and T_0 is the temperature at the base of the thermosphere. In

the case of a hydrogen dominated thermosphere $j = k$. After some approximations, one obtains

$$T_\infty^{s_j} \approx \frac{\varepsilon_j \, I_{\mathrm{XUV}} \, k_\mathrm{B} \, \sigma_{c_j}}{\alpha \, K_{0_j} \, m_j \, g \, \sigma_{a_j}} + T_0^{s_j}, \tag{2.32}$$

in which σ_{c_j} and σ_{a_j} are the collision and absorption cross-section, respectively. T_0 is negligible in cases where T_∞ is large. If planets 1 and 2 have an identical gas composition j in their thermosphere one obtains the following scaling relation [71, 72]

$$\frac{\left(T_\infty^{s_j} - T_0^{s_j}\right)_1}{\left(T_\infty^{s_j} - T_0^{s_j}\right)_2} = \frac{I_{\mathrm{XUV}_1} g_2}{I_{\mathrm{XUV}_2} g_1}. \tag{2.33}$$

One can see from 2.33 that T_∞ depends on I_{XUV}, which decreases with distance from the star, and on g, which is related to the mass and size of the planet. Thus, 2.33 allows us to estimate T_∞ and the thermal escape of hydrogen-rich exoplanets as a function of orbital distance, planetary mass and planetary size.

From satellite drag observations it is known that the terrestrial exospheric (daytime) temperature ranges from ~700 K at solar minimum to ~2000 K at solar maximum, i.e., a variation by a factor of about 2.5 while the exact variation of the XUV energy flux over a solar cycle has yet to be established. Since atomic oxygen is the principal constituent of the terrestrial thermosphere, according to $T_\infty \propto I_\infty^{1/0.71}$ one can infer from the temperature ratio of 2.5, that the XUV energy flux should have changed by a factor of ~1.9. From studies of the solar control of the ionospheres of Venus and Mars [64, 71] the dependence of neutral scale height H at ionospheric levels on solar activity expressed by $F_{10.7}$ for the solar XUV input was found to be $H \propto F_{10.7}^m$ with $m \approx 0.15$ for both planets. Since the scale height $H = k_\mathrm{B} T/mg$, this dependence can be thought to hold for $T_\infty \propto F_{10.7}^m$. On the other hand according to the simplification of (2.32) $T_\infty \propto (I_{\mathrm{XUV}}/\overline{m}g)^{1/s}$. The mean molecular mass $\overline{m}$ in a multicomponent thermosphere is subject to diffusion and will vary with temperature and thus with solar activity, increasing at the thermospheric levels according to $\overline{m} \propto F_{10.7}^k$. Since $I_{\mathrm{XUV}} \propto F_{10.7}^{0.9}$ one obtains for the variability of exospheric temperature with the $F_{10.7}$ proxy

$$T_\infty \propto F_{10.7}^{(0.9-k)/s} \equiv F_{10.7}^m$$

where from the exponent $m \approx 0.15$ one finds for Venus and Mars (s = 1.23) the variability of the exponential of the mean molecular mass according to $k \approx 0.7$. For Earth the dependence of T_∞ on $F_{10.7}$ was empirically found from the analysis of a series of satellite missions to be $T_\infty \propto F_{10.7}^{0.25}$. By making the same comparison of exponents as above one finds that for $s = 0.71$ a value of $k \approx 0.7$ is found, i.e., a similar dependence as on Venus and Mars.

The exosphere temperature T_∞ is the characteristic planetary temperature for thermal escape and is thus an important factor for the evolution of planetary atmospheres and their water inventories. In contrast to the surface temperature, it is not directly correlated to the distance from the radiation source because of the dependence on both energy input and heat conduction.

The effective temperature T_{eff} is generally the result of equilibrium between short wave radiation according to the source absorbed by the surface and emission of the long wave radiation according to the Stefan–Boltzmann law. For an energy flux S at a distance d from the source (Sun, star, etc.)

$$\frac{S(1-A)\pi R_0^2}{d^2} = \alpha\pi R_0^2 \sigma_{\text{SB}} T_{\text{eff}}^4$$

and thus

$$T_{\text{eff}} = \left[\frac{S\,(1-A)}{\alpha\sigma_{\text{SB}} d^2}\right]^{\frac{1}{4}}$$

where A is the planetary albedo and σ_{SB} the Stefan–Boltzmann constant. This radiation surface temperature is only equivalent to the actual surface temperature T_{s} when the atmosphere of a planet is transparent to both the incoming short wave radiation (visible) as well as the outgoing infrared radiation (IR) in consequence of Wien's displacement law. If the atmosphere contains polyatomic gases capable of absorption and emission in the IR, the greenhouse effect will ensure making the actual surface temperature higher than T_{eff}

$$T_{\text{s}} = T_{\text{eff}}\,(1+\tau_{\text{IR}})^{\frac{1}{4}}$$

where τ_{IR} is the effective IR optical depth due to the presence of greenhouse gases.

The consequences of high exospheric temperatures for the escape (expansion) of gases from planetary atmospheres will be discussed in the following section. The escape becomes excessively large for a critical temperature

$$T_{\text{crit}} = \left[\frac{3GM}{2R_0^2}\,(R_0+h)\right]^{\frac{1}{2}}$$

corresponding to the condition when the thermal energy of the gas kinetic motion $(3k_{\text{B}}T)/2$ overcomes the gravitational energy corresponding to an escape parameter $X = (v_\infty/v_0)^2 = 1.5$ where v_∞ is the escape velocity and v_0 is the most probable velocity of a Maxwellian velocity distribution of temperature T_{crit}. This condition was also called *blow off* by the astrophysicist E. Öpik, who first recognized the importance of hydrodynamic escape [73].

II.3 Exosphere: Atmospheric Escape (Evaporation)

At any level of a planetary atmosphere there will be some particles which move upward with a velocity greater than that required for escape from the gravitational attraction of the planet. These particles are representative of the high velocity tail of the Maxwellian velocity distribution. The actual escape, however, will depend on how frequent (or rather how infrequent) collisions are with other particles. At high enough altitudes the collision frequency will be low enough (i.e., the mean free path long enough) for escape to take place. This region is called the exosphere. The probability for a molecule travelling a distance z without a collision is given by

$$P(z) = \exp\left(-\frac{z}{\lambda}\right) ,$$

where λ is the mean free path

$$\lambda = (n\sigma)^{-1}$$

with n the total number density and σ the gas-kinetic collision cross-section. Thus, the mean free path represents the distance for which this probability is 1/e. The base of the exosphere z_c (exobase), originally called the critical level, is usually (but somewhat arbitrarily) defined by this probability requiring that

$$\int_{z_c}^{\infty} \frac{\mathrm{d}z}{\lambda(z)} = \int_{z_c}^{\infty} n(z)\sigma \,\mathrm{d}z = n_c H\sigma \equiv \frac{H}{\lambda} = 1 .$$

Exospheric conditions, i.e., the possibility of evaporation, are therefore assumed to hold at altitudes where the mean free path is equal to or greater than the local scale height, $\lambda \geq H$. The density at the exobase is given by $n_c = (\sigma H)^{-1}$. This density value then defines the critical level or the exobase. Numerically, n_c [cm^{-3}] $\approx 3 \times 10^9/H$ [km] for $\sigma_a \approx 3 \times 10^{-15}$ cm^{-2} and the total content of an exosphere is

$$\mathfrak{N}_\infty \cong \sigma^{-1} \approx 3 \times 10^{14}\, cm^{-2} .$$

A "sharp" exobase obviously represents a highly idealized concept. Accordingly, it is assumed that below and at the critical level a Maxwellian velocity distribution prevails, whereas in the exosphere the velocity distribution is truncated, due to absence of particles with speed above the escape velocity. Thus, the barometric law applies below the exobase, i.e., in the barosphere, but does not hold strictly in the exosphere. For this reason, the exobase may also be called the baropause (the pressure at this level is $p_\infty \approx mg\mathfrak{N}_\infty$).

The minimum velocity for escape v_∞ is that for which the kinetic energy of the particle balances the potential energy in the gravitational field

$$v_\infty = \left(\frac{2GM}{R}\right)^{\frac{1}{2}} = \sqrt{2gR}$$

Table 2.5. Escape velocities from solar system bodies.

Planet	v_∞ [km/sec]
Mercury	4.3
Venus	10.4
Earth	11.2
Mars	5.1
Jupiter	59.5
Saturn	35.5
Uranus	$\sim$ 21.3
Neptune	$\sim$ 23.3
Pluto	1.2
Satellites	
Io	2.56
Europa	2.02
Ganymede	2.74
Callisto	2.45
Titan	2.64
Triton	3.1
Charon	0.75

where G is the universal gravitational constant ($G = 6.6695 \times 10^{-8}\,\mathrm{cm^3\,g^{-1}\,sec^{-2}}$), M is the mass of the planet and R is the radial distance from the center of the planet.

Table 2.5 lists the escape velocities for the planets and relevant satellites for $R = R_0$; note that the escape velocity is $\sqrt{2}$ times the circular orbital velocity. In the Russian literature the orbital velocity is referred to as the "first cosmic velocity", while the escape velocity is called the "second cosmic velocity". Our discussion of escape from planetary atmospheres is based on the classical Jeans treatment [74], with extensions based on other works [75, 76, 77], primarily in conjunction with the density distribution in a planetary exosphere. The basic assumptions of this treatment are: a) an isothermal atmosphere, b) a Maxwellian velocity distribution even at the escape level.

The outward flux of particles whose velocity exceeds the local velocity of escape at a planetocentric distance R, i.e., the escape flux F_∞ (also called the Jeans escape flux) is obtained by the product of the Maxwell–Boltzmann velocity distribution function and the vertical component of velocity ($v > v_\infty$) over the upward hemisphere.

The escape flux relating to the critical level R_c, (exobase) is given by the Jeans formula

$$F_\infty = \frac{v_0}{2\sqrt{\pi}} \cdot n_{cj}(1 + X_c)e^{-X_c} \tag{2.34}$$

where n_{cj} is the density of the escaping constituent at the exobase, $v_0 = (2k_B T_\infty/m_j)^{\frac{1}{2}}$ is the most probable velocity at a Maxwellian velocity distribution with a temperature T_∞ ($v_0 = 1.3 \times 10^4 (T_\infty/\hat{m})^{1/2}$ [cm/sec], with $\hat{m}$ in units of amu) and X is the escape parameter defined by

$$X(R) = \frac{GMm_j}{Rk_B T_\infty} = \frac{v_\infty^2}{v_0^2} . \tag{2.35}$$

The exobase is defined by the total density at that level, $n_c = \sum_j n_{cj}$. Thus, X_c is the escape parameter at the exobase. The escape flux at any level above the exobase can be expressed by

$$F_\infty = n_{cj}\langle v_R\rangle = \frac{v_0}{2\sqrt{\pi}} n_{cj}(1 + X_c)e^{-X_c} \cdot \left(\frac{X}{X_c}\right)^2 .$$

This flux decreases as R^{-2} to satisfy continuity; $\langle v_R\rangle$ is the so-called *effusion velocity* which is defined by the ratio of escape flux to the concentration of the escaping constituent. It should be noted that $\langle v_R\rangle$ is always subsonic.

The escape flux F_∞ is related to the maximum diffusive flux F_j^* of the escaping constituent in the barosphere by virtue of $R_l^2 F_j^* \equiv R_l^2 n_j w_j^* = R_c^2 F_\infty = n_{cj} R_c^2 \langle v_R\rangle$ where R_l is the lower boundary ($R_l < R_c$); i.e.; n_{jc} depends on the diffusive flux in the barosphere. If $w_j^* < \langle v_R\rangle$, then an "escape bottleneck" occurs leading to an adjustment of density.

The above expressions for the escape flux are based on the assumption of a Maxwellian velocity distribution at the exobase while escape itself leads to a perturbation of the Maxwellian velocity distribution. A statistical Monte Carlo treatment however shows that the simple Jeans formula in (2.34) overestimates the escape flux at worst by about 30% [77, 78, 79]. As long as the departure from a Maxwellian velocity distribution is not too great ($X \gg 1.5$), X can also be expressed as a height parameter $X = R/H$. It should be noted that escape is important for $X < 15$, an atmosphere is completely bound to a planet for $X \approx 30$, while for $X \leq 1.5$ the exosphere becomes unstable and escape may become almost arbitrarily high [73]. The latter corresponds to the case when the thermal energy of the gas kinetic motion, $(3/2)k_B T$, exceeds the gravitational energy, i.e., $\overline{u^2}/v_\infty^2 \leq 1.5$.

Remember that $u_0 : \overline{u} : u_{rms} = \sqrt{2} : \sqrt{8/\pi} : \sqrt{3}$; the mean square velocity is $\overline{u^2} = \frac{3}{2}u_0^2$; and $u_{rms} = (\overline{u^2})^{\frac{1}{2}}$. Typical values of the escape parameter X_c and for the most probable velocity for the lightest constituents of planetary atmospheres are listed in Table 2.6. A useful formula for the numerical evaluation of the escape parameter is

$$X \doteq 60\,\hat{m}[\text{amu}] \cdot v_\infty^2(R)\frac{[\text{km/sec}]}{T_\infty[\text{K}]} .$$

On a rotating planet, particles having velocities in the direction of the rotational motion will more easily attain escape velocity than those moving in

Table 2.6. Escape parameter X_c for hydrogen.

	H		D		He	
Planet	Sm	SM	Sm	SM	Sm	SM
Mercury	< 2.4		< 4.8		< 9.6	
Venus	25	20	50	40	100	80
Earth	10	3	20	6	40	12
Mars	5	3	10	6	20	12
Jupiter	~1400					

Sm: Solar minimum conditions; SM: Solar maximum conditions.

the opposite direction. The resulting escape flux will therefore be primarily in the forward direction; the magnitude of the escape flux at the equator is also several times greater than that at high latitudes. The parameter governing rotational effects is given by

$$Y = \left(\frac{m_j \Omega^2 R^2}{2k_B T_\infty}\right)^{\frac{1}{2}} \equiv \frac{\Omega R}{u_0} \tag{2.36}$$

where Ω is the angular rotation velocity.

The flux ratio between the pole and the equator for large Y is enhanced for increasing X. The difference between the fluxes at the pole is significant for different X values and is greater than that at the equator [80, 81]; the escape flux is always greater for smaller X (more efficient escape). The effect of rotation is illustrated in Fig. 2.7.

The concept of escape time is related to the available (total) column density for escape, $\mathfrak{N}_\infty$. The ratio $\mathfrak{N}_\infty/n_{cj}$, can be called the "escape length", corresponding to the length of a square centimeter column of density n_{cj} containing $\mathfrak{N}_\infty$ particles. The loss rate of $\mathfrak{N}_\infty$ is given by

$$\frac{d\mathfrak{N}_\infty}{dt} = -F_\infty = -\langle v_R \rangle n_{cj} = -\langle v_R \rangle \mathfrak{N}_\infty \left(\frac{n_{cj}}{\mathfrak{N}_\infty}\right). \tag{2.37}$$

Integration of (2.37) gives

$$\mathfrak{N}_\infty(t) = \mathfrak{N}_\infty(t=0) e^{-t/\tau_J}$$

where the *Jeans escape time* is

$$\tau_J = \frac{\mathfrak{N}_\infty}{(n_{cj}\langle v_R \rangle)}. \tag{2.37}$$

Thus, τ_j represents a time constant and the fraction of the total content lost by escape is given by $(1 - e^{-t/\tau_J})$. If $\tau_J \ll t_0$ (for $t_0 \cong 4.5 \times 10^9\, yr = 1.4 \times 10^{17}$ sec), e.g., $t_0 = \kappa\tau_j$ with $\kappa > 7$, then τ_J can also be considered as the time for (virtually) total escape, since $e^{-t_0/\tau_J} \lesssim 10^{-3}$.

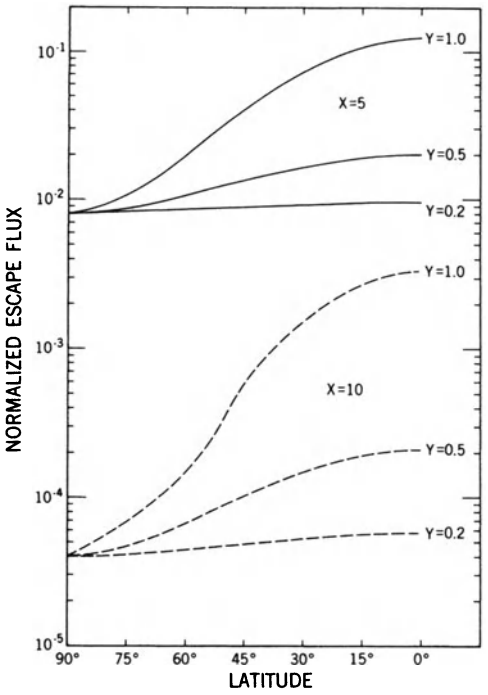

Fig. 2.7. Effect of planetary rotation on the escape flux as a function of latitude, for parametric values of the escape parameter $X = (v_\infty/u_0)^2$ and the rotational parameter $Y = \Omega R/u_0$. Normalized escape flux corresponds to $n_{jc}\langle v_R\rangle/u_0$ (courtesy of R. E. Hartle).

Normally the big uncertainty lies in the estimate of $\mathfrak{N}_\infty$, since the total content available for escape may include the constituent in non-escaping form, e.g., for hydrogen, water in an evaporating ocean.

Under the assumption that $\mathfrak{N}_\infty \simeq n_{cj} \cdot H$, the escape time is given by [75]

$$\tau_J \cong \frac{1}{g}\left(\frac{2\pi k_B T_\infty}{m_j}\right)^{\frac{1}{2}} \frac{e^{X_c}}{1+X_c}. \tag{2.38}$$

Density Distribution in an Exosphere

In computing the density distribution in an exosphere, not only the escape component but also the particles in elliptic ballistic orbits, i.e., those intersecting the exobase and in bound (satellite) orbits (not intersecting the exobase) must be considered. Because of the escape component, the velocity distribution in the exosphere departs from a Maxwellian velocity distribution and the barometric law ceases to describe the density distribution perfectly,

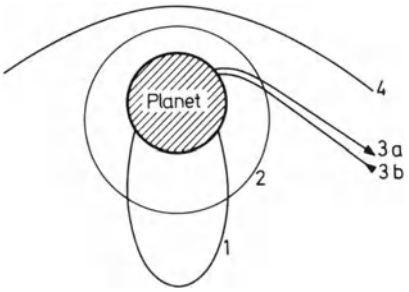

Fig. 2.8. Group of exospheric particles in different orbits: 1) ballistic orbits $v < v_\infty$; 2) bound satellite orbits; 3a) ballistic escape orbits and 3b) incoming capture orbits ($v > v_\infty$); and 4) hyperbolic orbits (interplanetary particles) (after F. S. Johnson [83]).

although it can provide in some cases a good approximation to altitudes well above the exobase. The contribution of the various exospheric components is derived by determining the fraction of a Maxwellian velocity distribution due to these components. The particle population in the exosphere can be divided into the following components as shown in Fig. 2.8: 1) *ballistic orbits* ($v < v_\infty$); 2) *satellite (bound) orbits*; 3) *ballistic (escape) orbits* (3 a) and *incoming capture obits* (3 b) ($v > v_\infty$) and 4) *hyperbolic orbits* not intersecting the exobase (interplanetary particles). The proportion of particles falling into each group can be obtained by integrating the velocity distribution function over appropriate ranges, represented by a partition function ζ [41, 82, 83]. The density at any level R in the exosphere can be expressed by the product of the "barometric" density $n_{\mathrm{M}j}$ (based on a complete Maxwellian velocity distribution), and the partition function ζ, according to

$$n_j(R) = n_{\mathrm{M}j}(R)\xi(X) = n_{cj}\mathrm{e}^{-(X_c - X)} \cdot \xi(X)\,. \tag{2.39}$$

For no dynamical restriction of orbits $\xi = 1$, $n_{\mathrm{M}j} = \int_0^\infty f(v)\,dv$.

The complete distribution of particles in the exosphere, normalized to the barometric density, is given by

$$\xi = \xi_1 + \xi_2 + \xi_3 + \xi_4 = 1$$

where the subscripts refer to the components of the total particle population identified above and illustrated in Fig. 2.8. Particles related to the critical level are represented by the partition functions [41, 76]

$$\xi_1 + \xi_3 = 1 - \frac{(X_c^2 - X^2)}{X} \exp\left\{\frac{X^2}{(X + X_c)}\right\} \tag{2.40}$$

and particles not reaching the critical level (exobase) by

$$\xi_2 + \xi_4 = \frac{(X_c^2 - X^2)^{\frac{1}{2}}}{X} \exp\left\{-\frac{X^2}{(X + X_c)}\right\}. \tag{2.41}$$

The elliptic components ($v = v_\infty$) can be expressed by

$$\xi_1 + \xi_2 = \Phi(X^{\frac{1}{2}}) + \tfrac{1}{2}\Phi''(X^{\frac{1}{2}}) \tag{2.42}$$

where Φ(X) is the error function and Φ'' its second derivative, which are tabulated. The hyperbolic components ($v > v_\infty$) are expressed by

$$\xi_3 + \xi_4 = 1 - \Phi(X^{\frac{1}{2}}) - \tfrac{1}{2}\Phi''(X^{\frac{1}{2}}). \tag{2.43}$$

The bound (satellite) component is given by

$$\xi_2 = \frac{(X_c^2 - X^2)^{\frac{1}{2}}}{X_c} \exp\left\{-\frac{X^2}{(X + X_c)}\right\} \cdot \left[\Phi\left(\frac{X}{(X + X_c)^{\frac{1}{2}}}\right) + \frac{1}{2}\Phi''\left(\frac{X}{(X + X_c)^{\frac{1}{2}}}\right)\right] \tag{2.44}$$

while the hyperbolic interplanetary component is given by

$$\xi_4 = \frac{(X_c^2 - X^2)^{\frac{1}{2}}}{X_c} \exp\left\{-\frac{X^2}{(X + X_c)}\right\} \cdot \left[1 - \Phi\left(\frac{X}{(X + X_c)^{\frac{1}{2}}}\right) - \frac{1}{2}\Phi''\left(\frac{X}{(X + X_c)^{\frac{1}{2}}}\right)\right]. \tag{2.45}$$

The above equations lead to the components at the exobase

$$\begin{aligned} \xi_1 &= \Phi(X_c^{\frac{1}{2}}) + \tfrac{1}{2}\Phi''(X_c^{\frac{1}{2}}) \quad \ldots\ (v < v_\infty) \\ \xi_3 &= 1 - \Phi(X_c^{\frac{1}{2}}) - \tfrac{1}{2}\Phi''(X_c^{\frac{1}{2}}) \ldots\ (v > v_\infty) \\ \xi_2 &= X_4 = 0\,. \end{aligned} \tag{2.46}$$

Equations (2.46) show that ξ_3 is practically negligible for a constituent whose escape rate is very small, i.e., which has a large value of X_c. Figure 2.9 shows exospheric distributions of various components, represented by the partition functions ξ given above, for hydrogen in the Earth's exosphere at $T_\infty = 1500\,\mathrm{K}$ ($X_c = 4.65$). The relative concentrations of terrestrial hydrogen and helium at $T_\infty = 1700\,^\circ\mathrm{K}$ are shown in Fig. 2.10 [41]. The hydrogen distribution based on the ballistic and escaping components departs strongly from the hydrostatic (barometric) law ($X_c = 4.35$), whereas the departure is almost non-existent for helium at the same temperature ($X_c = 17.4$). For a constituent subject to escape, the density decreases with increasing temperature, in contrast to constituents controlled by the barometric law. The fraction of particles with velocity $v > v_\infty$ as a function of the escape parameter X is illustrated in Fig. 2.11, and Fig. 2.12 shows the escape parameter

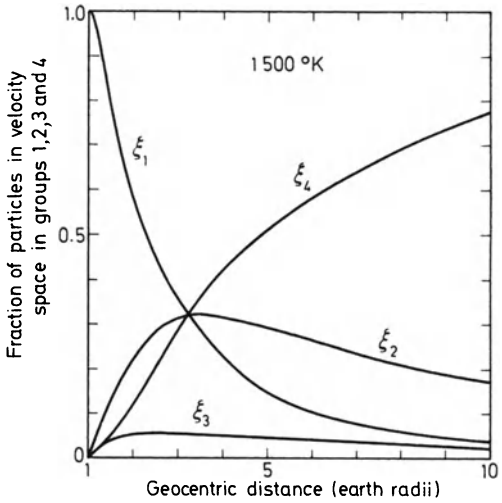

Fig. 2.9. Partition functions ξ for the group of particles shown in Fig. 2.8 as a function of geocentric distance R for $X = 4.65$ (i.e., H at 1500 °K) (After F. S. Johnson [83]).

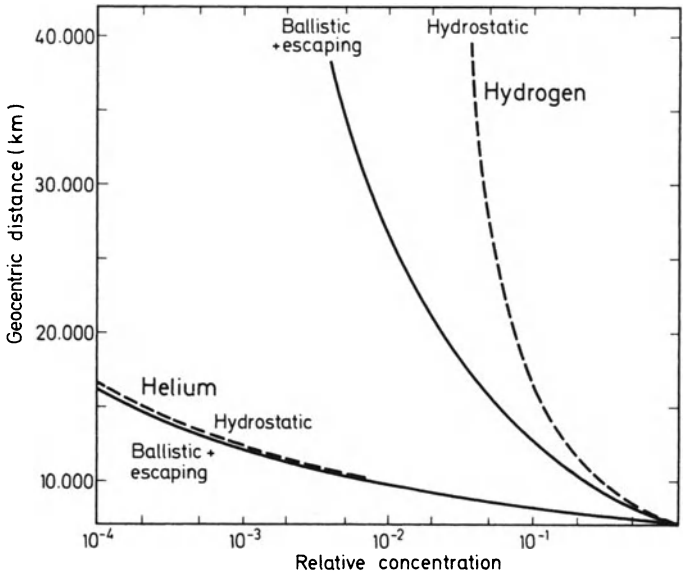

Fig. 2.10. Distribution of H and He in the terrestrial exosphere at 1700 K showing the departure from a hydrostatic distribution for H due to escape (after M. Nicolet [41]).

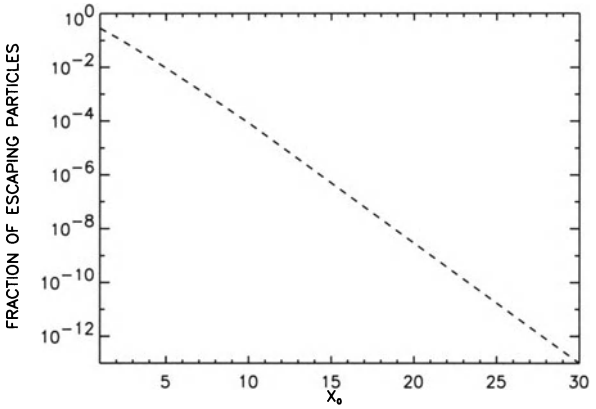

Fig. 2.11. Fraction of exospheric particles (ξ) whose velocity v exceeds the escape velocity v_∞, as function of the escape parameter X. The critical value of $X = 1.5$ represents Öpik's condition for atmospheric "blow-off" [73].

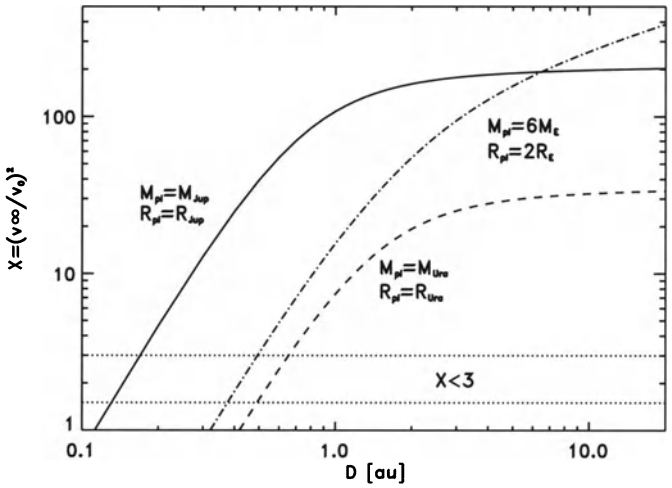

Fig. 2.12. Escape parameter X for hydrogen atoms as a function of orbital distance for a migrating Jupiter-class (solid line), a Uranus-class (dashed line) and an exoplanet with the size of two Earth radii and six Earth masses (dashed-dotted line) [84] at XUV energy flux values for G-type stars 1 Gyr after their arrival at the ZAMS, where the XUV flux is about 6 times larger than for a 4.5 Gyr old G star. One can see that migrating hydrogen-rich exoplanets can easily reach small escape parameters due to XUV heating so that exospheric blow-off conditions will develop.

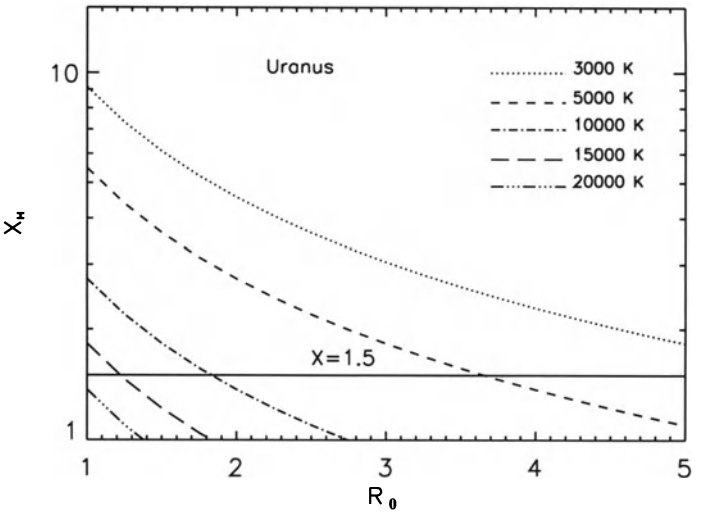

Fig. 2.13. Escape parameter X for hydrogen atoms for an Uranus-like planet as a function of exobase levels in planetary radii (R_0) for different exospheric temperatures.

X for hydrogen atoms as a function of orbital distance for migrating exoplanets with various masses and sizes. Figure 2.13 shows X for hydrogen atoms for an Uranus-like planet as a function of exobase levels in planetary radii (R_0) for various exospheric temperatures. Since for exospheric temperatures $T_\infty > 10,000$ K the exobase level must expand to greater altitudes as shown in Fig. 2.14 (cf. Sect. II.3) the corresponding escape parameter X will decrease, reaching the critical value $X = 1.5$ at altitudes much closer to the planet. As the result of escape, the Maxwellian velocity distribution is truncated. Thus, at high altitudes the temperature at the exobase T_∞ is not representative. However, a kinetic temperature can be defined by the second moment of the velocity distribution function in the moving frame of reference, i.e., moving with velocity $\langle v_R \rangle$, according to

$$T_{kin} = \frac{2T_\infty}{3u_0^2}[\langle v^2 \rangle - \langle v_R \rangle^2] . \tag{2.47}$$

The ratio of the kinetic temperature to the temperature at the exobase for $X_c \gg 1.5$ is given by [76]

$$\frac{T_{kin}}{T_\infty} = \frac{\pi^{\frac{1}{2}}(3 + 2X_c)X^{\frac{1}{2}}}{16X_c^2} + \frac{2}{5}X . \tag{2.47a}$$

When the mean energy is dominated by the escaping component, the ratio approaches [76]

$$\frac{T_{kin}}{T_\infty} \to 0.12 . \tag{2.47b}$$

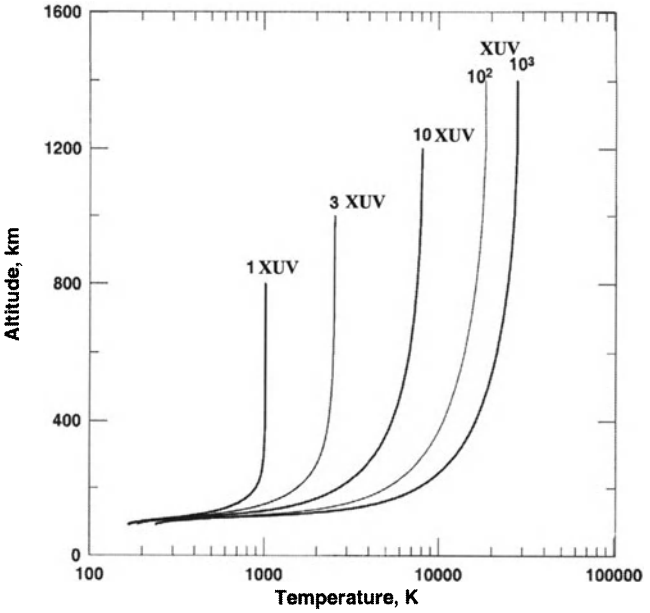

Fig. 2.14. Rise of exobase levels for an Earth-like planet with present Earth's atmospheric species as a function of exospheric temperature for various XUV energy flux values. 1 XUV corresponds to the XUV energy flux of a 4.5 Gyr old solar-like G star. One should note that the critical temperature for "blow off" of atomic hydrogen on Earth is about 5000 K (courtesy of Yu. N. Kulikov / Polar Geophysical Institute, Russian Academy of Sciences, Murmansk, Russia).

The density distribution of (2.38) applies to a stationary (non-rotating) planet. A generalization of the velocity distribution for a corotating exobase, satisfying the collisionless Boltzmann equation, leads to a density distribution in which the density at the equator exceeds that at the pole, for a given planetocentric distance [80]. Further refinements [81], including a non-homogeneous (in temperature and density) exobase, lead to even more drastic effects of rotation. Features of a rotating versus a stationary exosphere are illustrated in Fig. 2.15. The effect of rotation becomes pronounced when the rotational parameter of (2.36) $Y = \Omega R/u_0 > 1$, i.e., when the rotational velocity exceeds the most probable thermal velocity of the exospheric constituent.

Table 2.7 lists the values of the rotational parameter at the exobase Y_c for important constituents in the exospheres of Venus, Earth, Mars and Jupiter. Since $Y_c \propto u_0^{-1}$, rotational effects for a given planet are most pronounced at low temperatures and for high mass numbers. The upper limits of Y_c in Table 2.7 are based on estimated exospheric temperatures for minimum solar activity.

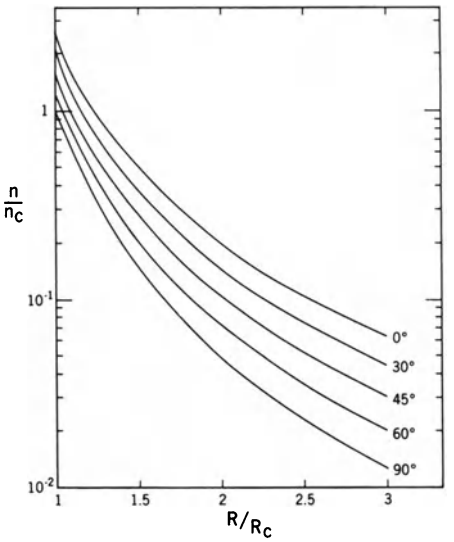

Fig. 2.15. Normalized density distribution for an exospheric constituent ($X = 4.65$, $Y = 1.0$) in a rotating exosphere as a function of latitude when the exobase is uniform (after R. E. Hartle [81]).

Table 2.7. Rotational escape parameter.

Y_c	H	He	O
Venus	$\lesssim$ 0.06	$\lesssim$ 0.12	$\lesssim$ 0.24
Earth	$\lesssim$ 0.15	$\lesssim$ 0.3	$\lesssim$ 0.6
Mars	$\lesssim$ 0.13	$\lesssim$ 0.26	$\lesssim$ 0.52
Jupiter	$\lesssim$ 7.5	$\lesssim$ 15	–

II.4 Hydrodynamic Escape and Atmospheric Expansion

If the escape parameter reaches values $1.5 < X < 3$ for the main atmospheric constituent at the exobase the atmospheric gas starts to expand, so that the escape is a process similar in many respects to the supersonic flow of plasma from the solar wind [72, 85]. By considering a dynamically expanding non-viscous gas of constant molecular weight, in which the pressure is isotropic, the steady state equations and energy conservation can be written as

$$\nabla \cdot (n_j v) = 0, \tag{2.48}$$

$$m_j n_j \, (u \cdot \nabla T) + \nabla \, (n_j k_B T) = n_j m_j g \tag{2.49}$$

$$\nabla \cdot (K_j \nabla T) = \nabla \cdot \left[\frac{5}{2} n_j k_B T v_j + n_j \left(\frac{m_j v_j^2}{2} \right) v_j \right] - n_j m_j g \cdot v_j - Q_{XUV} \tag{2.50}$$

where v_j is the bulk velocity of the gas j, g the acceleration of gravity, K_j the thermal conductivity parameter and Q_{XUV} is the volume-heating rate caused by the XUV radiation. To apply these equations to a dense thermosphere one can assume that at a distance

$$r_0 = \frac{GMm_j}{k_B T_0 X_0} \tag{2.51}$$

in the upper atmosphere where no escape takes place ($X_0 \approx 30$), the temperature is fixed at $T_0 \approx T_{eff}$ and that the atmosphere is sufficiently dense that the optical depth of the lower boundary to the XUV flux is much greater than 1 [85]. Moreover, one can also assume that the XUV flux is absorbed in a distance at a somewhat higher altitude r_1. Since, there is little energy deposited above r_1 and the gas is continually expanding, the temperature declines as $r \to \infty$. The pressure of the gas also declines toward zero because the gas must expand according to a critical solution of the hydrodynamic equations. For the estimation of the atmospheric expansion radius r_1 and the corresponding atmospheric loss rates one can define the following dimensionless parameters [72, 85] for the flux φ

$$\varphi = L_{H_j} \left(\frac{k_B^2 T_0}{\kappa_0 GMm_j} \right) \tag{2.52}$$

and for the energy ϵ

$$\epsilon = I_{XUV} \left(\frac{GMm_j}{k_B T_0^2 \kappa_0} \right) \tag{2.53}$$

where L_{H_i} is the hydrodynamic energy-limited loss rate of constituents j

$$L_{H_j} = \frac{4\pi r_1^3 I_{XUV}}{GMm_i} \tag{2.54}$$

where κ_0 is a thermal conductivity parameter of $\approx 4.45^4$ erg cm^{-1} s^{-1} K^{-1} [85]. The corresponding equations for the maximum escape flux φ_{m_i} and associated escape parameter at the atmospheric level r_1 where the escape takes place, are [72, 85]

$$\varphi_{m_i} = \frac{2}{s_i + 1} \left[\frac{\left(\frac{X_1}{2}\right)^{(s_i+1)/2} + 1}{X_0 - X_1} \right]^2 \tag{2.55}$$

where X_0 and X_1 are the escape parameters at $r = r_0$ and $r = r_1$. One gets for X_1

Table 2.8. Atmospheric expansion r_1 for HD209458 b, Jupiter and Saturn as function of orbital distance D, T_0 and corresponding XUV energy flux I_{XUV} with $X_0 = 30$.

d [AU]	$T_0 \approx T_{\mathrm{eff}}$ [K]	$I_{\mathrm{XUV}}/I_{1\mathrm{AU}}$	HD209458 b r_1 [r_{pl}]	Jupiter r_1 [r_{pl}]	Saturn r_1 [r_{pl}]
0.023	1700	1890	2.2	4.3	1.5
0.045	1200	495	3	6	2
0.1	800	100	4.5	9	3
0.2	565	25	6.5	12.5	4.5

$$X_1 = \left\{ \frac{\epsilon}{\varphi_{\mathrm{m}}} \left[X_0 - \left(\frac{2}{(1+s_i)\,\varphi_{\mathrm{m}}} \right)^{\frac{1}{2}} \right]^{-1} \right\}^{\frac{1}{2}} . \tag{2.56}$$

The simultaneous solutions of these equations for φ_{m} and X_1 can be accomplished by numerical methods with specified values of ϵ and X_0.

Table 2.8 lists the calculated atmospheric expansion r_1 in planetary radii r_{pl} as function of orbital distance d, temperature $T_0 \approx T_{\mathrm{eff}}$ and corresponding I_{XUV} energy flux for a 4.5 Gyr old G-star (the present Sun) for the giant exoplanet HD209458 b ($R_0 = 1.43 \pm 0.04\ R_{\mathrm{Jup}}$, $M_0 = 0.69 \pm 0.02\ M_{\mathrm{Jup}}$); [86] and for "hypothetical" exoplanets with the exact size and mass of Jupiter and Saturn. It should be noted that short-periodic evaporating gas giants at very close orbital distances may expand their upper atmospheres up to the Roche radius (Roche lobe). In cases where the Roche lobe is lower than the hydrodynamic driven expansion r_1, the Roche radius limits the expansion and the escape leads to a strong mass transfer from the planet to the host star [87].

One can also see from Table 2.8 that an increase of T_0 tends to decrease the expansion. The expansion radii r_1 decrease if $T_0 \leq T_{\mathrm{eff}}$ increases, because one can see from 2.50 that r_0 decreases if T_0 grows and X_0 is kept as a constant value of 30.

By knowing the expansion radii $r_1 = (X_0/X_1)r_0$ of the upper atmosphere we can calculate the maximum XUV-driven energy- limited loss rate $L_{\mathrm{H_j}}$ with (2.53). After planets have lost their dense hydrogen atmospheres due to the energy-limited loss, heavier particles like O, N, O_2, N_2, CO_2, CH_2, CH_4, NH_3 and other species, which may be present in deeper atmospheric levels or may dominate the lower thermosphere, will decrease the energy-limited escape rates, since the light hydrogen must diffuse through the heavier constituents [88, 89].

Analytical escape approximations by planetary winds of atmospheric constituents can be derived by assuming that the lowermost subsonic regions of the hydrodynamic flow controls the differential escape. One should note that a real hydrodynamic wind would be transonic and a subsonic approxima-

tion is not obviously reasonable, but an analogous treatment for diffusion of a heavy trace constituent in a subsonic escaping hydrogen wind provides a good approximation to escape rates derived from corresponding transonic winds [88].

The escape flux ϕ_j of a heavy atmospheric constituent in a lighter escaping atmospheric species by considering ($m_j > m_i$) can be written as [88]

$$\phi_j = f_j \left[\phi_i - \frac{GM\,(m_j - m_i)\,b_{i,j}}{r_0^2 k_B T\,(1 + f_j)} \right] \tag{2.57}$$

where f_j is the mixing ratio of the heavy gas in the lighter one. It is assumed that f_j is constant over the distances of the density scale height. ϕ_i is the escape flux of the lighter atmospheric constituent and $b_{i,j}$ is the binary diffusion coefficient [43]

$$b_{i,j} = \frac{k_B T}{\mu_{i,j} k_{i,j}} \tag{2.58}$$

with $\mu_{i,j}$ the reduced mass and $k_{i,j}$ the collision coefficient. The escape flux of the heavy constituent can also be expressed in terms of the escape parameter X_j [88]

$$X_j = 1 - \frac{GM\,(m_j - m_i)\,b_{i,j}}{\phi_i r_0^2 k_B T\,(1 + f_j)} \tag{2.59}$$

or

$$X_j = 1 - \frac{g\,(m_j - m_i)\,b_{i,j}}{\phi_i k_B T\,(1 + f_j)}.$$

The escape parameter X_j cannot be negative and if $f_j \to 0$ the heavy component does not escape, then $X_j = 0$ and 2.59 reduces to

$$\phi_i = \frac{GM\,(m_j - m_i)\,b_{i,j}}{r_0^2 k_B T\,(1 + f_j)} \equiv \phi_{\text{diff}}, \tag{2.60}$$

so that the escape flux of the lighter constituent in (2.60) is identical to the diffusion limited flux ϕ_{diff} [88, 89]. If the mixing ratio $f_j \ll 1$, so that the second constituent is no longer major, the presumption that $X_j = 0$ breaks down and the mixing ratio f_j must be calculated indirectly for an isothermal wind.

From the equations above one can see that diffusion limited escape is generally the case, in which a light atmospheric constituent like hydrogen escapes at the maximum rate for which a heavy major atmospheric constituent is retained. Numerical solutions for an isothermal hydrogen wind escaping transonically through the hydrostatic background gas must be applied. At low temperatures the presence of a second major atmospheric constituent

tends to inhibit escape of a lighter trace gas, but under certain conditions its escape flux can be enhanced by buoyancy with respect to the heavy major species [21, 88, 89]. For a given temperature there exist a threshold mixing ratio of the heavy major constituent below which a static solution cannot be obtained. Under these conditions diffusion limited flux cannot hold and the heavy major atmospheric constituent must also escape.

Mass fractionation by XUV-driven hydrodynamic escape of hydrogen on planets is a promising mechanism for explaining the observed elemental and isotopic abundance patterns in terrestrial planetary atmospheres [20, 21, 88]. Due to high XUV fluxes of young or active stars (cf. Chap. I) this thermal loss process can even remove primitive water oceans from terrestrial planets [89].

By assuming the amounts of oxygen that are believed to be involved in crustal iron oxidation on Venus and Mars, as well as in the massive Venusian atmosphere, one finds that primitive water oceans equivalent to, respectively 0.45–0.2 times the present terrestrial ocean with equivalent depths of 1300–600 m could be lost with respectively 30–50% of oxygen initially contained in the ocean released to space by XUV-driven hydrodynamic escape [89].

Giant gaseous exoplanets with small initial masses close to their host stars may even evolve into volatile-rich large terrestrial planets [84] during high XUV active periods of their host stars. The remnant cores of giant exoplanets orbiting close to their host stars may be detectable for the first time with the new generation of space observatories like CoRoT or Kepler. Moreover, these considerations show that XUV-driven hydrodynamic escape at close orbital distance is a major loss process that should be included in any realistic model of the mass and radius evolution of close-in exoplanets.

II.5 Atmospheric Sputtering

Atmospheric sputtering [90, 91] is a collision based energy transfer process similar to collisional sputtering from a solid surface [92, 93], which employs a so-called collision cascade model. This model is most relevant for cases in which the incident ion energy losses by elastic collisions with target nuclei are much greater than losses in elastic collisions, which may result in ionization or excitation of target particles. In order for solid particles to escape they must overcome the surface binding.

For the escape of atmospheric particles, they must overcome the gravitational attraction of the atmosphere, where their escape will be unhindered by energy degradation through collisions with neighboring particles in the exosphere and its lower boundary the exobase. These atmospheric altitude regions are equivalent to the first monolayer of material in the sputtering of condensed materials. Sputtering from the exosphere is calculated in an exact analogy with sputtering from a solid, planetary surface, producing par-

Table 2.9. Experimental values of $\hat{\alpha}$ as a function of mass fraction between the sputtered particle and the sputter agent [91, 95].

$\hat{\alpha}$	m_B/m_A
0.1	0.12
1	0.17
2	0.2
5	0.35
10	0.5

ticles, which escape directly, or lacking the velocity to escape which will enter ballistic trajectories and form an atmospheric corona [91, 94].

The sputtering yield Y can be defined as the number of atmospheric species ejected per ion incident on an exobase of a gravitationally bound gas. This yield includes particles ejected directly in a collision with the ion and those ejected due to a cascade of collisions initiated by the ion [94]

$$Y = \frac{0.5\sigma_{(U_T \geq U_\infty)}}{\sigma_D cos\theta} + \frac{3\hat{\alpha}S_n}{\pi^2(cos\theta)^{1.6}U_\infty\sigma_D} \tag{2.61}$$

where θ is the pitch angle of the incident particle, U_∞ is the escape energy of the particle at the exobase, $\sigma_{U_T > U_\infty}$ the collision cross-section for a particle receiving an energy transfer and σ_D, is the cross-section for escape of the struck particle in order of about 10^{-15} cm^2, according to

$$\sigma_D = \frac{1}{n_c H} \tag{2.62}$$

with n_c the number density at the exobase, and H the scale height of the dominant species at this altitude level. The constants $3/\pi^2$ and $\hat{\alpha}$ are obtained from the transport equation [94]. One can see from Table 2.9 that the factor α depends on the mass fraction m_B/m_A, where m_B is the target particle mass and m_A is the mass of the incident particle [95]. S_n is the so-called stopping cross-section [91, 94]

$$S_n = 2\pi\frac{A^2}{\gamma E_A}[2\varepsilon s_n(\varepsilon)] \tag{2.63}$$

where $s(\varepsilon)$ is the reduced stopping cross-section with $[2\varepsilon s_n(\varepsilon)] = ln(\varepsilon)$ for $\varepsilon > 30$ and $ln(1 + 1.138\varepsilon)/(1 + 0.0132\varepsilon^{-0.787} + 0.196\varepsilon^{0.5})$ for $\varepsilon < 30$. The collision cross-section σ for a particle receiving an energy transfer $U_T > U_\infty$ is [91, 94]

$$\frac{d\sigma}{dt} = \frac{\pi a_U^2 f(t^{1/2})}{2t^{3/2}} \tag{2.64}$$

with the scaling quantities of length a_U, energy ε, A and energy transfer t

$$a_U = \frac{0.8853 a_0}{(Z_A^{0.23} + Z_B^{0.23})} \tag{2.65}$$

$$\varepsilon = \frac{(\gamma E_A) a_U}{2A} \tag{2.66}$$

$$A = \frac{1}{\varepsilon_0} \left(\frac{2m_A}{m_A + m_B} Z_A Z_B e^2 \right) \tag{2.67}$$

$$t = \frac{\varepsilon^2 U_T}{\gamma E_A} \tag{2.68}$$

where a_0 is the Bohr radius of hydrogen, Z_A and Z_B the nuclear charge of the incident and target particles, γ the ratio of masses $(4m_A m_B)/(m_A + m_B)^2$, e the elementary charge, ε_0 the dielectricity constant, E_A the energy of the incident particle and U_T the energy transfer to the target particle. Since t is a function of ε, $f(t^{1/2})$ can be evaluated from

$$f(\varepsilon) = \frac{\mathrm{d}}{\mathrm{d}\varepsilon} \left[\varepsilon s_n(\varepsilon) \right]. \tag{2.69}$$

The stopping cross-section S_n is between the energy range 0.5–3 keV for incident solar wind protons which hit nitrogen or oxygen molecules in the order of about 8×10^{-15} eV cm^2. The energy transfer cross-section σ of incident protons with molecular nitrogen or oxygen target molecules is, for 0.1 keV, about 10^{-14} cm^2, for 1 keV about 4×10^{-15} cm^2 and for 3 keV protons about 2×10^{-15} cm^2. The escape rate for atmospheric sputtering S_{sp} from a planetary exosphere who is not protected by an intrinsic magnetic field if the incident particles are ions is obtained by [91, 94]

$$S_{sp} \approx \phi_i \left(2\pi R_c^2\right) \left[\frac{0.5\sigma_{(U_T \geq U_\infty)}}{\sigma_D cos\theta} + \frac{3\hat{\alpha} S_n}{\pi^2 (cos\theta)^{1.6} U_\infty \sigma_D} \right] \tag{2.70}$$

with R_c the exobase distance, and ϕ_i the incident ion flux which can be solar wind protons or back-scattered heavy ions that originate from a planetary corona or magnetospheric plasma in the case of a satellite which orbits inside the magnetosphere of a giant planet.

II.6 Physical Properties of Planetary Atmospheres

It is commonly accepted that the atmospheres of the terrestrial planets (Mercury, Venus, Earth and Mars) are of secondary origin, having lost their primordial constituents a long time ago. This, however, is not the case for the gas giants (Jupiter, Saturn, Uranus and Neptune). The secondary atmospheres are most likely due to outgassing of volatile materials from the planetary interior and radioactive decay products such as He^4 (from the decay of uranium

and thorium) and Ar (from potassium K^{40}), with the exception of oxygen in the Earth's atmosphere, which is related to the evolution and presence of life. (See Table 2.10 for constituents of planetary atmospheres.)

The Terrestrial Planets: Mercury, Venus, Earth, and Mars

Before the Mariner 10 fly-by, it was generally thought that Mercury possessed a thin atmosphere similar in composition to the atmospheres of Venus and Mars. It was argued that the terrestrial planets should have evolved along parallel lines and that a CO_2 atmosphere could be preserved by freezing out on the cool darkside. Mariner 10 was therefore designed to search for H, O, C, CO and CO_2, as well as the noble gases He, Ar and Ne. By scaling terrestrial noble gas production and diffusion rates and assuming a Lunar-like solar wind surface interaction the above mentioned noble gases were thought to be the most abundant species [96].

The Mariner 10 spacecraft encountered Mercury on 29 March 1974 and observed only H, He and O from the UVS instrument [97]. Mariner 10 discovered also that a direct solar wind interaction was generally not possible, since the planet was found to possess a weak magnetosphere [98].

A decade after the Mariner 10 fly-bys ground-based observations discovered the spectrum of Mercury strong emission features at the Fraunhofer Na D lines attributed to resonant scattering of sunlight from Na vapor in the planetary exosphere [99]. A Na column density of 10^{11}–10^{12} cm^{-2} was estimated, which corresponds to a Na atom surface density of 2.0×10^4 to 1.5×10^5 cm^{-3}. Since the column content of the observed constituents is of the order of about 10^{12} cm^{-2} which is less than the defined column content of an exosphere of about 10^{14} cm^{-2} the gaseous envelope of Mercury represents an exosphere [100] where the planet's surface is the exobase.

Observations of the broad wings in the observed Na D line profile, however, suggest that Na extends up to about 700 km above Mercury's surface [99, 101]. This observation indicates the presence of hot Na atoms to match the broad wings of the observed line profile. Neither photon-stimulated desorption [102] nor thermal vaporization produce a non-thermal velocity distribution enabling Na particles to reach such altitudes.

Magnetospheric models have shown that Mercury's magnetosphere could be open to the solar wind over substantial areas when the interplanetary magnetic field turns southward [103]. Solar wind particles can therefore reach the surface where they act as sputtering agents for surface particles. It can be shown that particle sputtering could be a source of hot Na atoms with ejection speeds larger than 2 km s^{-1} [94]. Micrometeoroid impact vaporization could also be responsible for hot components in Mercury's exosphere [100, 102, 104, 105, 106].

The Na and O column densities were estimated in earlier work [97, 99, 104, 107] on the basis of scale heights of about 50 and 80 km, respectively,

corresponding to subsolar dayside surface exospheric temperatures of 500–575 K. Small concentrations of K in Mercury's exosphere were also discovered [108] so that one can suggest that solar wind ion sputtering might account for their existence. Recently Ca was discovered as the sixth element in Mercury's exosphere [109].

A more astounding and unexpected discovery was made by the study of radar-bright regions near Mercury's poles, since these areas were attributed to H_2O ice. The radar-bright regions at the poles of Mercury have been used to argue for the presence of condensed volatile species in a manner analogous to that suggested for permanently shadowed regions on the Moon, although it has been suggested that cold silicate minerals would also produce similar results.

In spite of their widely different atmospheres at the present time, it has been proposed that the main outgassing constituents from the planetary interiors have been the same for Venus, Earth and Mars, i.e., water vapor and CO_2 with a small amount ($<1\%$) of N_2. Their different evolutionary paths have been suggested to be the consequence of the initial effective surface temperature due to their distance from the Sun together with a "runaway" greenhouse effect on Venus due to H_2O and CO_2 [110, 111, 112]. Venus has a dense and hot atmosphere, while Mars has a thin and cold one relative to Earth [113]. The surface pressures of Venus, Earth and Mars are in the approximate ratio 100 : 1 : 0.01, while their dayside surface temperatures T_s are about 750 K, 300 K and 250 K, respectively. Both Venus and Mars have CO_2 as their principal atmospheric constituent, whereas Earth has N_2 and O_2 [48]. The temperature and pressure distribution for Venus, Earth and Mars are shown in Figs. 2.16 and 2.17. It has been suggested that because of the initial high surface temperature of Venus, H_2O, if present at the formation of the planet, was always in the atmosphere in the form of vapor, since the surface temperature was always above the boiling point of water at the given pressures in the early history of the planet. The complete absence of liquid water together with the high surface temperature then allowed a substantial accumulation of CO_2 in the atmosphere, since reactions between silicates in the crust and CO_2 proceed rapidly only in the presence of liquid water and are also strongly temperature dependent. The present lack of H_2O is explained as either due to photodissociation by solar ultraviolet radiation, with the hydrogen having escaped and the oxygen consumed by various oxidation processes at the surface, having escaped or lacking due to an initial absence of H_2O.

The composition of the Earth's atmosphere is thought to be due to the initial (lower) surface temperature at an orbit inside the liquid water habitable zone, allowing water to condense at the surface and accelerating chemical weathering and carbonate formation of atmospheric CO_2 and the accumulation of the inert gas, nitrogen, supplied from volcanic activity and oxygen associated with life.

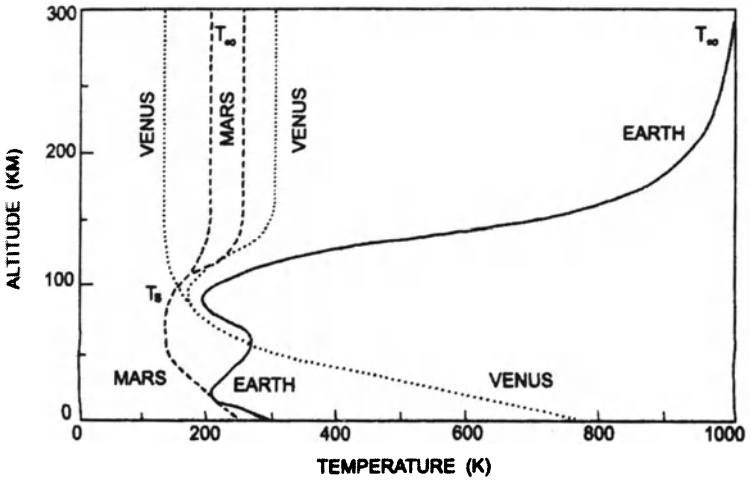

Fig. 2.16. Temperature distributions for Venus, Earth and Mars consistent with our present understanding of these planetary atmospheres. For Venus the low night-side exosphere temperature results from the slow retrograde rotation rate.

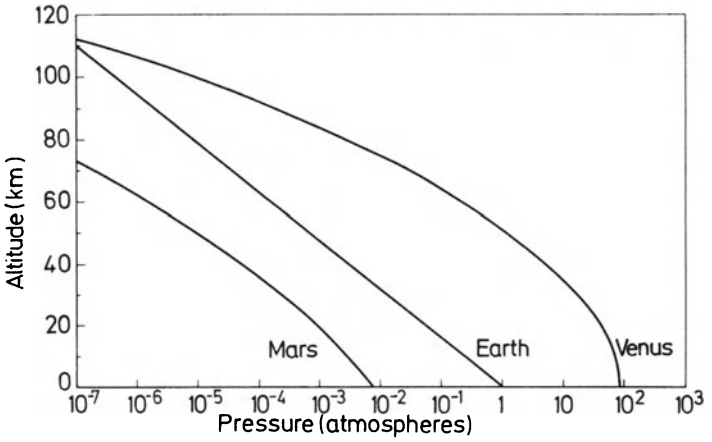

Fig. 2.17. Model pressure distributions for the atmospheres of Venus, Earth and Mars based on observations and theory.

Mars, on the other hand, with its low initial temperature, caused the volcanic steam to freeze at the surface and allowed the accumulation of CO_2 in the atmosphere, but to a much lesser extent on account of its low temperature [113]. Although the above evolutionary path of the atmospheres of the terrestrial planets is largely speculative, it is reasonably consistent with present ground based and spacecraft observations.

The physical parameters of Earth have, of course, been well established by observations. In addition to the principal atmospheric constituents and their dissociation products, the upper atmosphere of Earth contains helium (which is of radiogenic origin) and hydrogen (which is the result of photodissociation of water vapor and methane) as the major light constituents, in addition to atomic oxygen. Because of the range of exospheric temperatures over the solar cycle, the terrestrial hydrogen corona is variable. A hydrogen corona has also been observed for Mars [113] and Venus [111, 112]. Helium, though probably present, particularly on Venus, has yet to be identified directly. The presence of oxygen in the upper atmospheres of both the Venus and Mars has been established, but its concentration is extremely small compared to Earth, raising the interesting question of the stability of a CO_2 atmosphere. Since photodissociation should be very effective, competing processes of recombination exist if the main heavy constituent of the upper atmospheres of Mars and Venus is indeed CO_2. The CO_2 problem remains one of the most enigmatic ones regarding the atmospheres of Mars and Venus [114].

Because of the relatively small scale heights the exobase for Mars and Venus occurs at a much lower altitude (~ 220 km) than for Earth (~ 500 km). Due to the absence of a significant planetary magnetic field, the solar wind can therefore interact with the exospheres of Venus and Mars at rather low altitudes.

The Gas Giants: Jupiter, Saturn, Uranus, and Neptune

In contrast to the terrestrial planets, the gaseous giants or outer planets have reducing atmospheres with large amounts of hydrogen, suggesting that they represent primordial atmospheres whose origin is similar to that of the Solar System. According to spacecraft observations, Jupiter [115] and Saturn [116] have atmospheres which in addition to hydrogen contain helium (He), methane (CH_4) and ammonia (NH_3), while Uranus [117] and Neptune [118] are richer in the heavier elements, which may have their origin from their icy-rocky cores. Although, the composition of the material in the deep layers of Uranus and Neptune is not well known, it must be much denser than hydrogen or He, but not as dense as Mg-Si and rocky iron material which compromises terrestrial planets that formed in the inner Solar System. It is commonly believed that this material may largely consist of abundant ices which contain H_2, CH_4 and NH_3 and rock, which is a solar mix of those elements, which are the major constituents of rock on Earth [119, 120, 121]. The compositions of this rock may be 38% SiO_2, 25% FeS and 12% FeO [120] or 39% SiO_2, 32% Fe, 27% MgO and 2% Ni [119, 120].

As the result of their great distance from the Sun, the exospheric temperature contribution from the XUV radiation of the outer planets is close to their effective temperature (~ 125 K for Jupiter) [70], but there are other sources of thermospheric heating such as dissipation of acoustic energy, particle heat-

ing, and atmospheric gravity waves, which result in exospheric temperatures between 700 and 1000 K.

The Reduced Atmospheres of Titan, Triton, and Pluto

Saturn's and Neptune's large satellites Titan and Triton as well as the planet Pluto have reduced atmospheres consisting of CH_4 and N_2 and at confirmed in Titan's case organic molecular compounds like HCN. Generally these small bodies may represent small cores of Uranus-type planets. Bodies like Titan are also thought to have a rocky core, which is hidden below a H_2O ice layer with trapped CH_4, NH_3 and other volatiles. Recent ground based observations with the United Kingdom Infrared Telescope (UKIRT) support this suggestion, because the characteristic of H_2O ice was discovered on Titan's surface in narrow wavelengths centered at 0.83, 0.94, 1.07, 1.28, 1.58, 2.0, 2.9 and 5.0 micrometers [122]. During the formation of Saturn and Titan the H_2O ice-clathrate melted, so that the trapped CH_4 and NH_3 could be released in large amounts and built up the atmosphere. The outgassed CH_4 reacted with NH_3 and produced Titan's dense N_2/CH_4 atmosphere. After the body cooled out, the orbital distance of about 10 AU is responsible for the present surface temperature of about 100 K so that the H_2O is in a frozen state. On the other hand CH_4 and C_2H_6 may be liquid on the surface and thin haze layers may cover Titan's icy surface and influence the albedo at short wavelengths, while leaving its 2.9 and 5.0 micrometer reflectivities unaffected [122].

Figure 2.18 shows the pressure and temperature distribution in the atmospheres of Venus, Earth, Mars, Jupiter, Saturn, Uranus, Neptune, Pluto and Saturn's large satellite Titan.

Table 2.10. Main gases identified in planetary atmospheres.

Mercury	Na, O, K, Ca, H, He, ?
Venus	CO_2, N_2, SO_2, H_2SO_4, CO, H_2O, O, H_2, H, D
Earth	N_22, O_2, H_2O, Ar, CO_2, Ne, He, CH_4, K, N_2O, H_2, H, O, O_3, Xe
Mars	CO_2, N_2, O_2, CO, H_2O, O, He, H_2, H, D, O_3
Jupiter	H_2, He, H, CH_4, NH_3, CH_3D, PH_3, HD, H_2O
Saturn	H_2, He, CH_4, NH_3, CH_3D, C_2H_2, C_2H_6
Uranus	H_2, He, CH_4, NH_3, CH_3D, C_2H_2,
Neptune	H_2, He, CH_4, NH_3, CH_3D, C_2H_2, C_2H_6, CO
Pluto	N_2, CH_4, ?
Titan	N_2,CH_4, HCN, organics
Triton	N_2, CH_4, ?

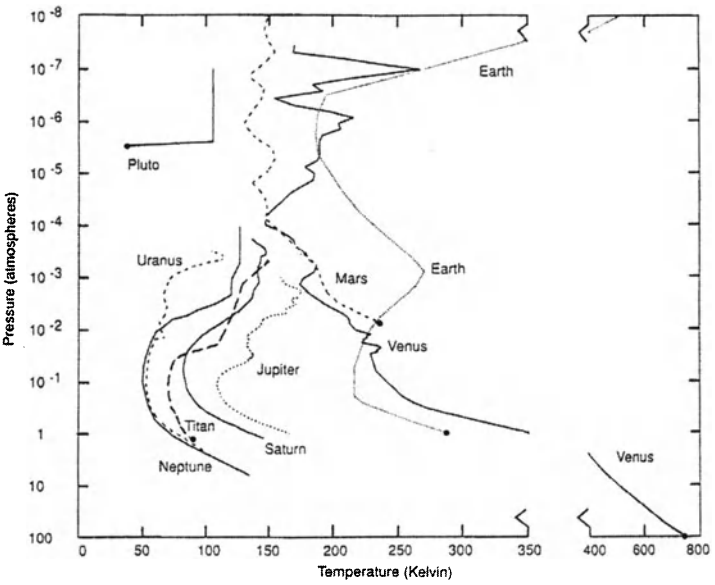

Fig. 2.18. Temperature versus pressure distribution in the atmospheres of the planets in the Solar System.

Exoplanets

The observation of the first giant exoplanet surrounding a solar-type main sequence star was announced in 1995, based on very precise radial velocity (Doppler) measurements. Before 1995 the question whether planets existed outside our solar system was a hypothetical one. Today (February 2004), we know 119 planets in 104 extrasolar systems, where 13 are multiple systems and which are investigated by various scientific groups all over the world [123]. With the discovery of planets outside our own Solar System modern science is continuing the Copernican revolution, placing our planetary system among a wealth of systems existing in the Universe. The exoplanetary systems discovered so far show a surprising diversity of orbital parameters. Most of these systems do not resemble our own Solar System. There is presently no consensus as to why these planetary systems are so diverse, but it seems that migration due to interactions between planets and the protoplanetary disk are an important ingredient [124, 125].

Figure 2.19 shows a comparison of 119 giant exoplanets as a function of Jovian mass and distance with the planets of our Solar System. Bodies with masses around and above 15 Jovian masses are brown dwarfs where fusion of deuterium isotopes can occur. The difference between a brown dwarf and a low mass M star is that the mass of brown dwarfs is so low that hydrogen fusion does not start. Among the large number of giant exoplanets detected up to now there is a subset of exoplanets in very close orbits around their host

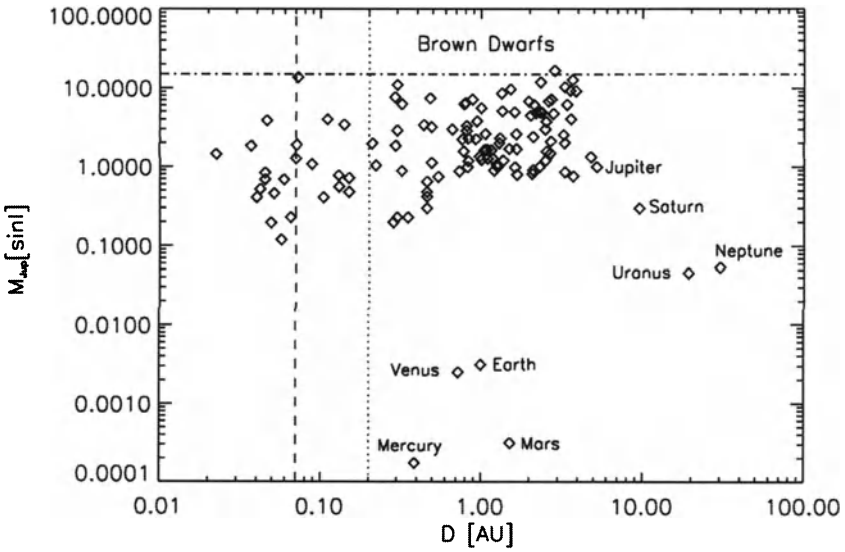

Fig. 2.19. Comparison of the discovered exoplanets in Jovian mass and orbital distance with Mercury, Venus, Earth, Jupiter, Saturn, Uranus and Neptune. The dotted line shows the orbital distance where giant hydrogen-rich exoplanets can experience hydrodynamic conditions. The dashed line marks the border where the mass loss of gas giants can be very effective.

stars. Through transit observations it was shown that at least two of them, namely HD209458 b and OGLE-TR-56 b, orbiting their hosts stars at 0.045 AU and 0.0225 AU, respectively, are known to be Jupiter-like gas giants with hydrogen as their main atmospheric constituent. The observed parameters for HD209458 b are $R_0 = 1.43 \pm 0.04\ R_{\rm Jup}$, $M_0 = 0.69 \pm 0.02\ M_{\rm Jup}$, $\tau = 5.2$ Gyr [86] and for OGLE-TR-56 b, $R_0 = 1.3 \pm 0.15\ R_{\rm Jup}$, $M_0 \approx 1.6\ M_{\rm Jup}$, and $\tau = 3 \pm 1$ Gyr [126, 127]. For all the other detected exoplanets only an estimated mass is known due to radial velocity measurements.

The recent observation of an extended and hydrogen-evaporating atmosphere for HD209458 b due to absorbtion in the Lyman-α line with the HST raises the question of atmospheric stability against escape at very short orbital distances [72, 128].

By solving (2.55) and (2.56) for getting the atmospheric expansion radius r_1 one obtains for HD209458 b a maximal energy-limited hydrodynamic loss rate of $\approx 10^{12}$ g s^{-1}, which is in good agreement with the value determined from planetary transit observations [128]. Indeed, a lower limit to the escape rate of $\approx 10^{10}$ g s^{-1} that can be orders of magnitude higher because of the saturation of the absorption line [72] was estimated. The dotted line Fig. 2.19 shows the border where giant hydrogen-rich exoplanets begin to experience XUV-driven hydrodynamic expansion and high loss rates. At orbits closer than 0.07 AU (dashed line) the hydrogen loss rates can be very high so that

Table 2.11. Main gases identified in the atmospheres of brown dwarfs and of the short-periodic giant exoplanet HD209458 b.

Brown dwarfs	CO, CH_4, NH_3, Na, H_2, H, ?
HD209458 b ("Hot Jupiter")	H_2, H, Na, C, O, ?

exoplanets may evaporate a large fraction of their atmospheric mass, even down to their core size during the early XUV active period of their host stars.

By comparing the spectra taken during the transits of the atmosphere of HD209458 b by several transits with the Space Telescope Imaging Spectrograph (STIS) instrument on the HST, with those taken at other times, it was found that traces of atomic Na in the spectra of the transits could have their origin only in the atmosphere of the exoplanet, although Na is not the major atmospheric component [129]. After the observation of a hydrodynamically driven strong planetary hydrogen wind [128] it is clear that the main atmospheric constituent of HD209458 b will be like that on the gas giants of our Solar System, H_2. Recent observations with the STIS of transits of HD209458 b revealed also the loss of heavy species C and O from the upper atmosphere of HD209458 b [130] as shown in Table 2.11. These heavy species, however, must be carried away from the planet due to the strong hydrodynamic-driven hydrogen wind as discussed in this chapter. For comparison, the escape rate resulting from the Jeans formula at a temperature equal to T_{eff} is < 1 g s^{-1}. For the closer exoplanet OGLE-TR-56 b, with a measured radius, one can estimate a present mass loss rate of $\approx 5 \times 10^{12}$ g s^{-1}. Due to much higher XUV fluxes after their host stars arrived at the ZAMS both exoplanets may have lost by evaporation a significant fraction, up to twice their original masses, during their lifetime [72].

The first transit observed (HD209458 b) was not a detection, since the planet was previously found by radial velocity searches. The OGLE project may have detected the first planet by the transit method (OGLE-TR-56 b). The reason for the small detection rates so far are mainly observational constraints. These will be overcome with the near-future space missions CoRoT (CNES), Kepler (NASA) and Eddington (ESA), which are expected to detect many gas giants and small terrestrial-like exoplanets by the transit method.

It also seems reasonable to assume that planets resembling Uranus and Neptune, or slightly less massive ones, may have formed in cold regions of a protoplanetary disk and migrated inward, possibly into the habitable zone of the host star where liquid water can be present at their surface. These planets, termed *ocean planets* [84], would be more interesting as their large radius makes them more easily detectable by transit missions like CoRoT, Kepler and Eddington.

On such ocean planets, expected primary volatiles would be H_2O, NH_3 and CO_2, because the assumed initial composition of ice is similar to that of

comets, e.g. w 90% H_2O, 5% NH_3 and 5% CO_2 [84]. A two Earth size and six Earth mass ocean planet can release hydrogen via photodissociation of NH_3 to an amount of about 1.6×10^{23} kg, corresponding to an atmospheric pressure of about 1.2 GPa which can be lost in a very short time ($\approx$ 25 Myr) by energy-limited hydrodynamic escape during the first Gyr when the planet orbits distances $\leq$ 1 AU from a young solar-like star due to a 100 times higher XUV flux during the first 0.1 Gyr after the star arrived at the ZAMS. After the majority of the hydrogen is lost, the heavier atmospheric species like CO_2, O and N become relevant in the upper atmosphere.

It seems logical that the atmospheres of exoplanets should consist of similar constituents to the planets in the Solar System. Future space missions like Darwin (ESA) or TPF (NASA) which will have the capability to study the atmospheres of exoplanets by thermal emission in the infrared or by reflected light in the visible should be prepared to observe hydrogen-dominated primordial atmospheres of exoplanetary gas giants, secondary atmospheres of terrestrial planets and reduced atmospheres of migrated more exotic sub-Uranus type bodies or atmospheres, which are outgassed by the cores of evaporated hydrogen-rich Uranus-class exoplanets.

III Thermal Structure of Upper Atmospheres

III.1 Departures from Thermal Equilibrium

Electrons released in the photoionization process due to the absorption of solar XUV radiation in planetary atmospheres may have initial kinetic energies of one 100 eV. The energy E of photoelectrons resulting from photons of energy $\hbar\nu$ interacting with an atmospheric constituent whose ionization potential is IP is given by

$$E = \hbar\nu - \mathrm{IP}\,.$$

These photoelectrons lose their excess energy by both inelastic and elastic collisions [131]. As long as the energy of the primary photoelectron exceeds IP, secondary ionization may occur, while below IP energy loss will occur by excitation of atmospheric constituents. The rate of energy loss per unit pathlength due to an *inelastic* collision with a neutral constituent whose density is n_j, can be expressed by

$$\frac{1}{n_j}\frac{\mathrm{d}E}{\mathrm{d}x} = E'\sigma_j \tag{3.1}$$

where E' is the excitation energy and σ_j is the appropriate cross-section.

For the principal atmospheric constituents of the terrestrial planets, photoelectron energies $E > 20\,\mathrm{eV}$ lead to optical excitation. For photoelectron energies $5 < E < 20\,\mathrm{eV}$, electronic excitation becomes the predominant energy loss process. Below 5 eV vibrational and, at the lowest energies, rotational excitation of molecular species leads to photoelectron energy loss by inelastic collisions with neutral particles. However, at energies below 2 eV, elastic *Coulomb collisions* are most important for the thermalization of photoelectrons. The rate of energy loss per unit path length for *elastic* collisions is given by

$$\frac{1}{N}\frac{\mathrm{d}E}{\mathrm{d}x} = -\frac{2m_\mathrm{e}m}{(m_\mathrm{e}+m)^2}\sigma_\mathrm{D}E \tag{3.2}$$

where N is the number density and m the mass of the collision partner and σ_D is the collision (momentum transfer or diffusion) cross-section [9].

Due to the mass dependence, photoelectrons will lose their energy in elastic collisions primarily to the ambient electrons, rather than to the ions, leading to a preferential heating of the electrons gas, and an electron temperature greater than that of the heavy particles (ions and neutrals).

This can also be seen by considering the time constant for Maxwellianization of electrons or ions by self-interaction, according to

$$\tau_{jj} \propto m^{\frac{1}{2}} \frac{E^{\frac{3}{2}}}{N} . \tag{3.3}$$

Numerically, the self-collision time is given by [132]

$$\tau_{jj} = \frac{11.74 \hat{m}_j^{\frac{1}{2}} T^{\frac{3}{2}}}{N_j Z^4 \ln \Lambda} ,$$

where $\hat{m}_j$ is the mass in amu, and Z the charge of the particles whose density is N and temperature T.

Since $\hat{m}_e = 1/1836 \hat{m}_p$, the self-collision time for electrons is by a factor $1/43$ less than that for protons; $\ln \Lambda$ is a parameter called the *Coulomb logarithm* depending on T and N, having numerical values between 10 and 20 for typical conditions in planetary ionospheres (cf. Chap. V).

Equipartition between the hotter electrons and the cooler ions will then take place by electron–ion Coulomb collisions.

The equipartition time, τ_{ei} is defined according to

$$\frac{dT_e}{dt} = -\frac{T_e - T_i}{\tau_{ei}} \tag{3.4}$$

and is related to the electron self-collision time τ_{ee} by

$$\tau_{ei} \simeq \frac{1}{2} \frac{\hat{m}_i}{\hat{m}_e} \tau_{ee} \simeq \frac{5.7 \hat{m}_e \hat{m}_i}{N \ln \Lambda} \left(\frac{T_e}{\hat{m}_e} + \frac{T_i}{\hat{m}_i} \right)^{\frac{3}{2}} .$$

Since $\tau_{ei} \gg \tau_{ee}$, the electron temperature T_e can exceed the ion temperature T_i in altitude regions where the main cooling process for electrons is that of electron–ion collisions, as long as the electron gas is selectively heated.

The detailed thermal balance of a planetary ionosphere and the individual electron and ion temperature depend on the sources and sinks, both local and non-local, of the thermal energy of the ionospheric particles [133, 134, 135]. These topics will be discussed in the following sections.

III.2 Electron and Ion Temperatures

The temperature of the electrons and ions of a planetary ionosphere is governed by heat balance equations of the form

$$\frac{3}{2}Nk_B\frac{\partial T_{e,i}}{\partial t} + \sin^2 I\frac{\partial}{\partial z}\left(K_{e,i}\frac{\partial T_{e,i}}{\partial z}\right) = Q_{e,i} - L_{e,i} \tag{3.5}$$

as long as the energy of any bulk motion is small compared to that of the random thermal energy. The subscript "e" and "i" refer to the electron and ion properties, respectively. K refers to the thermal conductivities and Q and L refer to the rates of volume heat production and loss. If the ionosphere is pervaded by a magnetic field, the heat conduction term is strongly controlled by the direction of this field; the $\sin^2 I$ factor, where I is the inclination (dip angle) of the magnetic field, implies that heat conduction is important primarily along magnetic flux tubes, but is strongly inhibited across the field.

Electron Heating

As stated in the previous section, the initial source of energy for heating the charged particles in the ionosphere derives from the photoionization process in which energetic photoelectrons are created which eventually thermalize. This leads to an enhanced electron temperature; the difference between electron and ion (and neutral) temperatures, i.e., the absence of thermal equilibrium in a planetary ionosphere, is controlled by the detailed balance of sources and sinks of thermal energy for both the electrons and ions. The initial photoelectron energy spectrum, which depends on the characteristics of the ionizing solar XUV radiation and the composition and density distribution of the neutral atmosphere and appropriate cross-sections, represents the starting point for the ionospheric heat input. The local heating rate Q_e is related to the local ionization rate q by

$$Q_e = \varepsilon q \tag{3.6}$$

where ε is the energy per ion pair formation which is transferred locally to the electron gas in form of heat and

$$\varepsilon q = \int_{E_{th}}^{\infty} q(E)\, dE/[1 + (dE/dx)_n/(dE/dx)_e]$$

where E is the initial photoelectron energy, E_{th} is the thermal energy of the electron gas and the subscripts "n" and "e" refer to energy loss rate to neutrals and electrons, respectively.

From the previous definition of the ion production rate (cf. Chap. I) it can be seen that the local heating rate has an altitude dependence which is largely controlled by that of the ion production rate, and is thus given by

$$Q(z) = \varepsilon(z) n_0 \sigma_i \Phi_{XUV} \exp\left[-\frac{z}{H}\right] .$$

At altitudes where inelastic collisions of electrons with neutrals are important, the heating efficiency is roughly inversely proportional to the neutral gas

density, while at higher altitudes ε is strongly dependent on the electron, ion and neutral density. At these higher altitudes, specifically, where the electron mean free path $\lambda_{e,n}$ becomes comparable to the scale height of the neutral gas responsible for scattering, the photoelectrons can escape, i.e., travel significant distances before becoming thermalized [133]. This photoelectron escape flux is therefore responsible for non-local heating of the electron gas. The escape level for photoelectrons, in analogy to the definition of the neutral exobase, is defined by the condition $\lambda_{e,n} = H$ or $n = (\sigma_{sc} H)^{-1}$ where σ_{sc} is the scattering cross-section for electrons in the neutral gas ($\sigma_{sc} \cong 10^{-15}\,\mathrm{cm}^2$). The magnitude of the photoelectron escape flux can be estimated from simple scattering considerations [135]. The continuity equation for the photoelectron flux ϕ can be expressed by

$$\frac{\mathrm{d}\phi}{\mathrm{d}s} = \tfrac{1}{2} q - L(s) \tag{3.7}$$

where q is again the production rate of photoelectrons and L represents the loss due to electron–neutral particle scattering along the path s.

The factor 1/2 is based on the assumption of an initial isotropic photoelectron distribution, so that one half of the electrons produced at a given level where escape can take place are directed upward. If there is a planetary magnetic field pervading the ionosphere, the path of the photoelectrons is constrained by field lines and the scattering also depends on the local pitch angle α. For a probability of 0.5 for an inelastic collision to remove a photoelectron from the flux, the loss rate can be expressed by

$$L = \tfrac{1}{2} n \sigma_{sc} \phi \sec \alpha \,.$$

Integration of (3.7) gives for the unscattered photoelectron escape flux for the limit ($z \to \infty$)

$$\phi_\infty = q \lambda_{e,n} \cos \alpha$$

or (for $\alpha = 0$),

$$\phi_\infty = \frac{\sigma_i}{\sigma_{sc}} \Phi_\infty = \frac{J}{\sigma_{sc}} \,. \tag{3.8}$$

With ionization rate coefficients $J \cong 10^{-7}\ \mathrm{sec}^{-1}$ and scattering cross-sections $\sigma_{sc} \cong 10^{-15}\,\mathrm{cm}^2$, photoelectron escape fluxes of the order of $\phi_\infty \cong 10^8\,\mathrm{cm}^{-2}\,\mathrm{sec}^{-1}$ are obtained on Earth, and photoelectron energy fluxes of the order of $10^9\,\mathrm{eV\,cm}^{-2}\,\mathrm{sec}^{-1}$, assuming an average photoelectron energy of 10 eV. Such energy fluxes can lead to heating rates at high altitudes which are orders of magnitudes larger than those resulting from local ion production. Thus, escaping photoelectrons can represent an important source of heating in the upper portions of planetary ionospheres, and can also lead to heating of nighttime ionosphere, if the magnetically conjugate point is already sunlit [136, 137]. The heating rate due to a flux of photoelectrons is given by

$$Q_{\mathrm{pe}}(z) = \int_0^\infty \left(\frac{\mathrm{d}\phi}{\mathrm{d}E}\right)\left(\frac{\mathrm{d}E}{\mathrm{d}z}\right)\mathrm{d}E \tag{3.9}$$

where $\mathrm{d}E/\mathrm{d}z$ is the energy loss of photoelectrons due to elastic collisions with ambient electrons, leading to heating of the electron gas. The energy loss of photoelectrons due to elastic collisions has usually been determined from the formula of Butler and Buckingham [131, 138, 139, 140, 141]

$$\frac{\mathrm{d}E}{\mathrm{d}t} \equiv v\frac{\mathrm{d}E}{\mathrm{d}z} = -\frac{8\sqrt{\pi}}{m_{\mathrm{e}}}\frac{Ne^4}{v_{\mathrm{th}}}\mathfrak{F}\left(\frac{v}{v_{\mathrm{th}}}\right)\ln\Lambda \tag{3.10}$$

where

$$\mathfrak{F}(u) = \frac{2}{\sqrt{\pi}}\left(\int_0^u \mathrm{e}^{-x^2}\,\mathrm{d}x - 2u\mathrm{e}^{-u^2}\right)$$

v_{th} is the electron thermal speed and $\ln\Lambda$ is the Coulomb logarithm. For energies $E > 3\,\mathrm{eV}$ this equation can be approximated by [135]

$$\frac{\mathrm{d}E}{\mathrm{d}t} \cong -\frac{10^{-5}}{E^{\frac{1}{2}}}N_{\mathrm{e}} \qquad [\mathrm{eV\,sec^{-1}}]\,. \tag{3.11}$$

In the presence of a magnetic field the right-hand side of (3.11) is modified by a factor $(\cos\alpha \sin I)^{-1}$. The Butler and Buckingham formula neglects the energy loss of photoelectrons due to the generation of plasma waves by the Cerenkov mechanism. The complete expression for the energy loss of fast photoelectrons to thermal electrons is given by [138, 139]

$$\frac{\mathrm{d}E}{\mathrm{d}t} = -\frac{\omega_{\mathrm{N}}^2 e^2}{v}\left\{\mathfrak{F}\left(\frac{v}{v_{\mathrm{th}}}\right)\ln\frac{2\Lambda}{3\gamma} + \frac{v}{v_{\mathrm{th}}}\mathfrak{G}\left(\frac{v}{v_{\mathrm{th}}}\right)\right\} \tag{3.12}$$

where $\mathfrak{G}(v/v_{\mathrm{th}})$ represents the energy loss due to plasma wave generation and ω_{N} is the plasma frequency $\omega_{\mathrm{N}} = (4\pi Ne^2/m_{\mathrm{e}})^{\frac{1}{2}}$. For energies $E \gg k_{\mathrm{B}}T$, this formula can be approximated by

$$\frac{\mathrm{d}E}{\mathrm{d}t} = -\frac{\omega_{\mathrm{N}}^2 e^2}{v}\cdot\begin{cases}\ln\left(\dfrac{mv^3}{\gamma e^2\omega_{\mathrm{N}}}\right) & \text{for } k_{\mathrm{B}}T \ll E < \dfrac{me^4}{2\hbar^2} \\ \ln\left(\dfrac{mv^2}{\hbar\omega_{\mathrm{N}}}\right) & \text{for } E > \dfrac{me^4}{2\hbar^2}\end{cases}. \tag{3.13}$$

where $2\pi\hbar$ is Planck's constant and $\gamma = 1.781$ is Euler's constant. Energy loss rates based on the Butler and Buckingham formula, as applied by many authors, may be as much as 70% lower than those based on (III.2) [138, 140]. A useful analytic form of (III.2) is given by [141]

$$\frac{\mathrm{d}E}{\mathrm{d}t} = -\frac{2\times 10^{-4}N^{0.97}}{E^{0.44}}\left(\frac{E-E_{\mathrm{e}}}{E-0.53E_{\mathrm{e}}}\right)^{2.36} \tag{3.14}$$

where

$$E_e 8.618 \times 10^{-5} T_e \,.$$

Photoelectron excitation of neutral constituents also produces *airglow* emissions of otherwise forbidden lines, e.g., the 1356/1358 Å doublet of O and the 2972 Å line of O; the oxygen green line (5577 Å) and red line (6300 Å) can also be produced by photoelectron excitation. Another example is the 1830 Å line of metastable He, the Cameron a–X bands of CO (1900–2500 Å), the first negative bands of CO^+ (2100–2400 Å) as well as the first negative system of N_2 (3914 Å).

Electron Cooling

The thermal electrons can lose energy by elastic collisions with neutrals and ions, as well as by inelastic collisions with neutral species, leading to rotational, vibrational or electronic excitation of neutrals [131].

The heat loss or cooling rate of the electrons can be expressed in general form by

$$L_e = \frac{d}{dt}\left(\frac{3}{2} N_e k_B T_e\right) = \int_{E_0}^{\infty} v \frac{dE}{dx} f(E, T_e)\, dE \equiv \int_{E_0}^{\infty} \frac{dE}{dt} f(E, T_e)\, dE \tag{3.15}$$

where dE/dx is the loss rate per unit path travelled for the appropriate collision process and $f(E, T_e)$ is the Maxwellian velocity distribution for the temperature T_e. The heat loss of electrons by elastic collisions with neutrals is given by

$$L_e(\text{elast.}, n_j) = -\frac{2m_e}{m_j} N_e \nu_{en} \frac{3}{2} k_B (T_e - T_n) \tag{3.16}$$

where ν_{en} is the collision frequency between electrons and neutrals, which depends on the momentum transfer cross-section σ_D according to

$$\nu_{en} = \frac{4}{3} n_j \left(\frac{8 k_B T_e}{\pi m_e}\right)^{\frac{1}{2}} \sigma_D \,.$$

Because of the mass factor $2m_e/m_j$, this particular cooling rate is rather small; energy loss of electrons occurs much more rapidly as the result of inelastic collisions. Electron cooling by rotational excitation of nonpolar molecules such as N_2, O_2 and CO_2 can be expressed by

$$L_e(\text{rot.}) = -a_j N_e n_j T_e^{-\frac{1}{2}} (T_e - T_n) \qquad [\text{eV cm}^{-3} \text{sec}^{-1}] \tag{3.17}$$

where the constant a_j has values of the order 10^{-14} for the previously mentioned nonpolar molecular species. For polar molecules such as CO, the relation (3.17) does not apply and cooling rates have to be derived from a

general expression for energy transfer by inelastic collisions [131]. The electron heat loss by vibrational excitation of molecular species is determined by the relation

$$L_e(\text{vib.}) \cong N_e n_j \exp\left(-\frac{\Delta E}{k_B T_n}\right)\left[\exp\left(\frac{\Delta E}{k_B T_n}\cdot\frac{T_e - T_n}{T_e}\right) - 1\right] \tag{3.18}$$

where ΔE is the energy difference of two vibrational states. For typical conditions in planetary ionospheres, vibrational cooling of the electron gas may become important when the electron temperature is high. Similarly, electron heat transfer due to electronic excitation of atmospheric constituents becomes primarily important for very high electron temperatures.

A very important energy transfer process at electron temperatures normally found in planetary ionospheres ($T_e \simeq 1000$ K) is that due to the excitation of fine structure transitions in atomic oxygen. The electron cooling rate for fine structure excitation of the ground state of atomic oxygen can be expressed by

$$L_{e,n}(\text{f.str.O}) = -3 \times 10^{-12} N_e n(O) \cdot T_n^{-1}(T_e - T_n) \qquad [\text{eV cm}^{-3}\,\text{sec}^{-1}]. \tag{3.19}$$

The electron cooling rate resulting from heat transfer to another species can also be expressed by (3.4)

$$\frac{dT_e}{dt} = -\frac{T_e - T_j}{\tau_{ej}}$$

where τ_{ej} is the equilibration time. At some altitude where the electron–ion density is large enough, the equilibration time between electrons and ions τ_{ei} will be less than that between electrons and neutrals, and the electron cooling will occur primarily by elastic Coulomb collisions between electrons and ions. The electron cooling rate due to Coulomb collisions is given by

$$L_{e,i} = -7.7 \times 10^{-6} N_e N_i \left(\frac{T_e - T_i}{\hat{m}_i T_e^{\frac{3}{2}}}\right) \qquad [\text{eV cm}^{-3}\,\text{sec}^{-1}]. \tag{3.20}$$

The energy transfer rate has a critical value for $T_e = 3T_i$ corresponding to [133]

$$L^*_{e,i} = -3 \times 10^{-16} \frac{N_e N_i}{\hat{m}_i T_i^{\frac{1}{2}}} \qquad [\text{eV cm}^{-3}\,\text{sec}^{-1}]. \tag{3.21}$$

For local heat input into the electron gas $Q_e > L^*_{e,i}$, T_e would not be limited by energy transfer to the ions, and would rise ("runaway") until controlled by other loss processes or heat conduction.

Ion Heating and Cooling Processes

The electron cooling rate due to Coulomb collisions provides the principal heat input to the ions. Accordingly, we have for the ion heating rate

$$Q_{\mathrm{i}} = 7.7 \times 10^{-6} N_{\mathrm{e}} N_{\mathrm{i}} \left(\frac{T_{\mathrm{e}} - T_{\mathrm{i}}}{\hat{m}_{\mathrm{i}} T_{\mathrm{e}}^{\frac{3}{2}}} \right) \qquad [\mathrm{eV\,cm^{-3}\,sec^{-1}}] \,. \tag{3.22}$$

Cooling of the ions takes place by energy transfer to the neutrals; the rate of heat transfer between ions and neutrals due to the temperature difference of the two gases, as well as that due to the possible difference of the bulk velocities $\boldsymbol{v}_{\mathrm{i}}$, $\boldsymbol{v}_{\mathrm{n}}$, (frictional heating) can be expressed by

$$L_{\mathrm{in}} = 2N_{\mathrm{i}} \frac{m_{\mathrm{i}} m_{\mathrm{n}}}{(m_{\mathrm{i}} + m_{\mathrm{n}})^2} \nu_{\mathrm{in}} \left\{ -\frac{3}{2} k_{\mathrm{B}} (T_{\mathrm{i}} - T_{\mathrm{n}}) + \frac{1}{2} m_{\mathrm{n}} (\boldsymbol{v}_{\mathrm{i}} - \boldsymbol{v}_{\mathrm{n}})^2 \right\} \tag{3.23}$$

where ν_{in} is the ion-neutral collision frequency

$$\nu_{\mathrm{in}} \cong 2\pi \left(\frac{\alpha e^2}{\mu_{\mathrm{in}}} \right)^{\frac{1}{2}} n \,, \tag{3.24}$$

where α is the polarizability of the neutral constituent whose density is n and μ_{in} is the reduced mass. Ions in their parent gas also experience cooling by resonance charge transfer. In this case ν_{in} is modified by a factor $(T_{\mathrm{i}} + T_{\mathrm{n}})^m$; for most atmospheric gases $0.3 \lesssim m \lesssim 0.4$ [142].

Heat Transport in the Ionosphere

In addition to local heat input and loss by energy transfer processes (collisions), heat can also be transported in the ionospheric plasma by conduction. The change in temperature is then given by the divergence of the heat flux, which is expressed by

$$\mathfrak{F}_{\mathrm{e,i}} = K_{\mathrm{e,i}} \boldsymbol{\nabla} T_{\mathrm{e,i}} \,. \tag{3.25}$$

For a fully ionized plasma, the thermal conductivity is primarily due to the random motions of the electrons and is given by [135]

$$K_{\mathrm{e}} = 7.7 \times 10^5 T_{\mathrm{e}}^{\frac{5}{2}} \qquad [\mathrm{eV\,cm^{-1}\,^{\circ}K\,sec^{-1}}] \,. \tag{3.26}$$

K_e can also expressed in units of erg $\mathrm{K^{-1}\ cm^{-1}\ sec^{-1}}$ [$1\,\mathrm{eV} = 1.6 \times 10^{-12}$ erg]. Since planetary ionospheres are not fully ionized plasmas, particularly at lower altitudes where electron-neutral collisions occur, a more appropriate form for the electron conductivity is [135]

$$K'_{\mathrm{e}} = \frac{K_{\mathrm{e}}}{1 + K_{\mathrm{e}}/K_{\mathrm{en}}} \tag{3.27}$$

where

$$K_{\text{en}} = \frac{57 N_{\text{e}} T_{\text{e}}^{\frac{1}{2}}}{\sum_j n_j \sigma_{\text{D}}}$$

with σ_{D} the momentum transfer cross-section for the neutral constituents. The thermal conductivity for the ion gas is much smaller due to the smaller thermal velocity of the ions. The ion conductivity is given by

$$K_{\text{i}} = 4.6 \times 10^4 \frac{T_{\text{i}}}{\hat{m}_{\text{i}}^{\frac{1}{2}}} \qquad [\text{eV cm}^{-1}\,\text{K sec}{-1}] \tag{3.28}$$

where $\hat{m}_{\text{i}}$ is the ion mass in amu.

When a magnetic field is present, the heat flow is parallel to the field lines; in any other direction the thermal conductivity is reduced by $\sin^2 I$. The parallel thermal conductivity $K_{\parallel}$ is essentially the electron conductivity K_{e}, whereas perpendicular to the field lines, the ion conductivity predominates. The perpendicular conductivity $K_{\perp}$ can be expressed by

$$K_{\perp} \sim K_{\perp \text{i}} = K_{\parallel} \frac{\nu_{\text{ei}}}{\Omega_{\text{B}}^2} \left(\frac{m_{\text{i}}}{m_{\text{e}}} \right)^{\frac{1}{2}} \approx 3 \times 10^{-16} \frac{N_{\text{i}}^2}{B^2 T^{\frac{1}{2}}} \qquad [\text{erg K}^{-1}\,\text{cm}^{-1}\,\text{sec}^{-1}] \tag{3.29}$$

where Ω_{B} is the ion gyrofrequency, $\Omega_{\text{B}} = \text{eB/m}_{\text{ic}}$. The ratio $K_{\perp}/K_{\parallel}$ is extremely small. A more efficient heat transfer across field lines may occur when the plasma is turbulent. This may apply in cases where the solar wind interacts directly with the planetary ionosphere (e.g., Venus or Mars). The "turbulent" heat conductivity K_{B} should be related to the Bohm diffusion coefficient ($D_{\text{B}} \approx r_{\text{L}} v_{\text{th}}$)

$$D_{\text{B}} \approx \frac{c k_{\text{B}}}{16 e} \frac{T}{B} \cong 5.4 \times 10^2 \frac{T}{B} \qquad [\text{cm}^2\,\text{sec}^{-1}]$$

where B is the magnetic field strength in Gauss, $v_{\text{th}} = (k_{\text{B}} T/m)^{1/2}$, r_{B} is the Larmor or gyroradius (cf. Chap. VI); thus, K_{B} is given by

$$K_{\text{B}} \approx k_{\text{B}} N D_{\text{B}} \approx 10^{-13} N \frac{T}{B} \qquad [\text{erg K}^{-1}\,\text{cm}^{-1}\,\text{sec}^{-1}] \tag{3.30}$$

which is much greater than $K_{\perp}$.

Equilibrium Electron and Ion Temperatures

At altitudes where heat input into the electron gas is roughly balanced by the energy transfer to ions and where conduction can be neglected in first approximation (e.g., in the vicinity of the ionization peak), the electron temperature varies according to

$$T_e - T_i \propto \frac{Q_e}{N^2} \propto \frac{1}{N} \tag{3.31}$$

since the electron heating rate $Q_e \propto N$, while the loss rate $L_e \propto N^2$, where $N = N_e = N_i$. Thus, the electron temperature will be somewhat lower at F region altitudes, when the electron density is high such as at solar maximum conditions. The ion temperature under equilibrium conditions neglecting conduction can be expressed by [135]

$$T_i = \frac{T_n + a\frac{N}{n}T_e^{-\frac{1}{2}}}{1 + a\frac{N}{n}T_e^{-\frac{3}{2}}} \tag{3.32}$$

where

$$a \simeq 10^7 .$$

At low ionospheric altitudes where N/n is small, the ion temperature will be equal to the neutral gas temperature ($T_i = T_n$), due to the efficient energy transfer between ions and neutrals; at high altitudes where N/n becomes large, the ion temperature will approach the electron temperature ($T_i \to T_e$) since Coulomb collisions between electrons and ions are the predominant energy transfer process.

At high altitudes in a planetary ionosphere, the electron temperature is largely controlled by heat conduction, since heat loss by energy transfer becomes negligible, while heat input occurs due to the presence of suprathermal particles (photoelectrons). The heat flux

$$\mathfrak{F} = \int_z^\infty Q(z)\, dz \tag{3.33}$$

can maintain a positive temperature gradient according to

$$\mathfrak{F}_e = -K_e \frac{dT_e}{dz} . \tag{3.34}$$

Along a magnetic field line the maximum of the electron temperature occurs near the equator. A positive temperature gradient can also be maintained if heat is conducted into the ionosphere from an adjoining hot plasma, such as in the case of the solar wind interacting with a planetary ionosphere.

III.3 Heat Sources not Related to Photoionization

In addition to the principal heat source for the ionospheric plasma, viz. excess energy imparted to the photoelectrons in the photoionization process, other sources of energy input into the electron and ion gas exist.

Corpuscular Heating

A stream of fast electrons, as may exist in the magnetosphere, having an energy E [eV] which interact with the thermal ambient electrons, can heat them at a rate

$$Q_e \cong 2 \times 10^{-12} \frac{N_e}{E} \Phi_e \qquad [\mathrm{eV\,cm^{-3}\,sec^{-1}}] \tag{3.35}$$

where Φ_e is the flux in units of $\mathrm{cm^{-2}\,sec^{-1}}$. This is essentially the same effect as heating of the ambient electrons by photoelectrons, except that the fast electrons considered here have their origin in processes other than photoionization (e.g., acceleration by electrostatic fields).

Joule Heating

In regions of a planetary ionosphere containing a magnetic field, where electric currents flow (e.g., the auroral and equatorial electrojet in the terrestrial ionosphere) conversion of electric current energy into thermal motion through charged particle collisions (Joule dissipation) can lead to heating of the charged particles and the neutrals [143]. Joule heating is generally expressed by

$$Q = \mathbf{j} \cdot \mathbf{E} \tag{3.36}$$

and in terms of conductivity by

$$Q = \sigma_1 E^2 = \frac{j}{\sigma_3} \tag{3.37}$$

where j is the current flowing in the ionospheric plasma as the result of the electric field E; σ_1 is the Pedersen and σ_3 the Cowling conductivity (cf. Chap.V).

The heating rate for electrons, for the case where the electric field, **E** is perpendicular to the magnetic field can be expressed by [143, 144]

$$Q_e = \frac{E_\perp^2 c^2}{B^2} \left[N_e \sum_j \nu_{ej} + N_i \frac{\nu_{ei}}{1 + \sum \frac{\Omega_B}{\nu_{ij}}} \right] \tag{3.38}$$

where B is the magnetic field strength, ν is the collision frequency with the subscripts e, i, j referring to the electrons, ions and neutrals, respectively, and Ω_B is the ion gyrofrequency, $\Omega_B = eB/m_i c$. Similarly, the heat input into the ions is given by [135]

$$Q_i = \frac{E_\perp^2}{B^2} c^2 \sum N_i \cdot \frac{\sum_j \mu_{in} \nu_{ij}}{1 + \sum \frac{\nu_{ij}}{\Omega_B}} \tag{3.39}$$

where μ_{in} is the reduced mass $m_i m_j/(m_i + m_j)$. In the absence of other heat sources for the electrons, the ion-heating due to (3.39) would lead to ion temperatures greater than T_e.

Solar/Stellar Wind Heating

The hot solar wind plasma in the transition region between the bow shock and the "ionopause" (cf. Chaps. I and VI), particularly for non-magnetic planets, can represent an additional heat source for the planetary ionosphere. The interaction between the solar wind and the planetary obstacle leads to the generation of hydromagnetic and acoustic energy.

This energy can be transported in the form of waves of the appropriate modes into the planetary ionosphere. If we assume that a fraction α of the solar wind energy, represented by its pressure p_{sw} (or equivalently its energy density), is deposited with a scale length L over an altitude range from the ionopause level z_u downward and a velocity v of the waves (hydromagnetic, ion-acoustic, etc.) whose damping leads to the heating, the stellar wind heat input can be expressed by [145]

$$Q_{sw} = \left(\frac{\alpha V p_{sw}}{L}\right) \exp\left\{\frac{(z - z_u)}{L}\right\} . \tag{3.40}$$

If the waves are hydromagnetic in nature, the heating may occur for both electrons and ions, while acoustic modes will heat the ions preferentially.

Another source of solar wind heating is heat conduction from the hot solar wind plasma outside the ionopause into the topside planetary ionosphere. In this case a turbulent heat conduction coefficient may have to be invoked (3.30), since even a small horizontal magnetic field in the ionopause region ($B > 10^{-1}\gamma$; [$1\,\gamma = 10^{-5}$ Gauss]) may otherwise inhibit heat conduction.

IV Chemical Processes

IV.1 General Comments

Chemical reactions provide the only true sink of ionization by *recombination* of ion pairs. In addition to this loss process, *charge exchange* reactions act as sources or sinks for particular ion species without perturbing the overall ionization balance [146].

The rate of change of ionized constituents resulting from a recombination process can be expressed by

$$\frac{\partial N_{\mathrm{ei}}}{\partial t} = -\alpha N_{\mathrm{i}} N_{\mathrm{e}} = -\alpha N^2 \quad (\text{for } N_{\mathrm{e}} = N_{\mathrm{i}} \equiv N) \tag{4.1}$$

where α is the recombination coefficient, which is temperature-dependent. Loss of ion pairs by recombination is therefore represented by a square law. Solution of (4.1) gives

$$\frac{1}{N} = \frac{1}{N_0} + \alpha t\,. \tag{4.2}$$

The time constant $\tau \equiv [(1/N)(\partial N/\partial t)]^{-1}$ for recombination can be expressed by

$$\tau_{\mathrm{C}\alpha} = \frac{1}{\alpha N}\,. \tag{4.3}$$

The rate of change of an ion species due to a charge exchange process is given by

$$\frac{\partial N_{\mathrm{i}}}{\partial t} = -kn(M)N_{\mathrm{i}} \tag{4.4}$$

where M refers to the neutral species involved in the charge exchange process; k is the rate coefficient, which can be expressed by

$$k = \langle \sigma_{\mathrm{r}} v_{\mathrm{r}} \rangle \tag{4.5}$$

with σ_{r} the cross-section for the reaction and v_{r} the relative speed between the reacting particles, averaged over the velocity distribution function. The

product $kn(M) = \beta$ is often called the *loss coefficient*, which is altitude-dependent, since it depends on the density of the constituent M. Solution of (4.4) yields

$$N_i = N_{i0} e^{-\beta t} . \tag{4.6}$$

Charge transfer reactions correspond to a linear loss law

$$\frac{\partial N}{\partial t} = -\beta N . \tag{4.7}$$

The time constant for charge exchange is given by

$$\tau_{C\beta} = \frac{1}{\beta} = \frac{1}{kn(M)} . \tag{4.8}$$

The controlling chemical process will be determined by the shortest time constant.

Recombination and charge exchange are representative of *two-body (binary) reactions*, i.e., involving two collision partners, for which the rate equation for the concentration of constituent $[X]$ can be expressed in general form as

$$\frac{d[X]}{dt} = -k[X][Y] \tag{4.9}$$

where the rate coefficient k has the dimension $cm^3\,sec^{-1}$. At altitudes where the atmospheric pressure is relatively high ($p \geq 10^{-2}$ [1 torr = 133 Pa = 1.33^{-3} bar]), i.e., in the D-region of planetary ionospheres, three-body reactions can become important. In this case the rate equation can be expressed in general form by

$$\frac{d[X]}{dt} = -k_3[X][Y][Z] \tag{4.10}$$

where the three-body reaction coefficient has the dimension $cm^6\,sec^{-1}$. Similarly, the rate of a one-body (spontaneous) process, such as photodetachment, can be expressed by

$$\frac{d[X]}{dt} = -\nu[X] \tag{4.11}$$

where ν is the frequency $[sec^{-1}]$ of the process. However, two- and three-body processes can also be expressed in the form of a linear loss law appropriate to a one-body process; in that case the frequency of the process, which then will not be a constant, is given by $\nu = k[Y]$ or $k_3[Y][Z]$.

IV.2 Recombination

There are two classes of recombination processes: *electronic recombination*, involving charge neutralization of an electron–ion pair, and *ion–ion recombination* where the charge neutralization occurs as the result of a reaction between a positive and a negative ion. Two types of electronic recombination [147] can occur in a planetary ionosphere; the one involving atomic ions is called radiative recombination, while the one for molecular ions is called dissociative recombination.

Radiative Recombination

At low electron densities, and in the absence of molecular neutral species, i.e., at high altitudes in a planetary ionosphere, but more importantly in interplanetary space radiative recombination process represents a chemical sink for atomic ions. This process can be expressed by

$$X^+ + e \rightarrow X^* + \hbar\nu \tag{4.12}$$

where $*$ indicates an excited state of species X. Quantum-mechanical calculation of radiative recombination coefficients at 250 °K give values for typical atmospheric constituents as shown in Table 4.1. Theoretically, a temperature dependence $\alpha_r \propto T^{-\frac{1}{2}}$ is predicted; however, a better empirical representation of this dependence is given by $\alpha_r \propto T^{-n}$, where $0.7 \leq n \leq 0.75$. Since α_r is typically of the order of $10^{-12}\,\mathrm{cm}^3\,\mathrm{sec}^{-1}$ at ionospheric temperatures (1000 K), the lifetime against radiative recombination τ_r is extremely long, so that other processes will be responsible for the loss of atomic ions.

Table 4.1. Radiative recombination coefficients.

Ion	H^+	He^+	C^+	N^+	O^+
$\alpha_r \times 10^{12}\,\mathrm{cm}^3\,\mathrm{sec}^{-1}$	4.8	4.8	4.2	3.6	3.7

Dissociative Recombination

This process can be expressed by

$$XY^+ + e \rightarrow XY^* \rightarrow X + Y + \Delta E\,. \tag{4.13}$$

Dissociative recombination occurs as a result of a radiationless transition forming a quasimolecule at small internuclear distance, where the potential energy curve of XY^+ has a minimum, while that of XY^* is repulsive, leading

to a separation of the atoms X and Y. This process leads to a dissociative recombination coefficient α_D, which is about 10^5 greater than the radiative recombination coefficient α_r. Dissociative recombination is therefore one of the most important chemical loss processes [146]. Numerical values of α_D for important molecular ions in planetary ionospheres are shown in Table 4.2. The dissociative recombination coefficient shows a complicated temperature dependence: according to experiments, $\alpha_D(NO^+) \propto T_e^{-0.5}$; $\alpha_D(N_2^+) \propto T_e^{-1/3}$; $\alpha_D(O_2^+) \propto T_e^{-0.7}$ and $\alpha_D(CO_2^+) \propto T_e^{-0.5}$, while the variation with isothermal temperature ($T_e = T_i = T$) is $\propto T^{-1}$ for all except $\alpha_D(N_2^+)$ which is almost constant and $\alpha_D(H_3O^+) \propto T^{-2}$. From theoretical considerations a temperature dependence of about $T_e^{-0.5}$ is expected. The dissociative recombination coefficient may also depend on the ion temperature, due to its dependence on the vibrational structure of the molecular ion.

Table 4.2. Dissociative recombination coefficients.

Ion	α_D [$cm^3\,sec^{-1}$]*
CO_2^+	3×10^{-7}
O_2^+	2×10^{-7}
N_2^+	2×10^{-7}
NO^+	4×10^{-7}
H_2^+	3×10^{-8}
H_2O^+	4×10^{-7}
H_3^+	$\sim 10^{-8}$
H_3O^+	$\sim 10^{-6}$

* For $T_e = T_i = T_n = 300\,K$.

Ion–Ion Recombination

In the lower part of planetary ionospheres (D-Layer) negative ions can form as the result of electron attachment. These can recombine directly with positive ions in a process, which is also called *mutual neutralization*, according to

$$X^+ + Y^- \rightarrow X^* + Y + \Delta E \tag{4.14}$$

where the positive ion may become electronically excited. The excess energy ΔE of the reaction goes into kinetic energy of the neutralized particles or in the case of molecules into vibrational or rotational excitation. The rate coefficients for ion–ion recombination (mutual neutralization) α_{mn} are of the order of $10^{-7}\,cm^3\,sec^{-1}$ [148].

Table 4.3 shows values of α_{mn} at $T = 300\,K$ for some constituents for which experimental data, though at higher temperature, are available. A

Table 4.3. Mutual neutralization coefficients.

	$\alpha_{mn} \times 10^7\,cm^3\,sec^{-1}$	
Ions	Theoretical	Experimental
$H^+ + H^-$	1.2/4.0	4.0 ± 1.8
$N^+ + O^-$	1.8	2.9 ± 1
$O^+ + O^-$	1.1	2.8 ± 1

temperature dependence of $\alpha_{mn} \propto T^{-0.5}$ is predicted theoretically for low energies.

IV.3 The Formation of Hot Neutral Atoms and Planetary Coronae

Thermal ions in planetary ionospheres can be converted to fast neutral atoms with ballistic trajectories reaching very high altitudes. One of the most important mechanism for the production of hot atomic atoms X (mostly N and O) and their isotopes from planetary atmospheres is dissociative recombination of ionospheric O_2^+ ions on Mars and Venus and N_2^+ ions on Saturn's satellite Titan. Generally one can suspect the production of hot oxygen atoms on planets with dense CO_2 atmospheres, while, planetary bodies where nitrogen is the major atmospheric constituent like it was on early Earth after the CO_2 was transformed into carbonates, hot atomic nitrogen atoms should be produced.

To understand the formation of the hot atoms, O_2^+ with its four possible channels [149, 150] is shown as an example. The oxygen atoms may be formed in the ^{3}P, ^{1}D, ^{1}S and ^{1}D states:

$$\begin{aligned}
O_2^+ + e &\rightarrow O(^3P) + O(^3P) + 6.96\,eV \\
O_2^+ + e &\rightarrow O(^3P) + O(^1D) + 5.00\,eV \\
O_2^+ + e &\rightarrow O(^1D) + O(^1D) + 3.02\,eV \\
O_2^+ + e &\rightarrow O(^1D) + O(^1S) + 0.8\,eV\,.
\end{aligned}$$

The branching ratios br for dissociative recombination of oxygen atoms for the final channels are measured as: $O(^3P) + O(^3P) : O(^3P) + O(^1D) : O(^1D) + O(^1D) : O(^1D) + O(^1S) = 0.22 : 0.42 : 0.31 : 0.05$ [151].

The energy density distribution of the hot atoms can be estimated by a Monte Carlo technique. The hot atoms produced are assumed to become thermalized eventually by a series of elastic hard sphere collisions with the background gases. Inelastic collisions are negligibly small at these low energies. On Mars all oxygen atoms with energies greater than 2 eV at the exobase are able to escape.

After its release, a hot oxygen atom may collide with the neutral background gases, may change its direction, lose its energy or the atom may travel long distances in the atmosphere without collisions. We express the collisional probability of the oxygen atoms with the ambient atmosphere as [20, 152]

$$C_{\mathrm{P}} = 1 - \exp\left(-\int_{z_1}^{z_2} \frac{\mathrm{d}z}{\lambda(z)}\right) \tag{4.15}$$

with $\lambda(z)$ the mean free path length

$$\lambda(z) = [n(z)\sigma]^{-1}\,, \tag{4.16}$$

and σ is the momentum transfer cross-section of about 10^{-15} cm^2 [150]. Each collision step can be generated by equating a random number R_1 to the following integral:

$$R_1 = \exp\left(-\int_{z_1}^{z_2} \frac{\mathrm{d}z}{\lambda(z)}\right). \tag{4.17}$$

The path that a single hot atom follows from altitude z_1 to altitude z_2 may be highly erratic. If a collision occurs one can simulate the direction of the velocity vector with a second random number R_2. If R_2 is between 0 and 0.5 the hot oxygen atom's new direction points downwards. If the random number is between 0.5 and 1 the atom travels upwards. At the j$^{\mathrm{th}}$ collision step, the energy from hard sphere collisions between the hot oxygen atoms and the surrounding atmosphere is taken to be

$$E_j = R_3 \frac{4 m_{\mathrm{hot}} m}{(m_{\mathrm{hot}} + m)^2} E_{j-1} \tag{4.18}$$

with m_{hot} the mass of the hot atoms (O* or N*) and m the mass of the main atmospheric constituents of a planetary atmosphere and R_3 a third random number representing the type of collision and simulates the effectiveness of the energy transfer between the colliding particles. This simulates everything between a full head-on and a glancing collision. The random numbers R_j (j=1, 2, 3) are from a sample of random numbers uniformly distributed over an interval between 0 and 1 and the energy-dependent flux $F(E, z)$ of the ballistic hot atoms is given by

$$F(E,z) = \int_{z_1}^{z_2} \frac{[1 - P(E,z)]\alpha[X_2^+]^2}{E} \mathrm{br} \quad \mathrm{d}z \tag{4.19}$$

where X_2^+ is the molecular ion (O_2^+ or N_2^+) responsible for the production of the hot atoms and the value of the dissociative recombination coefficient in the order of $\alpha = 1 \times 10^{-7}\mathrm{cm}^{-3}\mathrm{s}^{-1}$ for all possible recombination channels. $P(E, z)$ is the escape fraction which defines the fraction of atoms that are produced with a specified initial energy at a specified altitude and reach

the exobase with energies greater than the escape energy, and br are the branching ratios of the reactions involved.

At the vertical distance, the distribution of the hot atom flux as a function of the kinetic energy $F(E, z)$ is then converted to the corresponding energy density distribution function $f(E, z_e)$ through the following equation:

$$f(E, z_c) = \frac{F(E, z_c)}{v(E)} \tag{4.20}$$

where $v(E)$ is the velocity of the hot oxygen atoms corresponding to energy E. It should again be noted that the absolute values of the number densities are not divided by a factor of 2 to account for the downward component.

The simulations are started below the exobase levels at altitudes where the hot atoms are produced. After the particles are released by the chemical reactions the hot atoms are traced in the atmosphere up to the exobase level with a discrete step size Δz. After a simulation with $\geq 5 \times 10^5$ particles the model simulations match nature very well.

To obtain the number density n_c of the hot atoms at the exobase level, the energy distribution function $f(E, z_c)$ must be integrated over the energy interval

$$n_{\mathrm{hot}_c} = \int_{E_1}^{E_2} f(E, z_c) \mathrm{d}E. \tag{4.21}$$

By using Liouville's equation one finds the corresponding exospheric density distribution of the hot atoms.

The number density of the hot atoms n_{hot} as a function of planetocentric distance R is the product of the barometric density and partition functions corresponding to ballistic ζ_1, satellite ζ_2 and escaping ζ_3 particle trajectories

$$n_{\mathrm{hot}}(R) = n_{\mathrm{hot}_c} \mathrm{e}^{-(z/H)} \left[\xi_1(X_c, X) + \xi_2(X_c, X) + \xi_3(X_c, X)\right] \tag{4.22}$$

where H is the scale height, X_c is the escape parameter at the exobase and X is that above as a function of the planetocentric distance R. Figures 4.1 and 4.2 show cold and hot atmospheric species in the Venusian and Martian upper atmospheres. The kinetic energy release in the dissociative recombination process can also play an important role in the generation of anomalous $^{15}N/^{14}N$ isotope ratios in low mass Martian-like bodies due to the preferred escape of the lighter ^{14}N isotope. Dissociative recombination of N_2^+ can proceed via three possible channels [149, 151]:

$$\begin{aligned}
N_2^+ + e &\rightarrow N(^4S) + N(^2D) + 3.44\,eV \\
N_2^+ + e &\rightarrow N(^4S) + N(^2P) + 2.24\,eV \\
N_2^+ + e &\rightarrow N(^2D) + N(^2D) + 1.06\,eV.
\end{aligned}$$

The escape energy of a ^{14}N isotope in the Martian exobase is about 1.722 eV. In dissociative recombination of $^{29}N_2^+$ a ^{15}N isotope is released with

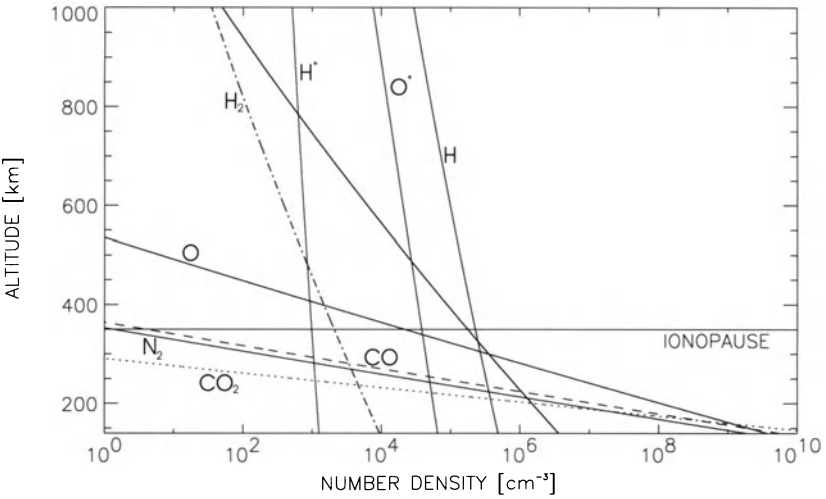

Fig. 4.1. Cold and hot (*) density distribution corresponding to medium solar activity of atmospheric constituents in the Venusian atmosphere. The hot O* and H* particles follow ballistic trajectories up to high altitudes above the cool background gas (courtesy of U. V. Amerstorfer).

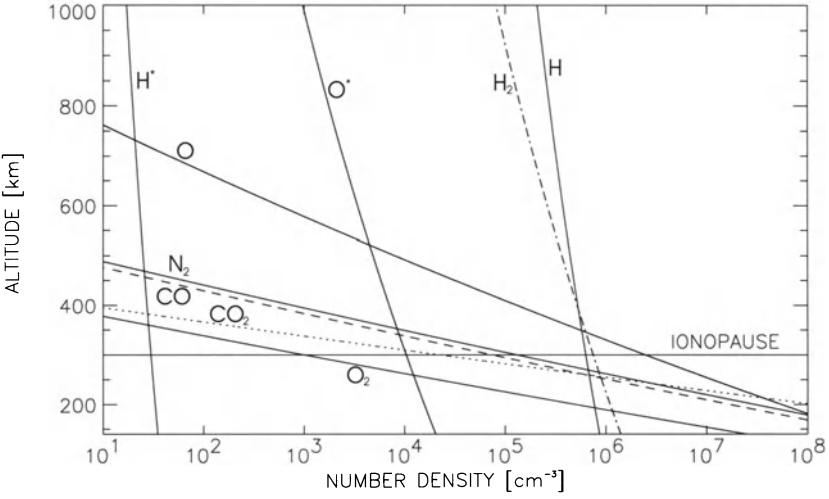

Fig. 4.2. Cold and hot (*) density distribution corresponding to medium solar activity of atmospheric constituents in the Martian atmosphere. The hot O* and H* particles follow ballistic trajectories up to high altitudes above the cool background gas (courtesy of U. V. Amerstorfer).

14/29×3.44 eV, which yields an energy of 1.66 eV, significantly less than the Martian escape energy of about 1.844 eV. It is important to note that this is not the case on a smaller body like Titan. Reactions which release the isotopes with energies of 1.081 eV and 0.511 eV contribute to the escape on Titan because their energy is greater than the escape energy of about 0.33 eV.

The branching ratios for dissociative recombination of N_2^+ molecular ions for nitrogen isotopes were measured in the $X^2\Sigma_g^+$ electronic ground state at the heavy ion storage ring ASTRID [151]. The branching ratios for the final channels are $N(^4S) + N(^2D) : N(^4S) + N(^2P) : N(^2D) + N(^2D) = 0.46 : 0.08 : 0.46$. The amount of isotopes released with energies of about 1.12 eV is negligible small, since the corresponding reaction has a small branching ratio.

If the isotopes have energies much closer to the escape energy, the separation effect is relevant at altitudes below the exobase level. Fewer collisions are needed for the isotopes in the lower energy regime to get energies lower than their escape energy. At altitudes where the mean free path is larger than the scale height, only few or no collisions and therefore no isotope separation occurs anymore.

It is also important to note that the escape fraction in altitude regions where the separation is more efficient can occur in altitude regions where only a small fraction of isotopes reach the exosphere with energies greater than the escape energy [20, 153].

Since dissociative recombination of ionospheric constituents is an important source of suprathermal neutral atoms in planetary upper atmospheres, charge exchange reactions between solar-wind particles and particles from these extended hot neutral gas coronae occur up to altitude levels much higher than the ionopause on magnetic field free planetary bodies. The neutral gas of the coronae can than be ionized and incorporated into the stellar plasma flow round the planet.

IV.4 Charge Exchange Reactions

Ion–neutral or ion–molecule reactions lead to the exchange of charge between these species as the result of collisions [154]. Charge exchange reactions include charge transfer processes in which one or more electrons are transferred, as well as ion–atom interchange (charged rearrangement) processes in which a charged or neutral atomic or molecular species is transferred similar to an ordinary chemical reaction. Charge exchange reactions play an important role in planetary ionospheres where atomic ions and neutral molecular species are present, since in this case they represent the controlling chemical process, due to their rather high rate coefficient. The rate coefficient k can be defined as

$$k = \int_0^\infty v\sigma(v)f(v)\,\mathrm{d}v = \langle \sigma v \rangle \tag{4.23}$$

where v is the relative velocity of the colliding particles, σ is the reaction cross-section and $f(v)$ is a normalized velocity distribution function. Theoretical estimates for charge exchange reaction rate coefficients can be made on the basis of the Langevin–Eyring–Gioumousis and Stevenson theory [154] which yields a reaction cross-section based on the ion-induced dipole interactions

$$\sigma = \pi e \left(\frac{2 m_\mathrm{i} \alpha}{\mu E_\mathrm{i}} \right)^{\frac{1}{2}} \tag{4.24}$$

where m_i is the ion mass, $\mu = m_\mathrm{i} m_\mathrm{n}/(m_\mathrm{i} + m_\mathrm{n})$ is the reduced mass of the ion–neutral system, α is the polarizability of the neutral species and E_i is the ion kinetic energy and e is the electronic charge.

Since the velocity of the ion is $v_\mathrm{i} = (2E_\mathrm{i}/m_\mathrm{i})^{\frac{1}{2}}$, the rate coefficient, according to (4.23), is given, using (4.24), by

$$k = 2\pi e \left(\frac{\alpha}{\mu} \right)^{\frac{1}{2}} = 2.3 \times 10^3 \left(\frac{\alpha}{\mu} \right)^{\frac{1}{2}} \ \mathrm{cm^3\,sec^{-1}} . \tag{4.25}$$

Typical values of k based on the Gioumousis–Stevenson formula are of the order $10^{-9}\,\mathrm{cm^3\,sec^{-1}}$, representing an upper limit. Based on the energy dependence of $\sigma (\propto E^{-\frac{1}{2}})$, the rate coefficient k should be independent of temperature; however, some experimental data suggest a temperature dependence $T^{-\frac{1}{2}}$, corresponding to a dependence of σ upon E^{-1}.

It has also been suggested that ion–neutral reactions may involve an activation energy, which in case of an otherwise endothermic reaction, must be at least equal to the endothermicity. The energy defect ΔE of the reaction $X^+ + Y \rightarrow Y^+ + X + \Delta E$, representing the difference in the ionization potentials of the reaction partners, determines if the reaction is possible (exothermic). $\Delta E = \mathrm{IP}(X) - \mathrm{IP}(Y) > 0$ represents an exothermic, $\Delta E < 0$ an endothermic and $\Delta E = 0$ a resonant reaction. In this case the temperature dependence of the rate coefficient can be represented by the Arrhenius relation [155]

$$k = A \exp \left[-\frac{E_\mathrm{a}}{k_\mathrm{B} T} \right] \tag{4.26}$$

where E_a is the activation energy (in eV), k_B the Boltzmann constant, and A is the so-called frequency factor. Although A is often considered to be a temperature-independent factor (following the Arrhenius theory), it may also be dependent on temperature, since it corresponds to a reduced collision frequency, which may be energy dependent, according to

$$A \equiv \nu'_\mu = 2\sigma (2\pi k_\mathrm{B} T \mu)^{\frac{1}{2}} \tag{4.27}$$

where μ is the reduced mass. (A is also sometimes referred to as the steric hindrance factor, borrowed from chemical reaction theory [155]).

Charge exchange reactions between energetic ions and atmospheric neutral atoms led to so-called energetic neutral atoms (ENA's). ENA distributions around Venus and Mars are characterized by ENA's who have their origin in the solar-wind and by a second particle population which comes from the planetary atmosphere. After a planetary neutral atom is transformed into an ion via charge exchange with solar-wind particles, solar UV or electron impact, it is accelerated to higher altitudes and energies by the interplanetary electric field and gradually guided by the solar wind plasma flow around the planetary obstacle. Some of the newly born planetary ions take part in a charge exchange reaction with particles of the upper atmosphere and will be thus transformed into planetary ENA's.

Charge Transfer Reactions

Reactions of this type proceed according to the scheme

$$X^+ + Y \rightarrow Y^+ + X\,. \tag{4.28}$$

When the neutral species is a molecule, dissociative charge transfer can also take place, according to

$$X^+ + YZ \rightarrow Y^+ + Z + X\,. \tag{4.29}$$

A special case is resonant (symmetric) charge transfer

$$X^+ + X \leftrightarrows X + X^+\,. \tag{4.30}$$

This reaction can be important for converting fast ions into thermal ions and at the same time producing fast neutrals. The cross-section for resonant charge transfer at low energies has an energy dependence

$$\sigma^{\frac{1}{2}} = a - b \log E$$

i.e., is largest at thermal energies. In addition to the resonant charge transfer involving like ion and neutral species, there is an accidentially resonant, but asymmetric, charge transfer process, when the difference in the ionization potentials (energy defect) is very small [156]. The classic example of this type of reaction, which is of great importance in the terrestrial ionosphere, is [157]

$$O^+ + H \leftrightarrows O + H^+\,. \tag{4.31}$$

The equilibrium concentrations associated with this process are given by [158]

$$\frac{n(H^+)}{n(O^+)} = \frac{9n(H)}{8n(O)}$$

Table 4.4.

Reaction	k [$cm^3\,sec^{-1}$]
$H^+ + H \rightarrow H + H^+$	$3(-9)^*$
$H^+ + O \rightarrow H + O^+$	$4(-10)$
$H^+ + CO_2 \rightarrow H + CO_2^+$	$1(-10)$
$H^+ + C_nH_m \rightarrow C_nH_m^+ + ...$	$4(-9)$
$He^+ + O_2 \rightarrow He + O + O^+$	$2(-9)$
$He^+ + CO_2 \rightarrow O^+ + CO + He$	$1(-9)$
$He^+ + CO \rightarrow C^+ + O + He$	$2(-9)$
$He^+ + N_2 \rightarrow He + N_2^+$	$2(-9)$
$He^+ + N_2^+ \rightarrow He + N + N^+$	$8(-10)$
$N^+ + O_2 \rightarrow N + O_2^+$	$5(-10)$
$O^+ + O_2 \rightarrow O + O_2^+$	$2(-11)$
$N_2^+ + O_2 \rightarrow N_2 + O_2^+$	$1(-10)$
$N_2^+ + CO \rightarrow N_2 + CO^+$	$7(-11)$
$N_2^+ + NO \rightarrow N_2 + NO^+$	$5(-10)$
$N_2^+ + C_nH_m \rightarrow CNH_m^+ + ...$	$1(-9)$
$N_2^+ + CO_2 \rightarrow N_2 + CO_2^+$	$9(-10)$
$CO^+ + O_2 \rightarrow CO + O_2^+$	$2(-10)$
$CO^+ + CO_2 \rightarrow CO + CO_2^+$	$1(-9)$
$CO_2^+ + O_2 \rightarrow CO_2 + O_2^+$	$1(-10)$
$CO_2 + H \rightarrow H^+ + CO_2$	$1(-10)$

* $(-X) \equiv 10^{-X}$.

where 9/8 is the ratio of the products of the statistical weights obtained from detailed balancing of reaction (4.31). The statistical weights $g_s = \sum(2J+1)$ for the reactants O^+, H, H^+ and O have values 4, 2, 1 and 9, respectively. However since the reaction is not truly resonant, i.e., $\Delta E = \mathrm{IP(O)} - \mathrm{IP(H)} = 0.02\,\mathrm{eV}$, the ratio of the products of the statistical weights should be modified by a factor $\exp(\Delta E/k_B T)$. While this leads to a ratio 9/8 for $T \rightarrow \infty$, at $T_s = 1000\,\mathrm{K}$ this ratio is $\frac{9}{7}$ and at $T_s = 600\,\mathrm{K}$ it is 7/5 [159].A cross-section of $7.6 \times 10^{-16}\,\mathrm{cm}^2$ has been derived for this reaction from ionospheric data, leading to a rate coefficient $k \cong 4.0 \times 10^{-10}\,\mathrm{cm}^3\,\mathrm{sec}^{-1}$. Some charge transfer reactions of importance in planetary ionospheres and their measured or theoretically estimated rate coefficients [147, 154] are listed in Table 4.4.

Ion–Molecule Interchange Reactions

In contrast to straightforward charge transfer, these reactions also involve the transfer of a charged or neutral atom according to

$$X^+ + YZ \rightarrow XY^+ + Z\,. \tag{4.32}$$

Table 4.5.

Reaction	k [$cm^3\,sec^{-1}$]
$H^+ + CO_2 \rightarrow COH^+O$	$6(-10)^*$
$H_2^+ + H_2 \rightarrow H_3^+ + H$	$2(-9)$
$He^+ + H_2 \rightarrow HHe^+ + H$	$< (-13)$
$C^+ + CO_2 \rightarrow CO^+ + CO$	$2(-9)$
$C^+ + O_2 \rightarrow CO^+ + O$	$1(-9)$
$N^+ + O_2 \rightarrow NO^+ + CO$	$5(-10)$
$N^+ + CO_2 \rightarrow NO^+ + CO$	$2(-11)$
$N_2^+ + C_nH_m \rightarrow H_2CN^+ +$ nitriles	$1(-9)$
$H_2CN^+ + H_2O \rightarrow H_3O^+HCN$	$1(-9)$
$H_2CN^+ + C_4H_2 \rightarrow C_4H_3^+ + HCN$	$2(-9)$
$O^+ + N_2 \rightarrow NO^+ + N$	$1(-12)$
$O^+ + CO_2 \rightarrow O_2 + CO$	$1(-9)$
$O_2^+ + N \rightarrow NO^+ + O$	$2(-10)$
$CO_2^+ + H \rightarrow COH^+ + O$	$6(-10)$
$CO_2^+ + O \rightarrow O_2^+ + CO$	$2(-10)$

* $(-X) \equiv 10^{-X}$.

This type of reaction is sometimes called *charged rearrangement.* Direct charge transfer between atomic ions and molecular species, as well as ion–atom interchange, represent important loss processes for atomic ions, since the molecular ions formed by this reaction will be subject to (fast) dissociative recombination. This represents an efficient removal path for atomic ions in planetary ionospheres [146]. In altitude regions where these processes occur, the loss of atomic ions will be governed by a linear loss law. Similarly to the other charge exchange reactions, the temperature dependence of the rate constants for ion–atom interchange is often quite complex and may involve an activation energy (cf. [154]). Table 4.5 lists some important ion–molecule interchange reactions and their rate constants [154]. At altitudes where water vapor molecules are present, some ions form hydrates according to [146, 160]

$$P^+ + H_2O + Z \rightarrow P^+ \cdot (H_2O) + Z \tag{4.33}$$

where P^+ represents O_2^+, NO^+, CO_2^+. Repeated reactions of this type (with a three-body rate coefficient $k_3 \approx 10^{-28}\,cm^6\,sec^{-1}$) lead to *cluster ions* of the form

$$P^+ \cdot (H_2O)_{n-1} + H_2O + Z \rightarrow P^+ \cdot (H_2O)_n + Z\,. \tag{4.34}$$

The three-body reaction chain is terminated by an exothermic binary reaction [$k \approx 10^{-10}\,cm^3\,sec^{-1}$] of the type

$$P^+ \cdot (H_2O)_n + H_2O \rightarrow H_3O^+ \cdot (H_2O)_{n-1} + P + OH \tag{4.35}$$

forming hydrated hydronium ions (H_3O^+). Such heavy cluster ions appear to be the predominant ion species in the D-region of a planetary ionosphere. Similar cluster ions are formed with CO_2, leading to $P^+ \cdot (CO_2)_n$, where P^+ may also be CO_2^+.

IV.5 Negative Ion Reactions

Negative ions can be formed by attachment of electrons to neutral species. Since this process depends on the collisions between electrons and neutral atoms and molecules, formation of negative ions will occur predominantly in the densest part of a planetary ionosphere (D-region). The stability of a negative ion depends on the electron affinity (i.e., the binding energy of the extra electron, typically of the order 1 eV). The following attachment processes are possible [146, 161, 162]:

1) *radiative attachment*

$$e + \begin{cases} X \\ XY \end{cases} \rightarrow \begin{cases} X^- \\ XY^- \end{cases} + \hbar\nu \tag{4.36}$$

2) *dissociative attachment*

$$e + XY \rightarrow X + Y^- \tag{4.37}$$

3) *three-body attachment*

$$e + XY + Z \rightarrow XY^- + Z \tag{4.38}$$

where Z represents the third collision partner, usually a molecule, such as XY.

Radiative and dissociative attachment processes are usually less important than three-body attachment, except in the uppermost part of the D-region where electron–neutral collisions become small. The rate coefficients for these two-body reactions are of the order $\sim 10^{-15}\,\mathrm{cm^3\,sec^{-1}}$. The dominant process for negative ion formation in the lowermost part of a planetary ionosphere ($p \geq 10^{-2}$ torr [1 torr = 133 Pa = 1.33^{-3} bar]) is thought to be three-body attachment which has a rate coefficient $a_3 \cong 10^{-30}\,\mathrm{cm^6\,sec^{-1}}$.

Although the various attachment processes are either two- or three-body reactions, they are often represented by a linear loss law appropriate to a one-body reaction.

$$\frac{dN_e}{dt} = -\beta_a N_e \tag{4.39}$$

where β_a is the rate of attachment per free electron [$\mathrm{sec^{-1}}$], given by the rate coefficient multiplied by the number density of the neutral species for

the two-body processes and multiplied by the square of the neutral density for the three-body process. The reciprocal of β_a is the lifetime of an electron against attachment τ_{att} [sec].

Destruction of negative ions occurs by detachment processes and ion–ion recombination (mutual neutralization). The following detachment processes can occur:

1) *photodetachment*

$$XY^- + \hbar\nu \rightarrow XY + e \tag{4.40}$$

2) *associative detachment*

$$XY^- + Z \rightarrow XYZ + e \tag{4.41}$$

3) *Penning detachment*

$$XY^- + XY^* \rightarrow XY + XY + e \tag{4.42}$$

which involves an excited (metastable) species XY. The last two types of attachment processes are also categorized as *collisional detachment.*

Again, photodetachment appears to be of lesser importance than the collisional detachment processes. The latter have rate coefficients of the order $10^{-10}\,cm^3\,sec^{-1}$; photodetachment rates are of order $0.3\,sec^{-1}$ [161, 162].

Analogously to charge exchange processes for positive ions, negative ion–molecule reactions lead to the transformation of one negative ion species into another [146]. Basically these are simple charge transfers of the type

$$X^- + Y \rightarrow X + Y^- \tag{4.43}$$

where X and Y are usually molecular species, and negative ion–molecule interchange,

$$X^- + YZ \rightarrow XY^- + Z \tag{4.44}$$

which can also occur as a three-body process. Examples of negative ion–molecule reactions [160] and their rate coefficients are listed in Table 4.6. The condition of charge neutrality requires that

$$N_+ = N_e + N_- \,. \tag{4.45}$$

Whenever negative ions are present, their effect on the ionization balance is expressed in terms of a parameter $\lambda^- = N_-/N_e$, and thus $N_+ = (1+\lambda^-)N_e$. The parameter λ^- depends on the rate coefficients for the various processes involved in the formation and destruction of negative ions, according to

$$\lambda^- \simeq \frac{\nu_{att}}{\nu_{coll.det.} + \nu_{ph.det.} + \nu_{mn}} \tag{4.46}$$

Table 4.6.

Reaction	Rate coefficient [$cm^3\,sec^{-1}$]
$O_2^- + O_3 \rightarrow O_3^- + O_2$	$3(-10)$
$O_2^- + NO_2 \rightarrow NO_2^- + O_2$	$8(-10)$
$O_3^- + NO \rightarrow NO_3^- + O$	$1(-11)$
$O_3^- + CO_2 \rightarrow CO_3^- + O_2$	$4(-10)$
$CO_3^- + NO \rightarrow NO_2^- + CO_2$	$9(-12)$
$CO_3^- + O \rightarrow O_2^- + CO_2$	$8(-11)$
$NO_2^- + O_3 \rightarrow NO_3^- + O_2$	$2(-11)$
$O_2^- + O_2 + Z \rightarrow O_4^- + Z$	$> (-30)$ [$cm^6\,sec^{-1}$]
$O_4^- + O \rightarrow O_3^- + O_2$	$4(-10)$
$O_4^- + CO_2 \rightarrow CO_4^- + O_2$	$4(-10)$
$CO_4^- + O \rightarrow CO_3^- \pm O_2$	$2(-10)$
$CO_4^- + NO \rightarrow NO_3^- + CO_2$	$5(-11)$
$CO_3^- + NO_2 \rightarrow NO_3^- + CO_2$	$8(-11)$

Table 4.7.

Negative Ion	Mass number
O_2^-	32
Cl^-	35, 37
CO_3^-	60
HCO_3^-	61
NO_3^-	62
$O_2^- \cdot (H_2O)_2$	68
CO_4^-	74
$CO_3^- \cdot H_2O$	78
$NO_2^- \cdot (HNO_2)$	93 ± 1
$CO_4^- \cdot (H_2O)$	104
$NO_2^- \cdot (HNO_2) \cdot H_2O$	111 ± 1
$CO_4^- \cdot (H_2O)_2$	122
$NO_3^- \cdot (HNO_3)$	$125 + 1$

where the ν_s are the frequencies per ion or electron for the appropriate processes, i.e., the rate coefficients times the number density, according to a linear (one-body) rate equation. With positive and negative ions present, the effective recombination coefficient is

$$\alpha_{\text{eff}} = \alpha_e + \lambda^- \alpha_i \tag{4.47}$$

where α_e is the electronic and α_i is the ionic recombination coefficient. Table 4.7 lists negative ions identified by mass spectrometers in the terrestrial ionosphere.

Table 4.8. Airglow emissions.

N_2	Second positive band	3371 Å
N_2	Lyman–Birge–Hopfield band	1354 Å
CO	Cameron band (a–X)	1993 Å
CO	Fourth positive band (A–X)	1478 Å
CO_2 (O; C)	(dissociative excitation)	1356; 1561, 1657 Å

IV.6 Chemical Reactions and Airglow

Photoelectrons with energies $\gtrsim 10\,\mathrm{eV}$ are also capable of exciting UV emissions (airglow) from the major constituents of planetary atmospheres [163]. Some planetary dayglow emissions excited by photoelectron impact are shown in Table 4.8. Recombination processes provide a source of airglow emission, which is particularly observable during the night (*nightglow*) [164]. Radiative recombination of atomic ions leads to emission according to

$$X^+ + e \rightarrow X^* + \hbar\nu \tag{4.48}$$

which can be followed by

$$X^* \rightarrow X\ (\text{ground state} + \sum \hbar\nu)$$

where $\hbar\nu$ is the direct recombination photon and $\sum \hbar\nu$ represent the photons emitted in cascade to the ground state. The emission rate from radiative recombination can be expressed by [164]

$$\mathfrak{J}_\lambda = k_\lambda \int_{z_1}^{z_2} \alpha_r N_i N_e \, dz = k_\lambda \int_{z_1}^{z_2} \alpha_r N^2 \, dz \tag{4.49}$$

where k_λ is the probability that line λ will be emitted from a given recombination, α_r is the radiative recombination coefficient and N_i and N_e are the ion and electron density, respectively; if the ion represents the predominant ion, $N_i = N_e \equiv N$, in the altitude range between z_1 and z_2. It has been suggested [165, 166] that nightglow emissions in the terrestrial ionosphere may be the result of the reaction

$$\begin{aligned} O^+(^4S) + e &\rightarrow O^* + \hbar\nu \\ O^* &\rightarrow O(^3P) + \sum \hbar\nu\,. \end{aligned} \tag{4.50}$$

The integrated (column) emission rate in the vertical direction from an energy level j, which is populated by X_j^* atoms per cm^3, can be expressed by

$$\mathfrak{J}_\lambda = A_\lambda \int_0^\infty [X_j^*] \, dz \tag{4.51}$$

where A_λ is the Einstein transition coefficient. The concentration $[X_j^*]$ is governed by an equation of continuity, where the production is given by radiative transitions, while the loss is primarily due to collisional deactivation ("quenching") [164]. Dissociative recombination usually provides for a substantial energy defect ΔE

$$XY^+ + e \rightarrow X + Y + \Delta E\,.$$

This type of reaction allows the dissociation products to be energetically in excited levels; transition to the ground level (or intermediate levels) then leads to the emission of radiation which is most easily observed as nightglow. Typical examples of nightglow emissions in the terrestrial ionosphere, associated with dissociative recombination, are the reactions

$$O_2^+ + e \rightarrow O + O + 6.96\,eV$$
$$NO^+ + e \rightarrow N + O + 2.76\,eV$$

which lead to the emission of the 5577 Å green line of oxygen and the 6300 Å red line of oxygen. The typical O transitions are shown in Fig. 4.3. Dissociative recombination of CO_2^+, according to reaction

$$CO_2^+(\tilde{X}^2\Pi_g) + e \rightarrow CO(a^3\Pi) + O$$

may also contribute to the observed emission of the CO(a–X) Cameron band (1900–2500 Å) in the atmosphere of Mars [167].

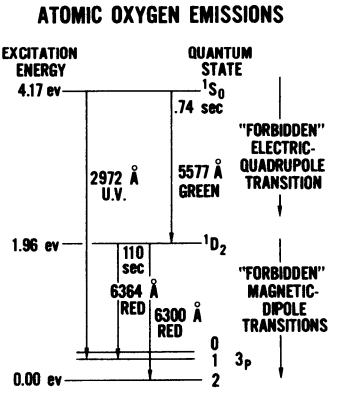

Fig. 4.3. Transitions in atomic oxygen leading to the 5577 Å and 6300 Å airglow emissions (e.g., in terrestrial auroras).

Resonance and Fluorescence Scattering of Solar XUV Radiation

Solar emission lines corresponding to resonance lines of atmospheric constituents lead to *resonance scattering*, i.e., the absorption of a solar photon

Table 4.9. Resonance reradiation (* also dissociation excitation of N_2; ** also dissociation excitation of H_2).

He^+	304 Å
Ne^+	461 Å
He	584 Å
A^+	724 Å
O^+	834 Å
A	1048 (866) Å
$N(N_2)$	1200 Å* (1135 Å)
$H(H_2)$	1216 Å**
O	1304 (1302, 1306) Å
C	1657 Å, 1561 Å

Table 4.10. Fluorescence.

U.V.	[Bands]	X-rays	[K_α emissions]
CO	1510 Å	C	44.54 Å
NO	2149 Å	N	31.56 Å
N_2	3914 Å	O	23.57 Å
CO_2	2882 Å, 3509 Å	Ne	14.59 Å
CO^+	2190 Å, 4264 Å	Ar	4.19 Å

leads to reradiation at the same wavelength. *Flourescence scattering* represents the case where the excited atom or molecule emits a photon at a wavelength longer than that of the absorbed photon. Airglow observations provide a sensitive technique for the detection of certain atmospheric constituents even though they may be extremely minor species of a planetary atmosphere [168, 169]. Constituents of planetary atmospheres which may be detected by resonance and flourescence scattering observations are shown in Tables 4.9 and 4.10. In addition to their identification, the concentration of the scattering constituents can be determined from airglow observations [168]. The *column emission rate* $\mathfrak{F}$ in photons $cm^{-2}\,sec^{-1}$ of an airglow layer is related to the column density of atoms or molecules through the emission rate factor $\mathfrak{g}$, according to

$$\mathfrak{F} = \mathfrak{g} \int_0^\infty n(R)\,ds\,. \tag{4.52}$$

The emission rate factor depends on the differential solar photon flux outside the atmosphere $\hat{\Phi}_\infty$ in photons $cm^{-2}\,sec^{-1}\,Å^{-1}$ and the oscillator strength of the transition, $\mathfrak{f}$

$$\mathfrak{g} = \hat{\Phi}_\infty \lambda^2 \left(\frac{\pi e^2}{mc^2}\right) \mathfrak{f}\,.$$

(Note that $\Phi_\infty = \int_\lambda^{\lambda+\Delta\lambda} \hat{\Phi}_\infty \, d\lambda$, where $\Delta\lambda$ is the instrumental bandwidth; the numerical value for the constant in parenthesis is 8.829×10^{-13} cm.) The column density in the line of sight (ds) can be related to the vertical column density by the Chapman function $\mathrm{Ch}(\chi)$ (see Chap. I)

$$\mathfrak{F} = \mathfrak{g}\mathrm{Ch}(\chi) \int_{R_s}^{\infty} n(R) \, dR = \mathfrak{g}\mathfrak{N}_0 \mathrm{Ch}(\chi) \tag{4.53}$$

where R_s is the planetocentric distance of the observation point and $\mathfrak{N}_0$ is the vertical column density.

For limb observations ($\chi = 90°$) outside a planetary exosphere whose density distribution can be approximated by a power law $n(R) = n(R^*)(R^*/R)^k$, the observed column emission rate is given by

$$\mathfrak{F} = \mathfrak{g} n(R^*) R^* \frac{2(\pi)^{\frac{1}{2}}}{k-1} \frac{\Gamma_\infty\left(\frac{(k+1)}{2}\right)}{\Gamma_\infty\left(\frac{k}{2}\right)} \tag{4.54}$$

where Γ_∞ is the complete gamma function. In this case $R_s \gg R^*$, the minimum distance of the grazing ray, so that the vertical total content above R^* is related to the column density in the line of sight from $-\infty$ to $+\infty$, or twice the Chapman function $\mathrm{Ch}(\pi/2, R^*)$. The observed column emission rate for limb observations ($\chi = 90°$) of a constituent which follows an exponential altitude distribution $n(R) = n(R^*)\exp((R - R^*)/H)$ is given by

$$\mathfrak{F} = \mathfrak{g} n(R^*)(2\pi H R^*)^{\frac{1}{2}}$$

noting that $\mathrm{Ch}(\chi = 90°, R^*) = ((\pi/2)(R^*/H))^2$ (see also Chap. I). From such observations, the density distribution $n(R)$ can be derived. It should be noted that the airglow emission rates are generally quoted in units of rayleighs; 1 rayleigh $(R) = 10^6$ photons $\mathrm{cm}^{-2}\,\mathrm{sec}^{-1}$.

IV.7 Meteor Reactions

Meteoroids entering the upper atmosphere at high speeds ($v_0 \geq v_\infty$) dissipate their energy and mass in the interaction with atmospheric molecules, producing the "visible" (either by eye or radar) meteor. The collisions with atmospheric molecules of the fast meteoric atoms and molecules, formed by ablation of the meteoroid, leads to excitation and ionization. Most of the meteors result from tiny pieces of compressed dust (thought to be of cometary origin) which are distributed in a continuous stream along highly eccentric orbit around the Sun. Thus, meteor streams intersect the planetary orbits out to the distance of Jupiter [170].

Table 4.11. Characteristic velocities [km/sec].

	v_{01}	$v_{\odot}$	v_{orb}	v_{02} (max)
Venus	10	50	35	85
Earth	11	42	30	72
Mars	5	34	24	58
Jupiter	60	19	13	32

The ionization rate due to meteoroids of given initial mass, velocity and zenith angle distribution is given in the general form by [171]

$$q = \int_{\mu_{01}}^{\mu_{02}} \int_{v_{01}}^{v_{02}} \Phi\alpha(h, \mu_0, v_0, \chi) \sec\chi f_1(\mu_0) f_2(v_0) f_3(\chi)\, \mathrm{d}\mu_0\, \mathrm{d}v_0\, \mathrm{d}\chi \qquad (4.55)$$

where Φ is the normalized total meteor flux, $\alpha(h, \mu_0, v_0, \chi)$ is the number of ion pairs produced per unit path-length, i.e., the line density [cm^{-1}] and $f_1(\mu_0)$, $f_2(v_0)$ and $f_3(\chi)$ are the distribution of meteoroid mass, velocity and of the meteor zenith angle, respectively. The integration limit μ_{01} refers to the minimum mass, represented by a boundary mass value between micrometeorites and meteoroids which suffer significant evaporation travelling through the atmosphere and which depends on the meteoroid mass density and velocity according to $\mu_{01} \sim \delta^{\frac{2}{3}} v_0^{-3}$; μ_{02} represents the mass of meteoroids which are heated uniformly throughout their volume while travelling through the atmosphere ($\mu_{02} \sim \delta_0^{-1}$). The meteoroid mass distribution is usually taken as $f_1(\mu_0) = 1/\mu^s$ with $s = 2$. The integration limits for velocity represent the minimum and maximum velocities in a planetary atmosphere, if it is assumed that the meteor streams are in heliocentric orbits; v_{01} therefore corresponds to the appropriate planetary escape velocity, while v_{02} represents a velocity which is the vector sum of the heliocentric escape velocity $v_{\odot}$ at the planet and the orbital velocity of the planet. Table 4.11 lists these values for a number of planets. One should note that at Jupiter, all meteoroids in heliocentric orbit will have the velocity v_{01}, since $v_{02} < v_{\infty}$. The number of ion pairs formed per unit path length (line density) for a given meteoroid mass, density and velocity is given by [170]

$$\alpha = C \left(\frac{\mu_0}{\delta}\right)^{\frac{2}{3}} \rho v_0^4 \qquad (4.56)$$

where C is a constant depending on shape factor, ionization efficiency and heat properties of the meteor.

The atmospheric density where the maximum of the line density α_{m} occurs is given by $\rho(h^*) \sim \alpha_{\mathrm{m}}/v_0^{\frac{1}{3}}$. Using this relation, the maximum of meteor ion production for a given mass, density and velocity is found to be given by the condition [172]

$$\rho(h^*) \cdot H \cong C^{\frac{3}{2}} \mu_0^{\frac{1}{3}} \delta^{-\frac{1}{2}} v_0^{-2} \tag{4.57}$$

where H is the atmospheric scale height. This condition also defines the penetration depth of meteors (h^*).

Detailed calculations of meteor ionization rates for the terrestrial atmosphere with realistic distributions of meteor mass and velocity and an average meteor particle flux $\Phi(\mu_0 > 2 \times 10^{-4}\, g) = 10^{-4}\,\mathrm{km}^{-2}\,\mathrm{sec}^{-1}$ have been made [172]. The results of these calculations are illustrated in Figs. 4.4 and 4.5. Fig. 4.4 shows the ionization rates for given meteor velocities as a function of altitude; the meteor mass range contributing to the ionization according to the formulas for μ_{01} and μ_{02} is between 10^{-2} g and 3×10^{-13} g.

Figure 4.5 shows the total ionization rate from meteors, including that from micrometeorites, corresponding to a mass range from 10^{-13} g to 3×10^{-7} g and a velocity range from 15 km/sec to 70 km/sec. The height of the meteor ionization maximum, i.e., the penetration depth of meteors in other planetary atmospheres, can be scaled from the terrestrial results by virtue of the condition $(\rho_m H_m)_E = (\rho_m H_m)_P$. Thus, the penetration depth h^* for planet P is related to that for Earth h_E^* through the number density at the meteor ionization maximum and the ratios of the acceleration of gravity and atmospheric temperature at the appropriate level, according to

$$n(h_P^* = n(h_E^*) \left(\frac{g_P}{g_E}\right) \left(\frac{T_E}{T_P}\right)$$

or the pressures according to

$$p(h_P^*) = p(h_E^*) \left(\frac{g_P}{g_E}\right) .$$

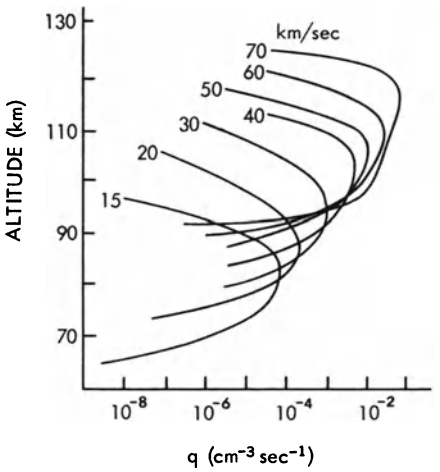

Fig. 4.4. Ionization rate in the terrestrial ionosphere due to meteors with different entry velocities (after V. N. Lebedivets [171]).

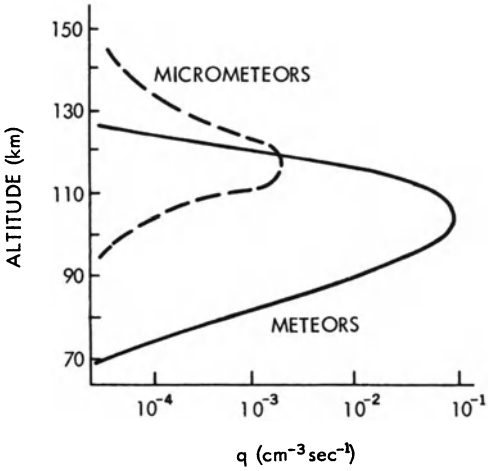

Fig. 4.5. Total ionization rate due to meteors and micrometeors in the terrestrial ionosphere (after V. N. Lebedivets [171]).

The approximate altitudes of maximum meteor ionization for the terrestrial planets, where the relatively small ionization rates ($q_m \cong 10^{-2}$ to $10^{-1}\,cm^{-3}\,sec^{-1}$) may contribute to the formation of an E-layer, are given in Table 4.12. The meteor flux due to cometary meteoroids and thus the corresponding meteor ionization rate in the vicinity of a planet P can be scaled according to $\Phi_P \propto D_P^{-1.5}$, where D_P is the planetary distance from the Sun in AU. In addition, the meteor flux near a planet is enhanced due to gravitational effects by a factor $G = 1 + v_\infty^2(P)/v_0^2$.

It can be demonstrated that an ionospheric layer in Titan's atmosphere composed of long-lived metal ions and due to the meteoric ablation should be formed at around 700 km [172]. The inclusion of metallic ions in ionospheric models of Titan changes the electron density predicted by models, which only consider the ionization by solar XUV radiation and electrons trapped in Saturn's magnetosphere.

The magnitude of the meteoric layer depends on the concentration of metals and the mean velocity of the interplanetary flux at Titan. Considering a

Table 4.12. Altitudes of meteor ionization maximum.

Planet	h^* [km]
Venus	~ 115
Earth	~ 105
Mars	~ 90
Titan	~ 650

typical composition of cometary meteoroids, an ionospheric layer should be formed by Si^+, Fe^+ and Mg^+. Taking into account the ionization rate due to micrometeoroids with an incoming velocity of 18 km s^{-1}, neglecting transport and a simple ionospheric model where ions are produced by direct meteoric ionization and lost by radiative recombination, the electron density peak is about 3000 cm^{-3} [172]. The addition of chemical reactions of association between metals and atmospheric neutrals in ion–neutral models do not produce a significant amount of metallic clusters, but decrease the electron concentration in Titan's atmosphere below 660 km. In this case the maximum of the electron density is about 1350 cm^{-3}.

V The Ionosphere as a Plasma

V.1 General Plasma Properties

A plasma represents a collection of charged particles (electrons and ions) which interact by long range (Coulomb) forces, exhibiting coherent behavior as the result of space charge effects [173].

The most fundamental length unit of a plasma is the Debye length λ_D which represents the distance beyond which the Coulomb field of an individual particle is no longer felt due to the shielding effect of a cloud of particles of opposite charge. For this reason λ_D is also called the Debye shielding distance. This means that in spite of long range Coulomb forces, charged particles in a plasma do not interact individually at distances greater than λ_D, so that for the plasma as a whole, effective Coulomb collision frequencies can be used. The Debye length is given by

$$\lambda_D = \left(\frac{k_B T}{4\pi e^2 N} \right)^{\frac{1}{2}} \tag{5.1}$$

and numerically by

$$\lambda_D = 6.9 \left(\frac{T}{N} \right)^{\frac{1}{2}} \qquad [\text{cm}]$$

where T is in K and N in cm^{-3}.

Because of space charge effects the electron and ion densities have to be averaged over dimensions much greater than λ_D so that quasi-neutrality ($N_e - \sum N_i \ll N_e$) can be assumed. The concept of a plasma also requires that the number of particles within a Debye sphere is

$$\hat{N}_D = \frac{4\pi}{3} N \lambda_D^3 \gg 1 \,. \tag{5.2}$$

The maintenance of electrons and ions in a plasma against recombination requires their kinetic energy to be greater than the potential energy. The distance where both are equal, the so-called critical distance or *critical impact parameter*, is given by

$$r_c = \frac{e^2}{k_B T} \tag{5.3}$$

while the plasma (electron) mean free path for Rutherford scattering (90° deflections) is given by

$$\lambda_e = (4\pi r_c^2 N)^{-1} \cong 4 \times 10^4 \frac{T_e^2}{N} \qquad [\mathrm{cm}]\,. \tag{5.4}$$

The Debye length can then also be expressed by

$$\lambda_D^2 = \lambda_e r_c\,. \tag{5.4a}$$

Generally, for a plasma the condition holds that

$$r_c \ll N^{-\frac{1}{3}} \ll \lambda_D \ll \lambda_e\,.$$

Another important (dimensionless) parameter is the Coulomb parameter

$$\Lambda = \frac{\lambda_D}{r_c} = \frac{\lambda_e}{\lambda_D} = 3\hat{N}_D \tag{5.5}$$

which measures the degree to which plasma phenomena dominate over individual particle phenomena. This quantity often appears as $\ln \Lambda$, the Coulomb logarithm.

A planetary ionosphere represents a relatively weakly ionized plasma, i.e., where the ratio of the electron–ion collision frequency to electron–neutral collision frequency in some regions is of the order of unity. Plasma transport coefficients applicable to the ionospheric plasma have been discussed in appropriate sections of this book.

Another fundamental characteristic of a plasma is the plasma frequency (f_N), which represents the characteristic eigenfrequency for electrostatic disturbances in the plasma. The angular plasma frequency is given by

$$2\pi f_N \equiv \omega_N = \frac{v_l}{\lambda_D} = \left(\frac{4\pi e^2 N}{m}\right)^{\frac{1}{2}} \tag{5.6}$$

where $v_l = (k_B T/m)^{\frac{1}{2}}$ is the (longitudinal) thermal velocity. Generally, the plasma frequency is defined in terms of the electron component, for which the numerical value is given by

$$f_N \cong (81\,N)^{\frac{1}{2}}$$

where f_N is in kHz and N in cm^{-3}.

The role of the Coulomb parameter in determining the relative importance of collective (plasma) phenomena versus individual particle processes can be seen from the ratio

Table 5.1. Plasma parameters for planetary ionospheres.

λ_e	10^2 m to 10^3 km
λ_D	1 mm to 10 cm
Λ	10^5 to 10^7
$\ln \Lambda$	12 to 16
f_N	100 kHz to 10 MHz

$$\frac{\nu_{ei}}{\omega_N} \propto \frac{\ln \Lambda}{\Lambda} ,$$

i.e., when the Coulomb parameter is large, plasma phenomena dominate. Typical values of the fundamental plasma parameters for planetary ionospheres are listed in Table 5.1. For many problems the ionospheric plasma can be treated as a single fluid, since electrons and ions are closely coupled with macroscopic properties derived from averages over the particle population. For a partially ionized plasma such as is the case for certain parts of an ionosphere, the neutral gas can be considered a separate component coupled to the plasma by appropriate collision and energy transfer processes.

If the effects of interactions between individual particles and waves in a plasma need to be considered, then a plasma kinetic approach has to be adopted. The description of the plasma components is then by means of the collisionless Boltzmann or Vlasov equation which represents an expansion in Λ^{-1} of the Liouville equation for a plasma, whereas the next higher order expansion which includes collision effects is given by the Fokker–Planck equation.

V.2 Equilibrium Models

The distribution of charged particles (electrons and ions) in a planetary ionosphere is governed by the equation of continuity

$$\frac{\partial N}{\partial t} = q - L(N) - \nabla \cdot (N\mathbf{v}) . \tag{5.7}$$

A steady state situation ($\partial N/\partial t = 0$) can often be assumed, except near sunrise and sunset or during other rapidly varying situations such as a solar eclipse. There are two limiting cases to the continuity equation:

1) *Chemical equilibrium* ($q = L$), when chemical processes are predominant; and
2) *Diffusive equilibrium* ($\nabla \cdot (N\mathbf{v}) = O$) when chemical processes can be neglected.

The applicability of either of these equilibrium models is determined by the appropriate time constants, i.e., the diffusion time $\tau_D \cong H_D^2/D_a$ and

the chemical life time $\tau_C = N/L$. The smaller of the two time constants determines the appropriate equilibrium model as an approximation to the full continuity equation.

Thus, if $\tau_C \ll \tau_D$, chemical equilibrium prevails. The classical example of a chemical (photochemical) equilibrium model for a planetary ionosphere is the Chapman layer, which corresponds to

$$q = \alpha N^2$$

with q represented by the photoionization production function (1.10) and the chemical loss rate due to a recombination process.

The Chapman model distribution of plasma density is given by

$$N = N_m \exp\left\{\frac{1}{2}\left[1 - \frac{z}{H} - \sec\chi \exp\left(-\frac{z}{H}\right)\right]\right\}$$

where

$$N_m = \left(\frac{q_m}{\alpha}\right)^{\frac{1}{2}} = \left(\frac{\eta_i \Phi_\infty \cos\chi}{eH\alpha}\right)^{\frac{1}{2}} . \tag{5.8}$$

The most important property of a Chapman layer is that the maximum of electron (ion) density is identical to the height of the ion production rate maximum which is determined by the condition requiring that the optical depth is $\tau(z) = \sigma_a n(z) H \sec\chi = 1$, occurring at an altitude

$$h_m(\chi) \equiv h^*(\chi) = h_0^* + H \ln\sec\chi .$$

A Chapman layer will therefore be appropriate for a situation where $\tau = 1$ is satisfied at low enough altitudes, so that diffusion and chemical processes other than recombination are negligible, i.e., when the ionizable constituent corresponds to a molecular species (e.g., the terrestrial E-layer). If on the other hand the ionizable constituent is an atomic species, and neutral molecular species are also present, then chemical loss processes involving molecular species (e.g., charge exchange reactions of the type $X^+ + YZ \rightarrow XY^+ + Z$) will be much faster than radiative recombination in removing the atomic ions, although the final charge neutralization may occur as dissociative recombination of the secondary molecular ions. In this case the chemical equilibrium is given by

$$q = \beta(z) N \tag{5.9}$$

which represents a height-dependent linear loss process, with the loss coefficient $\beta(z) = kn(YZ)$, leading to

$$N = \frac{q}{kn(YZ)} , \tag{5.10}$$

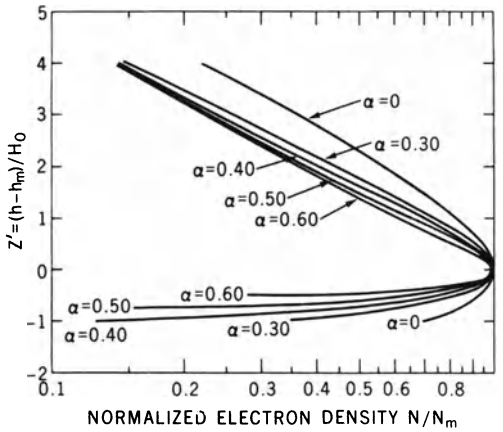

Fig. 5.1. Simple Chapman layer model (H =const.) and modified Chapman layer (exponentially varying scale height). The parameter $a = (H - H_0)/H$ represents the degree of departure from the ideal Chapman layer (after S. Chandra [175]).

i.e., N increases well beyond the level of maximum ion production, since $kn(YZ)$ decreases with altitude. At some altitude the further increase of N will be limited by diffusion, i.e., when $\tau_D \lesssim \tau_C$. A chemical equilibrium layer exhibiting this feature is often referred to as a Bradbury layer [174]. (The terrestrial F_2 region below the F_2 peak is an example of such a distribution; this is illustrated in Fig. 5.1.) From the solution of the steady state continuity equation it can be shown that the maximum of the plasma density distribution will occur where $\tau_D \cong \tau_C$ while its value is given by the chemical equilibrium formula [174]

$$N_m \cong \frac{q(h_m)}{\beta(h_m)} \cong \frac{q(h_m)}{kn(YZ|h_m)} . \tag{5.11}$$

Although the shape of the layer is controlled by chemical processes and diffusion, it can be expressed empirically by a Chapman-like distribution of the type [175]

$$N = N_m \exp\left[\frac{1}{2}\left\{1 - \frac{\frac{z}{H}}{1 - a\exp\left(\frac{az}{H}\right)} - \exp\left[\frac{-\frac{z}{H}}{1 - a\exp\left(-\frac{az}{2H}\right)}\right]\right\}\right] \tag{5.12}$$

where the parameter $a = (H - H_0)/H$ represents the departure from a simple Chapman layer resulting from a variable scale height. At altitudes well above the ionization peak N_m, it reduces to $N \propto \exp[-z/2H]$ which (fortuitously) corresponds to a diffusive equilibrium distribution for $T_e = T_i = T_n$, i.e., $\mathfrak{H} = 2H$. A Chapman layer and modified Chapman layers are illustrated in Fig. 5.1.

V.3 Realistic Models of Planetary Ionospheres

While equilibrium solutions of the continuity equation may provide a first order description for a particular region of a planetary ionosphere, they represent only approximations to the real situation.

The behavior of the ionospheric plasma is governed by the equations of continuity, momentum and heat transport. Since the ionosphere arises from the interaction of ionizing radiations with the neutral atmosphere, the appropriate equations of the electron, ion and neutral gases are coupled. Any change in the energy input not only affects the thermal structure, but also the composition and ionization of the atmosphere.

For realistic conditions, it is therefore necessary to solve simultaneously the equations of continuity

$$\frac{\partial N_j}{\partial t} = q_j - L_j - \nabla \cdot (N_j \mathbf{v}_j)\,, \tag{5.13}$$

the momentum equations

$$\begin{aligned} m_j N_j \left(\frac{\partial \mathbf{v}_j}{\partial t} + \mathbf{v}_j \cdot \nabla \boldsymbol{v}_j \right) = \; & \nabla p_j + m_j N_j \mathbf{g} - e N_j \left(\mathbf{E} + \frac{1}{c} [\mathbf{v}_j \times \mathbf{B}] \right) \\ & - \sum_k K_{ik} (\mathbf{v}_j - \mathbf{v}_k) \end{aligned} \tag{5.14}$$

and the equations of heat transport

$$\rho_j c_\mathrm{v} \frac{\partial T_j}{\partial t} - \nabla \cdot [K(T) \nabla T_j] = Q_j - L_j \tag{5.15}$$

for the charged and neutral species. The above equations have the general form

$$\frac{\partial \Psi_j}{\partial t} = A_j \left(z, t, \Psi_j, \frac{\partial \Psi_j}{\partial t}, \Psi_k \right) \frac{\partial^2 \Psi}{\partial z^2} + B_j (z, t, \Psi_j, \Psi_k) \frac{\partial \Psi_j}{\partial z} + C_j (z, t, \Psi_j, \Psi_k)\,. \tag{5.16}$$

The appropriate boundary conditions are expressed by

$$\begin{aligned} \Psi_j (z_\mathrm{l}, t) &= f_j (t) \\ \left. \frac{\partial \Psi_j}{\partial z} \right|_{z_\mathrm{u}, t} &= \phi_j (t) \end{aligned}$$

where z_l is the lower and z_u is the upper boundary level. Since no theoretical methods are available for an analytical solution of such a set of nonlinear differential equations, one has to resort to linearizing procedures. High speed computers are particularly suited for an approach involving partial linearization together with iterative steps. Such an approach has been employed in the

solution of the steady state and time-dependent continuity equations [176] for the terrestrial ionosphere, and for the ionosphere, of Venus [111, 112] with the additional upper boundary condition of pressure balance between the solar wind and ionospheric plasma. Although the approach outlined above is time consuming, it provides for the self-consistent solution of both neutral atmosphere and ionosphere properties. In this fashion no ad hoc models for the neutral atmosphere need to be invoked which may not be consistent with all aspects of ionospheric behavior (e.g., the ionizable neutral constituent may also be responsible for heat loss of the neutral and ionized species and thus control the thermal structure as well).

The use of this approach is well justified when some of the important input parameters are known, from which secondary inputs such as the wind field or thermal structure can be incorporated in a consistent manner. In addition, semi-empirical ionospheric models [177] can be developed which fit boundary conditions given by observations.

V.4 Observable and Derived Parameters

From observations of the electron density distribution in a planetary ionosphere a number of physical characteristics can be inferred. If the ionization peak is at a relatively low altitude, for which the condition of unit optical depth for overhead Sun can be satisfied, $\tau = 1$, the maximum density is given by

$$N_{\mathrm{m}} = \left(\frac{\Phi_{\infty} \cos \chi}{\mathrm{e} H \alpha} \right)^{\frac{1}{2}} \tag{5.17}$$

which is independent of the concentration of the number density of the ionizable constituent, but depends on the scale height of this (neutral) constituent as well as the ionizing flux outside the atmosphere and the recombination coefficient. The scale height can be determined from the observed decrease of electron density above the peak, according to

$$\frac{d(\ln N)}{dz} = -\frac{1}{H_{\mathrm{N}}} \tag{5.18}$$

where $H_{\mathrm{N}} = 2H$. With this information the consistency of a Chapman layer assumption can be checked.

The number density of the ionizable constituent at the altitude of the ionization peak h_{m} can be determined from the relation

$$n_{\mathrm{m}}(X) = \cos \chi (\sigma_{\mathrm{a}} H)^{-1}.$$

It should be noted that the observed scale height of a Chapman layer allows the determination of the neutral gas temperature only; it does not provide

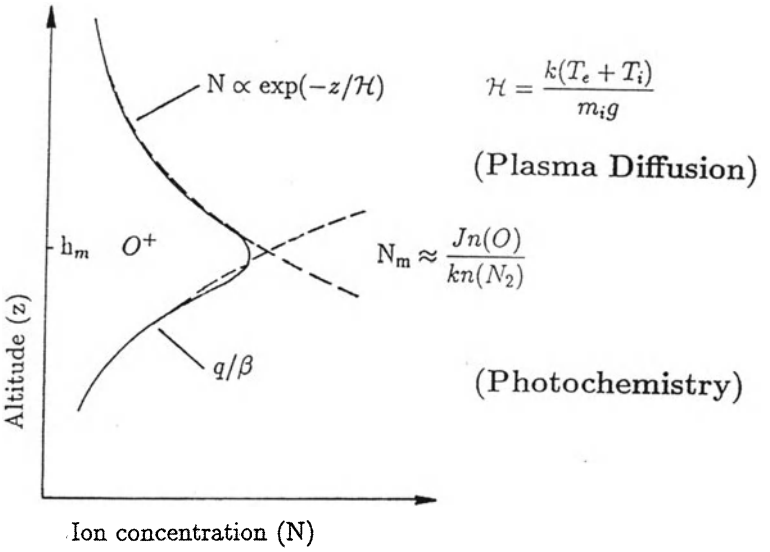

Fig. 5.2. F_2-layer formation theory.

any information regarding the temperature of the electrons and ions or the inference on the absence of thermal equilibrium.

For an F_2-layer (earlier called a Bradbury layer), the concentration of the ionizable atomic constituent (X) as well as the molecular species (YZ) responsible for the chemical loss process can be inferred from a knowledge of N_m. The ionization maximum occurs at an altitude $h(N_m) > h(q_m)$ where $\tau_C \cong \tau_D$ (Fig. 5.2),

$$h_m \cong H_{eff} \ln \left(\frac{D_0}{H^2_{(X)} \cdot kn_0(YZ)} \right) + h_0 \tag{5.19}$$

where $H_{eff} = k_B T/[m(X) + m(YZ)]g$ and h_0 is the reference level. In the presence of a plasma drift or wind vertical component velocity w, the height of the maximum will be changed by

$$\Delta h_m \simeq \frac{w}{H^2} D_a(h_m) \simeq \frac{w}{\beta(h_m)} .$$

The height of the maximum h_m corresponds to the low-attenuation region, and $N_m = q_m/kn(YZ)_m$ can therefore be expressed by

$$N_m = \frac{J_X n(X)_m}{kn(YZ)_m} \tag{5.20}$$

where $J_X = \langle \sigma_i \Phi_\infty \rangle$ is the ionization coefficient for species X and knYZ can be considered a height dependent linear chemical loss coefficient $\beta(z)$. From the condition $\tau_C = \tau_D$, we obtain

$$\frac{\mathfrak{B}}{n(X)H^2} = kn(YZ) \tag{5.21}$$

if it is assumed that ambipolar diffusion takes place through the ionizable constituent (X) and thus, $\mathfrak{B}/n(X) \equiv D_a$. It then follows that

$$n(YZ|h_m) = \frac{1}{kH}\left(\frac{\mathfrak{B}J_X}{N_m}\right)^{\frac{1}{2}}$$

and

$$n(X|h_m) = \frac{1}{H}\left(\frac{\mathfrak{B}}{J_X}N_m\right)^{\frac{1}{2}}. \tag{5.22}$$

The scale height can be derived from the decay of the electron density well above the peak

$$-\left(\frac{1}{N}\frac{\partial N}{\partial z}\right)^{-1} \equiv H_N = \frac{k_B(T_e + T_i)}{m_+ g},$$

assuming that the plasma temperature is constant. If this is not the case, the observed density scale height is modified by temperature gradients. It should be emphasized that the scale height of a diffusive equilibrium distribution is determined by the charged particle temperatures T_e and T_i and the mean ionic mass m_+, in contrast to that of a chemical equilibrium distribution, which depends on the temperature of the ionizable constituent, i.e., T_n. At altitudes well above the ionization peak, N_m, the plasma density distribution is generally well represented by a diffusive equilibrium distribution

$$N = N_0 \exp - \int_0^z \frac{dz}{H} \equiv N_0 \exp - \int_0^z \frac{m_+ g}{k_B(T_e + T_i)}\, dz\,. \tag{5.23}$$

If more than one ionic constituent is present, then the electron density distribution can be expressed by

$$N = N_0 \left[\frac{\sum_j N_{j0} \exp\left(-\frac{z}{H_j}\right)}{\sum_j N_{j0}}\right]^{1+\varepsilon}$$

where $H_j = k_B T_i/m_j g$ and $\varepsilon = (T_e/T_i)$. For a ternary ion mixture, and $T_e = T_i$, the plasma density distribution in diffusive equilibrium is given by

$$N = N_0\left\{\exp\frac{1}{2}\left[-\left(\frac{z}{H_1}\right) - \ln\left(1 + \eta_{21}\exp\left(\frac{z}{H_{12}}\right) + \eta_{31}\exp\left(\frac{z}{H_{13}}\right)\right)\right.\right.$$
$$\left.\left. + \ln(1 + \eta_{21} + \eta_{31})\right]\right\} \tag{5.24}$$

where $H_{ij} = k_B T/(m_i - m_j)g$ and η_{ij} is the ratio N_{i0}/N_{j0} at the reference level where the plasma density is N_0.

Another parameter of an ionospheric layer which may be observable is the total or integrated content. For a simple Chapman layer one obtains upon integration in terms of the error function [178]

$$N_T = \int_0^\infty N_m \exp \frac{1}{2}\left(1 - \frac{z}{H} - e^{-z/H}\right) dz = N_m \cdot H\sqrt{2\pi e} = 4.13 N_m \cdot H\,. \tag{5.25}$$

For a quasi-Chapman function, the total content will be less than for the simple *Chapman function*, i.e., roughly reduced by the factor $(1 - a)$. The ratio of the electron content above the ionization peak to that below for a Chapman layer is given by

$$\frac{N_a}{N_b} = \frac{\mathrm{erf}(\frac{1}{2}\sqrt{2})}{1 - \mathrm{erf}(\frac{1}{2}\sqrt{2})} = 2.15\,. \tag{5.26}$$

For a modified Chapman layer with a constant scale height gradient $dH/dz = \beta = \text{const}$.

$$N = N_m \left(\frac{1+\beta}{2}\right)[1 - \zeta - e^{-\zeta}] \tag{5.27}$$

this ratio is greater than 2.15 and can be expressed in terms of the incomplete (Γ_k) and complete (Γ_∞) Gamma functions ($\Gamma_\infty(p+1) = \int_0^\infty x^p e^{-x}\, dx$ and $\Gamma_k(p+1) = \int_0^k x^p e^{-x}\, dx$), according to

$$\frac{N_a}{N_b} = \frac{\Gamma_{\frac{1+\beta}{2}}[\frac{1}{2}(1-\beta)]}{\Gamma_\infty[\frac{1}{2}(1-\beta)] - \Gamma_{\frac{1+\beta}{2}}[\frac{1}{2}(1-\beta)]}\,. \tag{5.28}$$

V.5 Ionospheric Regions

In analogy with the terrestrial ionosphere the following ionospheric regions may be identified (although not all of them may be present) in a planetary ionosphere in order of increasing altitude of their peak (Fig. 5.3).

D layer: This region represents the lowermost part of a planetary ionosphere where the ionization sources are galactic and solar cosmic rays, meteors and the most penetrating EUV lines, such as Lyman-α. The unit optical depth condition for this region requires a column content of the absorbing constituent of $\mathfrak{N} \gtrsim 10^2\,\mathrm{cm}^{-2}$. A Chapman layer model is generally applicable, with molecular ions as principal constituent and dissociative recombination and three-body reactions being important chemical processes. Because of the

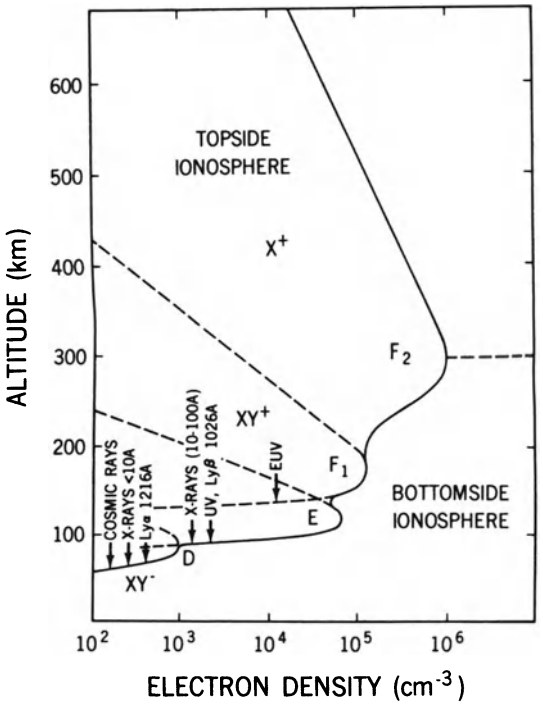

Fig. 5.3. Definition of regions in a planetary ionosphere in analogy to the terrestrial ionosphere. The principal ionization sources are also indicated.

relatively high number densities, ion clusters and negative ions resulting from electron attachment are present in this region.

E region: The ionization sources for this region are solar XUV radiation, low energy ($\sim$ keV) energetic particles and to a lesser extent meteors. Unit optical depth for this region requires a total content of the absorbing constituent of $\mathfrak{N} \simeq 10^{19}\,\mathrm{cm}^{-2}$. A Chapman layer model is applicable; molecular ions produced by the ionizing radiations are being lost by dissociative recombination. Because of the short chemical time constant, plasma transport processes are essentially negligible.

F_1 region: The ionization source for this region is the least penetrating XUV radiation. Unit optical depth requires a total content of the absorbing constituent of $\mathfrak{N} \simeq 10^{17}\,\mathrm{cm}^{-2}$. The F_1 region has an ion production peak; however, on Earth it is usually not noticeable as a distinct layer but only as a ledge in the plasma density distribution. Because of the presence of molecular ions, the chemistry is controlled by dissociative recombination. The F_1 region also conforms to a Chapman layer.

F_2 region: This region consists of atomic ions whose production maximum is in the F_1 region [178]. The electron density increases beyond the ion produc-

tion peak due to the presence of atomic ions which are lost by charge transfer processes with molecular neutral species, according to a linear loss law, and is therefore also called a Bradbury layer. The electron density peak (on Earth the F_2 peak represents the absolute maximum) occurs at an altitude where the chemical and diffusion time constants are approximately equal, i.e., where $\beta \cong D_a/H_D^2$. This condition requires a neutral density at that level of $n(h_m) \approx \tau_C \cdot 10^{19}/H_D^2$, corresponding to values $10^7 \lesssim n(h_m) \lesssim 10^{10}\,\mathrm{cm}^{-3}$. The F_2 region is controlled by chemical processes (charge transfer) and plasma transport processes. In the topside ionosphere, i.e., above the F_2 peak, plasma diffusion is the dominant process controlling the electron density distribution. The terrestrial topside ionosphere where H^+ is the predominant constituent is sometimes called the *protonosphere*.

The principal ionospheric layer on Venus and Mars can be considered as a Chapman-type F_1-layer. In both cases the principal ion is O_2^+ resulting from charge exchange reactions between the originally formed CO_2^+ (since CO_2 is the ionizable neutral constituent) and O originating from photodissociation of CO_2 (cf. Chap. IV). Although at higher altitude O^+ becomes an important ion it does not produce an F_2 layer, which seems to be an apparent terrestrial "anomaly". In spite of the long Venus night ($\sim$ 58 days) there is still nighttime ionization present, resulting from plasma transport from the dayside (cf. Sect. VI.6) as well as electron impact ionization.

All outer planets have extensive (Chapman-like) ionospheres whose ionization source appears to be solar XUV as well as impact ionization by magnetospheric particles. Since these atmospheres consist primarily of H_2, the principal ion species are likely to be H^+ and H_3^+ as well as H_2^+ and He^+. On Jupiter and Saturn ionospheric "sporadic" E-layers are also observed, which may be linked to ionospheric–magnetospheric coupling. The ionosphere of Jupiter's satellite Io consists most likely of S^+, O^+ and Na^+ while on Neptune's satellite Triton, N_2^+ and N^+ seems to be predominant.

For Saturn's large satellite Titan possessing an extensive N_2 atmosphere, the ionospheric species because of the presence of CH_4 and other hydrocarbons consist of nitrile ions such as H_2CN^+ and hydrocarbon ions like $C_nH_m^+$ as the result of ion–molecule reactions (cf. Chap. IV).

Ion exosphere: This term refers to a region where the plasma mean free path is of the order of the plasma scale height, allowing ions with sufficient kinetic energy to escape from the planetary force field when magnetic flux tubes are open or no magnetic field is present (cf. Chap. VI). The base of an ion exosphere can be defined by the condition $N_c \lesssim 10^{-4}(m_i/m_H)gT_e\ \mathrm{cm}^{-3}$. An ion exosphere may or may not be linked to a planetary ionosphere, i.e., ion-exospheric conditions may apply at a planetary surface.

Planetary bodies having an ion exosphere without an ionosphere are the Moon and Mercury. Under these circumstances no ionospheric layer can be formed. The ionization of exospheric species leads to electron-ion pair formation which is balanced by chemical loss and transport processes [94]. Since

radiative recombination is an extremely slow loss process for atomic ions, plasma diffusion under gravity, which has a short time constant, controls the ionized species. Thus, the densities of the ionized exospheric component do not exceed a few electrons/ions cm^{-3}. This yields an extremely low height-integrated Pedersen conductivity (cf. Sect. V.8), which must be taken into account in the understanding of convection processes in the magnetosphere.

V.6 The Ionosphere as a Dispersive Medium

A plasma such as a planetary ionosphere has dielectric properties, which permit the propagation of electromagnetic (transverse) and the existence of electrostatic (longitudinal) waves.

Electromagnetic Waves

For the propagation of electromagnetic waves the ionosphere behaves as a dispersive anisotropic medium, i.e. the refractive index depends not only on the number density of the mobile free electrons N_e, (plasma frequency f_N) but also on the frequency of the wave propagating ion in the medium, the anisotropy being the result of a magnetic field B constraining the motion of the electrons (gyrofrequency f_B).

The ionospheric refractive index $\mu(N_e, B, F)$ or expressed in terms of the characteristic frequencies $f_N \sim (N_e)^{1/2}$ and electron gyrofrequency $f_B \sim B/m_e$ is expressed according to the so-called magneto–ionic theory by the Appleton–Hartree formula in terms of the magneto–ionic parameters

$$X = \left(\frac{f_N}{f}\right)^2$$

and

$$Y = f_B/f$$

as

$$\mu^2 \simeq 1 - \frac{X}{1 \pm Y}\,. \tag{5.29}$$

The greatest deviation of μ from 1 (the free space value) occurs for frequencies where X and Y are large. Because characteristic frequencies, f_N and f_B are in the MHz range the largest ionospheric effects will occur for meter wavelength radio waves. Since the signal propagation velocity in a dispersive medium is given by the so-called group velocity v_g

$$v_g = \mu c$$

the ionosphere will produce a retardation of radio waves since $\mu \lesssim 1$. This has to be considered when high precision ranging even at GHz frequencies is desired. Planetary occultation of radio sources, therefore, allows a distinction between the neutral atmosphere $\mu \gtrsim 1$ and the ionosphere $\mu \lesssim 1$ to be made.

Non-thermal emission of radio waves can occur in the magnetoplasma of an ionosphere as the result of deviation from a Maxwellian due to the asymmetry of energetic electrons moving up and down magnetic field lines, primarily in the auroral zone. This emission is close to the electron gyrofrequency and is thus a measure of the planetary magnetic field (cf. Sect. VI.1).

Hydromagnetic Waves

In addition to electromagnetic radio waves one of the class of transverse waves ($f < f_B$) can propagate in a dispersive magnetoplasma. They are called hydromagnetic waves with a characteristic Alfvén velocity

$$v_A = \frac{B}{4\pi\rho_p}, \tag{5.30}$$

with $\rho_p = N_i m_i + N_e m_e$ the mass density of the ionsopheric plasma. Together with longitudinal waves they make up the so-called magneto-acoustic waves. It has been suggested that the dissipation of hydromagnetic wave energy absorbed by the ionosphere may represent an additional source of heating of upper atmospheres [179]. Hydrodynamic power dissipation is most efficient at higher frequencies. The hydromagnetic heat source for a given frequency has a maximum at an altitude where

$$\omega_{hm}^2 \approx \nu_{in}\sigma_3 \left(\frac{v_{hm}}{c}\right)^2$$

with ν_{in} the ion–neutral collision frequency, σ_3 the Cowling conductivity (cf. Sect. V.8) and the subscript *hm* referring to the particular hydrodynamic mode. Although for the terrestrial ionosphere, hydromagnetic heating is almost negligible compared to XUV this may not be the case for other planetary atmospheres.

V.7 Plasma (Ambipolar) Diffusion

Plasma transport can act as an apparent local source or sink in a planetary ionosphere. Transport processes occur as the result of pressure gradients and gravity (plasma diffusion), the action of an electric field (plasma drift) or as the result of frictional forces (plasma wind).

In a weakly ionized plasma, such as a planetary ionosphere, electrons and ions diffuse through the ambient atmosphere, similar to minor constituents in

the neutral atmosphere. However, since electrons, because of their higher mobility, diffuse faster than the ions, a polarization field is set up which prevents charge separation. As the result of this polarization field $\mathbf{E}$, the electrons and ions diffuse with the same velocity. This process is called *ambipolar diffusion* [43]. The plasma diffusion velocity $\mathbf{v}_D = \mathbf{v}_e = \mathbf{v}_i$ can be derived (for the steady state) from the equations of motion for the electrons and ions considering the effects of their partial pressure gradients ∇p and the effect of gravity, $\mathbf{g}$, according to

$$\begin{aligned} \nabla p_e &= -\rho_e \mathbf{g} - q_e \mathbf{E} - \rho_e \nu_{en}(\mathbf{v}_e - \mathbf{v}_n) \\ \nabla p_i &= -\rho_i \mathbf{g} - q_i \mathbf{E} - \rho_i \nu_{in}(\mathbf{v}_i - \mathbf{v}_n) \end{aligned} \tag{5.31}$$

with $p_j = N_j k_B T_j$, $\rho_j = N_j m_j$ and $q_j = |e| N_j$. Assuming the neutral atmosphere at rest, $\boldsymbol{v}_n = 0$, and taking into account $m_i \gg m_e$ and $m_i \nu_{in} \gg m_e \nu_{en}$, i.e., ion–neutral collisions to be more important than electron–neutral collisions, we obtain for the plasma (ambipolar) diffusion velocity

$$\boldsymbol{v}_D = -D_a \left[\frac{\nabla p_N}{p_N} + \frac{1}{\mathfrak{H}} \right] \tag{5.32}$$

with the plasma pressure $p_N = N k_B (T_e + T_i)$ and the plasma scale height

$$\mathfrak{H} = \frac{k_B (T_e + T_i)}{m_i g} \tag{5.33}$$

and the ambipolar diffusion coefficient

$$D_a = \frac{k_B (T_e + T_i)}{m_i \nu_{in}} \tag{5.34}$$

(For $T_e = T_i$, $D_a = 2D_i$; i.e., twice the ion diffusion coefficient.) The ion–neutral collision frequency can be expressed for $T < 2000\,°\mathrm{K}$ by

$$\nu_{in} \cong 2\pi \left(\frac{\alpha e^2}{\mu_{in}} \right)^{\frac{1}{2}} n$$

where α is the polarizability, e is the ionic charge, $\mu_{in} = m_i m_n / (m_i + m_n)$ is the reduced mass and n is the number density of the neutrals.

For diffusion of ions in their parent gas (X^+ in X), the ion–neutral collision frequency is modified due to resonance charge transfer [142] introducing a dependence on the neutral and ion temperature

$$\nu_{in} \propto (T_i + T_n)^m$$

where $0.3 \lesssim m \lesssim 0.4$ for most atmospheric constituents, so that

$$D_a(X^+, X) \propto (T_e + T_i)(T_i + T_n)^{-m}\,. \tag{5.35}$$

Typical ambipolar diffusion coefficients at $T_e = T_i = T_n = 1000$ K for ions in their parent gas are listed below:

$$D_a(O^+, O) \approx \frac{10^{19}}{m(O)} \qquad [\mathrm{cm^2\,sec^{-1}}]$$

$$D_a(H^+, H) \approx \frac{2.5 \times 10^{19}}{n(H)} \qquad [\mathrm{cm^2\,sec^{-1}}]\,.$$

Since the ambipolar diffusion coefficient D_a is inversely proportional to the density of the (neutral) constituent through which the electron–ion gas diffuses, it can also be expressed by

$$D_a = D_0 \exp\left(\frac{z}{H_D}\right) \tag{5.36}$$

where $H_D = k_B T_j / m_j g$ is the scale height of the constituent through which ambipolar diffusion takes place.

For the case of an isothermal atmosphere ($\mathfrak{H} = \text{const}$), the diffusion velocity has the form

$$v_D = -D_a \left[\frac{1}{N}\frac{\partial N}{\partial z} + \frac{1}{\mathfrak{H}}\right]. \tag{5.37}$$

When a planetary magnetic field is present, plasma diffusion is constrained along **B**. The diffusion velocity in the vertical (z) direction is then given by

$$v_z = v_D \sin^2 I \tag{5.38}$$

where I is the inclination (dip) of the magnetic field $\boldsymbol{B}$ (with respect to the surface). The reason for the $\sin^2 I$ factor is as follows: ambipolar diffusion under gravity in the presence of an inclined magnetic field leads to a diffusion velocity along B, $v_\parallel = v_D \sin I$; the z-component is $v_z = v_\parallel \sin I$; thus $v_z = v_D \sin^2 I$ [180, 181].

The diffusion velocity enters into the ionospheric continuity equation in the form of the divergence of a flux, $\boldsymbol{\nabla} \cdot (N \boldsymbol{v}_D)$. For the simple case of an isothermal atmosphere $H = \text{const}$. $T_e = T_i = T_n$ and $m_i = m_n$, representing diffusion of an ion through its parent gas, $\mathfrak{H} = 2H$, we obtain

$$\boldsymbol{\nabla} \cdot (N \boldsymbol{v}_D) \simeq \frac{\partial}{\partial z}(N v_D) = D_a \left\{\frac{\partial^2 N}{\partial z^2} + \frac{3}{2}\frac{\partial N}{\partial z} + \frac{N}{2H^2}\right\}. \tag{5.39}$$

The term *effective plasma temperature* is sometimes employed according to $T_p' = (T_e + T_i)/2 \cong (T_e + T_n)/2$. The condition for diffusive equilibrium [182] can be expressed by

$$\boldsymbol{\nabla} \cdot (N \boldsymbol{v}_D) \simeq \frac{\partial (N v_D)}{\partial z} = 0\,. \tag{5.40}$$

Equation (5.40) can be satisfied uniquely by two solutions:

$$\begin{aligned} &\text{(a) } Nv_{\mathrm{D}} = \text{const}, \\ &\text{(b) } v_{\mathrm{D}} = 0\,. \end{aligned} \tag{5.41}$$

Of these solutions (a) is not a true equilibrium condition since it corresponds to a constant flux $F = Nv$ leading to an outflow of ionization to a sink at infinity. This solution, however, could be considered as a dynamic equilibrium. Solution (b) represents a true (static) equilibrium, i.e., the solution where the plasma has reached a stable distribution as the result of ambipolar diffusion. The time constant for reaching diffusive equilibrium is given by

$$\tau_{\mathrm{D}} \simeq \frac{H_{\mathrm{D}}^2}{D_{\mathrm{a}}} \tag{5.42}$$

which can be obtained from the solution of

$$\frac{\partial N}{\partial t} = -\boldsymbol{\nabla} \cdot (N \boldsymbol{v}_{\mathrm{D}})$$

for the condition of maximum flux (see below) and $\mathfrak{H} > H_{\mathrm{D}}$, noting that

$$\tau \equiv \left(\frac{1}{N} \frac{\partial N}{\partial t} \right)^{-1} .$$

The general solution of (5.40) is given by

$$N = A\mathrm{e}^{-z/\mathfrak{H}} + B\mathrm{e}^{-z/H_{\mathrm{D}}} \tag{5.43}$$

where the appropriate boundary conditions

$$N = O \text{ at } z \to \infty \text{ and } N = N_0 \text{ at } z \to 0$$

lead to

$$\begin{aligned} F = Nv_{\mathrm{D}} &= \frac{D_0 B(\mathfrak{H} - H_{\mathrm{D}})}{H_{\mathrm{D}}\mathfrak{H}} \\ B &= N_0 - A \\ A &= N_0 - \frac{F H_{\mathrm{D}} \mathfrak{H}}{(\mathfrak{H} - H_{\mathrm{D}}) D_0} \,. \end{aligned} \tag{5.44}$$

$B = 0$ $(A = N_0) \to F = 0$ represents the diffusive equilibrium solution b), whereas $A = 0$ represents the maximum upward flux for steady state conditions, i.e.,

$$F^* = \frac{D_0 N_0}{H_{\mathrm{D}}\mathfrak{H}} (\mathfrak{H} - H_{\mathrm{D}}) \,. \tag{5.45}$$

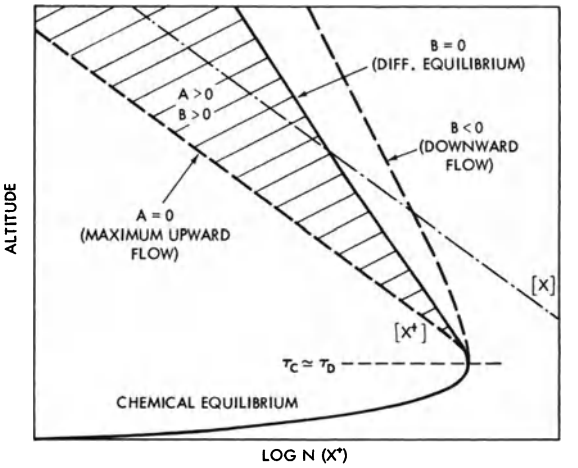

Fig. 5.4. Chemical equilibrium, diffusive equilibrium and the effects of flow (i.e., ambipolar diffusion through the neutral gas X) for a major ion X^+.

$B > 0$ represents an upward flux and $B < 0$ a downward flux of ionization. The solution for maximum upward flux ($A = 0$) corresponds to a plasma density distribution having a scale height H_D, representing a constituent through which the plasma diffuses, similar to the diffusion of minor neutral constituents (cf. Chap. II). This is illustrated in Fig. 5.4. The plasma density distribution in the presence of flow can also be written as

$$N = N_0 e^{-z/\mathfrak{H}} \left[1 - \frac{F H_D \mathfrak{H}}{N_0 D_0 (\mathfrak{H} - H_D)} \left(1 - e^{-\left(\frac{\mathfrak{H} - H_D}{\mathfrak{H} H_D}\right) z}\right)\right] \tag{5.46}$$

where the first term represents the diffusive equilibrium distribution [182] and the second term the modification due to a flux F. For the maximum flux $F^* = (D_0 N_0 / H_D \mathfrak{H}(\mathfrak{H} - H_D)$, the factor of the second term becomes unity, leading to a distribution $N = N_0 e^{-z/H_D}$. This is identical to the situation discussed for the diffusion of a minor neutral constituent.

The diffusive equilibrium distribution for electron and ions can also be derived directly from equations neglecting all terms containing velocities. If one considers more than one ionic species, one obtains

$$\frac{1}{p_N} \frac{\partial p_N}{\partial z'} = -\frac{m_+ g}{k_B (T_e + T_i)} \equiv -\frac{1}{\mathfrak{H}'} \tag{5.47}$$

where $m_+ = \sum \rho_i / N$ is the mean ionic mass and $p_N = k_B (T_e + T_i)$ is the plasma pressure, and z' is the reduced altitude $\left(z' = \int_0^z (g/g_0)\, dz\right)$ accounting for the height variation of the acceleration of gravity. However, plasma pressure is not a directly observable quantity, but plasma density and temperatures are generally measured.

The plasma density distribution can be defined in terms of a density scale height H'_N

$$\frac{1}{N}\frac{\partial N}{\partial z'} \equiv \frac{\partial(\ln N)}{\partial z'} = -\frac{1}{H'_N}$$

where

$$H'_N = \mathfrak{H}\left[1 + \mathfrak{H}\frac{\partial(T_e + T_i)/\partial z'}{T_e + T_i}\right]^{-1} \tag{5.48}$$

and $H_N \equiv \mathfrak{H}$ only when T_e, T_i = const.

In contrast to the behavior of neutral constituents in diffusive equilibrium, the diffusive equilibrium distribution of a particular ion X^+ in an ion mixture having a mean ionic mass m_+ is not independent of the other ions [183, 184]. This is due to the existence, in addition to gravity, of the polarization field $\mathbf{E}$ in a plasma which acts on all ions and which depends on the mean ionic mass and the charged particle temperatures. The distribution of an ion species X^+ in diffusive equilibrium ($v_e = v_i = 0$) can be derived together with the condition for charge neutrality $\sum N_i = N_e$ and the definition of mean ionic mass $m_+ = \sum \rho_i / N$, and is given by [185]

$$N_i(X^+) = N_{i0} \exp\left\{-\int_0^z \left[\left(m(X^+) - \frac{m_+ T_e}{T_e + T_i}\right)\frac{g}{k_B T_i} + \frac{\partial(T_e + T_i)/\partial z}{T_e + T_i}\right] \mathrm{d}z\right\}. \tag{5.49}$$

It can be shown that $\nabla \cdot \mathbf{E} \approx 0$, i.e., the charge excess due to the polarization field E is $(N_i - N_e)/N_e \simeq G m_i^2 / 2e^2 \simeq 4 \times 10^{-37}$ (for $T_e = T_i$ and $m_i = m_H$), where G is the universal gravitational constant and e is the electronic charge [186]. This result follows from $\nabla \cdot \mathbf{E} = -\phi_E \cong (m_i/2e)\Delta\phi_g$, where ϕ_E is the electric and ϕ_g the gravitational potential, satisfying the Poisson equation $\Delta\phi_E = -4\pi e \sum_j Z_j N_j$ and $\Delta\phi_g = 4\pi G \sum_j N_j m_j$. The electrostatic polarization field

$$eE = \frac{m_+ g T_e}{T_e + T_i} \tag{5.50}$$

counteracts the effect of gravity leading to an increase in the concentration of a light minor ion X^+ (neglecting temperature gradients) while in diffusive equilibrium, as long as

$$\hat{m}(X^+) < \frac{\hat{m}_+ T - e}{(T_e + T_i)}.$$

The effect of this polarization field is to give minor light ions a substantial effective upward acceleration, e.g., for H^+ in a CO_2 ionosphere this acceleration is $(\hat{m}(X^+) - \hat{m}_+/2)g \cong 21g$, assuming $T_e = T_i$. The distribution of minor ions H^+ and He^+ in an O^+ ionosphere is shown in Fig. 5.5.

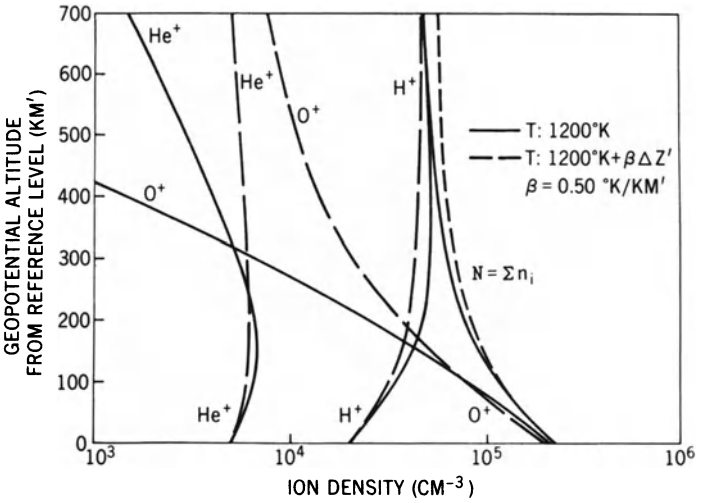

Fig. 5.5. Diffusive equilibrium distributions for minor ions H^+ and He^+ in an O^+ ionosphere for isothermal ($T_e = T_i = \text{const.}$) conditions and for a temperature gradient $dT_e/dz = dT_i/dz = \beta = \text{const.}$

While the altitude distribution of individual ions is also dependent on the electron temperature, as the result of the effect of the polarization field, the relative abundance (ratio) of ionic species in diffusive equilibrium depends on the ion temperature only, since the terms containing T_e cancel. Thus,

$$\frac{N_i(X^+)}{N_i(Y^+)} = \frac{N_0(X^+)}{N_0(Y^+)} \exp\left(\frac{z}{H_{XY}}\right) \tag{5.51}$$

where

$$H_{XY} = \frac{k_B T_i}{(m(X^+) - m(Y^+))g}.$$

Similarly to the case illustrated for the electron (major ion) density distribution, fluxes also modify the diffusive equilibrium distribution of a minor ion. E.g., a large upward flux will cause the distribution of the minor ion to follow approximately the scale height of the major ion through which it diffuses (see Fig. 5.6). The mutual diffusion coefficient for ions is given by [43]

$$D_{12} \approx \frac{10^8 T_i^{\frac{5}{2}}}{\sqrt{\mu_{in}} N_i} \qquad [\text{cm}^2\text{s}^{-1}]$$

When gradients in the charged particle temperature are present the process of thermal diffusion also becomes possible [187, 188, 189]. This effect can be expressed, for a minor ion N_j through the diffusion equation

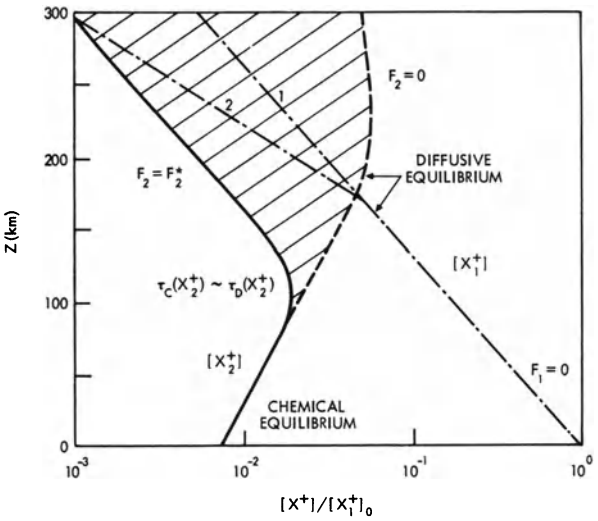

Fig. 5.6. Altitude distribution for a minor ion ($X_2^+ = H^+$) in chemical and diffusive equilibrium and under flow conditions in an ionosphere with a major ion ($X_1^+ = O^+$); the distribution of X_1^+ labelled 1 corresponds to $m_+ \approx m(X_1^+)$, while 2 corresponds to $m_+ \approx m(X_2^+)$.

Table 5.2.

$\frac{m_j}{m_+}$	α_j
16	2.4
4	1.7
0.25	−1.1
0.0625	−1.2

$$\frac{1}{N_j}\frac{\partial N_j}{\partial z} = -\frac{m_j g}{k_B T_i} - \frac{T_e}{T_i}\frac{1}{N}\frac{\partial N}{\partial z} - \frac{(1-\alpha_j)}{T_i}\frac{\partial T_i}{\partial z} - \frac{1}{T_i}\frac{\partial T_e}{\partial z} \tag{5.52}$$

where α_j is the thermal diffusion coefficient which depends on the ratio m_j/m_+ according to Table 5.2. Since the effective polarization field changes due to thermal diffusion according to

$$e\mathbf{E} = -\frac{k_B T_e}{N}\nabla N - (1+\alpha)k_B \nabla T_e \tag{5.53}$$

the altitude distribution of a minor ion is affected by thermal diffusion.

Changes in effective scale height of ions in the terrestrial ionosphere at 700 km for a temperature gradient $\partial T_i/\partial z = 4\,\mathrm{K}\,[\mathrm{km}^{-1}]$ and thermal diffusion are illustrated in Table 5.3 [187]. While thermal diffusion has important consequences for the distribution of minor ions, its effect is negligible for the major ion (electron) density distribution.

Table 5.3.

$\frac{10^8}{N}\frac{\partial N}{\partial z}$ cm^{-1} [at 700 km]			
	O^+	He^+	H^+
with thermal diffusion	−6.0	−0.99	+8.74
without thermal diffusion	−6.0	+2.1	+4.2

The above discussion has assumed that no planetary magnetic field is present. If, however, such a field is present, then the distributions apply along a dipole field line [190, 191]. Similarly, the equations are modified for multiply charged ions [184] since in the foregoing discussion we have tacitly assumed that all ions are singly charged.

V.8 Plasma Drift and Winds

In addition to diffusion resulting from the action of pressure gradients and gravity, electrodynamic forces and neutral winds affect the ionospheric plasma. The time constants controlling these motions are the collision times

$$\tau_{jn} = \frac{m_j}{\mu_{jn}\nu_{jn}} \tag{5.54}$$

where m_j is the mass of the ions, μ_{in} is the reduced mass of the collision partners, and the gyration time in the magnetic field

$$\tau_{Bj} = \Omega_{Bj}^{-1} \tag{5.55}$$

where $\Omega_{Bj} = eB/m_j c$ is the ion gyrofrequency. The equation of motion, ignoring the force terms due to gravity and pressure gradients, can be written

$$\frac{\partial \mathbf{v}}{\partial t} \simeq \frac{\mathbf{v}}{\tau} = \frac{e\mathbf{E}}{m_j} + \frac{1}{\tau_{Bj}}\frac{(\mathbf{v}\times\mathbf{B}}{c} + \frac{1}{\tau_{jn}}(\mathbf{v}_n - \mathbf{i})\,. \tag{5.56}$$

In general, the controlling time constants are τ_{Bj} and τ_{jn}. For $v_n \leq v_i$ and $\tau_{in} \gg \tau_{Bj}$ (5.56) reduces to

$$\mathbf{E} + \frac{1}{c}(\mathbf{v}_j \times \mathbf{B}) = 0\,. \tag{5.57}$$

According to (5.57), $\mathbf{v}_e = \mathbf{v}_i \equiv \mathbf{v}_E$ represents the electrodynamic drift velocity which is given by

$$\mathbf{v}_E = \frac{c(\mathbf{E}\times\mathbf{B})}{B^2}\,. \tag{5.58}$$

The electric field $\mathbf{E}$ represents a polarization field which forces $\mathbf{v}_\mathrm{E}$ to lie in an equipotential surface S defined by

$$\nabla S = -\mathbf{E} = \frac{1}{c}(\mathbf{v}_\mathrm{E} \times \mathbf{B}) .$$

The electrons and ions are "frozen in" with the magnetic flux tube.

In the regime where $\tau_\mathrm{in} \leq \tau_\mathrm{Bi}$, the ions are strongly coupled with neutrals, and the ion velocity is much less than that of the electrons, leading to an electric current, according to Ohm's law

$$\mathbf{j} = (\boldsymbol{\sigma}\mathbf{E}) . \tag{5.59}$$

Since the ionosphere in the presence of a magnetic field is highly anisotropic, the conductivity σ is expressed by a tensor.

The current flowing in an anisotropic medium can be expressed in terms of components parallel and perpendicular to the magnetic field

$$\begin{aligned} j_\parallel &= \sigma_0 E_\parallel \\ j_\perp &= \sigma_1 E_\perp + \sigma_2 \frac{c(\mathbf{B} \times \mathbf{E}_\perp)}{B^2} . \end{aligned} \tag{5.60}$$

The conductivities are defined in this case as follows: σ_0 is the longitudinal conductivity which corresponds to that parallel to $\mathbf{B}$ (called Birkeland conductivity) or that in the absence of a magnetic field; σ_1 is the Pedersen conductivity which is perpendicular to B and σ_2 is the Hall conductivity which is perpendicular to both the magnetic and the electric field. These conductivities are defined in terms of the appropriate collision and gyrofrequencies according to

$$\left.\begin{aligned} \sigma_0 &= e^2 \sum_{\mathrm{i,e}} \frac{N_j}{m_j \nu_{j\mathrm{n}}} \simeq \frac{N_\mathrm{e} e^2}{m_\mathrm{e} \nu_\mathrm{en}} \\ \sigma_1 &= e^2 \sum_{\mathrm{i,e}} \frac{N_j}{m_j \nu_{j\mathrm{n}}} \left(\frac{\nu_{j\mathrm{n}}^2}{\nu_{j\mathrm{n}}^2 + \omega_{\mathrm{B}j}^2} \right) \\ \sigma_2 &= e^2 \sum_{\mathrm{i,e}} \frac{N_j \omega_{\mathrm{B}j}}{m_j (\nu_{j\mathrm{n}}^2 + \omega_{Bj}^2)} . \end{aligned}\right\} \tag{5.61}$$

In the ionosphere, where the vertical scale is small compared to the horizontal scale, vertical currents are essentially zero. The horizontal current can be thought of as flowing in a thin layer with the x coordinate directed southward and the y coordinate eastward according to

$$\begin{pmatrix} j_\mathrm{x} \\ j_\mathrm{y} \end{pmatrix} = \begin{pmatrix} \sigma_\mathrm{xx} & \sigma_\mathrm{xy} \\ -\sigma_\mathrm{xy} & \sigma_\mathrm{yy} \end{pmatrix} \begin{pmatrix} E_\mathrm{x} \\ E_\mathrm{y} \end{pmatrix} . \tag{5.62}$$

For magnetic dip angles $I > 3°$

$$\begin{aligned} \sigma_{xx} &\simeq \frac{\sigma_1}{\sin^2 I} \\ \sigma_{yy} &\simeq \sigma_1 \\ \sigma_{xy} &\simeq \frac{\sigma_2}{\sin^2 I} \end{aligned} \tag{5.63}$$

and near the magnetic equator, i.e., for $I < 3°$

$$\begin{aligned} \sigma_{xx} &= \sigma_0 \\ \sigma_{yy} &= \sigma_1 + \frac{\sigma_2^2}{\sigma_1} \equiv \sigma_3 \\ \sigma_{xy} &= 0\,. \end{aligned} \tag{5.64}$$

At the magnetic equator, the Cowling conductivity σ_3 is large, leading to a large current, the so-called *equatorial electrojet*. The region where this current flows (e.g., the terrestrial E region) is also referred to as the "dynamo region", since the motion of the neutral gas by tidal and thermal forces which are coupled with the plasma lead to an induced current in the presence of a magnetic field, similar to a "dynamo". These dynamo currents are responsible for geomagnetic variations. Above the dynamo region, i.e., where $\tau_{Bi} \leq \tau_{in}$, the electrostatic polarization field generated by the dynamo currents which is communicated along magnetic field tubes can cause a plasma drift. (This region is sometimes referred to as "motor the region", although dynamo effects can also appear there. In the terrestrial ionosphere this corresponds to the F-layer.)

As the result of pressure gradients in the thermosphere, horizontal neutral winds are generated which can drive the ionization, provided $\tau_{Bi} \leq \tau_{in}$ [192]. In the presence of a magnetic field $\mathbf{B}$, the ionospheric plasma will move along magnetic field lines as the result of a neutral wind of velocity v_n, with a plasma (wind) velocity

$$v_{w\parallel} = \frac{(\mathbf{v}_n \cdot \mathbf{B})\mathbf{B}}{B^2} = v_n \cos I\,. \tag{5.65}$$

The component of the plasma motion in the z direction will therefore be

$$v_{wz} = v_n \cos I \sin I \tag{5.66}$$

which can be either upward or downward, depending on the direction of the neutral wind.

As the result of the interaction between the neutral wind and the plasma, the horizontal (x) neutral wind and plasma velocities differ by

$$v_n - v_{wx} = v_n \sin^2 I\,. \tag{5.67}$$

This effect is called *air drag*, causing a dependence of the neutral gas motions on the magnetic dip angle I.

The converse situation, where neutral air is accelerated by collisions between ions and neutral particles as the result of plasma drift due to an electric field, $(\mathbf{v}_i \equiv \mathbf{v}_E)$, can be described by

$$\frac{\partial \mathbf{v}_n}{\partial t} = \frac{1}{\tau_{ni}}(\mathbf{v}_i - \mathbf{v}_n) + \frac{\eta}{\rho}\frac{\partial^2 \mathbf{v}_n}{\partial z^2} . \tag{5.68}$$

The acceleration of air by the plasma motion (first term) which is called *ion drag* is important as long as $\tau_{ni} = (n/N_i)\tau_{in}$ is small enough so that the motion is not hindered by viscosity (η) effects, represented by the second term.

In the steady state, ion drag causes the neutral gas to move (horizontally) with a speed $v_n = v_i \csc I$, while the ions are dragged along field lines with a speed $v_i \cot I$ due to prevailing neutral winds.

The geometry of drift and wind effects is shown in Fig. 5.7.

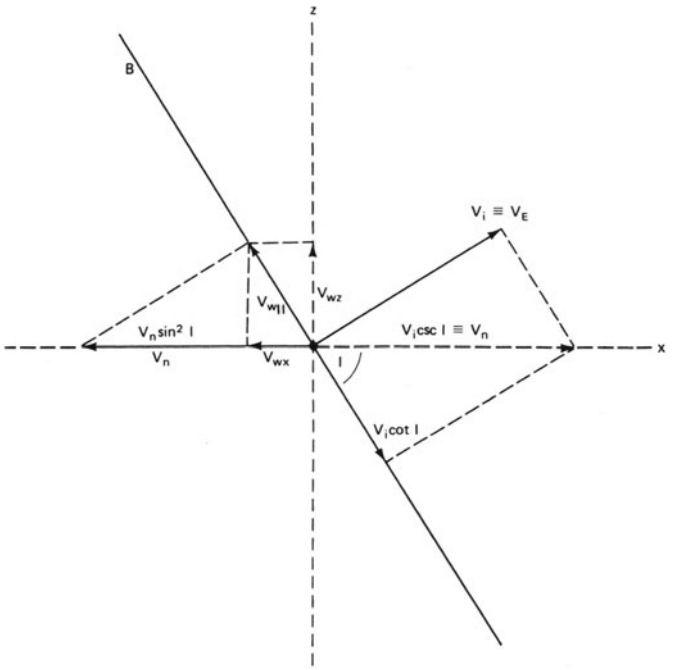

Fig. 5.7. Geometry of plasma transport processes in a magnetic dipole field for a dip angle I. The left side of the figure illustrates the effects of a neutral wind, while the right-hand side shows the effects of a plasma drift due to an $\mathbf{E} \times \mathbf{B}$ force (with $\mathbf{E}$ perpendicular to the plane of the paper) on the ionospheric plasma and the neutral gas.

VI Plasma Escape

According to our definition, a planetary ionosphere represents the thermal plasma (electrons and ions) produced by the interaction of ionizing radiations with the neutral atmosphere, which is controlled by the force field (gravity, magnetic field) of the planet. Thus, a planetary ionosphere may be thought to extend as far as the actions of these force fields allow the plasma to be confined in the planet's vicinity. Further, various processes exist where plasma can be lost from a planetary atmosphere of a non- or weakly magnetized planetary body or from a planet whose magnetosphere is highly compressed due to a strong solar/stellar wind.

VI.1 The Extent of Planetary Ionospheres

The plasma density distribution for a rotating planet can be expressed in terms of the potential (per unit mass) ϕ_g of the gravitational and inertial (centrifugal) force and the potential ϕ_E of the electrostatic polarization field which ensures charge neutrality, according to

$$N(R) = N_M \exp\left[-\frac{m_i\phi'_g + e\phi'_E}{k_B T_i}\right] \tag{6.1}$$

where

$$\phi'_g = \phi_g(R) - \phi_g(R_M)$$

and

$$\phi_g(R) = -\frac{g_0 R_0^2}{R} - \frac{1}{2}\Omega^2 R^2$$

with g_0 the surface gravity and Ω the angular speed of rotation of the planet of radius R_0 and

$$e\phi'_E = -\frac{m_i T_e}{T_e + T_i}\phi'_g\,.$$

Accordingly we obtain

$$N(R) = N_{\mathrm{M}} \exp\left[\frac{-m_{\mathrm{i}}\phi'_{\mathrm{g}}}{k_{\mathrm{B}}(T_{\mathrm{e}} + T_{\mathrm{i}})}\right] . \tag{6.2}$$

Since the force field is related to the potential by $\mathbf{F} = \boldsymbol{\nabla}\phi$, the plasma density has a minimum where $\boldsymbol{\nabla}\phi = 0$. This condition defines a distance R_∞ according to

$$\frac{g_0 R_0^2}{R_\infty^2} = \Omega^2 R_\infty ,$$

i.e., where the gravitational force balances the centrifugal force.

Thus, the maximum distance R_∞ (in the equatorial plane) where the plasma can corotate with the planet is given by

$$R_\infty = \sqrt[3]{\frac{g_0}{\Omega^2 R_0}} R_0 . \tag{6.3}$$

Unless the plasma is confined by a corotating magnetic field, effective corotation will cease at much smaller distances, i.e., where ion-exospheric conditions ($N_{\mathrm{c}} \lesssim 10^{-4}(m_{\mathrm{i}}/m_{\mathrm{H}})gT_{\mathrm{e}}$) prevail.

For a magnetic planet like Earth, motion of the ionospheric plasma is also constrained by the magnetic dipole field that can be described as function of planetocentric distance R and magnetic latitude λ by

$$B(R, \lambda) = \frac{\mathfrak{M}}{R^3} \left(1 + 3\sin^2\lambda\right)^{\frac{1}{2}} ,$$

where $\mathfrak{M} = B_0 R_0^3$ is the magnetic moment with B_0 the field intensity at the magnetic equator ($\lambda = 0$) and R_0 the planetary radius. A magnetic dipole field line can be characterized by the so-called L parameter

$$L = \frac{r_0 \cos^2\phi}{R_0},$$

with r_0 the apex distance in the magnetic equatorial plane. In this case the corotation limit R_∞ determined by the balance of gravitational and centrifugal force is modified due the convection electric force according to the so-called *Alfvén's two-thirds law* of [193, 194] leading to a reduced corotation limit expressed in terms of $L_\infty = R_\infty/R_0$ as

$$L'_\infty = \left(\frac{2GM}{3\Omega^2 R_0^3}\right)^{\frac{1}{3}} \tag{6.4}$$

and

$$L'_\infty = \left(\frac{2}{3}\right)^1 3L_\infty, \tag{6.5}$$

noting that $g_0 = GM/R_0^2$.

Table 6.1.

Planet	R_∞ [R0]	R'_∞ [R0]
Venus	$16\,R_♀$	
Earth	$6.6\,R_⊕$	$5.77\,R_⊕$
Mars	$5.9\,R_♂$	
Jupiter	$2.2\,R_♃$	$1.92\,R_♃$

Table 6.1 lists this distance R_∞ for planets with an established ionosphere. The domain where the planetary magnetic field dominates is called the *magnetosphere* [195]. Its boundary the *magnetopause* is determined by the balance between the solar wind streaming pressure p_{sw}, and the magnetic field pressure according to

$$p_{sw} = \frac{B_b^2}{8\pi} \tag{6.6}$$

where B_b is the planetary magnetic field at the boundary and

$$p_{sw} = KNmv^2 \cos^2 \psi \tag{6.7}$$

with $K \simeq 1$ the accommodation coefficient, and N, m and v, the number density, the mass, and the flow velocity of the solar wind ions (protons), respectively, and ψ the solar wind aspect angle. Applying this pressure balance and expressing B_b in terms of the surface field B_S, according to

$$B_b \simeq \tfrac{1}{2} B_S L_b^{-3}$$

where $L = R_b/R_0$; the location of the magnetopause is given by

$$L_b = \left[\frac{B_S^2(1 + 3\,\sin^2 \varphi_{ss})}{4\pi N m v^2}\right]^{\frac{1}{6}} . \tag{6.8}$$

Here φ_{ss} is the magnetic latitude at the subsolar point, accounting for the inclination of the dipole axis and the planet's orbit to the ecliptic, i.e., the seasons. Ahead of this magnetic obstacle a bow shock is formed at a distance $\Delta L \simeq 0.25 L_b$ from the magnetopause. Within the magnetosphere there is not only thermal plasma of ionospheric origin but also "trapped radiation" (*Van Allen belts*) of high energies, resulting from the interaction of cosmic rays with the neutral atmosphere [196].

For Earth $L_b \sim 11$ whereas L'_∞ is about 5.77, thus the corotating ionospheric plasma lies within the magnetosphere. This corotating regime of ionospheric plasma is called the *plasmasphere* and its termination is called the *plasmapause*. In contrast to the ideal corotation limit of $L'_\infty = 5.77$, the actual plasmapause identified by an abrupt drop is plasma density by at least

two orders of magnitude has been found empirically to vary as a function of magnetic disturbance, according to $L_{pp} = 5.77 - 0.47K_p^*$, with K_p^* the maximum value of planetary magnetic index K_p in the preceding 12 hours.

Since K_p was shown to be correlated with the solar wind velocity v_{sw}, it is clear that the interaction of the solar wind with the magnetosphere must be involved in the varying location of the plasmapause. The plasmapause represents the boundary between the convective motions due to an $\mathbf{E} \times \mathbf{B}$ drift resulting from the solar wind induced down-to-dusk convection electric field

$$E_{conv} = -\mathbf{v}_{sw} \times (\mathbf{B}_{IMF} + \mathbf{B}_{pol}),$$

where $\mathbf{B}_{IMF}$ is the interplanetary magnetic field carried by the solar wind and $\mathbf{B}_{pol}$ the polar cup magnetospheric field. This magnetic field together with the electric field causes a plasma drift perpendicular to both fields according to

$$v_D = \frac{\mathbf{E} \times \mathbf{B}}{B^2},$$

while the corotation electric field is given by

$$\mathbf{E}_{rot} = -\mathbf{v}_{cor} \times \mathbf{B}, \tag{6.9}$$

and

$$\mathbf{E}_{rot} = -\Omega \times \mathbf{R}, \tag{6.10}$$

because

$$\mathbf{v}_{cor} = \Omega \times \mathbf{R}.$$

The scalar value of the corotation field is in the equatorial plasma

$$E_{cor} = \frac{B_0 \Omega R_0}{L^2},$$

with B_0 the equatorial field and L the length parameter r/R_0. Figures 6.1 and 6.2 show the configuration of the convection electric field induced by the solar wind interaction with the magnetosphere and the corotational electric field in the form of equipotential contours in the equatorial plane, as well as the superposition of the two leading to a plasmapause configuration as the separation between the two regimes, with a bulge in the evening sector [196].

For a fast rotating magnetic planet like Jupiter having a magnetic moment much stronger than the Earth, the corotational electric field will be much stronger than the convection electric field and beyond the magnetospheric corotation limit L'_∞ plasma will be concentrated in a plasma layer near the magnetic equator due to the large centrifugal force (Fig. 6.3) deforming the

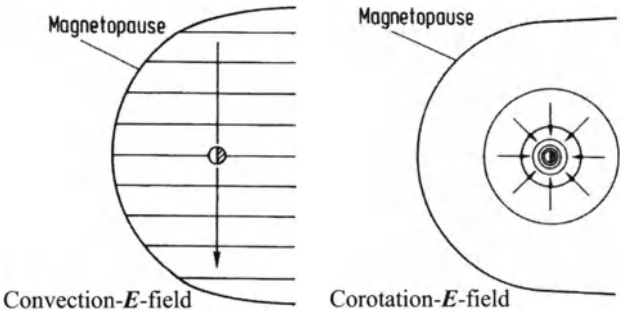

Fig. 6.1. Configuration of the convection electric field (left) induced by the solar wind plasma interaction with the magnetosphere and the corotational electric field (right) for contours in the equatorial plane (after H. O. Rucker [196]).

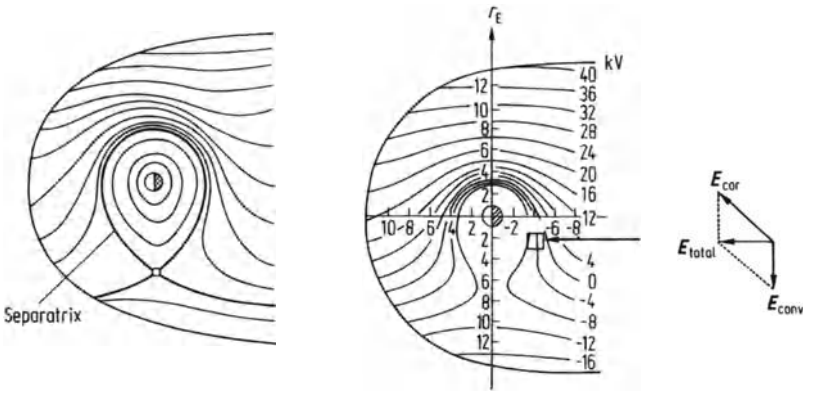

Fig. 6.2. Superposition of the convection and corotational electric fields. Theoretical illustration of the areas which are separated by a separatrix (left) and typical values for the potential difference in the terrestrial magnetosphere (after H. O. Rucker [196]).

magnetosphere. Because Jupiter's satellite Io has an atmosphere resulting from volcanic supply of gases and thus an ionosphere, an increased Io plasma torus will appear in Jupiter's magnetosphere at $L \approx 6$ [197]. Figure 6.4 shows comparative magnetospheres between the Earth, Jupiter, Saturn and a pulsar [198], while Table 6.2 lists a summery of planetary magnetic fields, their solar wind stagnation points L_b and rotation periods P_{rot} [203].

It is important to note that the internal magnetic field of exoplanets orbiting close to their host stars may be very weak due to tidal locking. Fortunately, there are several analytical models from which an estimate for a

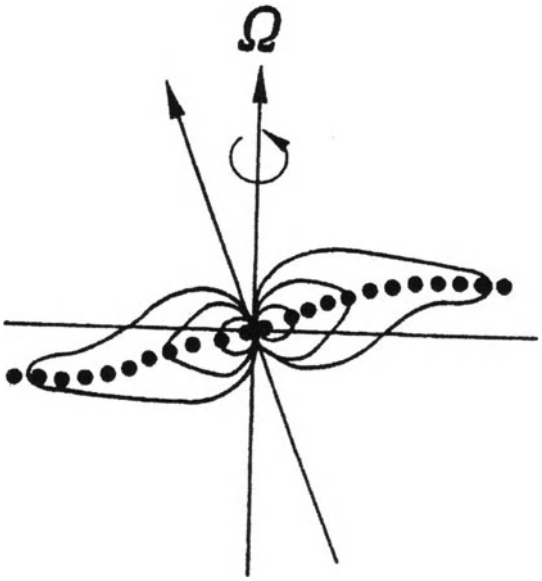

Fig. 6.3. The dotted line shows a centrifugally controlled plasma layer on a rapidly corotating magnetosphere as observed on Jupiter (after H. O. Rucker [196]).

planetary magnetic dipole moment parallel to the rotation axis can be gained. These models yield the following scaling laws

$$\mathfrak{M} \propto \rho_c^{1/2} \Omega r_c^4 \text{ [199]} \tag{6.11}$$

$$\mathfrak{M} \propto \rho_c^{1/2} \Omega^{1/2} r_c^3 \sigma_0^{-1/2} \text{[200]} \tag{6.12}$$

$$\mathfrak{M} \propto \rho_c^{1/2} \Omega^{3/4} r_c^{7/2} \sigma_0^{-1/4} \text{ [201]} \tag{6.13}$$

$$\mathfrak{M} \propto \rho_c^{1/2} \Omega^{1/2} r_c^3 \sigma_0^{-1/2} \text{ [202]} \tag{6.14}$$

$$\mathfrak{M} \propto \rho_c^{1/2} \Omega r_c^{7/2} \text{[203]} \tag{6.15}$$

where $\mathfrak{M}$ is the planetary magnetic dipole moment, r_c the radius of the dynamo region (frequently also called the "core radius"), ρ_c the core density, σ_0 the core conductivity and Ω the velocity of rotation of the planet around its axis [37, 203]. Table 6.3 shows the magnetic moment $\mathfrak{M}$ for the non-tidal locking and tidal-locking cases for the two "hot Jupiters" HD209458 b and OGLE-TR-56 b [37]. Relevant parameters used for the calculation of the magnetic moment are given in units normalized to Jupiter, while the relative core radius is normalized to the planetary radius [37]. The magnetic moment $\mathfrak{M}$ is given for two cases: "tidal locking" and "fast rotation" (for the hypothetical case $\Omega = \Omega_{\text{Jup}}$).

According to our present understanding of the detailed processes responsible for the termination of planetary ionospheres it seems certain that the solar-wind interaction determines the extent of the ionospheres of both mag-

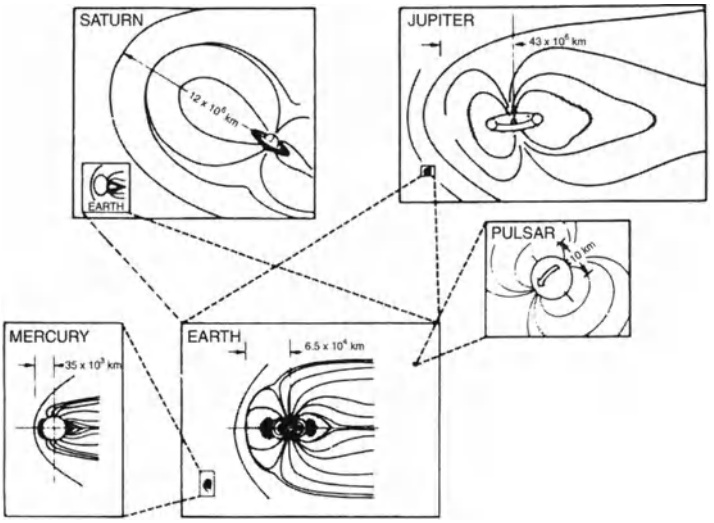

Fig. 6.4. Comparative magnetospheres of Mercury, Earth, Jupiter, Saturn and a pulsar [198].

Table 6.2. Known planetary magnetospheres in our Solar Systems [1 Gauss cm^3 = 10^3 Am^2; 1 nT=10^{-5}G] (after N. F. Ness [203]).

Planet	$\mathfrak{M}$ [Gauss cm^3]	Tilt and sense [°]	B_0 [nT]	L_b [R_0]	P_{rot} [$2\pi/\Omega$]
Mercury	5×10^{22}	+14	330	1.4	58.7^d
Earth	8×10^{25}	+11.7	31000	10.4	23.9^h
Jupiter	1.6×10^{30}	−9.6	428000	65±15	9.92^h
Saturn	4.7×10^{28}	0	21200	20±3	10.66^h
Uranus	3.8×10^{27}	−58.6	23000	20	17.24^h
Neptune	2.0×10^{27}	−46.8	14000	26	16.1^h

netic and non-magnetic planets. Figure 6.5 shows the upper boundaries of the ionospheres of non-magnetic Venus and magnetic Earth. For weakly or essentially non-magnetic planets such as Mars and Venus ($\mathfrak{M} < 10^{-4}\,\mathfrak{M}_\oplus$, where $\mathfrak{M}_\oplus = 8 \times 10^{25}$ Gauss cm^3) there is no magnetosphere to shield the planetary ionosphere from a direct interaction with the solar wind.

Since the solar wind with its "frozen-in" interplanetary magnetic field cannot penetrate another plasma, the solar wind is deflected around the ionosphere preventing its penetration to lower levels in the atmosphere where collision effects are dominant, or to the surface where it would be absorbed as is the case for the Moon. Thus, the ionosphere represents an obstacle to the solar wind flow which leads to the formation of a bow shock upstream, similar to that where a magnetosphere is present [205, 206].

Table 6.3. Decrease of magnetic moments due to tidal locking of short periodic giant exoplanets. Note that two different core radii are presented (after J.-M. Grießmeier et al. [37]).

Parameters	HD209458 b	OGLE-TR-56 b
Semimajor axis r [AU]	0.045	0.0225
Radius R_0 [$R_{\rm Jup}$]	1.42	1.3
Mass M [$M_{\rm Jup}$]	0.69	0.9
Rotation rate ω [$\omega_{\rm Jup}$]	0.12	0.34
Core density $\rho_{\rm c}$ [$\rho_{\rm c,J}$]	0.24	0.41
Relative core radius $r_{\rm c}/R_0$	0.54	0.66
Relative core radius $r_{\rm c}/R_0$	0.34	0.50
Magnetic moment $\mathfrak{M}$ [$\mathfrak{M}_{\rm Jup}$] (for tidal locking)	0.005 ... 0.06	0.058 ... 0.25
Magnetic moment $\mathfrak{M}$ [$\mathfrak{M}_{\rm Jup}$] (for fast rotation)	0.042 ... 0.30	0.17 ... 0.56

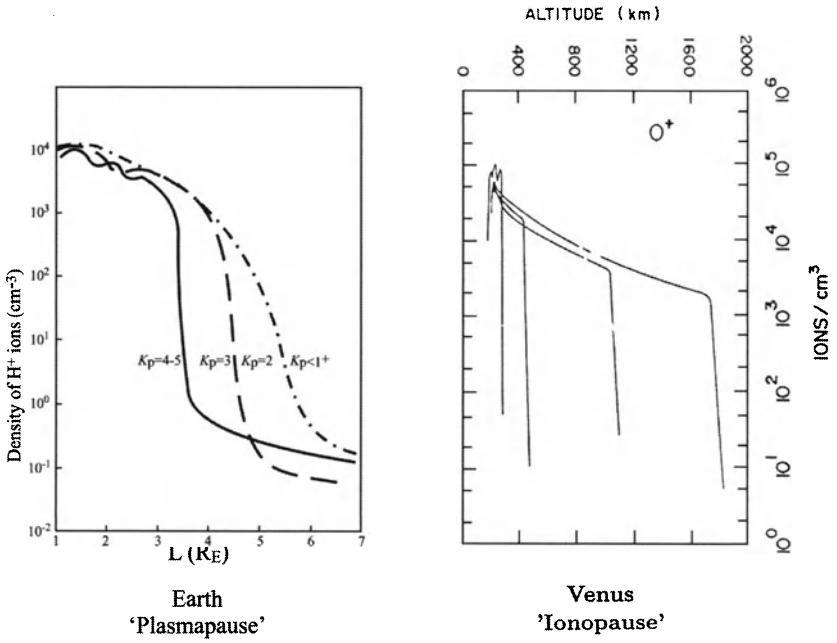

Fig. 6.5. Upper boundaries of the ionospheres of Earth and Venus [204].

The condition for pressure balance between the solar wind and ionospheric plasma, assuming that this pressure is much greater than the magnetic pressure on either side of this level ($p \gg B^2/8\pi$), can be expressed by

$$p_{\rm sw} = K\rho_\infty v_{\rm sw}^2 \cos^2\psi = N_{\rm i} k_{\rm B}(T_{\rm e} + T_{\rm i}) \equiv p_{\rm ion} \tag{6.16}$$

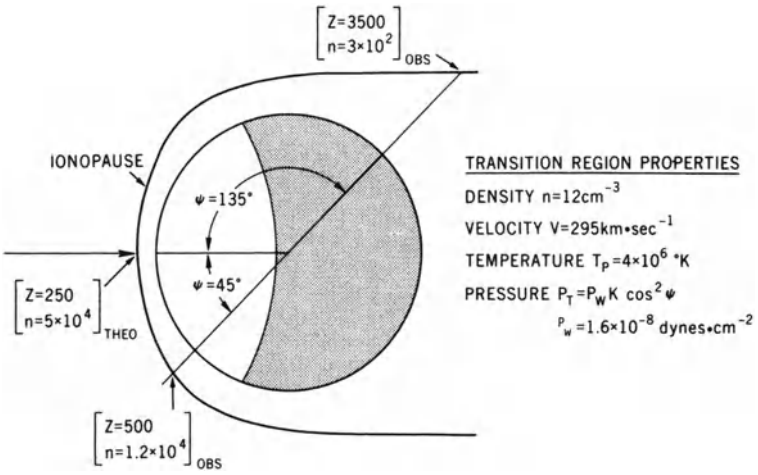

Fig. 6.6. An example of the configuration of the ionopause of Venus resulting from the solar wind interaction with the topside ionosphere of Venus. Pressure balance between solar wind and ionospheric plasma is based on the Mariner 5 observations for the dayside occultation point ($\psi = 45°$); the shape of the ionopause is due to the $\cos^2 \psi$ dependence of the solar wind streaming pressure. In the antisolar direction there is a tail whose width is consistent with the nightside occultation data.

where $\rho_\infty = (nm)_{sw}$ and v_{sw} are the solar wind values upstream of the bow shock, $K \approx 0.34$ is the average loading fraction [208] and ψ is the angle between the flow direction of the undisturbed solar wind and the normal to the ionospheric boundary, which may be called the *ionopause*.

The configuration of the ionopause due to the $\cos^2 \psi$ variation is illustrated schematically for Venus in Fig. 6.6. Also indicated are the locations of the two electron density profiles obtained from the Mariner 5 dual-frequency radio occultation experiment; the dayside profile exhibited a sharp drop in electron density at an altitude of $\sim$ 500 km, which is interpreted as the ionopause, whereas the nightside profile extends to an altitude of $\sim$ 3500 km. The thickness of the ionopause is probably of the order of the solar wind proton gyroradius [207]. In addition to accumulation of magnetic field lines in front of the ionosphere forming an impenetrable surface where a tangential discontinuity exists in the horizontal component of the interplanetary magnetic field and the solar wind velocity, an induced magnetosphere representing a magnetic barrier which provides for a pressure balance with the solar wind has been suggested as being responsible for the ionopause as observed for Venus. In either case a bow shock would be formed upstream as the result of the interaction of the supersonic solar wind with the planetary environment [205].

For essentially magnetic field-free planets (Venus, Mars) mass loading would be substantial, so that it could provide a sufficient obstacle to the solar wind leading to the formation of a bow shock.

Mass loading due to photoions in a planetary ionosphere could lead to a deceleration of the solar wind to a velocity of the order of the sound speed in the ionosphere ($v_{sw} \rightarrow v' \sim c_i$) and thus to a downward transport of ionospheric plasma with a velocity $v' = \text{const.}$ [209]. This effect can be expressed by the continuity equation

$$v' \frac{dN}{dz} = q - L \,.$$

Since in the topside ionosphere, the time constant for the transport process $\tau_{v'} \simeq H/v'$ (for $v' \sim c_i$) is usually much smaller than the chemical time constant $\tau_C = 1/(\alpha N)$, the loss term may be neglected and the plasma density distribution, assuming the major ion to be a molecular species (XY^+), is then given by

$$N(XY^+|z) = \frac{H(XY)}{v'} J_{XY} n(XY|z)$$

where $q = J_{XY} n(XY^+|z)$ above the ion production peak (i.e., in the low attenuation region).

For a CO_2^+ (or O_2^+) ionosphere, such as Mars or Venus, the plasma density distribution then decreases according to

$$N(XY^+|z) \propto \exp\left(\frac{-z}{H(XY)}\right)$$

i.e., with the scale height of the ionizable constituent, whereas the photochemical equilibrium (Chapman distribution) at these altitudes corresponds to

$$N(XY^+|z) \propto \exp\left(\frac{-z}{2H(XY)}\right) .$$

Thus, as the result of the downward plasma transport initiated by the solar wind interaction, the scale height of the plasma density distribution is smaller by a factor of 2 than that of a Chapman or a diffusive equilibrium distribution.

Although Mars must be considered as a non-magnetic planet at present, observations with the Mars Global Surveyor (MGS) spacecraft have shown large crustal magnetic anomalies to exist [210] which can only be explained by the presence of an ancient magnetic field, perhaps of similar magnitude as that of Earth. These crustal magnetic anomalies may result in localized *mini-magnetospheres*, thus contributing a magnetic pressure P_B in the balance of the solar wind interaction with the Martian ionosphere such that

$$p_{sw} = p_{ion} + \frac{B_b^2}{8\pi} . \tag{6.17}$$

Although our present understanding of the detailed processes responsible for the termination of planetary ionospheres is still incomplete, it seems certain that the solar/stellar-wind interaction must determine the extent of the ionospheres of both magnetic and non-magnetic planets.

VI.2 Ion Pick Up and Mass Loading

Neutral atoms and molecules above the ionopause can be transformed to ions via charge exchange with solar-wind particles, solar UV or electron impact in planetary atmospheres, which are not protected by an intrinsic magnetic field. As ions they are accelerated to higher altitudes and energies by the interplanetary electric field and gradually guided by the solar- or stellar wind plasma flow around the planetary obstacle [211, 212, 213].

In the following an idealized model [152, 214] for the atmospheric loss caused by solar wind interaction is presented, which neglects complications like finite ion-gyroradii and non-spherical ionopause geometry, but whose results are in good agreement with more complicated test particle models [211, 213].

The mass loss from the atmosphere can be visualized by assuming that the ions with mass density ρ_i above the ionopause, produced by ionization rates J_j by photoionisation ($j = 1$), electron impact ionization ($j = 2$) and charge exchange ($j = 3$), with solar- or stellar wind protons of the neutral gas density ρ_n, are incorporated into the plasma flow, constrained by a mass loading limit [208, 214]. The total mass production rate q_ρ of pick up ions can be written as

$$q_\rho = \sum_{j=1}^{3} J_j \rho_n. \tag{6.18}$$

The rate of change of atmospheric mass M_a can be expressed as:

$$\frac{dM_a}{dt} = \frac{d\rho_n}{dt} V \tag{6.19}$$

where V represents the interaction volume consisting of a hemispherical shell whose inner radius is the planetocentric ionopause distance R_{IP}, while its outer radius lies one atmospheric scale height above $(R_{IP} + H)$. One gets

$$\frac{d\rho_n}{dt} = -q_\rho. \tag{6.20}$$

The planetary ions produced in this manner cannot disappear chemically in the transport-dominated environment (solar of stellar wind) and thus the steady state condition requires that [214]

$$q_\rho = div\,(\rho_i v_i) \approx \frac{\rho_i v_i}{H} \tag{6.21}$$

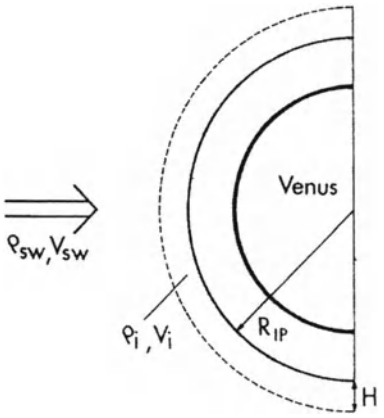

Fig. 6.7. Illustration of the solar/stellar wind interaction geometry for a non-magnetized planetary body (after S. J. Bauer [214]).

where v_i is the ion velocity, which is originally much less than the solar- or stellar wind velocity v_{sw}. Momentum balance considerations between the stellar plasma flow with mass density ρ_{sw} and the planetary ions lead to

$$\rho_i v_i = \rho_{sw} \frac{(v_{sw} - v_i)}{H}. \tag{6.22}$$

Thus, the interaction volume V is given as [214]

$$V = \frac{2\pi}{3}\left[(R_{IP} + H)^3 - R_{IP}^3\right] \approx 2\pi R_{IP}^2 H \tag{6.23}$$

because $R_{IP} \gg H$ and the rate of atmospheric mass loss as a result of stellar wind interaction can be written as

$$\frac{dM_a}{dt} \approx -K\,(\rho v)_{sw}\, 2\pi R_{IP}^2 \tag{6.24}$$

where K represents a momentum accommodation factor [208].

For studying atmospheric loss by ion pick up it is important to know the limited capacity K of the solar wind flow to accommodate added atmospheric mass. This limit determines how much atmospheric matter can be picked up by the plasma flow. One can assume that there exists a stellar wind stream line which passes deepest into the atmosphere before it returns to the interplanetary plasma flow (Fig. 6.7). There can be no steady solution when the supersonic solar or stellar wind interacts with the planetary atmosphere. The streaming plasma interacts with an atmosphere with a subsonic velocity and a shock must form to assure the appropriate boundary conditions, so that the Mach number M_{sub} in the post shock regions is

$$M_{sub} = \frac{v_i}{v_{sh}} \tag{6.25}$$

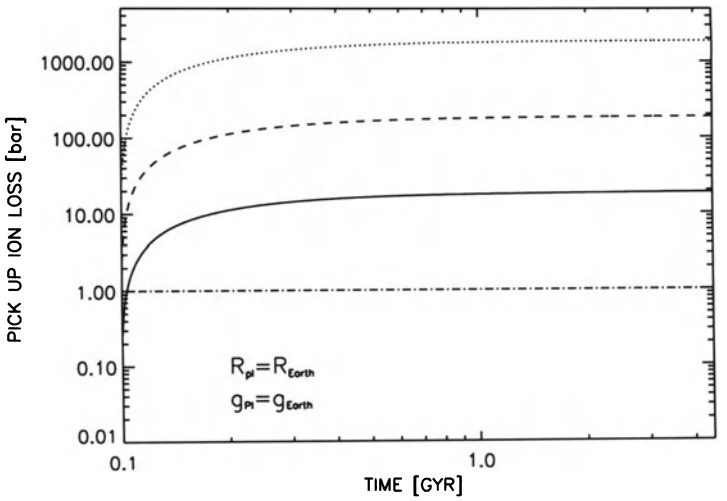

Fig. 6.8. Pick up ion loss for various Earth-size planets at orbital distances of 0.05 AU (dotted line), 0.38 AU (dashed line) and 1 AU (solid line), assuming an average stellar wind particle flux according to Fig. 1.13. One can see that a non-magnetized Earth would have lost about 20 bar. At the assumed stellar wind conditions a Venus-like planet at an orbit of Mercury would also have lost its 100 bar atmosphere and would look like Mercury, after 1 Gyr.

where v_i is the flow speed of the post shocked solar wind plasma, which is deflected around the planets in the ionopause interaction region before the ions get accelerated and incorporated in the plasma flow, and v_{sh} is the plasma flow velocity behind the bow shock. The integrated mass loading along the actual path of the stream line will be $\langle m_a \sin\theta \rangle$. For a thin shell atmosphere the important variation is only the angle, since the mass addition rate m_a is large near the stagnation point where θ goes to zero [208].

$$\langle m_a \sin\theta \rangle = \frac{2}{\pi} \int_0^{\frac{\pi}{2}} m_a \sin\theta d\theta, \tag{6.26}$$

where the Mach number M_{sub} is proportional to θ, while m_a is proportional to M^{-2} at small M so that $M_{sub} \rightarrow k_a \theta$ and m_a is

$$m_a = \frac{3}{16 M^2} \tag{6.27}$$

so that

$$m_a = \frac{3}{16 (k_a \theta)^2}$$

where k_a is an aerodynamic parameter of about 1.3/rad. The momentum accommodation factor K can thus be written as [208]

$$K = \langle m_a \sin\theta \rangle = \frac{6}{16\pi} \int_0^{\pi} \frac{\sin\theta}{\theta^2} d\theta. \tag{6.28}$$

After solving the integral one gets for K

$$K = -\left(\frac{3}{8\pi k_a^2}\right) ln\left(\frac{M_{sub}}{k_a}\right). \tag{6.29}$$

If one assumes an average interpenetration velocity v_i of the ions of about 1 km s^{-1} which was measured on Venus one gets a subsolar Mach number M_{sub} with a v_{sh} of about 100 km s^{-1} resulting in a mass loading limitation factor K of about 1/3 [208, 214].

Figure 6.8 shows the atmospheric loss caused by ion pick up on Earth-size non-magnetic, weak-magnetic planets or planets where the magnetopause is compressed to the ionopause distance due to a much higher stellar wind at orbital distances of 0.05 AU, 0.38 AU and 1 AU.

One can see from Fig. 6.8 that intrinsic magnetic fields may be essential for the atmospheric stability and hence habitability of terrestrial planets (cf. Chap. VII). Due to high stellar winds during the first Gyr after the star arrived at the ZAMS, atmospheres of terrestrial planets, which are not protected by a magnetosphere, can be eroded and may therefore evolve to Mercury-type planets.

VI.3 Ion Exosphere

In cases where the exosphere is exposed to high XUV radiation, or if large exospheric temperatures evolve due to a close orbital distance of a planet to its host star the majority of the exospheric constituents can be ionized. If an ion exosphere develops the weight of the ions is reduced due to the account of electrostatic fields caused by the diffusion of free electrons. The weight reduction of the ions is about 1/2 of full gravity if one ion species is present and in different proportions when several ion species occur.

The values of the escape parameter X are reduced in the similar proportion as gravity is decreased. When two ion components are present whose number densities are ψN_e and $(1-\psi)N_e$, with N_e being the electron density, and whose relative atomic or molecular weights are $\hat{m}_j$ $(j = 1, 2)$ their ion escape parameters are given as [73]

$$X_{i1} = \frac{1}{2} X_1 \left[1 + (1-\iota)\left(1 - \frac{\hat{m}_1}{\hat{m}_2}\right)\right] \tag{6.30}$$

and

$$X_{i2} = \frac{1}{2} X_2 \left[1 + \iota\left(1 - \frac{\hat{m}_1}{\hat{m}_2}\right)\right] \tag{6.31}$$

where X_1 and X_2 are the values for the neutral constituents. In the case of negative values of X_{i1} or X_{i2} one must assume zero. The average value of X for ions is

$$X_i \frac{1}{2} X. \tag{6.32}$$

The escaping ions belong to the high velocity tail of a Maxwellian velocity distribution and thus have smaller cross-sections than the average thermal ions. Their average kinetic energy at escape is about $[(1/2)X + 1.5]kT$ corresponding to an ion temperature of

$$T_i = \left(1 + \frac{1}{3}X\right) T. \tag{6.33}$$

Their collisional cross-section for Colomb interactions can be set equal to [73]

$$\sigma_c \approx 2.25 \times 10^{-6} \left[\left(1 + \frac{1}{3}X\right) T\right]^{-2} \mathrm{Log}_{10}\left(1 + \frac{10^8 T^3}{N_e}\right) \quad [\mathrm{cm}^2]. \tag{6.34}$$

If ι is the degree of ionization or the ratio between the electron density and the total number density, the effective collisional cross-section σ becomes [73]

$$\sigma = \iota\sigma_c + (1 - \iota)\,\sigma_n, \tag{6.35}$$

where $\sigma_n \approx 2.0 \times 10^{-15}$ cm^2. With respect to the effective scale height the actual situation for ions is more complicated. For the upper portion of the ion exosphere the ion number density is

$$N_i = \frac{B_i}{(2\sigma r)} \tag{6.36}$$

and velocity

$$v_i = 1.03 \times 10^{-4} \left(\frac{M}{rX_i}\right)^{\frac{1}{2}} \tag{6.37}$$

so that one gets for the mass loss rate in the absence of an intrinsic planetary magnetic field and valid for the ion-exobase [73]

$$\frac{1}{M}\frac{dM_i}{dt} = -2.18 \times 10^{-16} \hat{m}_i \psi v_\infty^{-1} \cdot X_i X^{-\frac{1}{2}} \cdot (1 + X_i)\, e^{-X_i} \left(1 - \iota + \frac{\iota\sigma_c}{\sigma_n}\right)^{-1} [s^{-1}], \tag{6.38}$$

where the relative abundance of species S which escapes per second is ψ for the first component. $\iota \approx 1$ is expected to be valid whence X_i as for ions alone is assumed. It is difficult to define the altitude level of the exact ion-exobase. Observational data on Earth relating to the distribution of electron density

with altitude are not directly applicable as they are governed by Earth's magnetic field.

Generally one can assume that the ion-exobase is placed above the exobase of the neutral gas. If isothermacy holds between the neutral and ion exobase one can use the Jeans-Spitzer compensation of the N and e^{-X}, so that $SN\mathrm{e}^{-X} = \text{const.}$ and apply the ion escape formula to the exobase of the neutral without regard to the value of σ, but with correcting factors for the non-compensated variables r^2 and $(1 + X)$, which must refer to the actual ion-exobase level. In the absence of an intrinsic planetary magnetic field, the ion mass loss rate can be written as [73]

$$\frac{1}{M}\frac{dM}{dt} = -2.18 \times 10^{-16} \hat{m}_\mathrm{i} S_\mathrm{i} v_\infty^{-1} \cdot X_\mathrm{a} X^{-\frac{1}{2}} \left[\left(\frac{r_\mathrm{i}}{r_0} \right)^2 + X_\mathrm{i} \left(\frac{r_\mathrm{i}}{r_0} \right) \right] e^{-X_\mathrm{i}} \qquad [\mathrm{s}^{-1}] \tag{6.39}$$

where S_i is the extrapolated relative abundance of the ion species at the neutral exobase level, calculated on the assumption of the isothermal equilibrium from a given density N_i at the ion-exobase, and v_∞ and X correspond to the neutral gas of the ionized species. X_i is usually about $(1/2)X$ for the major constituent and X_a is the average for the neutral gas and all parameters refer to the neutral escape level.

The uncertainty in the ratio r_i/r_0 is less than the uncertainty in σ_c and e^{-X_i}, which effects (6.38). However the major uncertainty in this approximation rests with S_i, the extrapolated effective ion abundance. On Earth $S_\mathrm{i} \approx 0.1$ for the electron density. By setting $S_\mathrm{i} = 1$ (1=100%) the ion mass loss rate would yield an overestimation by one order of magnitude. However, there is hypothetically no limit to S_i, which may even exceed unity.

Equations (6.38) and (6.39) presume the absence of an intrinsic planetary magnetic field. If such a field is present the ion escape takes place only from the magnetic poles, from where the magnetic field lines reach far enough into space, to be lost in the interplanetary field. On a terrestrial planet with a magnetic field strength like Earth, this happens at about 13 Earth radii, implying magnetic field lines starting at magnetic latitudes of about 75°. The presence of such a magnetic field limits the escape to an area of about 0.04 of the total. Thus, by analogy one can assume that in the presence of an intrinsic magnetic dipole field, the ion escape rate is decreased approximately by a factor of 25 as compared with the values given in (6.38) and (6.39).

VI.4 Plasma Escape from Magnetized Planets

In analogy with the neutral atmosphere, if the condition that the plasma scale height become comparable to the electron–ion mean free path ($\lambda_\mathrm{e} \simeq 10^4 T_\mathrm{e}^2/N_\mathrm{e}$) is satisfied at the ion-exobase or baropause, ions (and electrons) can escape from the gravitational field, provided there is no magnetic field to

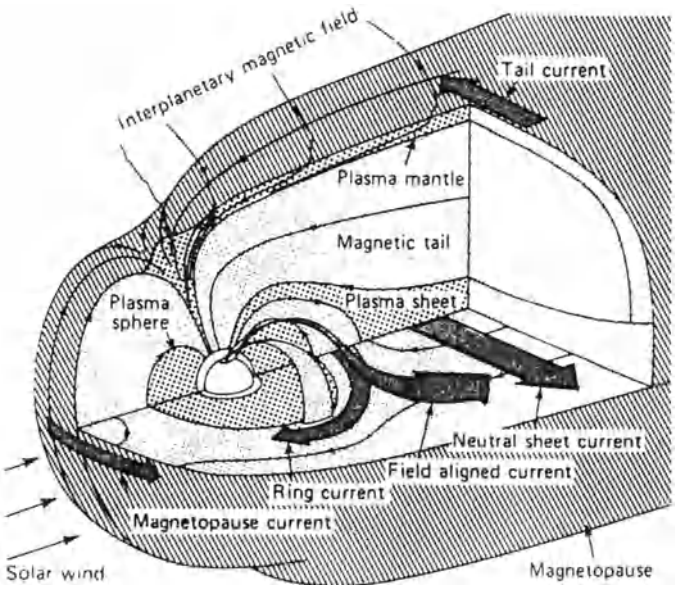

Fig. 6.9. Ionosphere–magnetosphere configuration for Earth showing the corotating plasmasphere and the polar wind region associated with the open geomagnetic tail [215].

constrain the plasma. In the presence of a planetary magnetic field, plasma escape is possible only where the field lines are not closed loops (Fig. 6.9). For a dipolar magnetic field, a simple ion-exosphere model results in a plasma density distribution along (closed) field lines, which decreases with altitude much more rapidly than according to a diffusive equilibrium distribution [216, 217]. The ion-exobase occurs at a density $N_e \lesssim 10^{-4}(m_i/m_H)gT_e$ [cm^{-3}], corresponding to $\mathfrak{H} \simeq \lambda_e$. By applying the law of conservation of energy together with the first magnetic invariant for the motion of charged particles in a dipole field, an idealized model for the distribution of plasma under ion-exospheric ("collisionless") conditions is given by [216]

$$N(R,L) = N_M \exp\left[\frac{-R'}{\mathfrak{H}}\right]\left\{1-\left(1-\frac{B}{B_M}\right)^{\frac{1}{2}}\exp\left[-\frac{R'B}{\mathfrak{H}(B_M-B)}\right]\right\} \quad (6.40)$$

where $\mathfrak{H}$ is the plasma scale height, R' is a reduced altitude parameter (taking into account the variation of gravity, along a magnetic field line ($R = R_0\cos^2\varphi$) whose apex (at the equator) has a planetocentric distance $L = R_a/R_0 = (\cos^2\varphi)$ with R_0 the planetary radius, and which originates at a geomagnetic latitude φ; the subscript M refers to the baropause level where a Maxwellian distribution applies.

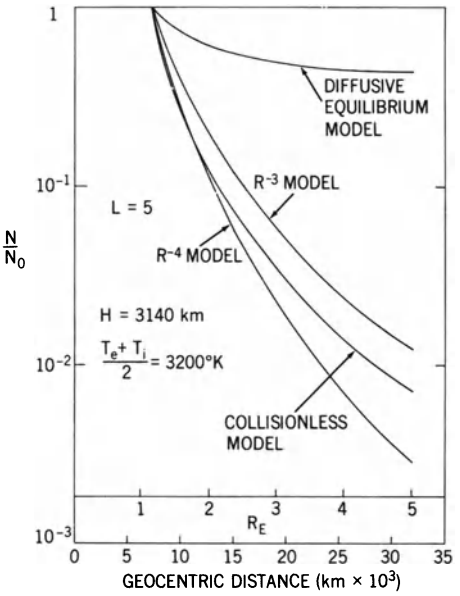

Fig. 6.10. Comparison of diffusive equilibrium, collisionless (ion exosphere) and power-law distributions along a magnetic field line for $L = 5$, i.e., whose apex is at a geocentric distance of $5\,R_E$ (after S. J. Bauer [182]).

The first term of (6.40) represents the diffusive equilibrium distribution, and the second term a weighting function due to the "collisionless" motion of the charged particles in the magnetic field of intensity B $(B_a \propto L^{-3})$. Comparisons between a diffusive equilibrium, an ion exosphere and two powerlaw distributions for the case of the terrestrial ionosphere are shown in Fig. 6.10. This type of distribution is applicable to closed dipole lines. An L^{-4} power-law represents an essentially constant number of particles in a magnetic flux tube, whose volume varies as L^4, while its cross-section varies as L^3. However, as the result of the solar wind interaction with a planetary magnetosphere or ionosphere, magnetic field lines can be dragged in a tail-like formation in the antisolar direction (e.g., the geomagnetic tail) with the field lines parallel and essentially open.

Under these circumstances plasma can escape from the ionosphere. This escape is enhanced relative to the neutral particles as the result of the electrostatic polarization field which accelerates minor light ions and even for the major ions reduces the effect of gravity.

Two types of plasma escape have been suggested [218]. One is evaporative in nature, i.e., similar to the escape of neutrals based on the thermal energy of the plasma, leading to outflow of plasma with subsonic and sonic velocities near the exobase [219, 220]; the other is based on the hydrodynamic properties of the plasma leading to the possibility of supersonic velocities

for the out-flowing plasma [221, 222]. The latter has been termed the "polar wind" in analogy to the solar wind, whereas the former amounts to a "polar breeze" only. The controversy as to the validity and relative merits of the two approaches to plasma escape has recently subsided. In fact, both approaches should lead to identical results although originally this was not the case.

The hydrodynamic approach [221, 222] is based on the bulk properties of the medium and high (supersonic) flow velocities are obtained even near the ion-exobase. As discussed before, the electrostatic polarization field in a hydrostatic (diffusive equilibrium) ionosphere $E = -\mathrm{d}(\ln p_\mathrm{e})/\mathrm{d}z = -m_+ \cdot g/2$ (for $T_\mathrm{e} = T_\mathrm{i}$), accelerates light ions $m_\mathrm{l} < m_+$ upwards, leading to a massflow. Coulomb collisions between the light and major ions result in frictional drag which impedes their upward flow.

Assuming ambipolar motion $\left(N_\mathrm{e} v_\mathrm{e} = \sum_j N_j v_j\right)$ along magnetic field lines (s) and speeds low relative to the electron thermal speed, i.e., $v_j^2 \ll k_\mathrm{B} T_\mathrm{e}/m_\mathrm{e}$, and neglecting electron collisions, the momentum equations for electrons and ions (j-th species) can be written [222]

$$\begin{aligned} \frac{1}{N_\mathrm{e}} \frac{\partial p_\mathrm{e}}{\partial s} &= eE_\perp \\ v_j \frac{\partial v_j}{\partial s} + \frac{1}{N_j m_j} \frac{\partial p_j}{\partial s} - \mathbf{g} \cdot \hat{\mathbf{s}} - \frac{eE_\parallel}{m_j} &= -\sum_k \nu_{jk} (v_j - v_k) \,. \end{aligned} \tag{6.41}$$

For a dipole field $ds = R_\mathrm{a} \cos\varphi (4 - 3\cos^2\varphi)^{\frac{1}{2}}\, d\varphi$. Eliminating the electric field and introducing the local ion Mach number $M_j = v_j/c_j$, with $c_j = (2k_\mathrm{B} T_j/m_j)^{\frac{1}{2}}$ the ion sound speed, the equation for the ion plasma motion can be expressed by

$$\begin{aligned} \frac{1}{M_j} \frac{\partial M_j}{\partial s} (M_j^2 - 1) = {} & \frac{\mathbf{g} \cdot \hat{\mathbf{s}}}{c_j^2} + \frac{1}{A} \frac{\partial A}{\partial s} - \frac{1}{c_j^2} \sum_k \nu_{jk} (v_j - v_k) - \frac{1}{F_j} \frac{\partial F_j}{\partial s} \\ & - \frac{1}{2T_j} \frac{\partial T_j}{\partial s} (M_j^2 + 1) - \frac{1}{T_j} \frac{\partial T_\mathrm{e}}{\partial s} - \frac{(T_\mathrm{e}/T_\mathrm{i})}{N_\mathrm{e}} \frac{\partial N_\mathrm{e}}{\partial s} \end{aligned} \tag{6.42}$$

where A is the area of a magnetic flux tube, $A \propto 1/|B|$, and

$$F_j = N_j(s) \cdot v_j(s) \cdot A(s) = \int_{s_0}^{s} (q_j - L_j) A \, ds + N_0 v_j A_0$$

is the ion escape flux, with q_j the ion production rate and L_j the chemical loss rate. Solutions of (6.42) can be found for appropriate boundary conditions. An example of such solutions for H^+ in a predominantly O^+ ionosphere is illustrated in Fig. 6.11. At high altitudes $M(\mathrm{H}^+) \geq 0$ while at low altitudes, where chemical processes are important, $M(\mathrm{H}^+) \to 0$. The boundary plasma pressure $p(\infty)$ determines the appropriate solution. For outside plasma pressures $0 \leq p(\infty) < p_\mathrm{B}(\infty)$, where $p_\mathrm{B}(\infty)$ is the asymptotic pressure of the

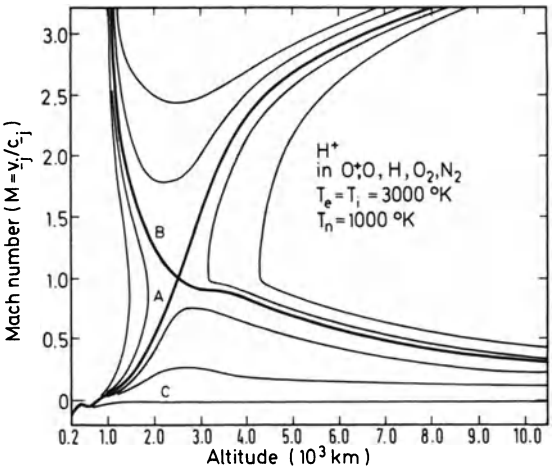

Fig. 6.11. Solutions for the Mach number $M(H^+)$ illustrating supersonic flow ("polar wind") – curve A; subsonic outflow ("polar breeze") – curve B and diffusive equilibrium – curve C (after P. M. Banks and T. E. Holzer [222]).

descending critical solution (B), curve A is the only correct solution, representing an *outward* flow of plasma which reaches supersonic velocity at the *critical point*, $M(H^+) = 1$.

Curve A applies ideally when $p(\infty) \to 0$ as $s \to \infty$. If $p(\infty) > p_B$ subsonic escape solutions ($M < 1$) apply, while for some $p(\infty)$, $M(H^+) \to 0$, diffusive equilibrium (curve C) applies.

Ion density profiles and H^+ escape fluxes are shown in Fig. 6.12 for a particular model ionosphere. It can be seen that as the result of the upward flux of H^+, the scale height of H^+ becomes comparable to that of O^+ ($d(\ln N(H^+))/dz \cong d(\ln N(O^+))/dz$) as discussed for diffusive flow. The asymptotic solution for the ion number density in the polar wind is given by

$$N_i \propto B[\ln(B)]^{-\frac{1}{2}} \propto R^{-3} .$$

The evaporative approach (ion exosphere) can lead to supersonic flow velocities as the result of a polarization field obtained by requiring quasi-neutrality and the escape *fluxes* of ions and electrons to be equal (rather than diffusive equilibrium, i.e., $\mathbf{v}_e = \mathbf{v}_i = 0$), or by the incorporation of a bulk flow below the ion-exobase [223]. While both, the modified evaporative and the hydrodynamic approach lead to supersonic velocities above the ion-exobase and to comparable escape fluxes, they both employ approximations which may not fully represent the true physical situation. In fact, the two approaches are complementary since the hydrodynamic approach is only appropriate in the collision-dominated region, whereas the kinetic (evaporative) approach can be applied only in the "collisionless" domain.

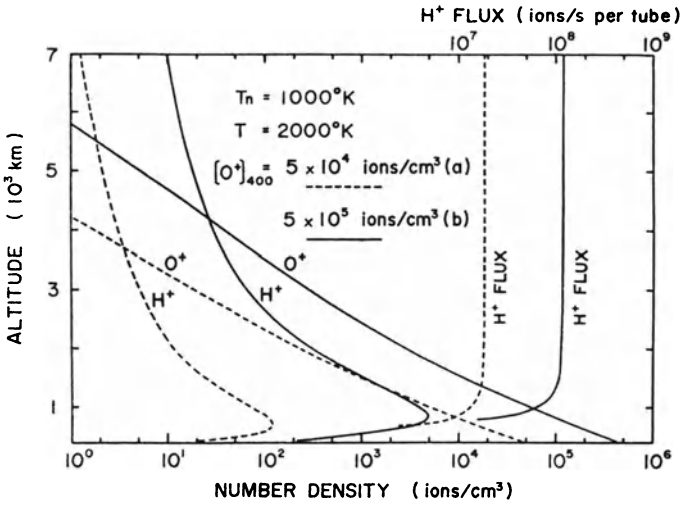

Fig. 6.12. Density distributions of H^+ and O^+ and escape flux of H^+ in the terrestrial polar wind regime (after K. Marubashi [223]).

VI.5 Ionospheric Plasma Instabilities

Although there exist a large number of plasma instabilities we shall consider only the few which seem particularly pertinent to planetary ionospheres [224].

There are basically two types of plasma instabilities: 1) macroscopic and 2) microscopic, the first referring to unstable configurations in geometric space, the second to those in velocity space. The latter are of great importance in wave–particle interaction phenomena occurring primarily in the magnetosphere. Since the macroscopic instabilities refer to perturbations of the configuration of the plasma, they are especially important at the boundary of planetary ionospheres (ionopause, plasmapause).

The gravitational (Rayleigh–Taylor) plasma instability refers to the case where a dense fluid is floating on a lighter one separated by a boundary layer, with gravity acting on the system. Such a configuration is unstable to perturbations although surface tension in the boundary acts as a stabilizing force [225]. A similar situation exists in the interaction between the solar wind plasma and the ionosphere of non-magnetic planets (e.g., Venus or Mars), and planets with highly compressed magnetospheres or planets in which case the boundary layer is represented by a magnetic barrier (due to the pile-up of interplanetary field lines or as the result of an "induced" magnetic field).

The condition for a stable configuration requires that the potential energy W be a minimum. Stability criteria can be developed by imposing a displacement and obtaining the change in W in terms of the variation δW. An alternate way of describing plasma instabilities is in terms of a wave dispersion relation, since perturbations of a stable equilibrium state result

in harmonic oscillations (waves). Such an approach is particularly useful for determining the growth rate of the instability [224].

In an equilibrium system $\delta W = 0$ to first order, a condition which is also called marginal stability. The system is truly stable when $\delta W > 0$; this condition corresponds to an increment in potential energy calculated to second order in the displacement [225]. For a magnetic boundary layer on top of a gravitationally supported plasma, a situation representative of the ionosphere boundary of Venus, the total potential energy of the system can be expressed by

$$W = \int \left(\frac{B^2}{8\pi} + \rho_i \phi_g \right) d\mathfrak{V}$$

where $B^2/8\pi$ is the energy density of the boundary layer magnetic field which in turn is balanced by the stellar wind streaming pressure p_{sw}, ρ_i is the mass density of the ionospheric plasma, ϕ_g is the gravitational potential ($\Delta\phi_g = -g$) and $d\mathfrak{V}$ is a volume element. The respective changes in gravitational potential and magnetic energy resulting from a displacement δR [225] are given in this particular case by

$$\delta W_g = \int \rho_i g \delta R \, d\mathfrak{V}$$

and

$$\delta W_B = - \int \frac{B^2}{4\pi R_b} \delta R \, d\mathfrak{V}$$

where R_b is the planetocentric distance of the ionopause. Thus, the total change in potential energy of the system can be expressed by

$$\delta W = \int \left[\rho_i g - \frac{B^2}{4\pi R_b} \right] \delta R \, d\mathfrak{V} .$$

Accordingly, $\delta W > 0$ when $\rho_i g > B^2/4\pi R_b$. For a stable boundary we thus obtain the condition ($\delta W > 0$)

$$\rho_i g \equiv N_i m_i g > \frac{B^2}{4\pi R_b} \equiv \frac{2 p_{sw}}{R_b} . \tag{6.43}$$

Using the appropriate values for the Venus ionopause based on the Mariner 5 observations, a requirement for a stable ionosphere boundary is that $m_i > m(H^+)$, i.e., the presence of ions heavier than protons at the altitude of the ionopause.

For an ionospheric plasma contained by a dipole magnetic field, the charged particles experience an outward force in the curved flux tubes (especially where the centrifugal force due to planetary rotation becomes predominant), i.e., in the direction of decreasing particle density. This situation is again similar to the classical Rayleigh–Taylor instability. Whereas

the Rayleigh–Taylor instability refers to a hydrostatic boundary, the Kelvin–Helmholtz instability arises at a hydrodynamic boundary, i.e., when two incompressible fluids are in relative motion to each other.

Since the plasma is confined by magnetic flux tubes, the instability tends to interchange flux tubes. This type of instability is therefore also known as interchange instability [226].

For adiabiatic (fast) interchange of flux tubes the condition for marginal stability ($\delta W = 0$) can be expressed by [227]

$$\frac{\mathrm{d}}{\mathrm{d}R}[pV^{\gamma}] = 0$$

where $p = Nk_{\mathrm{B}}T_{\mathrm{p}}$ is the plasma pressure (energy density) with $T_{\mathrm{p}} = T_{\mathrm{e}} + T_{\mathrm{i}}$ the effective plasma temperature; V is the volume of a flux tube ($V \propto R^4$) and γ is the ratio of specific heats ($\frac{5}{8} < \gamma < \frac{7}{4}$), depending on the pitch angle distribution, with $\gamma = \frac{5}{3}$ a representative value. From $pV^{\gamma} = \text{const.}$, we obtain

$$p \equiv Nk_{\mathrm{B}}T_{\mathrm{p}} \propto R^{-\frac{20}{3}} . \tag{6.44a}$$

Thus, as long as the energy density of the ionospheric plasma decreases more slowly than $\propto R^{-7}$, (e.g., a plasma density distribution $N \propto R^{-(3.5\pm0.5)}$ as is found for the "collisionless" regime of the outer ionosphere, i.e., inside the Earth's plasmasphere), such a distribution should be stable against interchange (even if $T_{\mathrm{p}} = \text{const.}$). At the plasmapause, however, the plasma density decreases much faster and this configuration, as illustrated in Fig. 6.13, would be unstable unless the effective plasma temperature T_{p} increased significantly in the same region in order to satisfy the condition $p \propto R^{-7}$. This

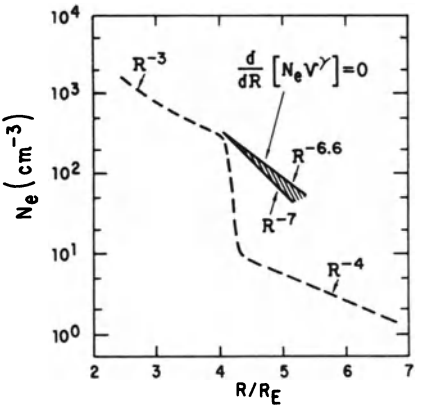

Fig. 6.13. Electron density profile in the equatorial plane of the plasmasphere from whistler observations and conditions for stability against plasma interchange (after F. L. Scarf [227]).

condition seems to be met for the terrestrial plasmapause, where T is found to increase appreciably [226]. For isothermal (slow) interchange ("thermal convection") of flux tubes the marginal stability criterion is given by

$$pV = \text{const.}$$

and thus,

$$p \equiv N k_B T_p \propto R^{-4} \tag{6.44b}$$

represents a plasma energy density distribution which is stable against slow (isothermal) interchange. This condition is also satisfied everywhere in the terrestrial plasmasphere, except near the plasmapause for $T_p = \text{const.}$

When the stability criterion is not satisfied, the amplitude a of perturbations will grow with time according to $a \propto \exp[(g'/L)^{\frac{1}{2}} t]$, where g' is the effective gravitational force per unit mass causing the instability (gravitational and/or centrifugal force) and L is the scale length of the density gradient; the growth rate [sec^{-1}] for the instability is given by

$$\gamma = \left(\frac{g'}{L}\right)^{\frac{1}{2}} . \tag{6.45}$$

When the plasma density distribution follows $N \propto R^{-n}$ (where n is greater than the exponent required for marginal stability), the scale length is given by $L \sim R/n$. Instabilities induced by the centrifugal force ($g' = R\Omega^2$) would then grow with a rate $\gamma = \sqrt{n}\,\Omega$; this process could be of importance in the Jovian ionosphere on account of the large angular rotation rate of Jupiter.

A plasma micro-instability known as two-stream instability can also be of importance in planetary ionospheres [224]. This instability occurs when two particle streams are flowing through each other. This is the case for ions in the polar wind or when the electrons and ions have different drift velocities in an electric field due to their difference in collision frequency with the neutrals and their gyrofrequencies. The latter condition applies to the dynamo regions.

The two-stream instability refers to the growth of longitudinal plasma ion waves which occurs when the relative velocity between the two streams (in the ideal case of a "collisionless plasma" without a magnetic field) is greater than the thermal velocity. Landau damping (important when the particle and wave velocities are comparable) has a stabilizing effect. The two-stream instability leads to the existence of plasma irregularities which travel with the ion acoustic velocity

$$c_i = (2k_B T/m_i)^{\frac{1}{2}} .$$

For a partially ionized plasma, such as a planetary ionosphere, the $\mathbf{E} \times \mathbf{B}$ drift in the (dynamo) electrojet region leads to a two-stream instability even when the drift velocity of the electrons is $\sim v_{th}^{(i)} \sim 0.01 v_{th}^{(e)}$, for $T_i \sim T_e$.

The velocity threshold for instability is lower than for the no field case (or propagation $\| B$), since Landau damping is absent for propagation of the ion plasma wave perpendicular to the magnetic field. The gradient drift or $\mathbf{E} \times \mathbf{B}$ instability appears to be responsible for ionospheric irregularities associated with both sporadic E and "spread" F in the terrestrial ionosphere.

Magnetohydrodynamic (MHD) instabilities at the boundary layer between the solar wind and the atmospheric plasma can cause loss by detached ionospheric bubbles. Since there is a shear velocity between the plasma flow in the solar wind (magnetosheath) and the plasma in the ionosphere, the above discussed Kelvin–Helmholtz instability can develop and evolve into a nonlinear stage, where ionized atmospheric constituents can detach from the ionosphere in the form of plasma clouds.

It was found by the Pioneer Venus Orbiter that plasma clouds are a common feature caused by the solar wind–ionosphere interaction on Venus. Analysis of data by the MAG/ER (Magnetometer/Electron Reflectometer) instrument of MGS revealed also cold electrons above the Martian ionopause, which indicate the presence of plasma clouds also on Mars.

In ideal MHD, the Kelvin–Helmholtz instability is treated by using the assumption of a negligible Larmor radius

$$r_{\mathrm{L}} = \frac{cmvB}{e}$$

of the particles, where e is the electron charge, c velocity of light and v the particle velocity. But in fact, this quantity is not negligible. One can show that the ideal hydrodynamic analysis of the Kelvin–Helmholtz instability at the boundary layer leads to the conclusion that the waves with the shortest wavelength are the most unstable ones.

As a consequence, there would be no limit in the growth rate with decreasing wavelength. Therefore, the ideal MHD formulation of the Kelvin–Helmholtz instability is inapplicable to the stability problem at the interface of two interacting fluids with different shear velocities. The effect of a finite ion Larmor radius was investigated by [228] who demonstrated that the finite Larmor radius effect tends to stabilize short wavelength perturbations and helps to avoid the zero wavelength anomaly [229]. This stabilization can be seen in Fig. 6.14. By including gravity, the process acts to stabilize the interface against long wavelength perturbations (see Fig. 6.14) [229, 230, 231]. It is pointed out that this term also works effectively when the density ratio across the discontinuity is large [232]. According to [233], the finite thickness of the boundary layer leads to the requirement that the wave number k for the maximum instability growth rate must satisfy the condition $k\,d/2 \approx 0.5$, where d is the thickness of the boundary layer.

One can use a coordinate system, where X points from the planet to the Sun, Z is directed parallel to the IMF direction, and Y completes the right-hand system. In such an IMF coordinate system, the components of the IMF are $(0, 0, |B_{\mathrm{IMF}}|)$.

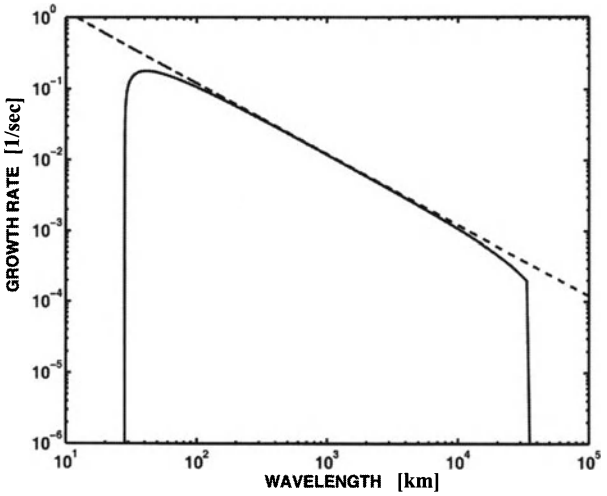

Fig. 6.14. Instability growth rate as a function of the instability wavelength in ideal magnetohydrodynamics (dashed line) and by including the finite Larmor radius effect and gravity (solid line). The viscous interaction leads to a short-wavelength stabilization, while gravity gives a long-wavelength stabilization (after T. Penz et al. [230]).

One derives a dispersion relation for the case that the wave vector is parallel to the solar wind flow and perpendicular to the IMF direction ($\mathbf{k} \parallel \mathbf{v} \perp \mathbf{B}$). One can use the dispersion relation appropriate for an incompressible plasma and an infinitely thin boundary layer including gravity and the finite Larmor radius effect by [229, 230]

$$\omega = k\,\frac{\rho_1 v_1 + \rho_2 v_2}{\rho_1 + \rho_2} + k\,|k|\,\frac{\nu_2\rho_2 - \nu_1\rho_1}{\rho_1 + \rho_2} \pm i\,\gamma\,, \tag{6.46}$$

with

$$\gamma = \left(k^2 \frac{\rho_1\rho_2(v_2 - v_1)^2}{(\rho_1 + \rho_2)} + 2\,|k^3|\,\frac{(\nu_1 + \nu_2)\rho_1\rho_2(v_2 - v_1)}{(\rho_1 + \rho_2)^2} - \right.$$

$$\left. -k^4 \left(\frac{\nu_2\rho_2 - \nu_1\rho_1}{\rho_1 + \rho_2} \right)^2 - |k|\,\frac{g(\rho_2 - \rho_1)}{\rho_1 + \rho_2} \right)^{1/2} \tag{6.47}$$

where ω is the frequency, and γ is the growth rate. v and ρ denote the plasma velocity and the plasma density, subscripts 1 and 2 denote ionosheath and ionospheric conditions, respectively, and g is the gravitational acceleration at the ionopause. In the ionosheath, the viscous coefficient is given as

$$\nu_1 = \frac{m_i v^2}{4\,e\,B}, \tag{6.48}$$

where m_i is the ion mass, e is the elementary charge and B is the magnetic field strength in the ionosheath. Since $B \approx 0$ in the ionosphere, the viscous coefficient can be written as $\nu_2 = v\,l$, where l denotes the mean free path of the particles [232]. If we assume that the IMF is not located purely in the $\hat{y}$ direction, the surface is stabilized, since there exists a magnetic tension $[\sim (\mathbf{k} \cdot \mathbf{B})^2]$, which impedes the Kelvin–Helmholtz instability [231].

Because the detaching of plasma clouds is a nonlinear process, it is necessary that the characteristic time scales in the system are below the instability growth rate. If this is the case, the instability can evolve into a nonlinear stage, giving rise to the development of ionospheric plasma clouds.

A characteristic time scale is the magnetic barrier formation time T_m [234], which can be estimated as the time of the transport of a "frozen-in" magnetic field line from the bow shock to the stagnation point

$$T_m = -\int_1^{x_s} \frac{1}{u_x}\,\mathrm{d}x\,. \tag{6.49}$$

Taking a simple linear approximation for the velocity u_x along the stagnation stream line

$$u_x = -\frac{u_s(x-1)}{\Delta_s} \tag{6.50}$$

we find the magnetic formation time as

$$T_m = \frac{\Delta_s}{u_s} \ln \frac{\Delta_s}{\alpha} \tag{6.51}$$

where Δ_s and u_s are the magnetosheath thickness and the velocity just downstream of the shock, respectively. α is a small length scale, where the "frozen-in" condition is not valid, because of kinetic plasma effects [234].

VI.6 Ion Loss due to Momentum Transport

The Automatic Space Plasma Experiment with a Rotating Analyzer (ASPERA) instrument on board the Phobos 2 spacecraft observed a strong interaction between the solar wind plasma and the cold ionospheric plasma in the Martian topside ionosphere in such a way that the solar wind plasma transfers momentum directly to the Martian ionosphere in a dayside transition region to the deep plasma tail [235] is

$$v_i = v_{sw} \Lambda \left[1 - \left(\frac{\eta_{sw} v_{sw}^2}{n_{sw} v_{sw}^2}\right)\right]^{\frac{1}{2}} \tag{6.52}$$

with

$$\Lambda = \left[\left(\frac{n_{sw} m_{sw} \delta_{sw}}{n_i m_i \delta_i} \right) \right]^{\frac{1}{2}} \tag{6.53}$$

where n_{sw} and n_i are the number density of the solar wind and ionospheric plasmas, η_{sw} is the density of the solar wind at the boundary of the planetary obstacle, m_{sw} and m_i are the mass of the solar wind protons and the dominant ionospheric O^+ ions, v_{sw} and v_{sw} are the velocities of the solar wind at the boundary of the planetary obstacle and outside the velocity shear, and δ_i and δ_{sw} correspond to the effective momentum flux thickness of the ionospheric flow and the velocity shear in the shocked solar wind [236, 237]. On Mars it is found that this momentum transport seems to be capable of accelerating ionospheric O^+ ions to velocities $v_i \approx 5$ km s^{-1} resulting in energies larger than the Martian escape energy of about 2 eV. Theoretical studies show that cool ion escape due to viscous ion momentum transport effects may play an important role in the loss of water from Mars [236, 237]. On a larger non-magnetized planet like Venus the similar process can transport major ions to the nightside.

VII Evolutionary Processes of Planetary Atmospheres

Planetary aeronomy as a study of the interaction between the stellar radiation and particle environment with planetary upper atmospheres now finds its application more and more in the newly detected exoplanets. Terrestrial exoplanets may also exist around other stars such as the many giant Jupiter-class exoplanets already discovered within the solar neighborhood. Space-borne telescopes will detect these planets in the near future and will characterize their atmospheres by interferometric and/or coronagraphic imaging. The discovery of other Earth-size planets in various orbital distances to their host stars will also enhance our understanding of the evolution of the terrestrial atmosphere in contrast to the CO_2 atmospheres of Venus and Mars or reduced secondary atmospheres of icy bodies like Saturn's large satellite Titan. Studies related to planetary aeronomy will therefore contribute to investigations of evolutionary processes, the stability of planetary atmospheres and their water inventories and the characterization of exoplanetary atmospheres as well as in a more detailed classification of the Habitable Zone (HZ).

VII.1 Future Outlook: Aeronomy of Exoplanets

After the discovery of more than 100 giant Jupiter-class exoplanets it is only a matter of time until Uranus-type and Earth-size exoplanets will also be discovered. The CoRoT and Kepler space observatories to be launched in 2006 and 2007 and Eddington will use high precision photometry for planetary detection by the transit method.

By applying the statistics of discovered short periodic Jupiter-class exoplanets to the suggested 180,000 light curves obtained by CoRoT one may expect the discovery of about 200 hot giant exoplanets (0.1 M_{Jup} with orbital periods < 10 days) after dropping 50% of the targets due to their radius or binary systems [238].

Because the maximum observation runs will last 150 days, the longest planetary orbital period unambiguously detectable by CoRoT will be about 75 days, which corresponds to orbital distances of 0.25–0.5 AU related to the spectral type. One should note that these orbital distances are inside the HZ of M and K stars. The radius of the smallest detectable exoplanets were estimated from blind transit detection using various algorithms on simulated

data-sets produced according to the definition of the CoRoT instrument [239]. For periodic transits, exoplanets with size comparable to that of the Earth can be detected if the host star is a bright solar-type one [239]. The detection is favored for scarce M0 stars [238]. More precisely, [240] have shown that exoplanets with sizes from 2 Earth-radii and larger thus appear clearly within CoRoT's detection capabilities.

A year later the Kepler mission will look for planetary transits across about 50,000 stars [241]. This mission is specifically designed like Eddington to detect and characterize hundreds of terrestrial and larger exoplanets in or close to the HZ of their host stars. From model simulations and studies on planetary formation theory the expected results of Kepler are predicted to be the discovery of terrestrial exoplanets, with periods from days to a few years of about 50 planets with the size of Earth, about 185 planets with the size of about 1.3 Earth-radii, about 640 planets with the side of about 2.2 Earth-radii and about 12% with two or more planets per system.

The main aim of these missions is to explore the structure and diversity of planetary systems due to a survey of large stellar samples. This goal will be archived by:

1) The discovery of terrestrial and larger exoplanets in or near the HZ of a wide variety of stellar spectral types.
2) The determination of sizes and semi-major axes of the discovered exoplanets.
3) Estimation of the frequency and orbital distributions of exoplanets in multiple-stellar systems.
4) The determinations of semi-major axis, albedo, size, mass and density of short-periodic exoplanets.
5) Identification of additional exoplanets of each photometrically discovered planetary system by using complementary techniques.
6) The determination of properties of those stars that harbour exoplanetary systems.

The suspected results of CoRoT, Kepler and Eddington can be used for primary target star selection and precursor studies of follow up missions like ESA's ground based interferometer Genie, NASA's Space Interferometry Mission (SIM), and the planned huge space based terrestrial planetary finding missions Darwin/TPF.

In the next decade the proposed Darwin mission [242] and the TPF [243] will attempt to observe terrestrial exoplanets directly either in the thermal infrared (IR) or visible/near-infrared wavelengths and will obtain spectra of the observed planetary atmospheres.

Once one knows the abundances of atmospheric key gases, one can also make informed speculations on the likelihood that life may exist on a discovered terrestrial exoplanet if it orbits inside the HZ [244]. Therefore, one of the main tasks of these missions is to look for bio-signatures on terrestrial exoplanets which orbit inside the HZ of their host stars and ask questions like:

1) What levels of atmospheric O_2 can be build up in the absence of life from non-organic photochemical processes?
2) Can abiotic O_2 result in detectable signatures of O_3 in the IR or visible?
3) Can abiotic and biotic cases in the origin of O_2 and O_3 identified and separated from observations?

Although current studies suggest that the simultaneous IR detection of O_3, CO_2 and H_2O, provided by Darwin should be a robust way to discriminate photochemical O_2 production from biological photosynthesis [244] it is important to know what it takes to create and maintain a habitable terrestrial planet for long time periods. Further, classifications of what such atmospheres might look like, or which physical parameters may prevent a terrestrial planet from becoming or remaining habitable must be carried out in the future.

By applying our own experience from Earth, only planets within the liquid water HZ may support the evolution of life on their surfaces so that their atmospheric gases can be studied wether they are inhabited by life forms and have developed a biosphere.

VII.2 Habitable Zone

The region around a star in which life-supporting planetary environments can exist had been termed the Habitable Zone (HZ) [245, 246], or the Ecosphere [247, 248] as shown in Fig. 7.1. The circumstellar HZ was defined and delimited by [249] based on the consideration of a planet of the size and mass

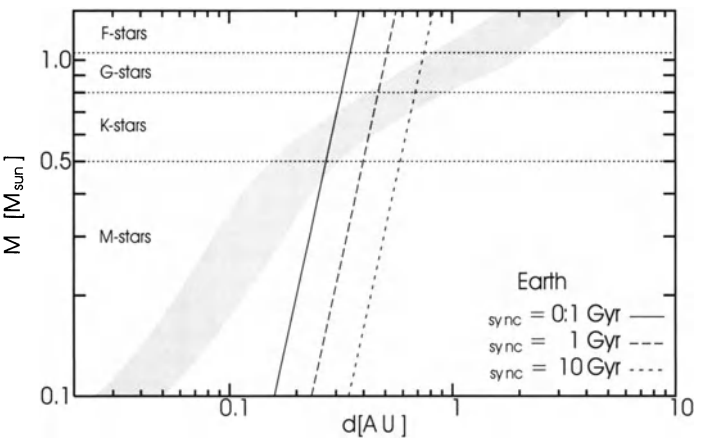

Fig. 7.1. Habitable zone (shaded area) as a function of stellar mass and orbital distance and evolutional areas of tidal locking boundaries (courtesy of F. Selsis and J.-M. Grießmeier).

of the Earth, containing large H_2O and CO_2 reservoirs at a distance d of its host star. If there is an amount of atmospheric CO_2 able to sustain stable liquid H_2O at the planetary surface, the distance d belongs to the HZ. If d is below a critical distance, the planet would experience a *runaway greenhouse effect*: the vaporized H_2O starts to increase the surface warming and thus enhance the evaporation in a positive feedback [250]. This results in a H_2O-rich atmosphere that keeps the surface temperature above 100 degree Celsius and in which H_2O vapor reaches the high altitudes, where it is photolyzed. Within a period of the order of 10–100 Myrs, the planet loses the hydrogen to space and becomes dry.

At the outer border of the HZ, an increase in the CO_2 pressure results in a surface cooling more than heating, due to enhanced Rayleigh back-scattering of the incoming stellar radiation to space. With this definition, the HZ only depends on the luminosity of the star (including its spectral energy distribution) and the surface temperature which is assumed to be stabilized above zero degrees Celsius through the carbon-silicate cycle [251].

The range of the HZ is slightly larger for planets that are larger than Earth and for exoplanets, which have higher N_2 partial pressures. The HZ moves to greater orbital distances with time because the star increases luminosity as it ages.

Stars later than F0 have relatively short main sequence life times ≤ 3 Gyr and may therefore also be candidates for harboring habitable terrestrial exoplanets in their HZ. The HZ of F-type stars is larger and may reach orbital distances between 1 and 2.5 AU, while the HZ of K and M dwarf stars is smaller and occurs closer to the star.

The current simplified definition of the HZ and the estimation of its inner and outer limits [249] are useful but several uncertainties still need to be debated so that at the best, the definition of the HZ can tell us that outside of its limits, habitable planets cannot be found. Indeed, if a planet needs to orbit within the HZ to be habitable, this condition is far from being sufficient. Though we do not know the conditions necessary for the emergence of life, we can identify some conditions that dramatically frustrate the existence or the evolution of a habitable world:

1) Due to their mass or to their metallicity or to the absence of giant planets, low mass dwarf stars may probably not have the capability to produce big enough terrestrial planets.
2) Planetary systems may not have stable orbits within the HZ due to the presence of short period giant planets [252].
3) Terrestrial planets, orbiting within the HZ, may experience an intense asteroid bombardment all along the lifetime of its star due to a specific configuration of the giant planets [253].
4) Terrestrial planets might have a negligible initial reservoir for outgassing products.

5) Most stars belong to a binary or multiple system, which could affect the long term stability of the orbits within the HZ [252].
6) The HZ of low mass K stars and M stars are in orbital distances, where the planets are tidally locked, which may result in climate effects and weak intrinsic magnetic moments [37, 254].
7) Since planets inside the HZ of M and some K stars are tidally locked, plate tectonics may not develop and super-volcanoes (big hot spot volcanoes) may frustrate life periodically or destroy the long-time habitability of the planet [255].
8) Strong stellar winds and coronal mass ejections (CME's) can compress the magnetospheres of terrestrial planets inside the close-in HZ of M stars.

Further, one important point, which is directly related to aeronomy, is the long time stability of planetary atmospheres. The HZ of low mass stars (late K and M: the large majority of stars) are submitted to strong XUV irradiation (cf. Chap. I) and with a high probability, to strong stellar winds as well. This radiation and particle exposure can make the atmosphere of an Earth-size planet unstable and may also limit the range of the purely climatologically defined HZ.

VII.3 Atmospheric Evolution of Terrestrial Planets

The known terrestrial planets with substantial atmospheres are Venus, Earth and Mars and as a special case Saturn's large satellite Titan. The initial major atmospheric gases on the three classic early terrestrial-type planets Earth, Venus and Mars were most probably CO_2, H_2O and N_2. Most of the Earth's CO_2 was transformed into the surface by chemical weathering and Venus has lost most of its water so that CO_2 remained. Mars' atmosphere may have been eroded by impacts due to large meteoroids during the first 500 Myr of the planet's origin.

From the current knowledge of our own terrestrial planets one can suggest that the critical phase if a water-bearing planet can evolve into a habitable world like Earth is its survival during:

1) The period of heavy bombardment by asteroids and comets [256, 257, 258].
2) The active XUV, stellar wind and CME period of the young star [25, 72].

Impact erosion, however, can erode a part of an atmosphere but also adds volatiles to it. The balance depends on the composition of the impacting object and on the mass of the growing planet. Once a planet attains nearly the present masses and escape velocities of Venus or Earth atmospheric erosion by impacts may not erode the atmospheres completely although erosion becomes very efficient. On a low mass planet like Mars impact erosion seems to be the major atmospheric loss process which may remove the majority of the atmosphere and out gassed water during heavy bombardment periods [256, 257].

An other criteria for the survival of a planetary atmosphere and its water inventory are the high X-ray and extreme ultraviolet fluxes of young stars as discussed in Chap. I. In fact hydrodynamic "blow off" (cf. Chap. II) and expansion of the hydrogen atmosphere of the Jupiter-class exoplanet HD209458 b was observed by [128, 130] and studied theoretically [72, 259, 260].

As discussed in Chap. II the loss rates caused by planetary winds are orders of magnitudes higher than thermal escape by the Jeans treatment. The loss of heavier constituents by planetary hydrogen winds is essentially aerodynamic drag. For water bearing terrestrial planets with early CO_2 atmospheres the escape flux of the light gas in the upper atmosphere may be limited by the rate at which it can diffuse through the upper atmosphere. However, long-time XUV radiation in the order of about 50–100 times the present value may affect the water inventory of a terrestrial exoplanet and possible even the stability of its whole atmosphere.

The latter problem may occur on a terrestrial H_2O-rich planet inside the HZ of a low mass M or K star, where there is observational evidence that their XUV energy fluxes stay active longer (cf. Chap. I). First the CO_2 may prevent extreme hydrodynamic escape due to its heavy mass and good IR cooling capabilities, but after the CO_2 is removed from the atmosphere like on Earth due to chemical weathering in a humid wet environment, nitrogen may become the dominant constituent in the upper atmosphere.

At a G-type star the high XUV energy flux decreases relatively fast but for M or K stars the XUV energy flux remains at high levels (cf. Chap. I) so that the exosphere may be heated up to "blow off" temperatures, which can evaporate the whole atmosphere although the planet orbits inside the HZ (cf. Chap. II). Such scenarios are "most likely" for terrestrial exoplanets at orbits inside the HZ on M stars, because these spectral types stay active in the XUV irradiation up to several Gyr. Recent studies of the XUV energy flux evolution of K stars suggest that the XUV energy flux of these stars decreases faster than at M stars, so that the atmospheres and water inventories of exoplanets orbiting such host stars may survive, although more detailed studies are needed [36].

A third point, which may even prevent the formation of an atmosphere at terrestrial exoplanets inside the HZ of M stars is the strong stellar wind at close orbital distances ≤ 0.3 AU. As discussed in Chap. I and Chap. VI terrestrial exoplanets at such orbital distances may never form an atmosphere because the outgassed constituents will be ionized and picked up by the strong stellar wind of the active young star. Particle sputtering will also be very effective at close orbital distances so that Earth-like exoplanets in orbits inside the HZ of M stars may evolve to Mercury-like bodies. Even a magnetosphere will not protect the atmosphere at close orbital distances because the strong stellar wind of the young star may compress the intrinsic magnetic field to the planetary surface. Moreover, exoplanets inside the HZ of M stars are tidally locked so that their magnetic dynamos and the resulting

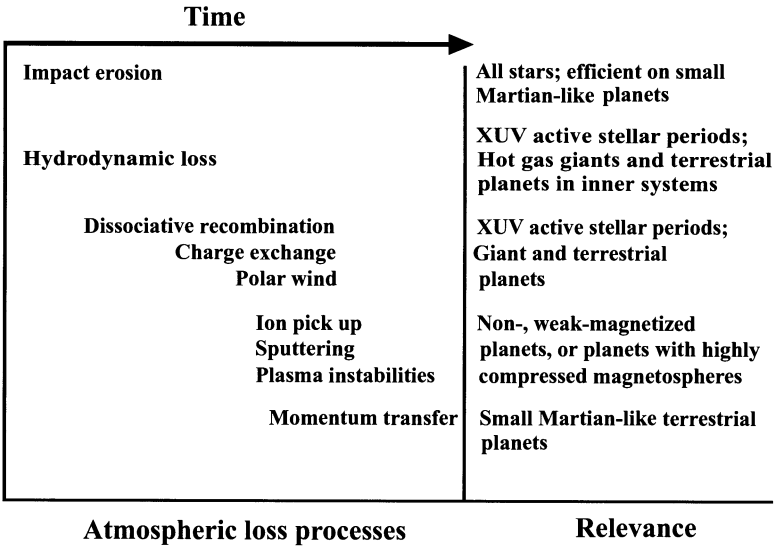

Fig. 7.2. Illustration of various loss processes, important for atmospheric evolution of terrestrial planets as a function of time.

magnetospheres will be weaker than the magnetosphere of Earth at 1 AU [37] (cf. Chap. VI).

Figure 7.2 illustrates the importance of various thermal and non-thermal atmospheric loss processes of a terrestrial planet as function of time. By considering all processes in Fig. 7.2, terrestrial exoplanets orbiting M stars may not be habitable, because they may not develop atmospheres or they may lose their atmospheres and their H_2O inventory due to the long-time activity in high XUV radiation and strong stellar winds. From this point of view we suggest that mid- to early K and G stars should be considered as good primary stellar candidates for the search of "hypothetically" habitable planets in future terrestrial planet finding missions.

VIII Appendix

Table A.1. Planetary data*

		Radius [km]	Mean density [g cm^{-3}]	Planetary mass [$\times 10^{27}$ g]	Distance [10^6 km]	from Sun [AU]	Year [Days]	Rotation [Days]
(Inner	Mercury	2440	5.247	0.33022	57.909	0.387	87.6	58.64
Planets)	Venus	6052	5.204	0.088	108.208	0.723	220	−243**
	Earth	6371	5.515	1.0	149.597	1.0	365	1.00
	Mars	3390	3.9335	0.149	227.936	1.52	687	1.025
(Outer	Jupiter	69911	1.326	1898.7	778.412	5.2	4219.4	0.41
Planets)	Saturn	58232	0.6873	568.51	1426.725	9.53	10758.4	0.44
	Uranus	25362	1.318	86.849	2870.972	19.191	30666.2	−0.71
	Neptune	24600	1.638	102.44	4498.252	30.06	60148.8	0.67
	Pluto	1151	1.1	0.013	5906.376	39.481	90491.0	153.28

* For gravitational acceleration and escape velocity see Tables 2.1 and 2.4 of the text.

** Minus sign denotes retrograde motion.

Table A.2. Physical parameters of large satellites.

Satellite	Planetary mean distance [km]	Siderial period [days]	Radius [km]	Mass [g]	Mean density [g/cm^3]
Io	421600.0	1.769	1815.0	8.94×10^{25}	3.57
Europa	670900.0	3.551	1569	4.8×10^{25}	2.97
Ganymede	1070000.0	7.155	2631.0	1.48×10^{26}	1.94
Callisto	1883000.0	16.689	2400.0	1.08×10^{26}	1.86
Titan	1221850.0	15.945	2575.0	1.35×10^{26}	1.88
Triton	354800.0	5.877	1350.0	2.14×10^{25}	2.07
Charon	19640.0	6.387	595.0	1.77×10^{24}	2.0

Table A.3. Physical constants in SI and cgs systems.

Physical constant	Symbol	Value	SI	cgs
Avogadro's number	N_A	6.0222	10^{26}/kmol	10^{23}/mol
Atomic mass unit	amu	1.6605	10^{-27} kg	10^{-24} g
Proton mass	m_p	1.6726	10^{-27} kg	10^{-24} g
Electron charge per mass ratio	e/m_e	1.7588	10^{11} C/kg	10^{7} emu/g
Electron charge	e	1.6022	10^{-19} C	10^{-20} emu/g
Electron mass	m_e	9.1096	10^{-31} kg	10^{-28} g
Bohr radius [a.u.]	a_0	5.2918	10^{-11} m	10^{-9} cm
Rydberg constant		1.097373	10^{7}/m	10^{5}/cm
Speed of light in the vacuum	c	2.99792	10^{8} m/sec	10^{10} cm/sec
Planck's constant	$\hbar$	6.6262	10^{-34} Jsec	10^{-27} erg sec
Gas constant	$\mathfrak{R}$	8.314	10^{3} J/kmol/K	10^{7} erg/mol/K
Gravitational constant	G	6.67259	10^{-11} $m^3kg^{-1}sec^{-2}$	10^{-8} $cm^3g^{-1}sec^{-2}$
Boltzmann constant	k	1.3806	10^{-23} J/K	10^{-16} erg/K
Stefan–Boltzmann constant	σ_{SB}	5.772	10^{-8} $W/m^2/K^4$	10^{-5} $erg/cm^2/K^4$

Table A.4. Energy conversion factors.

	1 erg	1 J or 1 Wsec	1 cal	1 eV	1 kJ/mol	1 kcal/mol
1 erg	1.0	1.0×10^{-7}	2.39×10^{-8}	6.24×10^{11}	6.02×10^{13}	1.44×10^{13}
1 J or 1 Wsec	1.0×10^{7}	1.0	2.39×10^{-1}	6.24×10^{18}	6.02×10^{20}	1.44×10^{20}
1 cal	4.184×10^{7}	4.184	1.0	2.61×10^{19}	2.52×10^{21}	6.02×10^{20}
1 eV	1.602×10^{-12}	1.602×10^{-19}	3.83^{-20}	1.0	96.5	2.31×10^{11}
1 kJ/mol	1.659×10^{-14}	1.659×10^{-21}	3.97×10−22	1.035×10^{-2}	1.0	2.39×10^{-1}
1 kcal/mol	6.94×10^{-14}	6.94×10^{-21}	1.66×10^{-21}	4.33×10^{-2}	4.184	1.0

Table A.5. Length units.

	1 mm	1 cm	1 m	1 km	1 nm	1 Å
1 mm	1.0	10^{-1}	10^{-3}	10^{-6}	10^{6}	10^{7}
1 cm	10.0	1.0	10^{-2}	10^{-5}	10^{7}	10^{8}
1 m	10^{3}	100.0	1.0	10^{-3}	10^{9}	10^{10}
1 km	10^{6}	10^{5}	10^{3}	1.0	10^{12}	10^{13}
1 nm	10^{-6}	10^{-7}	10^{-9}	10^{-12}	1.0	10.0
1 Å	10^{-7}	10^{-8}	10^{-10}	10^{-13}	10.0	1.0
1 AU	149.6×10^{12}	$149.6\times^{11}$	149.6×10^{9}	149.6×10^{6}	149.6×10^{20}	149.6×10^{21}

Table A.6. Astronomical length units.

1 Light year [Lyr]	9.4605×10^{12} km	0.3066 pc	63240.0 AU
1 parsec [pc]	30.857×10^{12} km	3.262 Lyr	206265.0 AU

Table A.7. Pressure units.

	1 Pa	1 N/mm^2	1 bar	1 Torr
1 Pa	1.0	10×10^{-6}	10×10^{-5}	0.0075
1 N/mm^2	10×10^{6}	1.0	10.0	7.5×10^{3}
1 bar	10^{5}	0.1	1.0	750.0
1 Torr	133.0	0.133×10^{-3}	1.33×10^{-3}	1.0

Table A.8. Magnetic units.

Magnetic field strengths	1 T	1 nT
1 Gauss	10^{-4}	10.0
1 Gamma [γ]	10^{-5}	1.0

Table A.9. The Sun.

Radius	9.960×10^{8} m
Mass	1.99×10^{30} kg
Luminosity	3.83×10^{26} W
Surface temperature	5780 K

References

1. Barstow, M. A., Holberg, J. B.: Extreme Ultraviolet Astronomy. Cambridge University Press (2003).
2. de Jager, C.: Solar ultraviolet and X-ray radiation. In: *Sun, Upper Atmosphere and Space.* (H. Odishaw, ed.), Ch. 1 Research in Geophys. Vol. **I**, MIT Press, 1–42 (1964).
3. Ivanov-Kholodnyi, G. S., Nikolski, G. M.: The Sun and the Ionosphere (short wave solar radiation and its effect on the ionosphere) Nauka, Moscow, 1969, Engl. Transl. NASA TTF-654 (1972).
4. Hunten, D. M.: Atmospheric evolution of terrestrial planets. Science **259**, 915–920 (1993).
5. Hall, L. A., Higgins, J. E., Chagnon, C. W., Hinteregger, H. E.: Solarcycle variation of the extreme ultraviolet radiation. J. Geophys. Res. **74**, 4181–4183 (1969).
6. Tobiska, W. K.: Recent solar extreme ultraviolet irradiance observations and modelling: A review. J. Geophys. Rev. **98**, 18879–18893 (1993)
7. Tobiska, W. K., Eparvier, F. G.: EUV97: Improvements to EUV irradiance modeling in the soft X-rays and FUV. Solar Phys., **177**, 147–159 (1998).
8. Chapman, S.: The absorption and dissociative or ionizing effect of monochromatic radiation in an atmosphere on a rotating earth. Proc. Phys. Soc. (London) **43**, 26–45 ; The absorption and dissociative or ionizing effect of monochromatic radiation in an atmosphere on a rotating earth. II. Grazing incidence. Proc. Phys. Soc. London, **43**, 483–501 (1931).
9. McDaniel, E. W.: Collision Phonomena in Ionized Gases, John Wiley and Sons, N. Y. (1964).
10. Hudson, R. D.: Critical review of ultraviolet photo-absorption cross sections for molecules of astrophysical and aeronomic interest. Rev. Geophys. **9**, 305–406 (1971).
11. Swider, W., Gardner, M. E.: On the accuracy of certain approximations for the Chapman function. Environmental Research Papers No. 272, Bedford, Mass.: Air Force Cambridge Research Labs (1967).
12. Van Allen, J. A.: On the nature and intensity of cosmic radiation. In: *Physics & Medicine of the Upper Atmosphere and Space* (White and Benson eds.) University of New Mexico Press, Albuquerque (1952).
13. Webber, W.: The production of free electrons in the ionospheric D layer by solar and galactic cosmic rays and the resultant absorption of radio waves. J. Geophys. Res. **67**, 5091–5106 (1962).
14. Rao, U. R.: Solar modulation of galactic cosmic radiation. Space Sci. Rev. **12**, 719–809 (1972).
15. Dubach, J., Barker, W A.: Charged particle induced ionization rates in planetary atmospheres. J. Atmospheric Terrest. Phys. **33**, 1287–1288 (1971).

16. Dalgarno, A.: Range and energy loss. In: *Atomic and Molecular Processes* (D. R. Bates ed.) Academic Press, New York 622–642 (1962).
17. Singer, S. F., Maeda, K.: Energy dissipation of spiraling particles in the polar atmospheres. Arkiv Geofysik **3**, 531–538 (1961).
18. Berger, M. J., Seltzer, S. M., Maeda, K.: Energy deposition by auroral electrons in the atmosphere. J. Atmospheric Terrest. Phys. **32**, 1015–1045 (1970).
19. Brown, R. R.: Solar cosmic ray effects in the lower ionosphere of Venus. Planetary Space Sci. **17**, 1923–1926 (1969).
20. Lammer, H., Stumptner, W., Molina-Cuberos, G. J., Bauer, S. J., Owen, T.: Nitrogen isotope fractionation and its consequence for Titan's atmospheric evolution. Planet. Space Sci. **48**, 529–543 (2000).
21. Becker, R. H., Clayton, R. N., Galimov, E. M., Lammer, H., Marty, B., Pepin, R. O., Weiler, R.: Isotopic signatures in terrestrial planets. Space Sci. Rev. **106**, 377–410 (2003).
22. Zahnle, K. J., Walker, J. C. G.: The evolution of solar ultraviolet luminosity. Rev. Geophys. **20**, 280–292 (1982).
23. Ayres, T. R.: Evolution of the solar ionizing flux. J. Geophys. Res. **102**, 1641–1651 (1997).
24. Guinan, E. F., Ribas, I.: Our changing Sun: the role of solar nuclear evolution and magnetic activity on Earth's atmosphere and climate. In: The Evolving Sun and its Influence on Planetary Environments. (B. Montesinos, A. Giménz, and E. F. Guinan, eds.) ASP, San Francisco **269**, pp. 85–107 (2002).
25. Wood, B. E., Müller, H.-R., Zank, G., Linsky, J. L.: Measured mass loss rates of solar-like stars as a function of age and activity. Astrophys. J. **574**, 412–425 (2002).
26. Newkirk Jr., G.: Solar variability on time scales of 10^5 years to $10^{9.6}$ years. Geochi. Cosmochi. Acta Suppl. **13**, 293–301 (1980).
27. Skumanich, A.: Timescales for CA II emission decay, rotational braking and lithium depletion. Astrophys. J. **171**, 565–567 (1972).
28. Simon, T., Boesgaard, A. M., Herbig, G.: The evolution of chromospheric activity and the spin-down of solar-type stars. Astrophys. J. **293**, 551–570 (1985).
29. Keppens, R., MacGregor, K. B., Charbonneau, P.: On the evolution of rotational velocity distributions for solar-type stars. Astron. Astrophys., **294**, 469–487 (1995).
30. Lammer, H., Lichtenegger, H. I. M., Kolb, C., Ribas, I., Guinan, E. F., Bauer, S. J.: Loss of water from Mars: Implications for the oxidation of the soil. Icarus **165**, 9–25 (2003).
31. Stelzer, B., Neuhäuser, R.: X-ray emission from young stars in Taurus-Auriga-Perseus: Luminosity functions and the rotation-activity-age relation. Astron. Astrophys. **377**, 538–556 (2001).
32. Pizzolato, N., Maggio, A., Micela, G., Sciortino, S., Ventura, P.: The stellar activity-rotation relationship revisited: Dependence of saturated and non-saturated X-ray emission regimes on stellar mass for late-type dwarfs. Astron. Astrophys. **397**, 147–157 (2003).
33. Schmitt, J. H. M. M., Fleming, T. A., Giampapa, M. S.: The X-Ray View of the Low-Mass Stars in the Solar Neighborhood. Astrophys. J. **450**, 392–400 (1995).
34. Vilhu, O., Walter, F. M.: Chromospheric-coronal activity at saturated levels. Astrophys. J. **321**, 958–966 (1987).

35. Stauffer, J. R., Caillault, J.-P., Gagne, M., Prosser, C. F., Hartmann, L. W.: A deep imaging survey of the Pleiades with ROSAT. Astrophys. J. Suppl., **91**, 625–657 (1994).
36. Ribas, I., Guinan, E. F.: Evolution of the solar magnetic activity over time and effects on planetary atmospheres: I. High-energy irradiances (0.1–170 nm). submitted to Astrophys. J. (2004).
37. Grießmeier, J.-M., Motschmann, U., Stadelmann, A., Penz, T., Lammer, H., Selsis, F., Ribas, I., Guinan, E. F., Biernat, H. K., Weiss, W. W.: The effect of tidal locking on the magnetospheric and atmospheric evolution of "Hot Jupiters". Astron. Astrophys. in press (2004).
38. Zhang, M. H. G., Luhmann, J. G., Bougher, S. W., Nagy, A. F.: The ancient oxygen atmosphere of Mars: implications for atmosphere evolution. J. Geophys. Res. **98**, 10915–10923 (1993).
39. Schwenn, R. 1990, in Physics of the Inner Heliosphere. Springer-Verlag, Berlin 99–181 (1990).
40. Kockarts, G.: Mean molecular mass and scale heights of the upper atmosphere. Ann. Geophys. **22**, 91 (1966).
41. Nicolet, M.: The structure of the upper atmosphere. In: Research in Geophysics. (H. Odishaw, ed.). Vol. I, Cambridge: The MIT Press, 243–275 (1964).
42. Mange, P.: Diffusion in the thermosphere. Ann. Geophys. **17**, 277 (1961).
43. Chapman, S., Cowling, T. G.: The Mathematical Theory of Nonuniform Gases. Cambridge University Press, 2nd, 431 (1952).
44. von Zahn, U., Kumar, S., Niemann, H., Prinn, R.: Composition of the Venus atmosphere. In: Venus. (D. M. Hunten, L., Colin, T. M. Donahue, V. I. Moroz eds.), The University of Arizona Press, 299–430 (1979).
45. von Zahn, U., Krankowsky, D., Mauersberger, K., Nier, A. O., Hunten, D. M.: Venus thermosphere: In-situ composition measurements, the temperature profile, and the homopause altitude. Science **203**, 768–770 (1979).
46. Hines, C. O.: Eddy diffusion coefficients due to instabilities in internal gravity waves. J. Geophys. Res. **75**, 3937–3939 (1970).
47. Donahue, T. M.: Deuterium in the upper atmosphere of Venus and earth. J. Geophys. Res. **74**, 1128–1137 (1969).
48. Hunten, P. M.: Hydrogen isotopes around the planets. Comm. Astrophys. & Space Phys. **III/1**, 1–5 (1971).
49. Izakov, M. N.: On theoretical models of the structure and dynamics of the Earth's thermosphere. Space Sci. Rev. **12**, 261–298 (1971).
50. Hines, C. O.: Internal gravity waves at ionospheric heights. Can. J. Phys. **38**, 1441–1481 (1960).
51. Charney, J. G., Drazin, P. G.: Propagation of planetary-scale disturbances from the lower into the upper atmosphere. J. Geophys. Res. **66**, 83–109 (1961).
52. Bates, D. R.: Some problems concerning the terrestrial atmosphere above about 100 km level. Proc. Roy. Soc. A **253**, 451–462 (1959).
53. Stewart, R. W: Radiative terms in the thermal conduction equation for planetary atmospheres. J. Atmospheric Sci. **25**, 744–749 (1968).
54. Harris, I., Priester, W.: Time dependent structure of the upper atmosphere. J. Atmospheric Sci. **18**, 286–301 (1962).
55. Rishbeth, H., Moffett, R. J., Bailey, G. J.: Continuity of air motion in the mid latitude thermosphere. J. Atmospheric Terrest. Phys. **31**, 1035–1047 (1969).
56. Jacchia, L. G.: Atmospheric density variations during solar maximum and minimum. Paper 17, Annls. IQSY, Vol. **5** Solar-Terrestrial Physics Terrestrial Aspects. MIT Press, 333–339 (1969).

57. Dickinson, R.E., Pablo Lagos, C., Newell, R. E.: Dynamics of the neutral gas in the thermosphere for small Rossby number motions. J. Geophys. Res. **73**, 4299–4313 (1968), [Correction: J. Geophys. Res. **73**, 6876 (1968)].
58. Volland, H., Mayr, H. G.: A theory of the diurnal variations of the thermosphere. Ann. Geophys. **25**, 907–919 (1970).
59. Chandra, S., Stubbe, P.: The diurnal phase anomaly in the upper atmospheric density and temperature. Planetary Space Sci. **18**, 1021–1033 (1970).
60. Mayr, H. G., Volland, H.: Diffusion model for the phase delay between thermospheric density and temperature. J. Geophys. Res. **77**, 2359–2367 (1972).
61. Bates, D. R., Moffett, R. J.: Response of a planetary thermosphere to heating by solar radiation. Planetary Space Sci. **16**, 1531–1537 (1968).
62. Rishbeth, H.: Superrotation of the upper atmosphere. Revs. Geophys. Space Phys. **10**, 799–819 (1972).
63. Hall, L. A., Hinteregger, H. E.: Solar radiation in the extreme ultraviolet and its variation with solar rotation. J. Geophys. Res. **75**, 6959–6965 (1970).
64. Bauer, S. J., Taylor, H. A.: Modulation of Venus ion densities associated with solar variations. Geophys. Res. Lett. **8**, 840–842 (1981).
65. Hantsch, M., Bauer, S. J.: Solar control of the Mars ionosphere. Planet. Space Sci. **38/4**, 539–542 (1990).
66. Tobiska, W. K.: Validating the solar EUV proxy. E10.7. J. Geophys. Res. **106**, 29969–29978 (2001).
67. Bauer, S. J.: Solar cycle variation of planetary exospheric temperatures. Nature **232**, 101–102 (1971).
68. Tsederberg, N. V.: Thermal Conductivities of Gases and Liquids. MIT Press (1965).
69. Dalgarno, A., Smith, F. J.: The thermal conductivity and viscosity of atomic oxygen. Planetary Space Sci. **9**, 1–2 (1962).
70. Gross, S. H.: On the exospheric temperature of hydrogen-dominated planetary atmospheres. J. Atmos. Sci., 29, 214–218 (1972).
71. Bauer, S. J., Hantsch, M. H.: Solar cycle variation of the upper atmosphere of Mars. Geophys. Res. Lett. **16**, 373–376 (1989).
72. Lammer, H., Selsis, F., Ribas, I., Guinan, E. F., Bauer, S. J., Weiss, W. W.: Atmospheric loss of exoplanets resulting from XUV heating. Astrophys J. Lett. **598**, L121–L124 (2003).
73. Öpik, E. J.: Selective escape of gases. Geophys. J. Roy. Astron. Soc., **7** 490–509 (1963).
74. Jeans, Sir James: The Dynamical Theory of Gases. Cambridge: University Press; (4th edition, Dover Publications, N.Y.) (1925).
75. Biutner, E. K.: The dissipation of gas from planetary atmospheres. Soviet Astron. AJ **2**, 528–537 (1958).
76. Chamberlain, J. W.: Planetary coronae and atmospheric evaporation, Planetary Space Sci. **11**, 901–96 (1963).
77. Chamberlain, J. W., Campbell, F. J.: Rate of evaporation of a non-Maxwellian atmosphere. Astrophys. J. **149**, 687–705 (1967).
78. Brinkman, R. T.: Departures from Jeans' escape rate for H and He in the earth's atmosphere. Planet. Space Sci. **18**, 449–478 (1970).
79. Pierrard, V.: Evaporation of hydrogen and helium atoms from atmospheres of Earth and Mars. Planet. Space. Sci., **51**, 319–327 (2003).
80. Hagenbuch, K. M., Hartle, R. E.: Simple model for a rotating neutral planetary exosphere. Phys. Fluids **12**, 1551 (1969).

81. Hartle, R. E.: Model for rotating and non-uniform planetary exospheres. Phys. Fluids **14**, 2592–2598 (1971).
82. Öpik, E. J., Singer, S. F.: Distribution of density in a planetary exosphere II. Phys. Fluids **4**, 221–233 (1961).
83. Johnson, F. S.: Density of an exosphere. Ann. Geophys. **22**, 56–61 (1966).
84. Léger, A., Selsis, F., Sotin, C., Guillot, T., Despois, D., Mawet, D., Ollivier, M., Labéque, F. A., Valette, C., Brachet, F., Chazelas, B., Lammer, H.: A new family of planets? "Ocean planets". Icarus, in press (2004).
85. Watson, A. J., Donahue, T. M., Walker, J. C. G.: The dynamics of a rapidly escaping atmosphere: applications to the evolution of Earth and Venus. Icarus **48**, 150–166 (1981).
86. Cody, A. M., Sasselov, D. D.: HD209458: Physical Parameters of the Parent Star and the Transiting Planet. Astrophys. J. **569**, 451–458 (2002).
87. Schneider, J., Rauer, H., Lasota, J. P., Bonazzola, S., Chassefière, E.: The cometary tail of giant extrasolar planets at small orbital distance. In: Brown Dwarfs and Extrasolar Planets. (R. Rebolo et al. eds.), ASP **134**, 241–245 (1998).
88. Zahnle, K., Kasting, J. F., Pollack, J. B.: Mass fractionation of noble gases in diffusion-limited hydrodynamic hydrogen escape. Icarus **84**, 502–527 (1990).
89. Chassefière, E.: Hydrodynamic escape of oxygen from primitive atmospheres: applications to the cases of Venus and Mars. Icarus **124**, 537–552 (1996).
90. Haff, P. K., Watson, C. C.: The erosion of planetary and satellite atmospheres by energetic atomic particles. J. Geophys. Res. **84**, 8436–8442 (1979).
91. Johnson, R. E.: Energetic Charged Particle Interactions with Atmospheres and Surfaces. Springer Verlag, Berlin (1990).
92. Sigmund, P.: Theory of sputtering. I. Sputtering yield of amorphous and polycristalline targets. Phys. Rev. **184**, 383–416 (1969).
93. Sieveka, E. M., Johnson, R. E.: Ejection of atoms and molecules from Io by plasma-ion impact. Astrophys. J. **287**, 418–426 (1984).
94. Lammer, H., Bauer, S. J.: Mercury's exosphere: Origin of surface sputtering and implications. Planet. Space Sci. **45**, 73–79 (1997).
95. Andersen, H. H., Bay, H. L.: Sputtering yield measurements, in: Sputtering by particle bombardment. (ed. R. Behrisch), Springer Verlag, Berlin (1981).
96. Killen, R. M., Ip, W.-H.: The surface-bounded atmospheres of Mercury and the Moon. Rev. Geophys. **37**, 361–406 (1999).
97. Broadfoot, A. L., Shemansky, D. E., Kumar S.: Mariner 10: Mercury atmosphere. Geophys. Res. Lett. **3**, 577–580 (1976).
98. Ness, N. F., Behannon, K. W., Lepping, R. P., Whang, Y. C., Schatten, K. H.: Magnetic field observations near Mercury: preliminary results from Mariner 10. Science **185**, 151–160 (1974).
99. Potter, A., Morgan, T. H.: Discovery of sodium in the atmosphere of Mercury. Science **229**, 651–653 (1985).
100. Wurz, P., Lammer, H.: Monte-Carlo simulation of Mercury's exosphere. Icarus **164**, 1–13 (2003).
101. Hunten, D. M., Morgan, T. M., Shemansky D. E.: The Mercury atmosphere. In: Mercury (F. Vilas, C. R. Chapman and M. S. Matthews, eds.). The University of Arizona Press, 562–613 (1988).
102. Lammer, H., Wurz, P., Patel, M. R., Killen, R., Kolb, C., Massetti, S., Orsini, S., Milillo, A.: The variability of Mercury's exosphere by particle and radiation induced surface release processes. Icarus **166**, 238–247 (2003).

103. Massetti, S., Orsini, S., Milillo, A., Mura, A., De Angelis, E., Lammer, H., Wurz, P.: Mapping of the cusp plasma precipitation on the surface of Mercury. Icarus **166**, 229–237 (2003).
104. Cheng, A. F., Johnson, R. E., Krimigis, S. M., Lanzerotti, L. J.: Magnetosphere, exosphere and surface of Mercury. Icarus **7**, 430–440 (1987).
105. Morgan, T. H., Zook, H. A., Potter, A. E.: Impact-driven supply of sodium to the atmosphere of Mercury. Icarus **75**, 156–170 (1988).
106. Sprague, A. L., Kozlowski, R. W., Hunten, D. M., Schneider, N. M., Domingue, D. L., Kells, W. K., Schmitt, W., Fink, U.: Distribution and abundance of sodium in Mercury's atmosphere, 1985–1988. Icarus, **129**, 506–527 (1997).
107. Killen, R. M., Morgan, T. H.: Maintaining the Na atmosphere of Mercury. Icarus **101**, 294–312 (1993).
108. Potter, A. E., Morgan, T. H.: Potassium in the atmosphere of Mercury. Icarus **67**, 336–340 (1986).
109. Bida, T. A., Killen, R. M., Morgan, T. H.:Discovery of calcium in Mercury's atmosphere. Nature **404**, 159–161 (2000).
110. Rasool, S. I., de Bergh, C.: The runaway greenhouse and the accumulation of CO_2 in the Venus atmosphere. Nature **226**, 1037–1039 (1970).
111. Hunten, D. M., Colin, L., Donahue, T. M., Moroz, V. I. (eds.): Venus. The University of Arizona Press (1979).
112. Bougher, S. W., Hunten, D. W., Phillips, R. J. (eds.): Venus II. The University of Arizona Press (1997).
113. Kieffer, H. H., Jakosky, B. M., Snyder, C. W., Matthews, M. S. (eds.): Mars. The University of Arizona Press (1992).
114. Donahue, T. M.: Aeronomy of CO_2 atmospheres: A review. J. Atmospheric Sci. **28**, 895–900 (1971).
115. Gehrels, T. (ed.): Jupiter. The University of Arizona Press (1976).
116. Gehrels, T., Matthews, M. S. (eds.): Saturn. The University of Arizona Press (1984).
117. Bergstrahl, J., Matthews, M. (eds.): Uranus. University of Arizona Press (1991).
118. Cruickshank, C. D.: Neptune and Triton. University of Arizona Press (1995).
119. Podolak, M., Hubbard, W. B., Stevenso, D. J. Models of Uranus' interior and magnetic field. In: Uranus (J. Bergstrahl, M. Matthews, eds.). University of Arizona Press, 29–61 (1991).
120. Hubbard, W. B., Podolak, M., Stevenson, D. J.: 1995, The Interior of Neptune. In: Neptune and Triton (C. D. Cruickshank, ed.). The University of Arizona Press, 109–138 (1995).
121. Marley, M. S., Gomez, P., Podolak, M.: Monte Carlo interior models for Uranus and Neptune. J. Geophys. Res. **100**, 23349–23353 (1995).
122. Griffith, C. A., Owen, T., Geballe, T. R., Rayner, J., Rannou, P.: Evidence for the exposure of water ice on Titan's surface. Science **300**, 628–630 (2003).
123. The extrasolar planets encyclopaedia: [http://www.obspm.fr/encycl/ encycl.html]
124. Lin, D. N. C., Bodenheimer, P., Richardson, D. C.: Orbital Migration of the Planetary Companion of 51 Pegasi to its Present Location. Nature, **380**, 606–607 (1996).
125. Trilling, D. E., Benz, W., Guillot, T., Lunine, J. I., Hubbard, W. B., Burrows, A.: Orbital Evolution and Migration of Giant Planets, Astrophys. J. **500**, 428–439 (1998).

126. Konacki, M., Torres, G., Jha, S., D. D. Sasselov D. D.: A new transiting giant planet. Astrophys. J. **596**, 1327–1331 (2003).
127. Sasselov, D. D.: The new transiting planet OGLE-TR-56 b: Orbit and atmosphere. Astrophys. J. **596**, 1327–1331 (2003).
128. Vidal-Madjar, A., Lecavalier des Etangs, A., Désert, J.-M., Ballester, G. E., Ferlet, R., Hébrand, G., Mayor, M.: An extended upper atmosphere around the extrasolar planet HD209458b. Nature **422**, 143–146 (2003).
129. Charbonneau, D., Brown, T. M., Noyes, R. W., Gilliland, R. L.: Detection of an Extrasolar Planet Atmosphere. Astrophys. J. **568**, 377–384 (2002).
130. Vidal-Madjar, A., Désert, J.-M., Lecavelier des Etangs, A., Hébrand, G., Ballester, G. E., Ehrenreich, D., Ferlet, R., McConnel, J. C., Mayor, M., Parkinson, C. D.: Detection of oxygen and carbon in the upper atmosphere of the extrasolar planet HD209458 b. sumitted to Astrophys. J. Lett. (2004).
131. Henry, R. J. W., McElroy, M. B.: Photoelectrons in planetary atmospheres. In: The Atmophere of Venus and Mars (J. C. Brandt and M. B. McElroy eds.). Gordon & Breach Science Publishers, New York (1968).
132. Spitzer, Lyman: Physics of Fully Ionized Gases. Interscience, New York (1956).
133. Hanson, W. B.: Electron temperatures in the ionosphere. Space Res. **111**, 282–303 (1963).
134. Dalgarno, A., McElroy, M. B., Moffett, R. J.: Electron temperatures in the ionosphere. Planetary Space Sci. **11**, 463–484 (1963).
135. Banks, P. M.: The thermal structure of the ionosphere. Proc. IEEE **57**, 258–281 (1969).
136. Nisbet, J. S.: Photoelectron escape from the ionosphere. J. Atmospheric Terrest. Phys. **30**, 1257–1278 (1968).
137. Nagy, A. F, Banks, P M.: Photoelectron fluxes in the ionosphere, J. Geophys. Res. **75**, 6260–6270 (1970).
138. Schunk, R. W., Hays, P. B.: Photoelectron energy losses to thermal electrons. Planetary Space Sci. **19**, 113 (1971).
139. Takanagi, J., Itikawa, Y.: Elementary processes involving electrons in the ionosphere. Space Sci. Rev. **11**, 380–450 (1970).
140. Schunk, R. W., Hays, P. B., Itikawa, Y.: Energy loss of low energy photoelectrons to thermal electrons. Planetary Space Sci. **19**, 125–126 (1971).
141. Swartz, W. E., Nisbet, J. S., Green, A. E. S.: Analytic expression for energy transfer rate from photoelectrons to thermal electrons. J. Geophys. Res. **76**, 8425–8426 (1971).
142. Dalgarno, A.: Inelastic collisions at low energies, Can. J. Chem. **47**, 1723–1729 (1969).
143. Cole, K. D.: Joule heating of the upper atmosphere. Australian J. Phys. **15**, 223–235 (1962).
144. Cole, K. D.: Electrodynamic heating and movement of the thermosphere. Planet. Space Sci. **19**, 59–75 (1971).
145. Rees, M. H., Walker, J. C. G.: Ion and electron heating by auroral electric fields. Ann. Geophys. **24**, 193 (1968).
146. Hasted, J. B.: Physics of Atomic Collisions. Washington: Butterworth (1964).
147. Bates, D. R.: Reactions in the ionosphere. Contemp. Phys. **11**, 105–124 (1970).
148. Bates, D. R., Dalgarno: Electronic recombination. In: Atomic and Molecular Processes. (D. R. Bates ed.), Ch. 7, New York: Academic Press, 245–271 (1962).
149. Fox, J. L., and Hać, A.: Spectrum of hot O at the terrestrial planets. J. Geophys. Res. **102**, 24005–24011 (1997).

150. Kim, J., Nagy, A. F., Fox, J. L., Cravens, T.: Solar cycle variability of hot oxygen atoms at Mars. J. Geophys. Res. **103** 29339–29342 (1998).
151. Kella, D. P., Johnson, P. J., Pedersen, H. B., Vejby-Christensen, Andersen, L. H.: The source of green light emission determined from a heavy-ion storage ring experiment. Science **276**, 1530–1533 (1997).
152. Lammer, H., Bauer, S. J.: Nonthermal atmospheric escape from Mars and Titan. *J. Geophys. Res.*, **96**, 1819–1825 (1991).
153. Lammer, H., Bauer, S. J.: Isotopic fractionation by gravitational escape. Space Sci. Rev. **106**, 281–292 (2003).
154. McDaniel, E. W., Cermak, V., Dalgarno, A., Ferguson, E. E., Friedman, L. Ion Molecule Reactions. Wiley-Interscience, New York (1970).
155. Polyanyi, J. C.: Chemical processes. In: Atomic and Molecular Processes (D. R. Bates, ed.). Ch. 21, Academic Press, New York 807–855 (1962).
156. Rapp, D.: Acidentally resonant asymmetric charge exchange in the protonosphere. J. Geophys. Res. **68**, 1773–1775 (1963).
157. Dungey, J. W.: The electrodynamics of the outer ionosphere. The Physics of the Ionosphere. Phys. Soc., London (1955).
158. Bates, D. R., Patterson, T. N. L.: Hydrogen atoms and ions in the thermosphere and exosphere. Planetary Space Sci. **5**, 257–273 (1961).
159. Fehsenfeld, F. C., Ferguson, E. E.: Thermal energy reaction rate constants for H^+ and CO^+ with O and NO. J. Chem. Phys. **56**, 3066–3070 (1972).
160. Ferguson, E. E.: D-region ion chemistry, Rev. Geophys. **9**, 997–1008 (1971).
161. Branscomb, L.: A review of photodetachment and related negative ion processes relevant to aeronomy. Ann. Geophys. **29**, 49–66 (1964).
162. Phelps, A. V.: Laboratory studies of attachment and detachment processes of aeronomic interest. Can. J. Chem. **47**, 1783–1793 (1969).
163. Stewart, A. I.: Photoionization coefficients and photoelectron impact excitation efficiencies in the daytime ionosphere. J. Geophys. Res. **75**, 6333–6338 (1970).
164. Peterson, V. L., van Zandt, T. E., Norton, R. B.: F-region night-glow emissions of atomic oxygen, 1. Theory. J. Geophys. Res. **71**, 2255 (1966).
165. Hanson, W. B.: Radiative recombination of atomic oxgen ions in the nighttime F region. J. Geophys. Res. **74**, 3720–3722 (1969).
166. Hanson, W. B.: A comparison of the oxygen ion-ion neutralization and radiative recombination for producing the ultraviolet nightglow. J. Geophys. Res. **75**, 4343–4346 (1970).
167. Dalgarno, A., Degges, T. C.: CO_2 dayglow on Mars and Venus. In: Planetary Atmospheres. (Sagan C. et al. eds.), I.A.U., 337–345 (1971).
168. Barth, C. A.: Planetary ultraviolet spectroscopy. Appl. Opt. **8**, 1295–1304 (1969).
169. Aikin, A. C.: X-ray glow from planetary atmospheres. Nature **227**, 1334 (1970).
170. McKinley, D. W. R.: Meteor Science and Engineering, McGraw-Hill, New York (1961).
171. Lebedinets, V. N., Shushkova, V. B.: Meteor ionization in the E layer. Planetary Space Sci. **18**, 1659–1663 (1970).
172. Molina-Cuberos, G. J., Lammer, H., Stumptner, W., Schwingenschuh, K., Rucker, H. O., Lopez-Moreno, J. J., Rodrigo, R., Tokano, T.: Titan's micrometeorite induced ionosphere. Planet. Space Sci. **49**, 143–153 (2001).
173. Kunkel, W B. (ed.): Plasma Physics in Theory and Application. McGraw-Hill Book Co., New York (1966).

174. Rishbeth, H.: A review of ionospheric F region theory. Proc. IEEE **55**, 1635 (1967).
175. Chandra, S.: Electron density distribution on the upper F region. J. Geophys. Res. **68**, 1937–1942 (1963).
176. Stubbe, P.: Simultaneous solution of the time-dependent coupled continuity equations, heat conduction equations, and equations of motion for a system consisting of a neutral gas, an electron gas and a four-component ion gas. J. Atmospheric Terrest. Phys. **32**, 865–903 (1970).
177. Nisbet, J. S.: On the construction and use of a simple ionospheric model. Radio Sci. **6**, 437–464 (1971).
178. Wright, J. W.: A model of the F-region above $h_{max}F_2$. J. Geophys. Res. **65**, 185–191 (1960).
179. Dessler, A. J.: Ionospheric heating by hydromagnetic waves. J. Geophys. Res. **64**, 397–401 (1959).
180. Ferraro, V C. A.: Diffusion of ions in the ionosphere. Tern Magn. Atmos. Electr. **50**, 215–222 (1945).
181. Kendall, P. C., Pickering, W. M.: Magnetoplasma diffusion at F_2-region altitudes. Planetary Space Sci. **15**, 825–833 (1967).
182. Bauer, S. J.: Diffusive equilibrium in the topside ionosphere. Proc. IEEE **57**, 1114–1118 (1969).
183. Mange, P.: The distribution of minor ions in electrostatic equilibrium in the high atmosphere. J. Geophys. Res. **65**, 3833 (1960).
184. Eddington, Sir A. S.: The Internal Constitution of the Stars. N. Y.: Dover Publications (1959).
185. Bauer, S. J.: Hydrogen and helium ions. Ann. Geophys. **22**, 247–251 (1966).
186. Lemaire, J., Scherer, M.: Model of the polar ion-exosphere. Planetary Space Sci. **18**, 103–130 (1970).
187. Walker, J. C. G.: Thermal diffusion in the topside ionosphere. Planetary Space Sci. **15**, 1151–1156 (1967).
188. Schunk, R., Walker, J. C. G.: Thermal diffusion in the F_2 region of the ionosphere. Planetary Space Sci. **18**, 535–557 (1970).
189. Bauer, S. J., Donahue, T. M., Hartle, R. E., Taylor, H. A.: Venus ionosphere: Photochemical and thermal diffusion control of ion composition. Science **203**, 109–111 (1979).
190. Chandra, S., Goldberg, R. A.: Geomagnetic control of diffusion in the upper atmosphere. J. Geophys. Res. **69**, 3187 (1964).
191. Angerami, J. J., Thomas, J. O.: Studies of planetary atmospheres, 1, The distribution of electrons and ions in the Earth's exosphere. J. Geophys. Res. **69**, 4537 (1964).
192. Rishbeth, H.: Thermospheric winds and the F region: A review. J. Atmospheric Terrest. Phys. **34**, 1–47 (1972).
193. Alfvén, H.: Partial corotation of a magnetized plasma. Icarus, **7**, 387–393 (1967).
194. Lemaire, J. F., Gringauz, K. I. (with contributions of D. L. Carpenter and V. Bassolo): The Earth's plasmashere. Cambridge University Press (1998).
195. Hess, W. N.: The Radiation Belt and Magnetosphere. Waltham, Mass.: Blaisdell Publ. Co. 1968.
196. Rucker. H. O.: Planetenatmosphären. In: *Erde und Planeten.* Bergmann Schaefer, de Gruyter, **7** 528–596 (1997).

197. Erkaev, N. V., Semenov, V. S., Shaidurov, V. A., Langmayr, D., Biernat, H. K., Rucker, H. O.: Propagation of nonlinear slow waves produced by pressure pulse along the Io flux tube. Adv. Space Res., **28**, 1481–1488 (2001).
198. National Research Council. Solar terrestrial research of the 1980's. National Academy of Sciences, Washington DC (1981).
199. Busse, F. H.: A model of the geodynamo. Geophys. J. R. Astr. Soc. **42**, 437–459 (1975).
200. Stevenson, D. J.: Planetary magnetic fields. Rep. Prog. Phys. **46**, 555–620 (1983).
201. Mizutani, H., Yamamoto, T., Fujimura, A.: A new scaling law of the planetary magnetic fields. Adv. Space Res. **12**, 265–279 (1992).
202. Sano, Y.: The Magnetic Fields of the Planets: A New Scaling Law of the Dipole Moments of the Planetary Magnetism. J. Geomag. Geoelectr. **45**, 65–77 (1993).
203. Ness, F. N.: Intrinsic magnetic fields of the planets: Mercury to Neptune. Phil. Trans. Royal Soc. Lond. A **349**, 249–260 (1994).
204. Bauer, S. J.: Physics of planetary ionospheres. In: Solar System Plasma Physics. (F. Mariani and N. F. Ness, eds.), **56**, 177–187 (1997).
205. Spreiter, J. R., Summers, A. L., Rizzi, A. W.: Solar wind flow past nonmagnetic planets; Mars and Venus. Planetary Space Sci. **18**, 1281 (1970).
206. Michel, F. C.: Solar wind interaction with planetary atmospheres. Rev. Geophys. **9**, 427–436 (1971).
207. Bauer, S. J., Hartle, R. E., Herman, J. R.: Topside ionosphere of Venus and its interaction with the solar wind. Nature **225**, 533 (1970).
208. Michel, F C.: Solar-wind induced mass loss from magnetic field-free planets. Planetary Space Sci. **19**, 1580–1583 (1971).
209. Cloutier, R. A., McElroy, M. B., Michel, F. C.: Modification of the Martian inosphere by the solar wind. J. Geophys. Res. **74**, 6215–6228 (1969).
210. Acuña, M. H., and 19 colleagues: Magnetic field and plasma observations at Mars: Initial results of the Mars Global Surveyor mission. Science **279**, 1676–1680 (1998).
211. Spreiter, J. R., Stahara, S. S.: Solar wind flow past Venus: Theory and comparisons. J. Geophys. Res. **98**, 17251–17262 (1980).
212. Luhmann, J. G.: A model of the ionospheric tail rays of Venus. J. Geophys. Res. **98**, 17615–17621 (1993).
213. Lichtenegger, H. I. M., Dubinin, E. M.: Model calculations of the planetary ion distribution in the Martian tail. Earth Planets Space **50**, 445–452 (1998).
214. Bauer, S. J.: Water on Venus: lack or loss? Ann. Geophys. **1**, 477–480 (1983).
215. National Research Council. The international magnetospheric study. Report of a Working conference on magnetospheric theory. National Academy of Sciences, Washington DC (1979).
216. Eviatar, A., Lenchek, A. M., Singer, S. F.: Distribution of density in an ionexosphere of a non-rotating planet. Phys. Fluids **7**, 1775–1779 (1964).
217. Hartle, R. E.: Ion-exosphere with variable conditions at the baropause. Phys. Fluids **12**, 455 (1969).
218. Donahue, T. M.: Polar ion flow: Wind or breeze?, Rev. Geophys. **9**, 1–10 (1971).
219. Dessler, A. J., Michel, F. C.: Plasma in the geomagnetic tail. J. Geophys. Res. **71**, 1421–1426 (1966).

220. Nishida, A.: Formation of a plasmapause, or magnetospheric plasma knee by combined action of magnetospheric convection and plasma escape from the tail. J. Geophys. Res. **71**, 5669–5680 (1966).
221. Banks, P. M., Holzer, T. E.: The polar wind. J. Geophys. Res. **73**, 6855–6868 (1968).
222. Banks, P. M., Holzer, T. E.: High latitude plasma transport: the polar wind. J. Geophys. Res. **74**, 6317–6332 (1969).
223. Marubashi, K.: Escape of the polar-ionospheric plasma into the magnetospheric tail, Rept. Ion. Space Res. Japan **24**, 322–346 (1970).
224. Hasegawa, A.: Plasma instabilities in the magnetosphere. Rev. Geophys. **9**, 703–772 (1971).
225. Thompson, W B.: An Introduction to Plasma Physics. London: Pergamon Press 1962.
226. Gold, T.: Motions in the magnetosphere of earth. J. Geophys. Res. **64**, 1219–1224 (1959).
227. Scarf, E. L.: Plasma in the magnetosphere. Adv. Plasma Phys. Vol. 1, A. Simon and W B. Thompson, eds. pp. 104–152. John Wiley, New York (1968).
228. Nagano, H.: Effect of finite ion Larmor radius on the Kelvin–Helmholtz instability of the magnetopause. Planet. Space Sci. **27**, 881–884 (1979).
229. Wolff, R. S., Goldstein, B. E., Yeates, C. M.: The onset and development of Kelvin–Helmholtz instability at the Venusian ionopause. J. Geophys. Res. **85**, 7697–7707 (1980).
230. Penz, T. Erkaev, N. V., Biernat, H. K., Lammer, H., Amerstorfer, U. V., Gunell, H., Kallio, E., Barabash, S. W., Orsini, S., Milillo, A., Baumjohann, W.: Ion loss on Mars caused by the Kelvin–Helmholtz instability. submitted to Planet. In press Planet. Space Sci. (2004).
231. Elphic, R. C., Ershkovich, A. I.: On the stability of the ionopause of Venus. J. Geophys. Res. **89**, 997–1002 (1984).
232. Terada, N., Machida, S., Shinagawa, S.: Global hybrid simulation of the Kelvin–Helmholtz instability at the Venus ionopause. J. Geophys. Res. **107**, 1471–1490, doi:10.1029/2001JA009224 (2002).
233. Ong, R. S. B., Roderick, N.: On the Kelvin Helmholtz instability of the Earth's magnetopause. Planet. Space Sci. **20**, 1–10 (1972).
234. Arshukova, I. L., N. V. Erkaev, N. V., Biernat, H. K., Vogl, D. F.: Interchange instability of the Venusian ionopause, Adv. Space Res. **22**, 1–7 (2004).
235. Lundin, R., Dubinin, E. M., Koskinen, H., Norberg, O., Pissarenko, N., Barabash, S. W.: On the momentum transfer of the solar wind to the Martian topside ionosphere. Geophys. Res. Lett. **18**, 1059–1062 (1991).
236. Pérez–de–Tejada, H.: Momentum transport in the solar wind erosion of the Mars ionosphere. J. Geophys. Res. **103**, 31499–31508 (1998).
237. Lammer, H., Kolb, C., Penz, T., Amersdorfer, U. V., Biernat, H. K., Bodiselitsch, B.: Estimation of the past and present Martian water-ice reservoirs by isotopic constraints on exchange between the atmosphere and the surface. Int. J. Astrobiology **2**, 195–202 (2003).
238. Moutou, C., Brage, P., Deleuil, M., Jorda, L. and the COROT Team: The exoplanet program of the CoRoT space mission. Space Sci. Rev., 1–4 (2004).
239. Defaÿ, C., Deleuil M., Barge, P.: A Bayesian method for the detection of planetary transits. Astron. Astrophys. **365**, 330–340 (2001).
240. Bordé, P., Rouan, D. & Léger, A.: Exoplanet detection cabability of the COROT space mission. Astron. & Astrophys., **405**, 1137–1144 (2003).

241. Borucki, W. J., Koch, D. G., Dunham, E. W., and Jenkins, J. M.: The Kepler mission: A mission to determine the frequency of inner planets near the habitable zone of a wide range of stars. In: Planets Beyond the Solar System and Next Generation of Space Missions. (D. Soderblom, ed.), ASP-CS, **119**, 153–173 (1997).
242. Léger, A., Mariotti, J.-M., Mennesson, B., et al. 1996. Could we search for primitive life on extrasolar planets in the near future? Icarus, **123**, 249–255.
243. Beichman, C. A., Woolf, N. J., and Lindensmith, C. A. 1999. The Terrestrial Planet Finder (TPF): A NASA Origins Program to Search for Habitable Planets. JPL Publication 99–003, on-line: http://tpf.jpl.nasa.gov/library/tpf_book/.
244. Selsis, F., Despois, D., Parisot, J.-P.: Signature of life on exoplanets: Can Darwin produce false positive detections? Astron. Astrophys. **388**, 985–1003 (2002).
245. Huang, S.-S.: Occurence of life in the Universe. Am. Sci. **47**, 397–402 (1959).
246. Huang, S.-S.: Life outside the solar system. Am. Sci. **202**, 55–63 (1960).
247. Dole, S. H.: Habitable Planets for Man. Blaisdell, New York (1964).
248. Shklovskii, I. S., Sagan, C.: Intelligent life in the Universe. Holden-Day, San Francisco (1966).
249. Kasting, J. F., Whitmire, D. P., Reynolds, R. T.: Habitable Zones around Main Sequence Stars. Icarus **101**, 108–128 (1993).
250. Kasting, J. F.: Runaway and moist greenhouse atmospheres and the evolution of Earth and Venus. Icarus **74**, 472–494 (1988).
251. Walker, J. C. G., Hays, P. B., Kasting, J. F.: A negative feedback mechanism for the long-term stabilization of Earth's surface temperature. J. Geophys. Res. **86**, 9776–9782 (1981).
252. Dvorak R., Pilat-Lohinger E., Funk B., Freistetter F.: Planets in habitable zones: A study of the binary Gamma Cephei. Astron. Astrophys. **398**, L1–L4 (2003).
253. Lunine, J. I.: The occurrence of Jovian planets and the habitability of planetary systems. Proc. Natl. Acad. Sci. **98**, 809–814 (2001).
254. Joshi, M. M. Climate model studies of synchronously rotating planets. Astrobiology **3**, 415–427 (2003).
255. Courtillot, V.: Evolutionary catastrophes: The science of mass extinctions. Cambridge University Press (2002).
256. Melosh, H. J., Vickery, A. M. Impact erosion of the primordial atmosphere of Mars. Nature **338**, 487–489 (1989).
257. Brain, D. A., Jakosky, B. M.: Atmospheric loss since the onset of the Martian geologic record: Combined role of impact erosion and sputtering. J. Geophys. Res. **103**, 22689–22694 (1998).
258. Pepin, O. R.: Evolution of Earth's noble gases: consequences of assuming hydrodynamic loss driven by giant impact. Icarus **126**, 148–156 (1997).
259. Lecavelier des Etangs, A., Vidal-Madjar, A., McConnell, J. C., Hébrard, G. Atmospheric escape from hot Jupiters. in press Astron. Astrophys. (2004).
260. Baraffe, I., Selsis, F., Chabrier, G., Barman, T. S., Allard, F., Hauschildt, P. H., Lammer, H. The effect of evaporation on the evolution of close-in giant planets. in press Astron. Astrophys. (2004).

Bibliography

Comprehensive Treatments of Topics Discussed in this Book

Atreya, S. K.: Atmospheres and ionospheres of the outer planets and their satellites. Springer Verlag, Heidelberg, New York (1986).

Atreya, S. K., Pollack, C. K., Matthews, M. S. (eds.): Origin and evolution of planetary and satellite atmospheres. The University of Arizona Press (1989).

Banks, P. M., Kockarts, G.: Aeronomy, Part A., Academic Press (1973).

Barstow, M. A., Holberg, J. B.: Extreme ultraviolet astronomy. Cambridge University Press (2003).

Chamberlain, J. W., Hunten, D. M.: Theory of planetary atmospheres (2nd Edition). Academic Press (1987).

Cockell, C. S.: Impossible extinction. Natural catastrophes and the supremacy of the microbial world. Cambridge University Press (2003).

Dorminey, B.: Distant wanderers: The search for planets beyond the solar system. Springer Verlag, New York, Heidelberg, (2002).

Hanel, R. A., Conrath, B. J., Jennings, D. E., Samuelson, R. E.: Exploration of the solar system by infrared remote sensing. Cambridge University Press (1992).

Horneck, G., Baumstark-Khan, C.: Astrobiology: The quest for the conditions of life. Springer Verlag, New York, Heidelberg, (2002).

Jakosky, B.: The search for life on other planets. Cambridge University Press (1998).

Johnson, R. E.: Energetic charged-particle interactions with atmospheres and surfaces. Springer Verlag, New York, Heidelberg (1990).

Kivelson, M. G., Russel, C. T. (eds.): Introduction to space physics. Cambridge University Press (1995).

Lewis, J. S.: Physics and chemistry of the solar system. Academic Press (1994).

Lewis, J. S., Prinn, R. G.: Planets and their atmospheres. Academic Press (1989).

Lunine, J. I.: Earth: Evolution of a habitable world. Cambridge University Press (1999).

Mendillo, M. Nagy, A. F., Waite, J. H. (eds.): Atmospheres in the solar system: Comparative aeronomy. AGU Monograph 130 (2002).

Schunk, R. W., Nagy, A.: Ionospheres: Physics, plasma physics and chemistry. Cambridge University Press (2002).

Tokano, T. (ed.): Water on Mars and Life. Springer-Verlag, New York, Heidelberg (2004).

List of Symbols

A	constant; area
a	constant, factor
$\boldsymbol{B}$ (B)	magnetic field vector (magnitude)
$\mathfrak{B}$ B	constant
b	constant
C	capacity (heat, electric)
Ch( )	Chapman function
C	velocity of light in vacuum
c_{i}	ion acoustic speed
c_{s}	speed of sound
D	distance; dispersion relation parameter
D_{a}	ambipolar (plasma) diffusion coefficient
D_{B}	Bohm (turbulent plasma) diffusion coefficient
D_{j}	molecular diffusion coefficient
d; d	diameter; day
$\boldsymbol{E}$ (E)	electric field
E	energy
e; e	base of natural logarithm; electron charge (esu)
$\boldsymbol{F}$	force
F_j	particle flux
$\mathfrak{F}$	heat flux
f; $\mathfrak{f}$	wave frequency; oscillator strength
$f( )$	distribution function
G	gravitational constant
g	acceleration of gravity
$\mathfrak{g}$	emission rate factor
H	atmospheric (pressure) scale height
H_ρ	density scale height
H_N	plasma density scale height
$\mathfrak{H}$	plasma (pressure) scale height
h; $\mathfrak{h}$	altitude; Planck's constant

I; I	intensity of radiation; magnetic dip (inclination)
$\mathfrak{I}$	column emission rate (airglow)
i	imaginary number $\sqrt{-1}$
J	ionization rate coefficient
$J(> P)$	integral rigidity spectrum
$j(E)$	differential energy spectrum
$\boldsymbol{j}$ (j)	electric current
$(\boldsymbol{K})$	dielectric tensor
$K(T)$	heat conductivity
K_{D}	eddy diffusion coefficient
$\boldsymbol{k}$, k	wave vector, propagation constant
k	rate constant
k_{B}	Boltzmann constant
L	scale length; loss rate; McIlwain parameter; dispersion relation parameter
$\mathfrak{M}$	magnetic moment $(R_0^3 B_{\mathrm{s}})$
M	planetary mass; Mach number
m	mean molecular mass
m_j	mass of jth constituent
$\hat{m}_j$	mass in amu
m_+	mean ion mass
N	plasma number density
$\tilde{N}$	refractivity
$\mathfrak{N}$	total content (number of particles in a column of $1\,\mathrm{cm}^2$ cross section)
n	harmonic number
n	neutral particle number density; refractive index
P	rigidity; dispersion relation parameter; phase path length; probability.
P'	group path length
p	pressure
Q	heating rate
q	ion-pair production (ionization) rate; charge density (eN)
R	planetocentric distance; dispersion relation parameter; geometric range
R_0	planetary radius
R^*	minimum radial distance of grazing ray
$\mathfrak{R}$	particle range $(\mathrm{g\,cm}^{-2})$
$\boldsymbol{r}$	radius vector
r_1	Expansion radius

r_B	Larmor (cyclotron, gyro) radius
s	surface
S	flux; sputter rate, dispersion relation parameter,
$F_{10.7}$	10.7 cm (2800 MHz) solar radio flux
s	pathlength
T	absolute temperature
t	time
v_0	most probable velocity
V	volume; electric potential (voltage)
V_A	Alfvén velocity
V_1, V_2	hydromagnetic wave mode velocities
$\boldsymbol{v}$, (v)	particle or wave velocity
$\boldsymbol{v}_D$	plasma (ambipolar) diffusion velocity
$\boldsymbol{v}_E$	plasma drift velocity
$\boldsymbol{v}_g$	group velocity
$\boldsymbol{v}_{ph}$	phase velocity
v_l	longitudinal electron velocity $(k_B T_e/m_e)^{\frac{1}{2}}$
v_∞	escape velocity
$\langle v_R \rangle$	effusion velocity
W	energy
$\boldsymbol{w}_j$	molecular diffusion velocity
w	wind speed
X	escape parameter $(v_\infty/u_0)^2$; magnetoionic parameter; atomic constituent
x	pathlength; cartesian coordinate; Chapman function parameter (R/H)
Y	rotational (escape) parameter $(\Omega R/u_0)$; magnetoionic parameter; sputter yield atomic constituent
y	cartesian coordinate
Z	normalized height parameter (z/H); magnetoionic parameter; charge number; atomic constituent
z	height parameter; cartesian coordinate.

α	polarizability; pitch angle; factor of proportionality; meteor line density; incoherent scatter parameter
α_D	dissociative recombination coefficient
α_j	thermal diffusion factor
α_{mn}	ion–ion recombination (mutual neutralization) coefficient
α_r	radiative recombination coefficient
$\hat{\alpha}$	sputter parameter

β	scale height gradient ($\mathrm{d}H/\mathrm{d}z$); linear loss rate coefficient
$\Gamma_\infty()$	complete gamma function
$\Gamma_\kappa()$	incomplete gamma function
γ	ratio of specific heats (adiabatic index); growth rate; Euler's constant
δ	mass density (meteor particles), declination (solar)
ε_j	heating efficiency
ζ	height parameter
η	viscosity
η_i	ionization efficiency ($\sigma_\mathrm{i}/\sigma_\mathrm{a}$)
η_{jk}	relative abundance
θ	angle between wave vector $\boldsymbol{k}$ and magnetic field $\boldsymbol{B}$
θ_c	Čerenkov cone half-angle
κ	attenuation factor
Λ	Coulomb parameter
λ	wavelength; mean free path
λ^-	negative ion–electron concentration ratio
λ_D	Debye length
μ_{jk}	reduced mass ($m_j m_k/m_j + m_k$)
ν	frequency
ν_{jk}	collision frequency between jth and kth constituent
ξ	partition function
Π_k	generalized plasma frequency (dispersion relation)
ρ	mass density
σ	cross-section (general)
σ_D	momentum cross-section
(σ)	conductivity tensor
τ	time constant; period
$\Phi()$	error integral
Φ	ionizing radiation flux
ϕ	potential; particle flux
φ	latitude
χ	zenith angle
Ψ	arbitrary variable
ψ	aspect angle
Ω	solid angle; rotation rate; angular frequency (ion modes)
ω	angular frequency

Subscripts

B	gyro-, cyclotron
b	boundary
C	chemical
c	critical
D	diffusion; dissociation
e; E	electron; electric field
g	gravitational
i	ion; ionization
j	jth constituent
k	kth constituent
l	longitudinal, i.e., parallel to wave vector $\boldsymbol{k}$
M	Maxwellian
m	maximum, peak
N	plasma
n	neutral
o; o	reference level; ordinary mode
P	planet
p	proton; plasma
R, r	radial
s	surface
w	wind
x	x-component; extraordinary mode
y	y-component
z	z-component; z-mode
$\parallel$	component parallel to $\boldsymbol{B}$
$\perp$	component perpendicular to $\boldsymbol{B}$
∞	upper limit; escape
$\odot$	Sun, solar
$\oplus$	Earth
σ	Mars
φ	Venus
$\mathfrak{U}$	Jupiter
+	(positive) ion
−	negative ion

Index